Processing and Mechanical Properties of AlCoCrCuFeNi and AlCuTaVW High - Entropy Alloys.

A thesis

Submitted by

G Ramya Sree

in partial fulfilment of the requirement for the award of the degree of

Doctor of Philosophy

in

Materials Engineering

Under the supervision of

Dr. Koteswararao V Rajulapati

School of Engineering Sciences and Technology

University of Hyderabad

India

DECLARATION

I, **G Ramya Sree**, declare that this thesis work entitled "**Processing and mechanical properties of AlCoCrCuFeNi and AlCuTaVW high-entropy alloys"**, submitted in partial fulfillment of the requirements for the award of **Doctor of Philosophy** (in Materials Engineering) in the School of Engineering Sciences and Technology (SEST), University of Hyderabad is completely my own work except for those referenced. This work was done under the supervision of **Dr. Koteswararao V Rajulapati**. This report is a record of bonafide work carried out by me and the results incorporated in it have not been reproduced / copied from any source. This work has not been submitted to any other University or Institute for the award of any other degree or equivalent.

G Ramya Sree
Reg. No.: 09ETMM01
School of Engineering Sciences and Technology
University of Hyderabad

DEDICATION

Dedicated to the glory of God

I would like to dedicate this work to my in-laws, **KLGS Rajakumari** and **D Purnachandra Babu**, as it would not have been possible without their tireless support and dedication. The hours you devoted to **Austin**'s (my son) upbringing have empowered me to dedicate myself to my career and empower me. Your selfless support has enabled me to fulfill my dreams, and for that am ever grateful.

G Ramya Sree

UNIVERSITY OF HYDERABAD
SCHOOL OF ENGINEERING SCIENCES & TECHNOLOGY

Dr. Koteswararao V. Rajulapati,
Associate Professor, SEST
University of Hyderabad
P.O. Central University
Hyderabad – 500 046, INDIA

Phone: 040 – 23134452
Fax: 040 – 23011087
E-mail: kvrse@uohyd.ernet.in

CERTIFICATE

This is to certify that the thesis work entitled "**Processing and mechanical properties of AlCoCrCuFeNi and AlCuTaVW high-entropy alloys**" submitted by **G Ramya Sree** bearing Reg. No. **09ETMM01** in partial fulfillment of the requirements for the award of the degree of **Doctor of Philosophy** in **Materials Engineering** is a bonafide work that has been carried out by her under my guidance. The thesis work has not been submitted previously in part or in full to this or any other University or Institute for the award of any degree or equivalent.

Thesis supervisor

Dr. Koteswararao V Rajulapati
Associate Professor
School of Engineering Sciences and Technology
University of Hyderabad

Approved by

Prof. M. Ghanashyam Krishna
Dean
School of Engineering Sciences and Technology
University of Hyderabad

CERTIFICATE

This is to certify that the thesis entitled **Processeing and Mechanical Properties of AlCoCrCuFeNi and AlCuTaVW High-Entropy Alloys** submitted by **G Ramya Sree** bearing registration number **09ETMM01** in partial fulfillment of the requirements for award of **Doctor of Philosophy** in the **School of Engineering Sciences and Technology** is a bonafide work carried out by him/her under my supervision and guidance.

This thesis is free from plagiarism and has not been submitted previously in part or in full to this or any other University or Institution for award of any degree or diploma.
Parts of this thesis have been:

A. published in the following publications:
   1. Acta Materialia, 125 (2017) 58-68, Section 4.1 and 4.2 in Chapter 4.
B. presented in the following conferences:
   1. HEA, 2015 (International)
   2. IUMRS, 2016 (International)
   2. IWHEM, 2017 (International)

Further, the student has passed the following courses towards fulfillment of coursework requirement for PhD and was exempted from doing coursework (recommended by Doctoral Committee) on the basis of the following courses passed during his M.Tech program and the M.Tech degree was awarded:

Course	Course Name	Credits	Pass/Fail
MT703	Thermodynamics of Materials	4	Pass
MT710	Concepts of Materials Science	4	Pass
MT715	Characterization of Materials	4	Pass
MT720	Synthesis and processing of Advanced	4	Pass
MT724	Seminar	2	Pass
MT730	Design and Selection of Engineering Materials	4	Pass
MT735	Materials processing & Characterization Laboratory	4	Pass
MT725	Diffusion and Kinetics	4	Pass
MT726	Modelling and Simulation in Materials Engineering	4	Pass
MT727	Materials Processing & Characterization Lab - II	4	Pass
MT728	Nano Materials and Technologies	4	Pass
MT729	Surface Engineering	2	Pass
MT730	Nuclear Materials	4	Pass
MT731	Ceramic: Science and Technology	4	Pass
MT732	Seminar	2	Pass
MT780	Dissertation	18	Pass
MT801	Research Methodology	4	Pass

(Supervisor) **(Dean of School)**

Acknowledgements

Thanks and glory be to **Jesus Christ** our Lord, the most benevolent, the omnipotent and omniscient, whose power working in me has enabled to complete this work in its entirety.

I acknowledge the privilege of working under the esteemed guidance of my supervisor **Dr. Koteswararao V. Rajulapati** who helped me in carving out this work in such an incredible way for which I am ever indebted. He has been a constant source of knowledge and his acute scientific thought has truly been of great impact not only on my work but also on my personal behavior. I cannot thank him enough for this extraordinary opportunity of working with him. I am thankful for the advice and guidance of **Prof. Ghanashyam Krishna**, Dean, SEST and to **Prof. K. Bhanu Sankara Rao** (Former Dean). I am also grateful for the suggestions from **Dr-Ing VVSS Srikanth**.

I express my sincere gratitude to **Dr. Ravi Chandra** for helping me in the characterization of my samples and also **Dr.Tata Narasinga Rao** and **Dr. Dibyendu Chakravarty** for helping in sintering the samples by SPS technique, three of these gentlemen from ARCI. The technical staff at the UoH have been very cordial and helped me whenever needed, especially **Mallesh, Padma, Venu, Dhinakar, Mallathi**. Many thanks to my dear friends **Harish Ojha, Sreedevi, Bhavana, Nagini, Pardhu, Rahul, Abhijit, Johny Varghese, Pavithra, Archana, Pramod, Supriya, Akanksha, Sunil Pandu, Rajesh, Navindra, Janaki Ram, Paul Praveen, Kaushi** and other friends who have been of great help in good times and bad too.

My dear husband, **D. Gnana Vardhan** and my loving son, **D. Gabriel Austin** to whom I have the pleasure of thanking deserve a special mention and I am blessed to have them in my life. I am grateful to God for my parents (**G.S. Raju, G. Usha Rani)** and heartily thank them. Also my In-

laws (**D. Purna Chandra Babu, K.L.G.S. Raja Kumari)** and my family members who prayed and stood by me all these days. The support and patience that they exhibited all through my working days has helped me stay committed to my work. Once again I thank God for this magnificent opportunity that was purposed for me and for the wisdom that God has bestowed upon me to complete this work.

G Ramya Sree

List of Publications

1. Ramya Sree Ganji, P. Sai Karthik, K. Bhanu Sankara Rao, Koteswararao V. Rajulapati, "Strengthening mechanisms in equiatomic ultrafine grained AlCoCrCuFeNi high-entropy alloy studied by micro and nanoindentation methods", Acta Materialia, 2017 Vol 125, pages 58-68 (Impact factor: 5.038).
2. Ramya Sree Ganji, Rajesh Bura, P.V.V. Srinivas, Koteswararao V. Rajulapati, A novel AlCuTaVW high-entropy alloy synthesized using mechanical alloying and spark plasma sintering: microstructural evolution and mechanical properties, (to be submitted Materials Science and Engineering A Journal).

Conferences Attended

1) Poster presentation at International Workshop on High Entropy Materials, on "Effect of sintering temperature on the structure and mechanical properties of ball milled multi-component AlCuTaVW alloy" held at University of Hyderabad, 2017.

2) Poster presentation at National workshop on High Entropy Alloys, Prospects and Challenges, on "Understanding Structural Evolution and Associated Mechanical Behavior in a Nanocrystalline AlCrCuCoFeNi High Entropy Alloy System" held at IIT Madras, 2015.

3) Attended One day Workshop on "Advanced Engineering Materials: An Industry Perspective" held at University of Hyderabad, 2016.

4) Participated in "National conference on new materials and Processes for improving Quality of Infrastructure" held at University of Hyderabad, 2012.

5) Attended a National Workshop on "Evaluation and Prevention of Corrosion and Failures" held at University of Hyderabad, 2012.

6) Oral presentation at International Symposium for Research Scholars on Metallurgy, Materials Science & Engineering, held at IIT Madras, 2012.

Contents

List of Figures

Chapter 1

Chapter 2

Chapter 3

Chapter 4

4.1 Microstructural evolution in equiatomic ultrafine grained AlCoCrCuFeNi high-entropy alloy

4.2 Strengthening mechanisms in equiatomic ultrafine grained AlCoCrCuFeNi high-entropy alloy studied by micro and nanoindentation methods

4.3 A novel AlCuTaVW High Entropy alloy synthesized using mechanical alloying and spark plasma sintering: microstructural evolution and mechanical properties

List of Tables

Chapter 3

Chapter 4

Abstract

The recent emergence of multi-component alloys with the presence of all the alloying elements in equi-atomic proportions has opened up a new paradigm for the engineers/scientists for the development of novel class of materials with enhanced properties over existing conventional materials. A major striking and interesting feature of these investigations is realization of simple solid solutions (fcc/bcc/hcp) in these equiatomic multicomponent systems instead of formation of amorphous structures or intermetallic compounds. Nanocrystalline HEAs have been less studied and the strengthening mechanisms operated in HEAs have not been investigated in detailed till now in the literature.

Nanocrystalline HEAs have been synthesized using mechanical alloying (MA) synthesis technique. To retain the nano structure even after consolidation to bulk sample, spark plasma sintering (SPS) techniques has been employed in the current investigation. Structural characterization was studied in detailed using X-ray diffractometry (XRD), scanning electron microscopy (SEM) and transmission electron microscopy (TEM). Evolution of mechanical properties being the main aim, Vickers microindentation and depth sensing nanoindentation techniques were employed.

Nanocrystalline AlCoCrCuFeNi and AlCuTaVW HEAs have been synthesized in equal atomic ratios, using ball milling for 60 h and 25 h respectively. It is observed that the MA process not only reduced the grain size but also refined the microstructure. To achieve high dense bulk alloy, different SPS parameters like sintering temperature and holding durations have been employed and their characterization has been studied in detailed in each case. The microstructural dependence on the SPS parameters have also been discussed in this work.

A single phase fcc based nanocrystalline solid solution in equiatomic AlCoCrCuFeNi HEA has been formed after 60 h of ball milling. The milled powders were of "plate-like" morphology and possessed a precise lattice parameter of 3.64 Å. Compaction of ball milled powders into bulk components using SPS at 750 ºC led to the precipitation of ordered bcc (B2). Detailed structural and microstructural investigations on the sintered alloy indicate the presence of bimodal grain size distribution with average grain sizes of 112 ± 46 nm and 1550 ± 500 nm, solid solutions (fcc and B2 phases), dislocations and twin boundaries. A high hardness value of 6.5 ± 0.1 GPa was measured for the sample sintered at 750 ºC/15 min using Vickers microindentation. Comprehensive analysis on probable strengthening mechanisms suggests that frictional stress, Taylor hardening, Hall-Petch strengthening, solid solution strengthening and twin boundary strengthening mechanisms are responsible. The Taylor hardening arising from intersection of dislocations and grain boundary (Hall-Petch) strengthening arising from grain boundary-dislocation interactions together account for 85% of the observed flow stress. The Tabor's ratio, $\left(H/\sigma_{flow}\right)$ attained a value of 2.7 which is in close agreement with that for conventional polycrystalline materials. Nanoindentation at a peak force of 8000 µN yielded a high hardness value of 8.13 ± 0.15 GPa and an elastic modulus of 172±10 GPa. A low strain rate sensitivity of 0.0084 and an activation volume of 13 b^3 (b is 0.23 nm) were measured, suggesting that grain boundaries, twin boundaries and interphase boundaries (fcc/B2) are influential in governing the deformation kinetics.

A novel equiatomic AlCuTaVW HEA resulted a single phase solid solution with a bcc crystal structure after 25 h of ball milling. The bcc phase lattice parameter is measured to be 3.17 Å and the crystallite size is measured as 7 nm. The compaction of milled powders is done by SPS at various temperatures from 415 to 1250 ºC. Two fcc phases and an ordered B2 phase have evolved

during SPS. With the increase in the sintering temperature, the phase transformation from bcc phase to ordered B2 phase is observed. The crystallite size measured after sintering at 1050 ºC is 11 nm and 1250 ºC is 13 nm. The morphology of the sintered pellets have a continuous white phase and a discontinuous dark phase. The dark phase is detected to be Al rich phase. The microhardness and nanohardness of the alloy sintered at 1050 ºC is 14 GPa and for the sample sintered at 1250 ºC is 13 GPa. The reported hardness values are high compared to other HEAs and conventional ceramics and cermets. Fracture toughness value of 11 MPa $m^{1/2}$ is measured from the cracks generated at the Vickers indentations edges at both the sintering temperatures of 1050 and 1250 ºC in AlCuTaVW alloy. The superior mechanical properties of AlCuTaVW HEA are attributed to the nanocrystalline nature in the bulk material, where the forest dislocations are pinned down at the grain boundaries and because of presence of refractory elements in the alloy.

Chapter 1 Introduction

1.1 Definition of high entropy alloys

Of all the substances that exist, metals have a distinguishing role in the human history. Ever since metals were discovered the quest for better and better materials continued and persists even today. As the knowledge of working with metals (which is termed as metallurgy) increased, metals became more significant in the development of tools, weapons and many more applications. The emergence of more complex alloys has paved the way for stronger and durable materials. Conventional alloys have a single or very rarely two principal elements [1, 2]. After extensive research, inventions and innovation on conventional alloys a remarkable and yet an unconventional approach to alloying resulted in the high entropy alloys (HEAs) [3-5]. This rudimentary alteration in the alloying by itself is a ground-breaking realization in the history of modern metallurgy and alloying materials.

A fundamental distinction of HEAs compared to the conventional alloys is that HEAs comprise of multiple principal elements in equimolar or near equimolar concentration, most plausible of a minimum of 5 ($N \geq 5$) elements, with the concentration of each principal element in the range of 5 through 35 atomic %, alongside discretionary minor elements with concentration ranging below 5 atomic % [4, 6, 7]. Contrary to the traditional physical metallurgical understanding, which says that multi-component alloys may result in solubility issues and also formation of complex inter-metallic compounds, these high mixing alloys result in simple solid solutions that are easy to analyze [8, 9]. In the below pictorial representation (**Fig. 1.1**) it is understood that the conventional alloys were designed with a focus on the corners of the phase diagram, while the designing of HEAs is done shifting the focus to the central region of the ternary phase diagram [10, 11]. Multi-principal HEAs form a random solid solutions with simple crystal structures (face-centered cubic

(fcc) or body-centered cubic (bcc) structures). The reason for the simple solid structure formation is probably high mixing of entropy which is discussed in detail in section 2.1.

At constant pressure, Gibbs phase rule is $F = C + 1 - P$ for multi component (C) systems. This rule is used to determine the number of phases (P) formed in thermodynamic equilibrium state [12]. In a binary alloy, maximum allowed number of phases is only 3 when the degrees of freedom is 0, however practically at room temperature the number of phases is 2. In a ternary alloys, using phase rule the possible number of phases formed in the alloy in equilibrium state are 4. However in multicomponent HEAs, the number of phases formed are the prediction of far below Gibbs phase rule. The reason behind this is still being worked upon by the research community [8, 13].

A set of rules for the complete solubility of elements in a binary alloy to form a solid solution as given by William Hume Rothery [12, 14, 15] are,

1. The crystal structure of the solute and solvent atoms must be same.
2. The atomic size difference between the solute and solvent atoms must not be more than 15%.
3. The solute and solvent atoms should have same valence and similar electronegativity. If there is a huge difference in electronegativity, intermetallic compound is formed instead of solid solution.

These are considered as the basic rules to explain the solid solution formation. However in the multi principal HEAs, all atoms are considered as solute atoms and have equal probability to occupy a lattice site [8] forming a solid solution. Hence finding the solid solution has become one of the primary interests. Many research groups attempted to explain the parameters for phase formation rules in HEAs [8, 11, 16], thereby to design a HEA for the desired applications with single solid phases [1, 17-23].

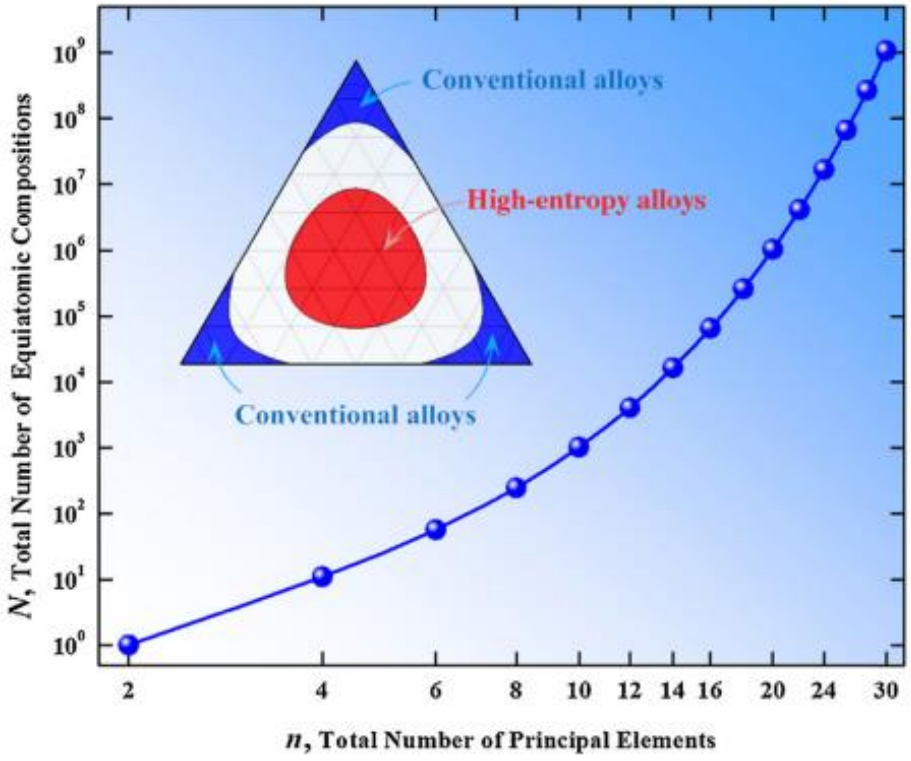

Fig. 1.1 A plot of number of principal elements against the number of equiatomic compositions. The insert is there ternary phase diagram illustrating conventional and high entropy alloys concentrations [7].

1.2 Development of HEAs

In a short span of 12 years that HEAs were introduced to the research community, there has been an incredible attention, predominantly because of the simple crystal structures and outstanding properties. In the late 70's Brain Cantor introduced the concept of multi-element alloys, however in 2004 these multi-element alloys were named as HEA by JW Yeh [1].

Researchers and academicians are exploring different compositions and studying them to know different physical properties for different applications. **Fig. 1.2** quantifies the ever increasing interest and exploration of the HEAs. The numerous publications is evidence that the research community has embraced the concept in its nascent stage and is thriving for its advancement. Elements in the periodic table is the limit to imagine and investigate.

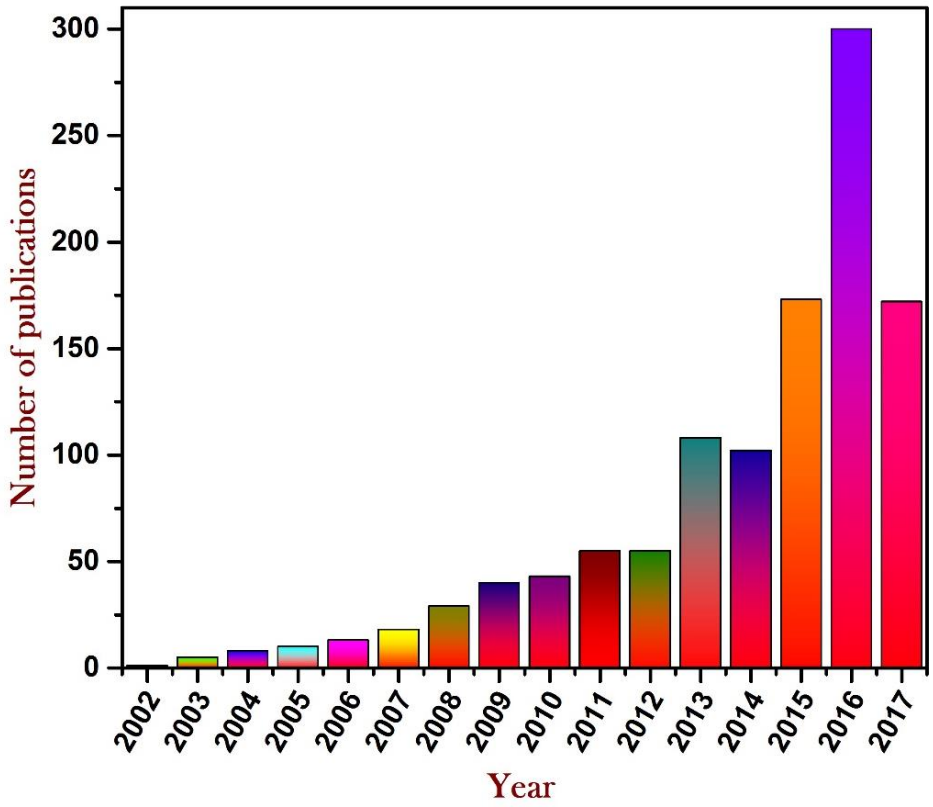

Fig. 1.2 Number of global publication on HEAs. (Updated on April 20th, 2017).

Out of 118 elements in the periodic table, only 45 elements can be used as structural metal HEAs [24]. With these 45 elements few thousands of 5 elements to 13 elements HEA combinations can be synthesized. Other than structural metals, there are refractory metal, rare earth metals, which were also included in the combinations thereby increasing the probability of different HEA compositions. On the other hand, to synthesize HEAs many different techniques have been explored viz. vacuum arc melting [25], laser cladding [26], magnetic sputtering [27], plasma spraying [28], mechanical alloying (MA) [29-32] and spark plasma sintering (SPS) [33-35]. Melting and casting is the most familiar one among all the processes but segregation of elements is the primary problem [36]. Whereas SPS is widely used for synthesis of advanced nanomaterials because of the rapid synthesis on application of pressure and temperature.

1.3 Motivation

HEAs are relatively new class of materials where several scientific aspects of them have to understand in great detail. Although several alloy systems have been developed and various properties of them have been reported, AlCoCrCuFeNi system is relatively widely studied. However the effect of microstructural length scales on the strengthening mechanisms as well as its rate sensitive characteristics have not been reported. Therefore in this investigation an ultrafine grained system with bimodal grain size distribution and other structural features has been developed. The underlying strengthening mechanism and dependence of flow stress on strain rate have been studied using Vickers microindentation and depth sensing nanoindentation.

In novel alloy system of equiatomic AlCuTaVW has been adopted with the assumption that this alloy would yield high temperature mechanical properties as well as acceptable levels of ductility. This alloy has been synthesized using combination of ball milling and spark plasma sintering. Mechanical properties have been evaluated using microindentation. It is to be mentioned here that this is the first ever study on this alloy system.

1.4 Objectives

Based on the above background and motivation, the objective of the present study are

- Synthesis of AlCoCrCuFeNi and AlCuTaVW HEAs using mechanical alloying with finer microstructural features.
- Fabrication of milled powders into a bulk compact using spark plasma sintering.
- Characterization of milled powders and the bulk consolidated alloy using different characterizing techniques.

- Measure the mechanical properties using Vickers microindentation and depth sensing nanoindentation techniques.
- Understanding various strengthening mechanisms in these alloys.
- Understanding the fracture toughness.
- Establishment of structure-property correlations.

1.5 Overview

The remaining part of the thesis is arranged as follows:

Chapter 2 gives the literature available on HEAs. This includes the thermodynamic concepts of the HEAs and the proposed core effects in HEAs in detail. Microstructural features and mechanical properties of HEAs are also discussed. Chapter 3 comprises of the experimental procedures and details. These include processing techniques mechanical alloying and sintering (SPS). Characterization techniques such as XRD, SEM, TEM with a detailed description of the sample preparation for the examination. A concise explanation about the methods employed for the evaluation of the mechanical properties using Vickers microindentation and nanoindentation has also been given.

Chapter 4 provides a detailed account of the microstructural evolution in equiatomic ultrafine grained AlCoCrCuFeNi high-entropy alloy. Chapter 5 deals with strengthening mechanisms in equiatomic ultrafine grained AlCoCrCuFeNi high-entropy alloy studied by micro and nanoindentation methods. Chapters 4 and 5 are based on the paper published in 'Acta Materialia' (Vol 125, pg 58-68) by Ramya Sree Ganji, P. Sai Karthik, K. Bhanu Sankara Rao, Koteswararao V. Rajulapati, entitled "Strengthening mechanisms in equiatomic ultrafine grained AlCoCrCuFeNi high-entropy alloy studied by micro and nanoindentation methods", in 2017. Chapter 6 gives the

details of AlCuTaVW HEA synthesized using mechanical alloying and spark plasma sintering. Fracture toughness has been measured from Vickers microhardness indents and its detailed analysis has been discussed. This chapter will be communicated to 'Materials Science and Engineering A'.

References

1. Yeh JW, Chen SK, Lin SJ, Gan JY, Chin TS, Shun TT, Tsua CH, Chang SY: **Nanostructured high entropy alloys with multiple principal elements: novel alloy design concepts and outcomes**. *Advanced Engineering Materials* 2004, **6**:299-302.
2. Cantor B, Chang ITH, Knight P, Vincent AJB: **Microstructural development in equiatomic multicomponent alloys**. *Materials Science and Engineering A* 2004, **375-377**:213-218.
3. Yeh JW, Chen SK, Gan JY, Lin SJ, Chin TS, Shun TT, Tsau CH, Chang SY: **Formation of simple crystal structures in Cu-Co-Ni-Cr-Al-Fe-Ti-V alloys with multiprincipal metallic elements**. *Metallurgical and Materials Transactions A* 2004, **35**:2533-2536.
4. Tsai MH, Yeh JW: **High-entropy alloys: a critical review**. *Material Research Letters* 2014, **2**:107-123.
5. Miracle DB, Senkov ON: **A critical review of high entropy alloys and related concepts**. *Acta Materialia* 2017, **122**:488-511.
6. Zhang Y, Qiao J-w, Liaw PK: **A Brief Review of High Entropy Alloys and Serration Behavior and Flow Units**. *Journal of Iron and Steel Research, International* 2016, **23**(1):2-6.
7. Pickering EJ, Jones NG: **High-entropy alloys: a critical assessment of their founding principles and future prospects**. *International Materials Reviews* 2016, **61**(3):183-202.
8. Zhang Y, Zhou YJ, Lin JP, Chen GL, Liaw PK: **Solid-solution phase formation rules for multi-component alloys**. *Advanced Engineering Materials* 2008, **10**(6):534-538.
9. Tong CJ, Chen YL, Chen SK, Yeh JW, Shun TT, Tsau CH, Lin SJ, Chang SY: **Microstructure characterization of $Al_xCoCrCuFeNi$ high entropy alloy system with multi principal elements**. *Metallurgical and Materials Transactions A* 2005, **36**:1-13.

10. Ye YF, Wang Q, Lu J, Liu CT, Yang Y: **High-entropy alloy: challenges and prospects**. *Materials Today* 2015, **http://dx.doi.org/10.1016/j.mattod.2015.11.026**.
11. Senkov ON, Miller JD, Miracle DB, Woodward C: **Accelerated exploration of multi-principal element alloys with solid solution phases**. *Nature communications* 2015, **6**:6529.
12. Cahn RW, Haasen P: **Physical metallurgy**, vol. 1. North Holland: Elsevier Science B.V; 1996.
13. Cantor B: **Multicomponent and high entropy alloys**. *Entropy* 2014, **16**(9):4749-4768.
14. Smallman RE, Ngan AHW: **Physical metallurgy and advanced materials**. Amsterdam: Butterworth-Heinemann; 2007.
15. Reed-Hill RE: **Physical metallurgy principles**. New York: D. Van Nostrand company; 2009.
16. Leong Z, Wrobel JS, Dudarev SL, Goodall R, Todd I, Nguyen-Manh D: **The effect of electronic structure on the phases present in high entropy alloys**. *Scientific Reports* 2017, **7**:39803.
17. Zhang Y, Yang X, Liaw PK: **Alloy design and properties optimization of high-entropy alloys**. *Jom* 2012, **64**(7):830-838.
18. Zhang C, Zhang F, Chen S, Cao W: **Computational thermodynamics aided high-entropy alloy design**. *Jom* 2012, **64**(7):839-845.
19. Yeh J-W: **Alloy design strategies and future trends in high-entropy alloys**. *Jom* 2013, **65**(12):1759-1771.
20. M.C. Gao CSC, O.N. Dogan, P.D. Jablonksi, J.A. Hawk, D.E. Alman: **Design of Refractory High-Entropy Alloys**. *Jom* 2015, **67**(11):2653-2669.
21. Ye YF, Wang Q, Lu J, Liu CT, Yang Y: **Design of high entropy alloys: A single-parameter thermodynamic rule**. *Scripta Materialia* 2015, **104**:53-55.
22. Sheikh S, Shafeie S, Hu Q, Ahlström J, Persson C, Veselý J, Zýka J, Klement U, Guo S: **Alloy design for intrinsically ductile refractory high-entropy alloys**. *Journal of Applied Physics* 2016, **120**(16):164902 164901-164905.
23. Feng R, Gao M, Lee C, Mathes M, Zuo T, Chen S, Hawk J, Zhang Y, Liaw P: **Design of light-weight high-entropy alloys**. *Entropy* 2016, **18**(9):333.

24. Miracle D, Miller J, Senkov O, Woodward C, Uchic M, Tiley J: **Exploration and development of high entropy alloys for structural applications**. *Entropy* 2014, **16**(1):494-525.
25. Baldenebro-Lopez FJ, Herrera-Ramírez JM, Arredondo-Rea SP, Gómez-Esparza CD, Martínez-Sánchez R: **Simultaneous effect of mechanical alloying and arc-melting processes in the microstructure and hardness of an AlCoFeMoNiTi high-entropy alloy**. *Journal of Alloys and Compounds* 2015, **643**:S250-S255.
26. Ye X, Ma M, Liu W, Li L, Zhong M, Liu Y, Wu Q: **Synthesis and characterization of high-entropy alloy AlxFeCoNiCuCr by laser cladding**. *Advances in Materials Science and Engineering* 2011, **2011**.
27. Braic M, Braic V, Balaceanu M, Zoita CN, Vladescu A, Grigore E: **Characteristics of (TiAlCrNbY)C films deposited by reactive magnetron sputtering**. *Surface and Coatings Technology* 2010, **204**(12-13):2010-2014.
28. Yue T, Xie H, Lin X, Yang H, Meng G: **Microstructure of laser re-melted AlCoCrCuFeNi high entropy alloy coatings produced by plasma spraying**. *Entropy* 2013, **15**(7):2833-2845.
29. Varalakshmi S, Kamaraj M, Murty BS: **Synthesis and characterization of nanocrystalline AlFeTiCrZnCu high entropy solid solution by mechanical alloying**. *Journal of Alloys and Compounds* 2008, **460**(1-2):253-257.
30. Chen Y-L, Hu Y-H, Tsai C-W, Hsieh C-A, Kao S-W, Yeh J-W, Chin T-S, Chen S-K: **Alloying behavior of binary to octonary alloys based on Cu–Ni–Al–Co–Cr–Fe–Ti–Mo during mechanical alloying**. *Journal of Alloys and Compounds* 2009, **477**(1-2):696-705.
31. Zhang KB, Fu ZY, Zhang JY, Wang WM, Lee SW, Niihara K: **Characterization of nanocrystalline CoCrFeNiTiAl high-entropy solid solution processed by mechanical alloying**. *Journal of Alloys and Compounds* 2010, **495**:33–38.
32. Gómez-Esparza CD, Ochoa-Gamboa RA, Estrada-Guel I, Cabañas-Moreno JG, Barajas-Villarruel JI, Arizmendi-Morquecho A, Herrera-Ramírez JM, Martínez-Sánchez R: **Microstructure of NiCoAlFeCuCr multi-component systems synthesized by mechanical alloying**. *Journal of Alloys and Compounds* 2011, **509**:S279-S283.

33. Praveen S, Anupam A, Sirasani T, Murty BS, Kottada RS: **Characterization of oxide dispersed AlCoCrFe high entropy alloy synthesized by mechanical alloying and spark plasma sintering**. *Transactions of the Indian Institute of Metals* 2013, **66**(4):369-373.

34. Wen H, Topping TD, Isheim D, Seidman DN, Lavernia EJ: **Strengthening mechanisms in a high-strength bulk nanostructured Cu–Zn–Al alloy processed via cryomilling and spark plasma sintering**. *Acta Materialia* 2013, **61**(8):2769-2782.

35. Ji W, Wang W, Wang H, Zhang J, Wang Y, Zhang F, Fu Z: **Alloying behavior and novel properties of CoCrFeNiMn high-entropy alloy fabricated by mechanical alloying and spark plasma sintering**. *Intermetallics* 2015, **56**:24-27.

36. Shao XH, Peng ZZ, Jin QQ, Ma XL: **Atomic-scale segregations at the deformation-induced symmetrical boundary in an Mg-Zn-Y alloy**. *Acta Materialia* 2016, **118**:177-186.

Chapter 2 Literature review

2.1 Thermodynamic concepts of HEAs

Thermodynamic methods are used to provide the criteria for equilibrium state of the material system and determine the external influence acting on the system [1-3]. The system attains equilibrium state when the Gibbs free energy (G) is constant or minimum. G is an extensive property i.e. it depends on the size of the system or number of mole concentration of a material at constant temperature and pressure. The equation for Gibbs free energy is given as following,

$$\Delta G_{mix} = \Delta H_{mix} - \mathrm{T}\Delta S_{mix} \quad \ldots\ldots\ldots\ldots\ldots\ldots\ldots\ldots\ldots\ldots\ldots\ldots\ldots\ldots (2.1)$$

where ΔH_{mix} is enthalpy of mixing, T is absolute temperature and ΔS_{mix} is entropy of mixing, if configurational entropy (S) increases, Gibbs free energy decreases [4-6] i.e., free energy for atoms to segregate or to form an ordered intermetallic phase is low. Equation 2.1 also gives an idea that randomly formed solid solution is more stable than the ordered intermetallic phases as in the case of conventional alloys until its melting point. The random solid solution displays excellent mechanical properties.

The formation of single solid solution phase is because of high configurational entropy, ΔS_{conf} and is defined as atoms in the alloy have ample ways to arrange themselves in the lattice sites. Among the four contributions in total entropy of mixing $\left(\Delta S_{conf} = R \ln N\right)$, configurational entropy has major contribution. The other three excess contributions are vibrational, magnetic dipole and electronic randomness [7, 8]. According to Boltzmann's hypotheses, the configurational entropy of mixing per mole is given as,

$$\Delta S_{conf} = -R \sum_{i=1}^{N} c_i \ln c_i \quad \ldots\ldots\ldots\ldots\ldots\ldots\ldots\ldots\ldots\ldots\ldots\ldots\ldots\ldots (2.2)$$

where R is the gas constant (8.1314 J mol^{-1} K^{-1}), C_i is molar fraction of i^{th} element and N is the total number of elements. It is evident from Equation 2.2, that ΔS_{conf} increases with increase in the number of elements and overcomes the enthalpies of intermetallic compound formations and hence form simple solid solutions. The configurational entropy varies from 1.61R for 5 element HEA to 2.57R for 13 element HEA. As per HEA definition, the alloy having 5 major elements in near equal proportions and minor alloying additions below the concentration of 5% is called a HEA [9-11]. The alloys with minor alloying elements have less ΔS_{conf} than 1.61R though they comprise of 5 principal elements. This contradiction of definition is again cleared by JW Yeh [7] and proposed 1.5R as a lower limit to HEAs because of high bonding energies of unlike atomic pairs at high temperatures. Implying, alloys having less than 1.5R as ΔS_{conf} are unstable at high temperatures. Moreover, 1R has been set as border line for low and medium entropy alloys because of weak bonding energies [7]. Miracle et al [12] confirmed the above findings and proposed the definition for HEAs should have $\Delta S_{conf} \geq 1.5\,R$. The configurational entropy of a low entropy alloys is 1R and medium entropy alloys ranges from $1.5R \geq \Delta S_{conf} \geq 1R$. Different entropy alloys of the current world are schematically shown in **Fig. 2.1**. Ye et al [13] depicted using contour map of ΔS_{mix} (**Fig. 2.2**), explained how the entropy of mixing is maximum at the centre of a ternary phase diagram where all atomic percentages of elements are equal and has high energy gain to suppress the intermetallic phase and form simple solid solutions. The maximum ΔS_{mix} value is 9.15 J mol^{-1} K^{-1} at the exact centre of the map shown in **Fig. 2.2**.

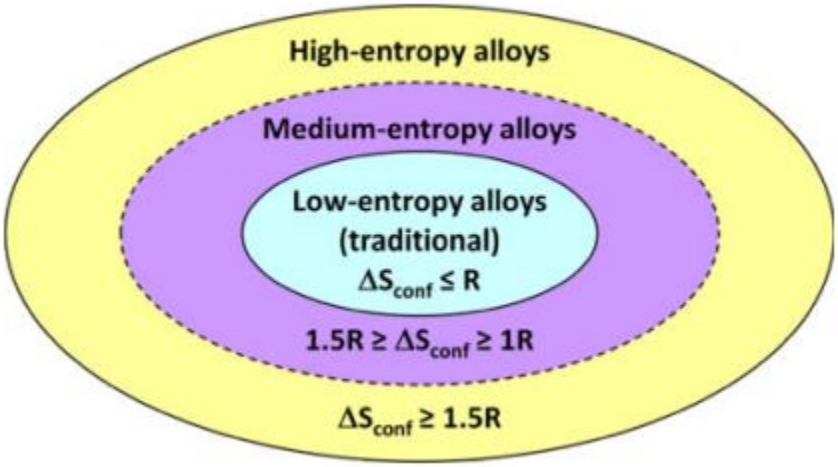

Fig. 2.1 Entropy alloys based on configurational entropy, ΔS_{conf} [7].

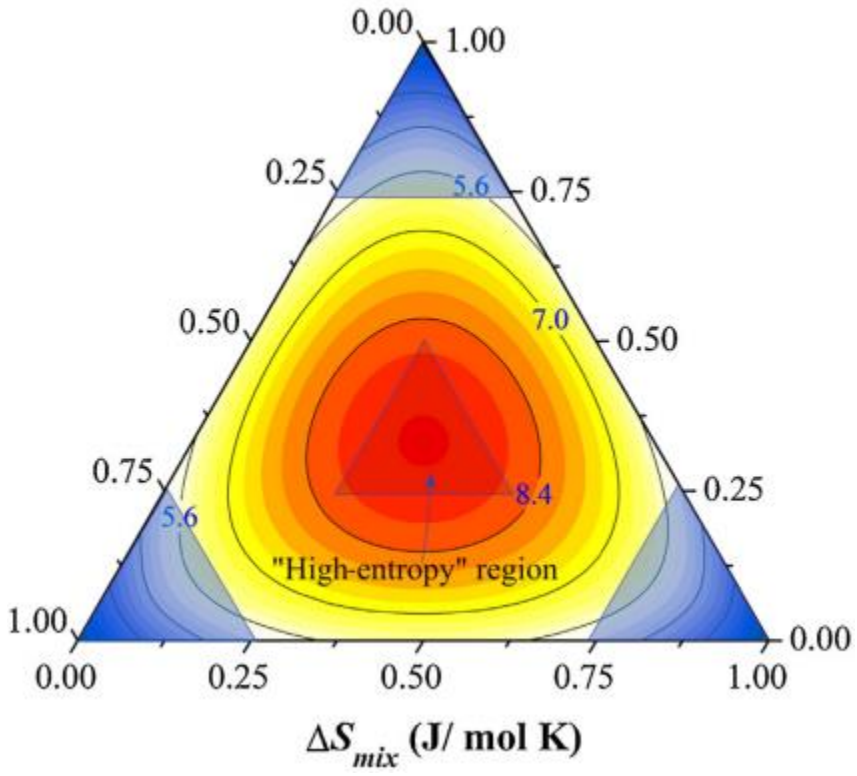

Fig. 2.2 The contour map depicting the high entropy alloys at the center and the conventional alloys at the corners (blue) (adapted from [13]).

For the design of HEAs, Zhang et al [14] introduced two parameters which helps to evaluate HEA in terms of solid solution or intermetallic compounds formation. The phase formation rules include the atomic size difference, δ and mixing enthalpy, ΔH_{mix}.

The atomic size difference, δ is expressed as,

$$\delta\,\% = 100\sqrt{\sum_{i=1}^{N} C_i\left(1-\frac{r_i}{\bar{r}}\right)^2} \quad \ldots\ldots\ldots\ldots\ldots\ldots\ldots\ldots\ldots\ldots\ldots\ldots (2.3)$$

where C_i is concentration of ith element, r_i is the atomic radius of ith element, N is number of elements, and $\bar{r}$ is average atomic size of elements and is expressed as $\bar{r} = \sum_{i=1}^{N} C_i r_i$. The equation for enthalpy of mixing of a solid solution is,

$$\Delta H_{mix} = \sum_{i=1, i\neq j}^{N} 4\,\Delta H_{ij}\left(C_i\,C_j\right) \quad \ldots\ldots\ldots\ldots\ldots\ldots\ldots\ldots\ldots\ldots\ldots\ldots (2.4)$$

where ΔH_{ij} is mixing enthalpy of binary alloy i and j, C_i, C_j are concentrations of ith and jth elements respectively. Zhang et al [14] explained and proved using 6 different HEA alloys that the solid solution formation facilitates only when the component atomic size difference is relatively small, and ΔH_{mix}not more negative to form intermetallic compounds. As δ is small, the atoms have equal probability to occupy the substitutional sites forming a solid solution. Whereas bulk metallic glasses (BMG) have huge atomic size difference and ΔH_{mix} is far negative compared to HEAs resulting in intermetallic compound formation. The combination of δ and ΔH_{mix} gives reasonable information for phase selection in HEAs rather than ΔS_{mix} because invariably it is high in all HEAs. Guo et al [15] shows phase formation criteria in HEAs as given in **Fig. 2.3**. It is clear from the **Fig. 2.3** that, solid solution forms when δ < 0.066 and ΔH_{mix} ranges between $-11.6 < \Delta H_{mix} < 3.2$ kJmol^{-1}.

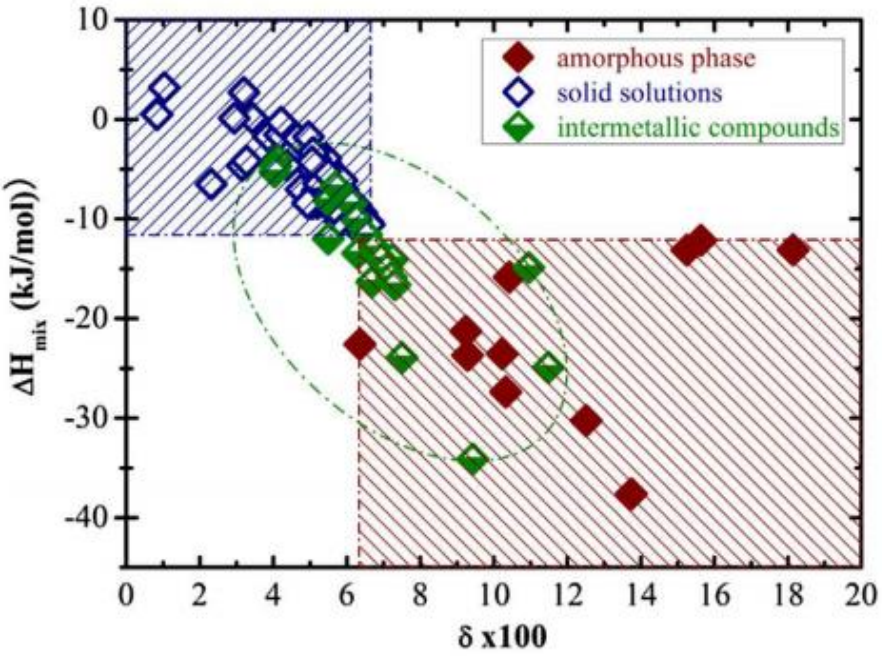

Fig. 2.3 Proposed criteria to predict the phase formation band on of δ and ΔH_{mix} values [15].

Whereas Guo et al [16] in another article clarified that the solid solution forms only when resultant parameters of HEA is in the range: $0 \leq \delta \leq 8.5$, $-22 \leq \Delta H_{mix} \leq 7$ kJmol^{-1} and $11 \leq \Delta S_{mix} \leq 19.5$ JK^{-1}mol^{-1}. This statistical data differs from researcher to researcher because of availability of huge data on HEAs [5, 6, 8, 17-19]. Recently Dwivedi et al [20] synthesized CrNbTiVZn HEA using mechanical alloying and reported that the phase formation parameters reported by Guo et al [16] are also valid for their alloy. Amorphous phases form when the δ values are higher and ΔH_{mix} values are more negative, however this statistical analysis show that the region for intermetallic compounds formation overlaps both with the solid solution region and the amorphous region (see **Fig. 2.3**). This overlap is because the solid solution phases formed could be disordered solid solution phases or ordered solid solutions. It could also be misinterpretation of ordered solid solution as intermetallic compounds [17].

Guo et al [17] described that δ and ΔH_{mix} have clear involvement in phase selection in HEA. And also added electronegativity difference, $\Delta\chi$ and valence electron concentration (VEC) do not

involve much in phase selection criteria, but $\Delta\chi$ gives the information about the segregation of elements and VEC dictates the type of crystal structure that the solid solution will form. $\Delta\chi$ and VEC are derived from the well-known Hume-Rothery rules to form substitutional solid solution. The expression for electronegativity difference, $\Delta\chi$ is,

$$\Delta\chi = \sqrt{\sum_{i=1}^{n} C_i\,(\chi_i - \bar{\chi})^2} \quad \ldots\ldots\ldots\ldots\ldots\ldots\ldots\ldots\ldots\ldots\ldots\ldots\ldots (2.5)$$

$\bar{\chi}$ is given as $\sum_{i=1}^{n} C_i\chi_i$, where χ_i is Pauling electronegativity of ith element, C_i is concentration of ith element, and n is total number of elements in the alloy. Valence electron concentration is defined as the total electron count in the valence band and is expressed as,

$$VEC = \sum_{i=1}^{n} C_i\,(VEC)_i \quad \ldots\ldots\ldots\ldots\ldots\ldots\ldots\ldots\ldots\ldots\ldots\ldots\ldots (2.6)$$

where C_i is concentration of individual ith element, and VEC_i is the valence electron number of ith element. Conventionally, the itinerant electrons per atom, e/a ratios of individual elements and total number of electrons including d electrons in the valence band (VEC) are considered for Hume Rothery rules to know the number of valence electrons. Guo et al [17] clarified that the existence of transition elements in HEA, considering e/a ratios is inappropriate. Moreover VEC gives relevant information in HEA. Guo et al [21] briefly discussed and claimed that fcc solid solution form when VEC ≥ 8, bcc solid solution phase form when VEC < 6.87 and a mix of both fcc and bcc phases form when 6.87 ≤ VEC < 8. Dwivedi et al [20] synthesized CrNbTiVZn HEA using mechanical alloying technique and VEC of this alloy is 6.4. They found the above given VEC principle for the phase formation is inconsistent because this alloy formed a fcc phase instead of a bcc phase predicted by VEC rule. Tsai et al [50] used VEC to predict the formation of σ phase in HEA in the same range of mixed fcc and bcc phases. Recently, Poletti and Battezzati [22] evaluated

the phase selection between fcc and bcc type solid solutions in HEAs, using both e/a and VEC. They claimed that fcc solid solutions are formed when VEC > 7.5 and 1.6 < e/a < 1.8, while bcc solid solutions are formed when VEC < 7.5 and 1.8 < e/a < 2.3. Guo et al [16] statistical analysis of ΔS_{mix}, δ, ΔH_{mix}, $\Delta \chi$, and VEC values explained how these parameters effect the phase stability. This group made similar conclusions as Zhang et al [14] by considering huge data to find out the rules for the formation of solid solution or amorphous phase. King et al [23] developed a methodology using a software for phase stability prediction at a given temperature. To form a single phase HEA, a new parameter Φ, is defined as a ratio of Gibbs free energy of solid solution to that of intermetallics. They reported after many experiment that a solid solution forms when Φ ≥ 1 and δ ≤ 6.6.

2.2 Core effects of HEA

There are few effects proposed by Yeh et al [9] explaining the exceptional properties of HEAs compared to traditional alloys. There are four core effects based on equal concentration of different elements in the alloy namely high mixing entropy effect, sluggish diffusion effect, lattice distortion effect and the cocktail effect.

2.2.1 High mixing entropy effect

As explained earlier in section 2.1, entropy arises because of huge concentration of individual elements in the alloy. Meaning the composition of different elements in equal concentrations, leads to disorder in the alloy. The rise in entropy decreases the overall Gibbs free energy as seen in Equation 2.1 ensuing formation of solid solutions by subduing intermetallic compound formation especially at elevated temperatures. Elements occupy different lattice sites in solid solutions instead of segregating to any preferred location and forming a compound [11].

2.2.2 Sluggish diffusion effect

Diffusion is a process of interplay of atoms in lattice sites in the structure of a metal. HEAs have different elements in each lattice site. In the diffusion process, an atom finds different environments with different potential energy in the neighboring lattice site owing to the different elements [24-26]. This makes it difficult to pass through or may need more external force to occupy another lattice site. If the potential energy in the new site is considerably high, there is a possibility for an atom to jump back to its original lattice site hence making the diffusion process very slow thereby increasing the mechanical properties like high temperature strength, creep resistance in multi principal HEA [12, 27-31].

2.2.3 Lattice distortion effect

There is a severe distortion in lattice because of different elements having different atomic radii. Large radius atoms will create more compressional stress on other atoms, small atoms have more vacant space to move around.

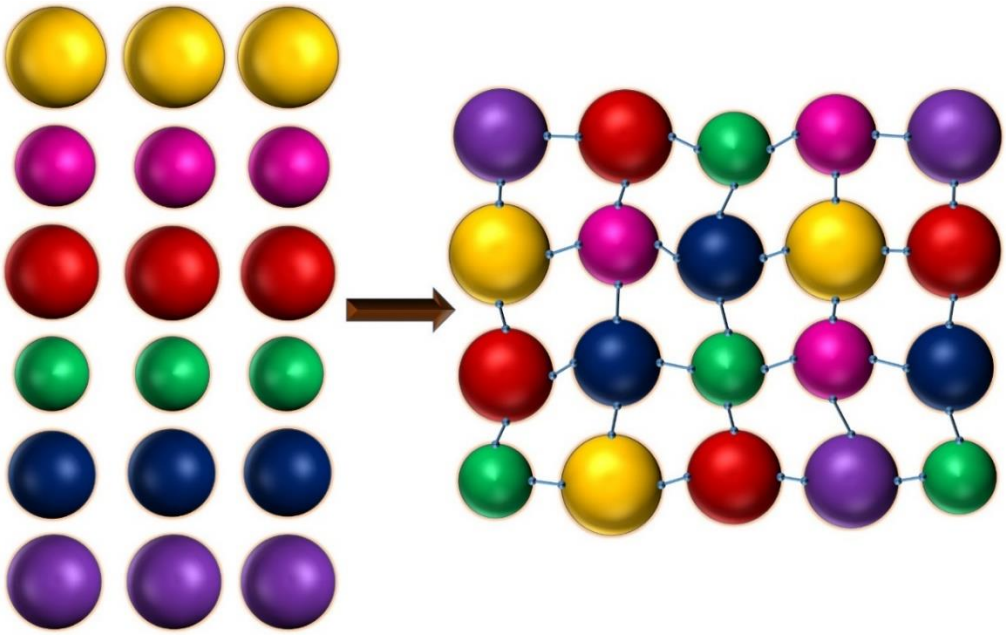

Fig. 2.4 A schematic of lattice distortion caused by atoms with different atomic sizes.

The localized strain raise because of this atomic radii difference prevent the dislocation movements and enhances solid solution strengthening [32, 33]. The schematic illustration of lattice distortion effect is given in **Fig. 2.4.** Other than difference in atomic size, different crystal structures of elements and their priorities to form bonds also result lattice distortion [14]. The decrease in XRD peak intensity is also an evidence for presence of severe lattice strain observed by various researchers [34, 35].

2.2.4 Cocktail effect

This effect is a combination of above said effects. The newly developed HEAs have two or more number of different phases. The interaction between these phases, their interaction with other effects are termed as cocktail effect contributing to the overall properties of HEA. There is increase in strength because of the interaction between atoms and phase as well as lattice distortion. The properties also depend on the composition, crystal structure and microstructure of HEA [36-38].

2.3 Microstructure of HEA

As HEA are new emerging alloys, researchers adopted different techniques to synthesize them [39-46]. The most commonly used fabrication method is arc melting and casting [23, 47-49]. Though it is widely used technique, it has some disadvantages and limitations. Formation of dendritic structure and selective segregation of alloying elements being the primary disadvantage in melting and casting methods. Often an additional step of heat treatment is required to homogenize the cast structure. Other processing techniques adopted to fabricate HEAs are magnetron sputtering [40, 41] and splat quenching [50]. Mechanical alloying has been widely used to synthesize nanocrystalline materials which is cost effective. The main disadvantage of segregation in the casting methods is appreciably avoided in mechanical alloying. Mechanical

alloying results nanocrystalline materials with homogenous microstructure. Mechanical alloying coupled with spark plasma sintering helps in retaining the nanocrystalline nature of the alloy, thereby effecting the overall properties [51-54]. Mechanical alloying in HEAs [55-58] has been equally popular as melting methods, where researchers and academicians are able to study the alloy at nano scale with homogenous compositions. The elements which are difficult to melt and process can be mechanically alloyed to produce a uniform distribution of elements throughout the microstructure.

HEAs exhibit higher hardness than the most commonly used Inconel 718 superalloy [32]. This is because of the sluggish diffusion in HEAs preventing the softening at elevated temperatures. Senkov et al [59, 60] on reported that over a temperature range up to 1600 ºC, the yield strength of Inconel 718 superalloy decreased but HEAs displayed outstanding steady yield strengths. Though, with the increase in temperature the growth rate of intermetallic and other phases form in HEAs is very less. Liu et al [61] also reported that the activation energy for the grain growth is very low in HEAs when compared to other steels. This confirms the stability of the microstructure at elevated temperatures. It has been reported that a passive layer is formed with the elements Cr and Ni to prevent corrosion whereas the presence of Cu is degrading it by forming a galvanic cell [62]. Chen et al [63] reported that HEAs display better corrosion resistance than 304 stainless steel. There are different types of HEAs like bulk metallic HEAs [64], refractory HEAs [32, 65-68], superalloy HEAs [39, 69], low density HEAs [59, 70, 71]. Microstructures depend on the processing routes, the cooling conditions and further heat treatments [11, 72]. Different types of phases form in HEAs like nanoprecipitates, amorphous, single solid solution phase, multiple solid solutions phases, intermetallic phases, laves phases or σ phases [11]. Intermetallic phases are treated as unwanted phases which deteriorate the mechanical properties. But in most of the

structural alloys like superalloys, these intermetallic phases are intentionally precipitated to enhance the high temperature properties. However the shape, size, volume fraction and distribution of the intermetallic phases in the matrix play a key role in enhancing the mechanical properties [11]. Yeh et al [73] who is one of the discoverers of HEAs worked on $Al_xCoCrCuFeNi$ HEA. Solid solutions with simple crystal structures were formed in the as-cast $Al_xCoCrCuFeNi$ HEA. The increase in Al concentration favored bcc phase formation. Yeh et al [73] also fabricated a 10 alloy HEA system, CuCoNiCrFeNiMoTiVZr and found two bcc structures and an amorphous phase. Cantor et al [74] who is another inventor of multi component alloys, casted 20 elements first in equal atomic proportions and 16 elements later. In both HEAs, they found brittle multiple phases. Cantor et al [74] also prepared an alloy with transition elements (Cr,Mn,Fe,Co,Ni) alone and found a single fcc phase with dendritic microstructure. AlCoCrCuFeNi HEA introduced by Yeh et al [73] and CoCrFeMnNi HEA fabricated by Cantor et al [74] are the most investigated HEAs. The later alloy is named after him as Cantor alloy. Any HEA designed is the derivative of these two alloys. The elemental effect on phase formation in the alloy has been well studied by reducing the concentration of individual element [75-80] and found that the bcc and fcc stabilizers as in steels also stabilize the respective phase in HEAs [11, 81, 82]. Li et al [83] studied the effect of Mn, Ti and V on AlCoCrCuFeNi HEAs. Their research work showed that the cast AlCoCrCuFeNi HEA resulted in a fcc phase and a bcc phase. Mn addition to this alloy resulted an additional unknown phase. AlCoCrCuFeNiTi and AlCoCrCuFeNiV HEAs consisted 2 bcc phases and a fcc phase. The as cast microstructure of AlCoCrCuFeNi alloy is shown in **Fig. 2.5**. A dendritic and interdendritic phases resulted with Cr, Fe and Co rich region in dendrite phase and Cu is rich in interdendrite areas. Yeh et al [34] fabricated CoCrCuFeNi HEA using melting and casting process. This alloy resulted in a simple fcc phase.

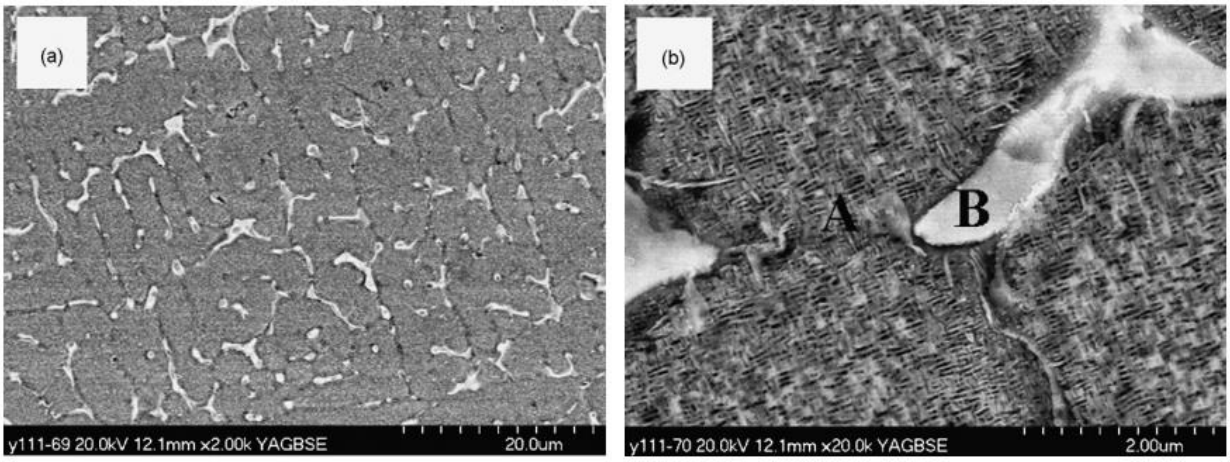

Fig. 2.5 Scanning electron micrographs of as cast AlCoCrCuFeNi HEA showing dendrite and interdendrite regions [83].

The micrograph shown in **Fig. 2.6** depicts typical dendritic and interdendritic regions with a slight segregation of Cu in the interdendritic region. This alloy displayed a microhardness of 1.3 GPa. Here they emphasized that though the elements in HEAs are of different crystal structures, they coagulate to form a single solid solution with no host element or matrix. All elements in the alloy are regarded as solute atoms with a random distribution in the crystal lattice.

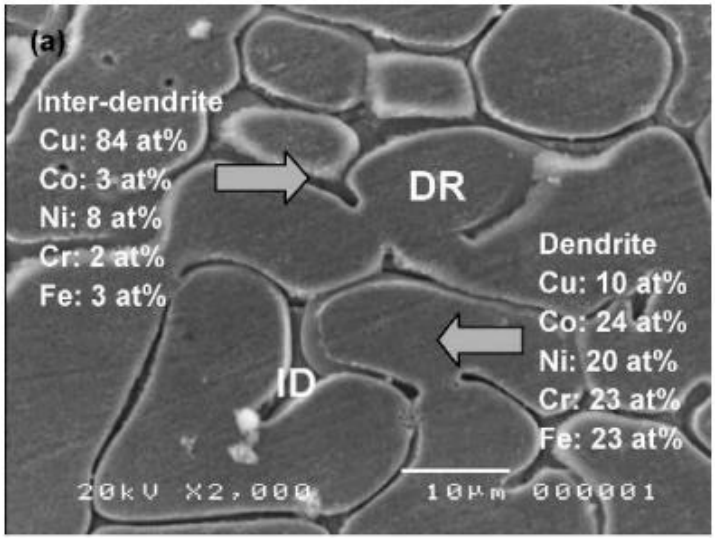

Fig. 2.6 Scanning electron micrograph of as cast CoCuCrFeNi showing dendritic and interdendritic regions. The chemical composition of the two phases were also shown [34].

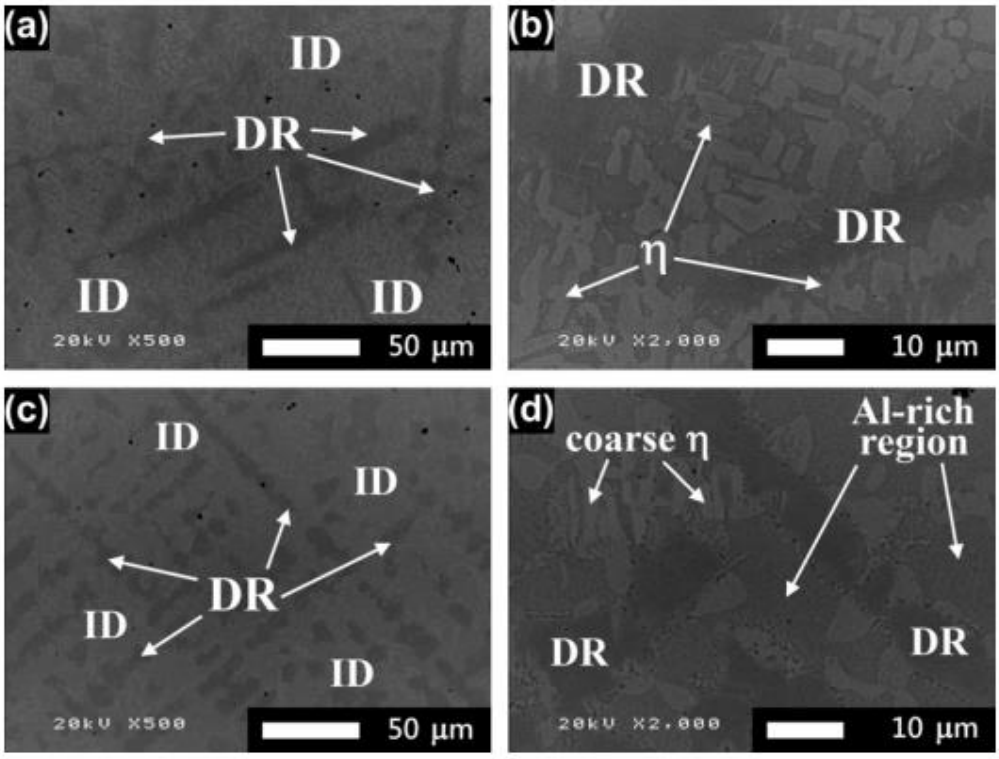

Fig. 2.7 Back scattering electron images of (a, b) $Co_{1.5}CrFeNi_{1.5}Ti$ alloy, (c, d) $Al_{0.2}Co_{1.5}CrFeNi_{1.5}Ti$ [47].

Chuang et al [47] melted and casted $Co_{1.5}CrFeNi_{1.5}Ti_{0.5}$, $Al_{0.2}Co_{1.5}CrFeNi_{1.5}Ti_{0.5}$, $Co_{1.5}CrFeNi_{1.5}Ti$ and $Al_{0.2}Co_{1.5}CrFeNi_{1.5}Ti$ HEAs. The microstructure of $Co_{1.5}CrFeNi_{1.5}Ti$ alloy has dendritic and interdendritic regions where Ti is deficient in dendrite and (Co, Cr, Fe) - rich matrix with course η $(Ni, Co)_3Ti$ precipitates found in interdendritic regions as shown in **Fig. 2.7**. Li et al [84] fabricated $Fe_{80-x}Mn_xCo_{10}Cr_{10}$ HEA using vacuum arc melting. This alloy is hot rolled to 50 % reduction, followed by homogenizing treatment at 1200 ºC for 2 h. There is a partial martensitic phase transformation of fcc to hcp phase. The XRD and electron back scattered diffractograms (EBSD) are shown in **Fig. 2.8**. It is observed that with decrease in Mn concentration, there is a change in the deformation mechanism. When Mn is 45 and 40 at. %, the alloy has a fcc phase where dislocation dominated plasticity mechanism operates. On further decrement of Mn concentration to 30 at. %, a new hcp phase is formed where twining induced plasticity mechanism

is observed. It is shown that the microstructure with twins and dual phases improved both strength and ductility of the alloy. Wang et al [85] studied the effect of 1.1 at. % carbon in FeNiMnAlCr HEA. This alloy is synthesized using melting and casting methods. Further it was cold rolled and underwent annealing treatments. The as-cast alloy has an fcc phase with coarse grains. The cold rolling and annealing treatment resulted ordered B2 phase in alloy without carbon. Whereas C-doped HEA resulted $M_{23}C_6$, M_7C_3 carbides as shown in **Fig. 2.9**. The doping of C into the lattice prevents the alloy to recrystallize though it was given annealing treatment. They also observed that the C and Mn segregated at the grain boundaries. Schuh et al [86] studied the mechanical properties of CoCrFeMnNi HEA after high pressure torsion. The as-cast alloy displayed a microhardness of 1.6 GPa and has a fcc phase.

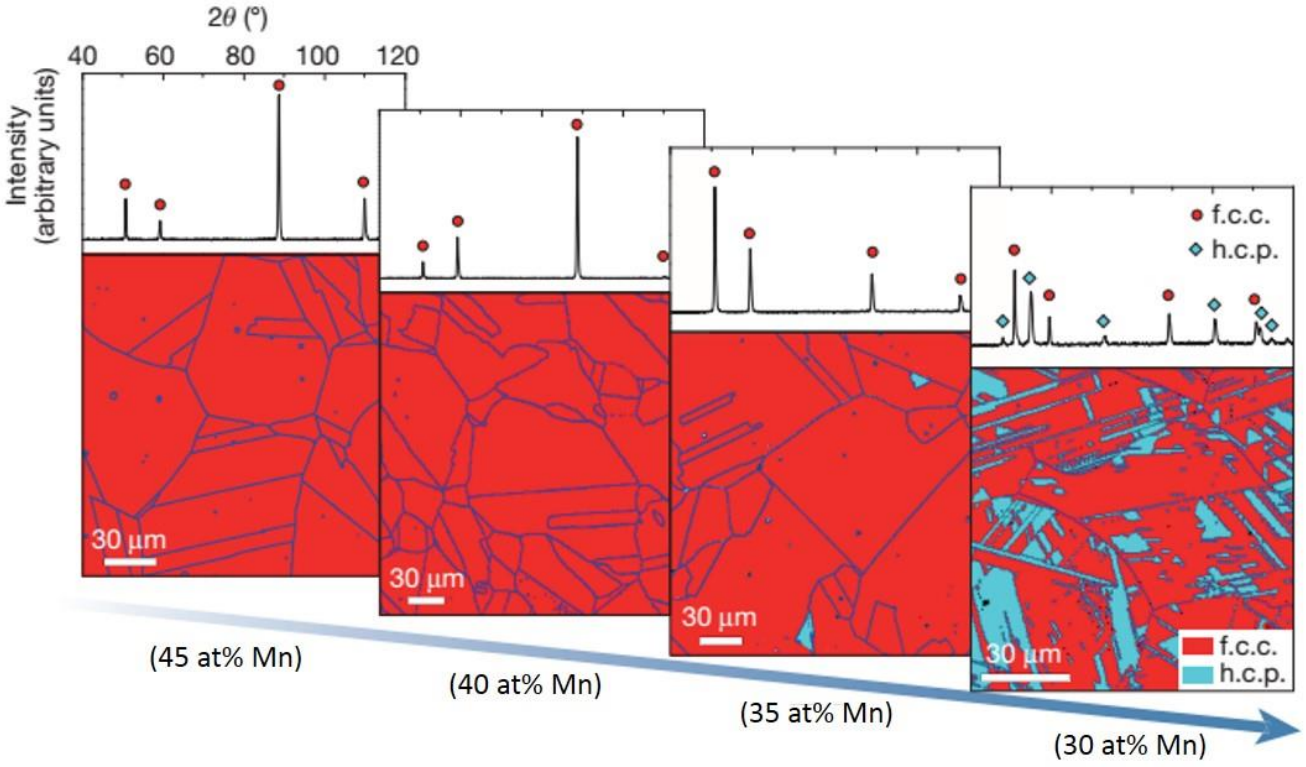

Fig. 2.8 X-ray diffractograms of Fe80-xMnxCo10Cr10 HEA and corresponding EBSD images [84].

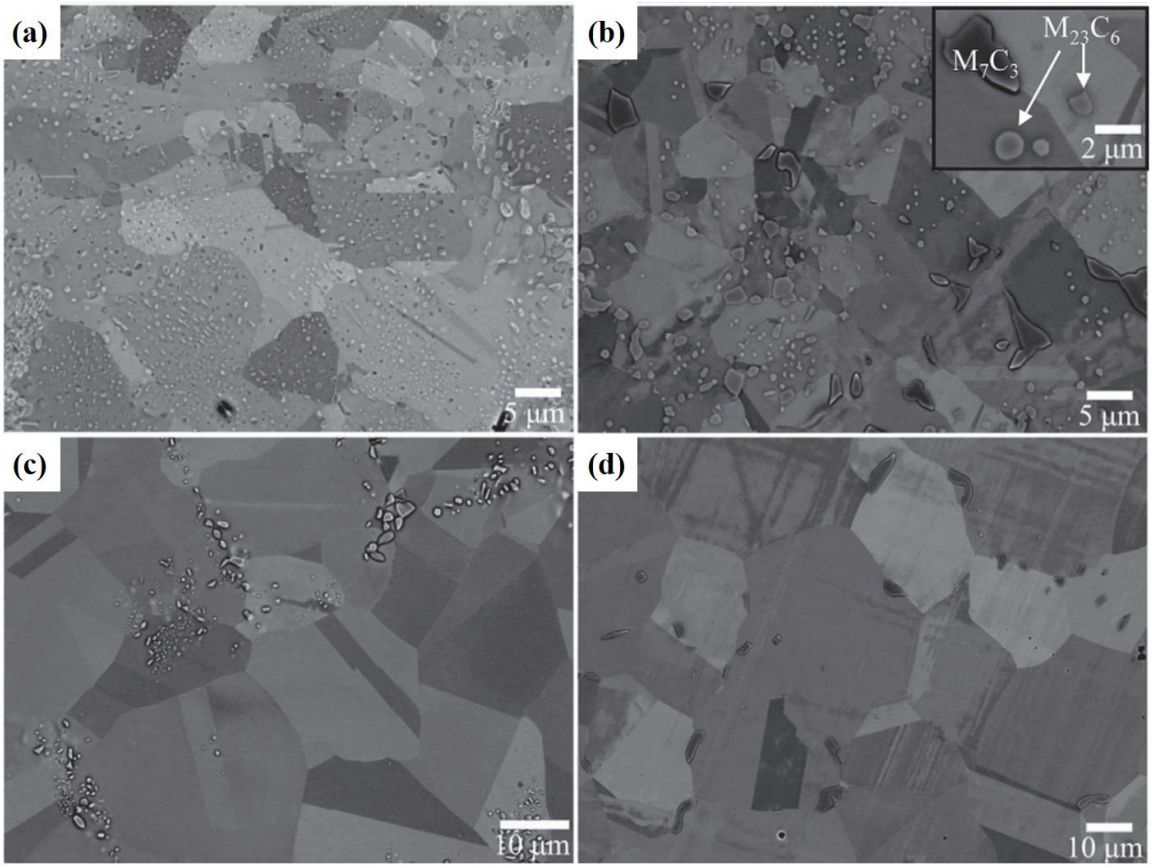

Fig. 2.9 Back scatter electron micrographs of undoped (a,c) and 1.1 at % C doped (b,d) HEA. The micrographs were taken after cold rolling and annealing heat treatment at (a) 800 ºC for 30 h, (b) 1000 ºC for 8 h (c) 900 ºC for 8 h and (d) 1100 ºC for 4 h [85].

Severe plastic deformation induced high strength and the microhardness increased to 5 GPa. With the increase in deformation the twin density in the alloy increased and the alloy continued to have a single solid solution phase with fcc crystal structure. This alloy is given an annealing treatment at 450 ºC and reported that the microhardness increased to 6.1 GPa and new phases have evolved. The new phases are MnNi phase, Cr rich phase and Fe-Co phase as shown in **Fig. 2.10**. The grain size of the alloy is in nanocrystalline range, the random arrangement of atoms in grain boundaries served as nucleation sites for the phase transformations. Fu et al [87] studied the $Co_{25}Ni_{25}Fe_{25}Al_{7.5}Cu_{17.5}$ alloy via mechanical alloying followed by spark plasma sintering (SPS). Mechanical alloying of the alloy resulted a fcc phase with an average grain size of 24 nm. The 49

h milled powders have flakes and lamellar morphology as shown in **Fig. 2.11**. This alloy after SPS had the same crystal structure with a bimodal grain size distribution. The TEM images showed twins in the alloy where the average twin width is 61 nm and the volume fraction of about 5 %. The alloy with twins and bimodal grain sizes exhibited superior mechanical properties. Pradeep et al [88] synthesized and studied AlCrCuFeNiZn HEA using mechanical alloying and hot pressing at 600 ºC for 15min under 650 MPa load. Both mechanical alloying and compaction resulted a major bcc phase and a minor fcc phase. The atom probe tomographical studies on the alloy shows Fe rich, Ni rich, α brass type Cu-Zn and Cr rich phases. This alloy has very high hardness of 8.5 GPa and elastic modulus of 1.4 GPa.

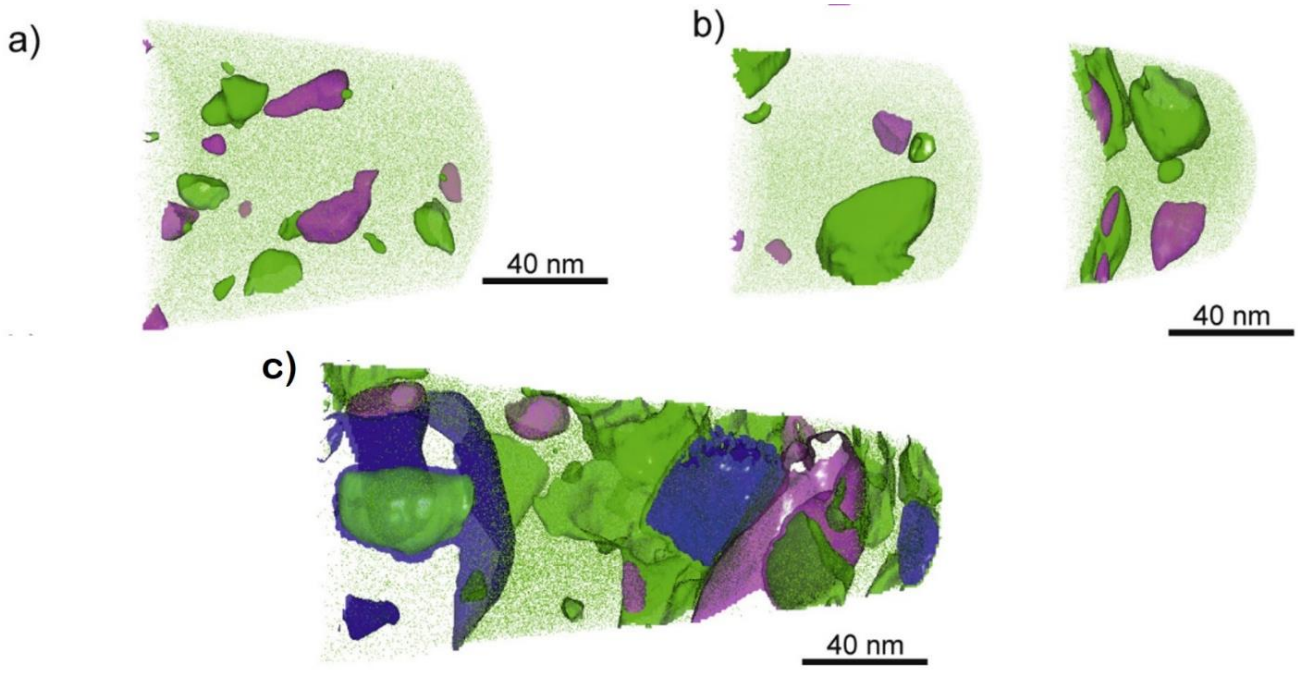

Fig. 2.10 3D Atom probe tomographic reconstruction of CoCrFeMnNi HEA after annealing treatment at 450 ºC for (a) 5 min (b) 1 h and (c) 15 h. The color indications: green → MnNi phase, purple → Cr rich phase and blue → Fe-Co phase [86].

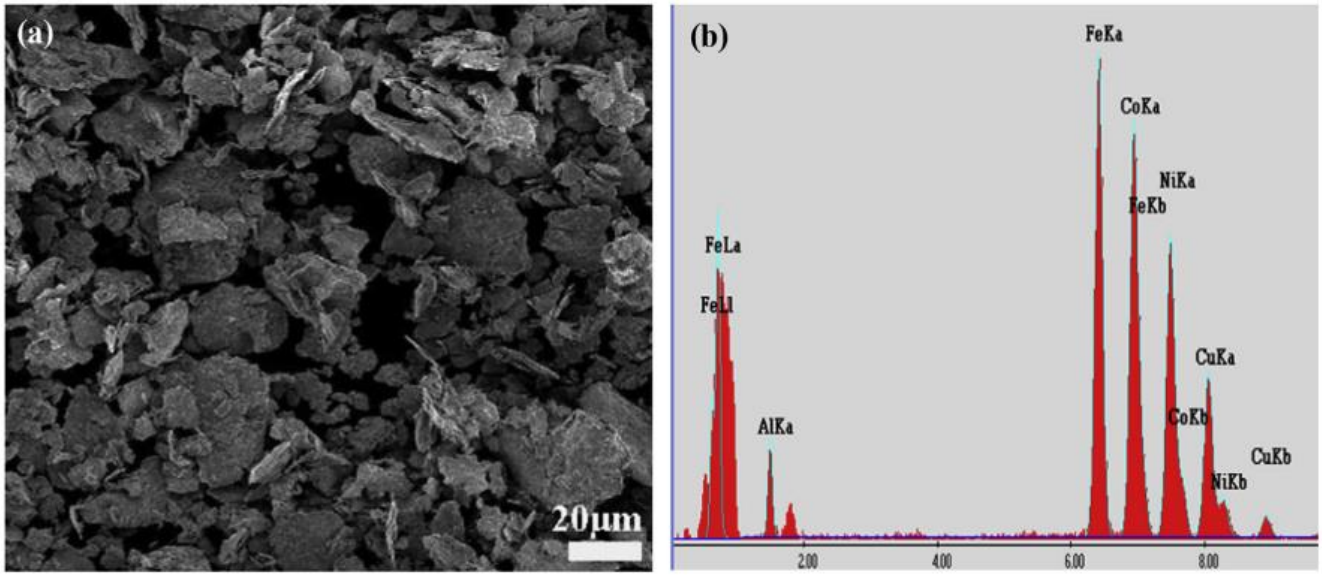

Fig. 2.11 (a) Scanning electron micrograph of 49 milled Co25Ni 25Fe25Al7.5Cu17.5 HEA, (b) corresponding EDS compositional distribution showing equiatomic concentrations [87].

Ji et al [89] investigated the mechanical alloyed and spark plasma sintered CoCrFeMnNi HEA. The 60 h mechanical alloying resulted bcc and fcc phases. They observed the decrement in the crystallite size upto 42 h of milling and further there was no crystal refinement. **Fig. 2.12 (a)** shows the mechanical alloyed powder morphology having elliptical shape. **Fig. 2.12 (b)** gives the bright field image of the milled powders and the insert showing the presence of two phases. However the sintered sample has only one phase with fcc crystal structure with two different grain diameters. They also found twins in the alloy. This alloy displayed a high microhardness of 6.3 GPa and room temperature compressive strength of 2 GPa. An equiatomic FeCoCrNi HEA is produced by Liu et al [90] using gas atomization and hot extrusion. Gas atomization resulted a 35.2 μm powder with a single fcc phase. Hot extrusion resulted equiaxed grains with no change in crystal structure. **Fig. 2.13** shows the EBSD images of hot extruded materials showing the microtextures of <101> and <001> orientations.

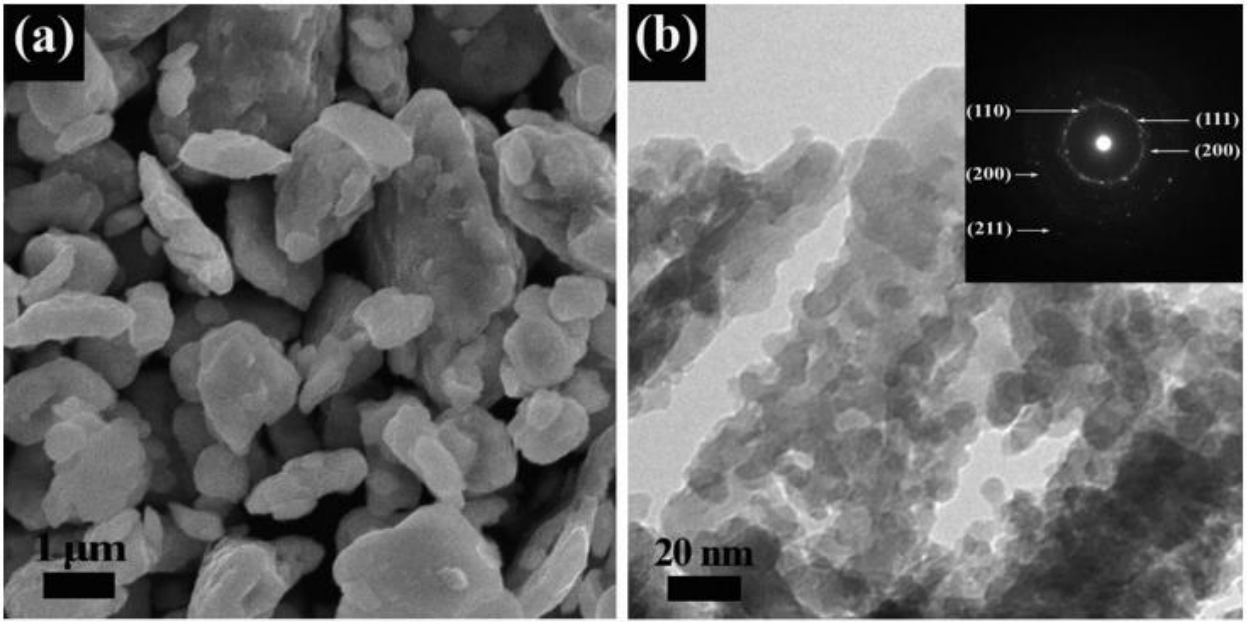

Fig. 2.12 (a) Scanning electron micrograph and (b) bright field image of 60 h ball milled powders of CoCrFeMnNi HEA [89].

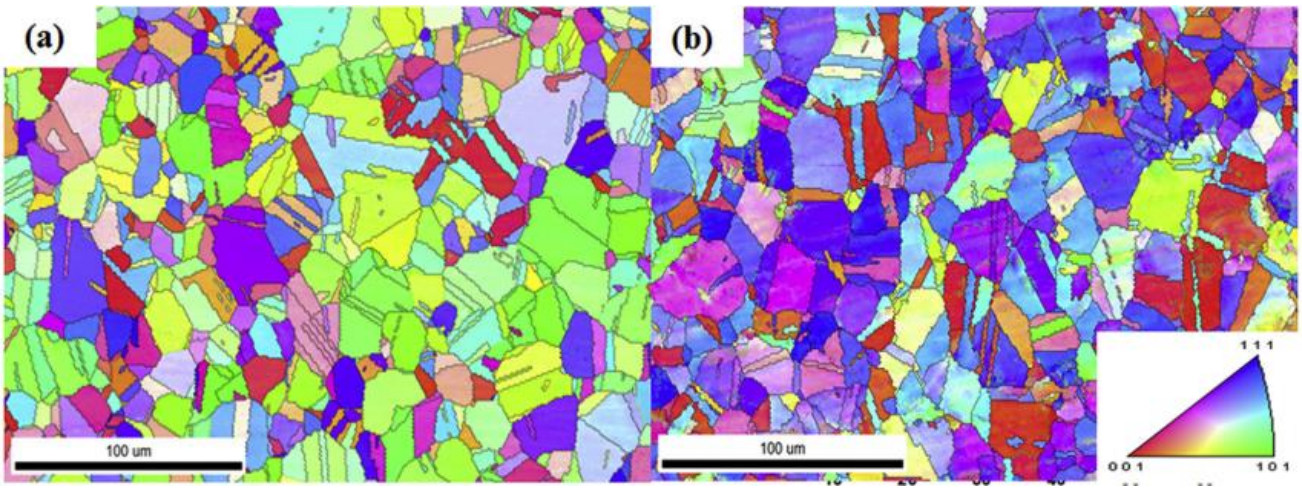

Fig. 2.13 EBSD images in (a) extrusion direction (b) transverse direction of FeCoCrNi HEA [90].

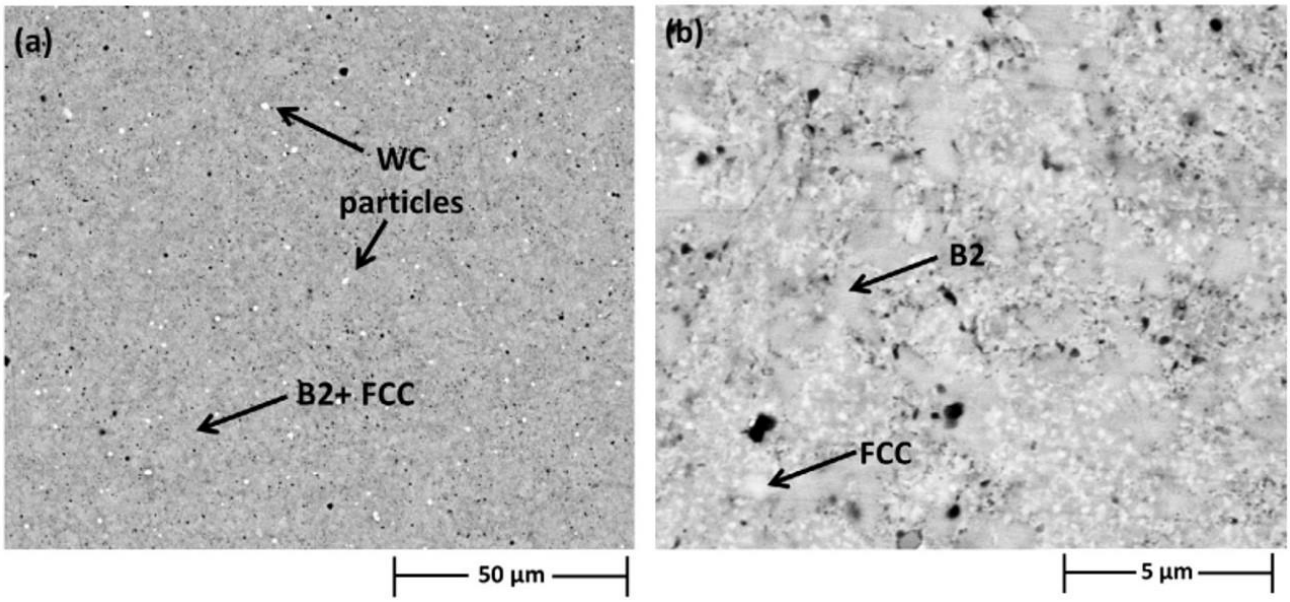

Fig. 2.14 Back scattering electron images of Al2.5CoCrCuFeNi HEA showing the phases formed after sintering [80].

Sriharitha et al [80] fabricated AlCoCrCuFeNi HEA using mechanical alloying followed by SPS by varying Al concentration. Lower Al concentration produced fcc 1, fcc2 and bcc phases. With increase in Al concentration, both fcc phases transformed to a single fcc phase and bcc phase transformed to an ordered B2 phase. These phases are shown in the Back scattering electron images of $Al_{2.5}$CoCrCuFeNi HEA (**Fig. 2.14**). They reported that B2 phase is rich in Al with Ni, Fe and Cr. Fcc phase is rich in Cu with Ni.

From all this investigations it is clear that microstructural evolution in HEAs is intriguing and needs extensive investigations by employing wide variety of alloy systems.

2.4 Mechanical properties of HEAs

HEAs are a new class of materials which could give better properties suitable for high temperature applications. Materials used at high temperatures need to have high strength, good structural stability throughout the temperature range, high creep resistance, low density and resistance to corrosion or oxidation. The HEAs designed with modified microstructures by introducing stable

elements into the alloy or by introducing dislocations into the lattice or by precipitation, the high temperature stability is achieved [44, 86, 91]. Not only the refined microstructure, the intermetallic phase [92, 93] and the unwanted σ and μ phases [94] helped in increasing the high temperature withstanding ability in HEAs. Due to the complex compositions, the core effects in HEA always are marked as the primary reasons for better properties. One among them is cocktail effect which deals with the interaction between the interfaces of the phases and the other core effects themselves making the dislocations very hard to move. And piling up of such blocked dislocations increases the local strain in the lattice, there results a tremendous increase in strength even at elevated temperatures. Different mechanical properties that are extensively studied in the field of HEAs are hardness, compressive properties, tensile properties, fracture toughness and strain rate sensitivity. A detailed explanation of these properties is reported in the literature given below.

2.4.1 Hardness

Chuang et al [47] have observed the increment in microhardness with increase of Ti concentration in $Al_xCo_{1.5}CrFeNi_{1.5}Ti_y$ HEA. The microhardness increased from 509 HV to 910 HV when Ti is increased from 0.5 at % to 1 at % . They observed the formation of η phase at the grain boundaries and interdendritic regions in the alloy. Maiti et al [95] manufactured TaNbHfZr HEA by arc melting and given annealing treatments for different durations up to 8 days. The variation in microhardness is recorded and is given in **Fig. 2.15**. It is clear that the microhardness increased with annealing time. As-cast alloy hardness is 3.6 GPa and with 1 day of annealing treatment microhardness increased to 5.5 GPa. This increase in hardness is attributed to solid solution strengthening and lattice distortion effect.

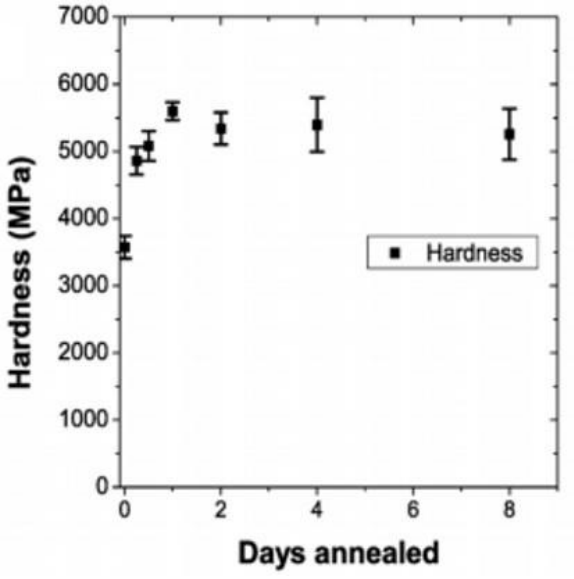

Fig. 2.15 Variation of microhardness in TaNbHfZr HEA with the annealing treatment durations [95].

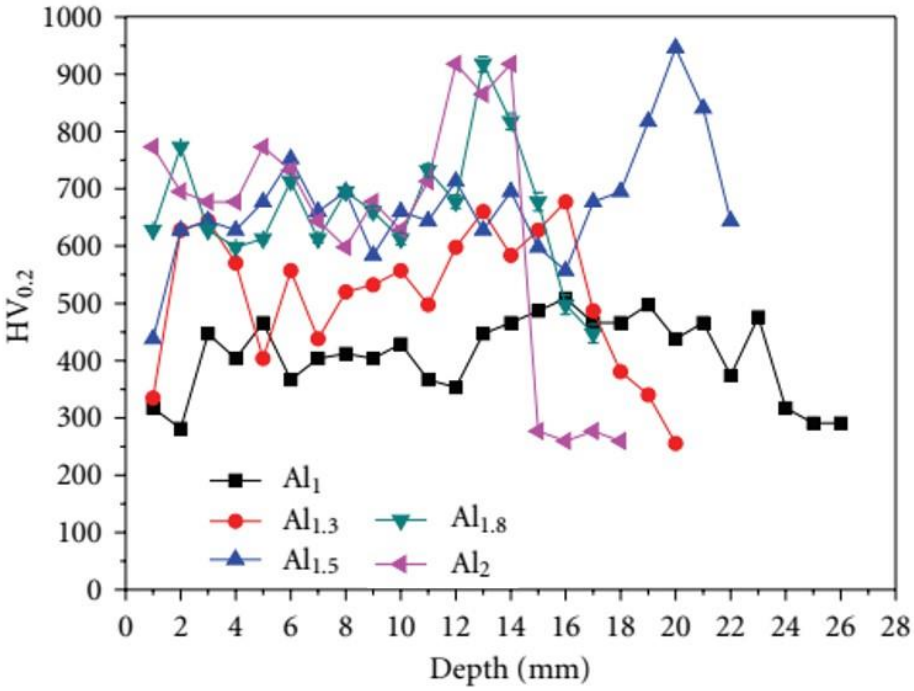

Fig. 2.16 Variation of microhardness in different AlxCoCrCuFeNi HEAs [97].

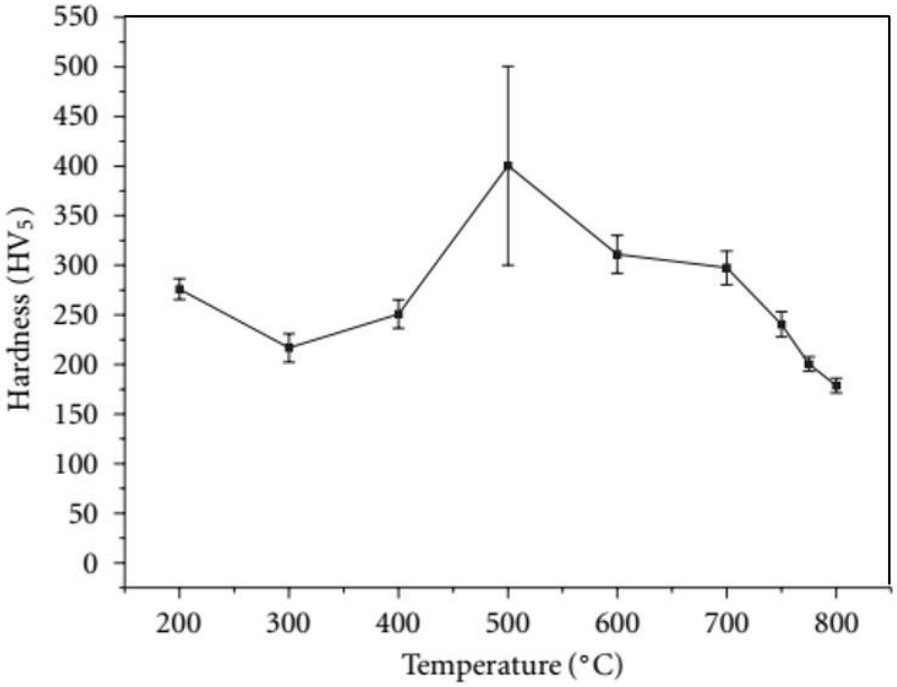

Fig. 2.17 Microhardness variation of AlCoCrCuFeNi HEA at high temperatures [97].

Senkov et al [67] reported how the mechanical properties were enhanced on compositional variation. In $CrMo_{0.5}NbTa_{0.5}TiZr$ parent alloy, when Cr is replaced by Al the microhardness increased from 5.3 GPa to 5.8 GPa and the brittle Laves phase is eliminated.Zou et al [96] melted and casted NbMoTaW HEA and homogenized at 1800 ºC for 7 days. The microhardness of the as-cast alloy is 4.8 GPa. The homogenizing treatment decreased the hardness to 4.5 GPa. Ye et al [97] synthesized $Al_xCoCrCuFeNi$ HEA using laser cladding method. They investigated that with increase in Al concentration, the hardness value increased as shown in **Fig. 2.16**. With the increase in Al at. %, fcc phase is transformed into bcc phase. The larger atomic size of the Al atoms increased the lattice distortion and enhanced solid solution strengthening. Al concentration of more than 1.5 at. % resulted brittleness in the material and found cracks while indenting. Hence this group suggested that the optimal concentration of Al is 1.5 to 1.8 at. %.

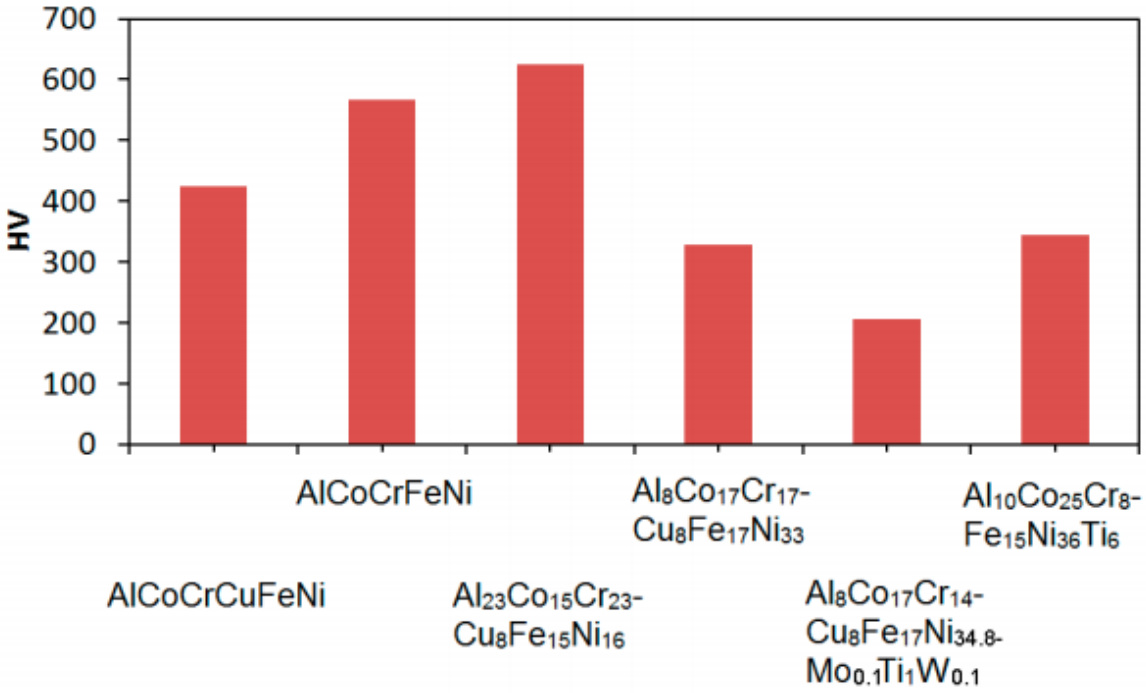

Fig. 2.18 Vickers microhardness of different HEAs [98].

AlCoCrCuFeNi HEA hardness is measured at high temperature. Against the conventional trend, the hardness of the alloy increased with increase in temperature up to 500 ºC as shown in **Fig. 2.17**. This increase in hardness is attributed to the formation of intermetallic phases which enabled high microhardness and thermal stability. Manzoni et al [98] aimed at optimizing the microstructure for high temperature application by varying the compositions and heat treatments. Six different alloys have been considered and their microhardness variation is given in **Fig. 2.18**. They found that HEAs with bcc phase have high hardness than the fcc phase alloys. However the bcc phase alloys were very brittle.

2.4.2 Tensile properties

Liu et al [94] made interesting investigation on $CoCrFeNiMo_x$ HEA. They found that the σ and μ intermetallic phases formed in $CoCrFeNiMo_{0.3}$ HEA enhanced the strength of the material without effecting the ductility. As-cast $CoCrFeNiMo_{0.3}$ have tetragonal structured σ phase distributed in

fcc matrix. The alloy on rolling up to 60 % reduction at 700 to 1000 ºC temperatures, a μ phase is precipitated with rhombohedral structure. The nanohardness values of $CoCrFeNiMo_{0.3}$ HEA are shown in **Fig. 2.19 (a)**. The measurements are made in a line across all the phases in the alloy. However the nanohardness of the precipitates could be around 15 GPa. Room temperature tensile testing is carried and the stress-strain curves with varying Mo concentration are shown in **Fig. 2.19 (b)**. The ultimate tensile strength increased with increase in Mo concentration upto 1.2 GPa. The % elongation of CoCrFeNi is 58 % and slightly decreased in $CoCrFeNiMo_{0.3}$ alloy to 49 %. This alloy displayed high strength and good ductility because of the intermetallic phases. The fractography analysis showed that the cracks were initiated at the intermetallic and grain boundary interface. He et al [99] prepared FeCoNiCr and $(FeCoNiCr)_{94}Ti_2Al_4$ HEAs by melting and casting methods. Both the alloys have a single fcc solid solution. The latter alloy was given thermomechanical treatments i.e, cold rolled to 30 % reduction and different annealing treatments (P1 and P2). Nanoprecipitates of $L1_2$ type are found in $(FeCoNiCr)_{94}Ti_2Al_4$ HEA after thermomechanical treatments. The results of tensile testing on all four samples are given in **Fig. 2.20**. The tensile strength of FeCoNiCr and $(FeCoNiCr)_{94}Ti_2Al_4$ HEAs is 453 and 503 MPa respectively. The tremendous increase in tensile strength and appreciable elongation (39% and 19% respectively) in P1 and P2 samples is because of the coherent nanoprecipitates. Equiaxed grains were obtained by Kuznetsov et al [100] in AlCoCrCuFeNi HEA by hot forging in all directions. Tensile testing up to 1200 ºC and at different strain rates is carried by this group. The stress strain curves given in **Fig. 2.21** shows the variation in tensile strength with the temperature measured at constant strain rate of 10^{-3} s^{-1}. Except for 700 ºC, material at high temperatures showed superplastic behaviour. The % elongation increased from 63 % at 700 ºC test temperature to 864 % at 1000 ºC, however with very low yield strength of 4 MPa at 1000 ºC.

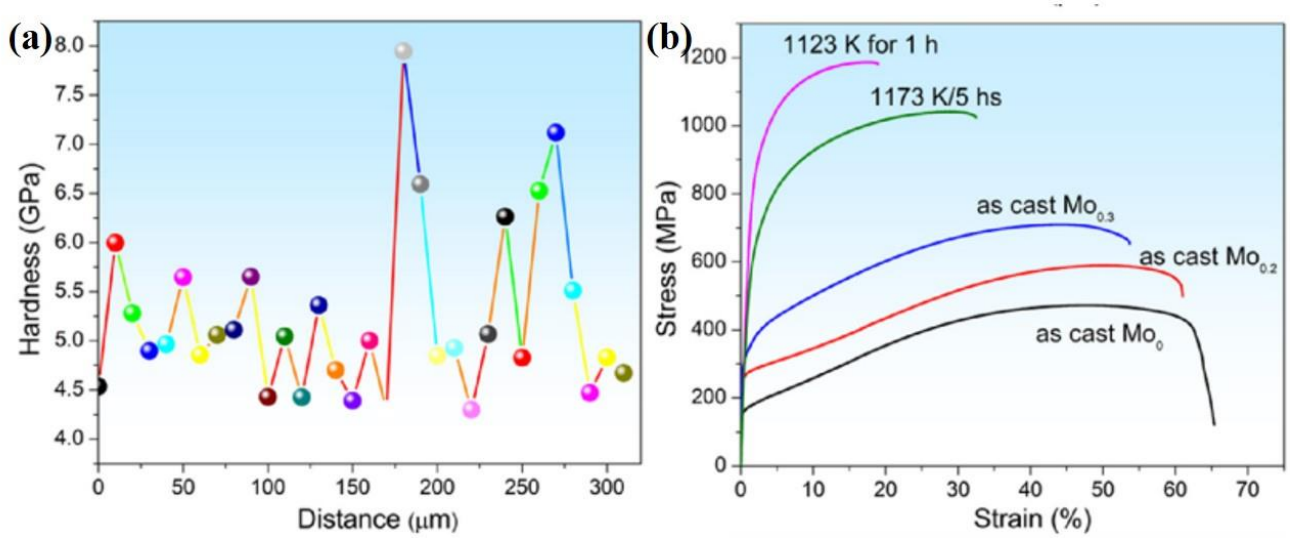

Fig. 2.19 (a) Nanohardness variation along a line in CoCrFeNiMo0.3 HEA, (b) engineering stress-strain curves of CoCrFeNiMox (x= 0, 0.2 and 0.3), and at different annealing treatments given to CoCrFeNiMo0.3 HEA [94].

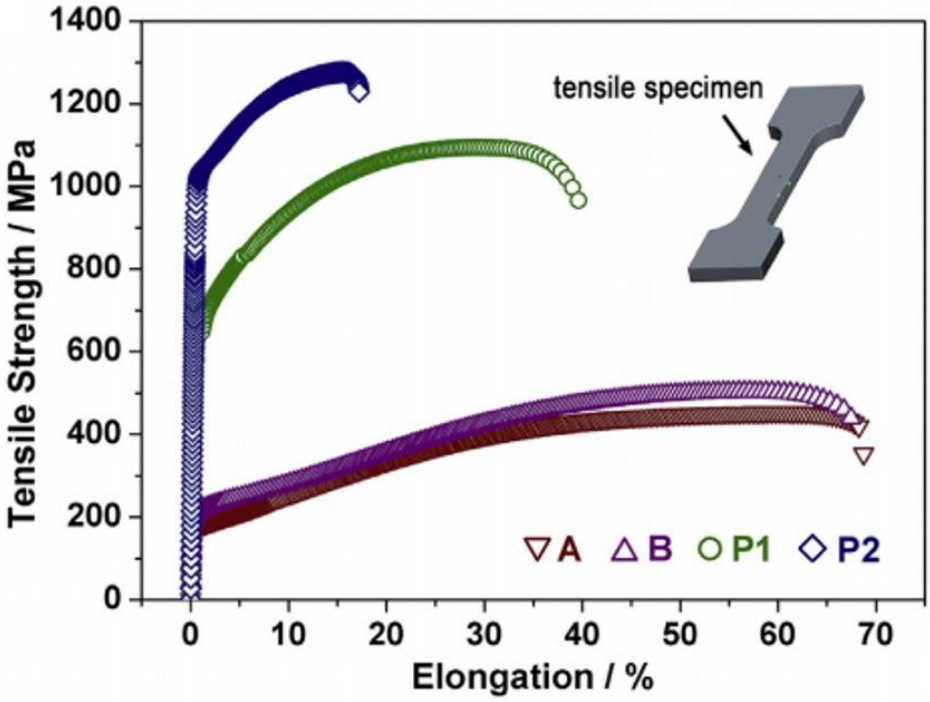

Fig. 2.20 Variation of tensile strength with elongation in FeCoNiCr (A), (FeCoNiCr)94Ti2Al4 (B) and thermomechanical treated (FeCoNiCr)94Ti2Al4 HEAs P1 and P2 [99].

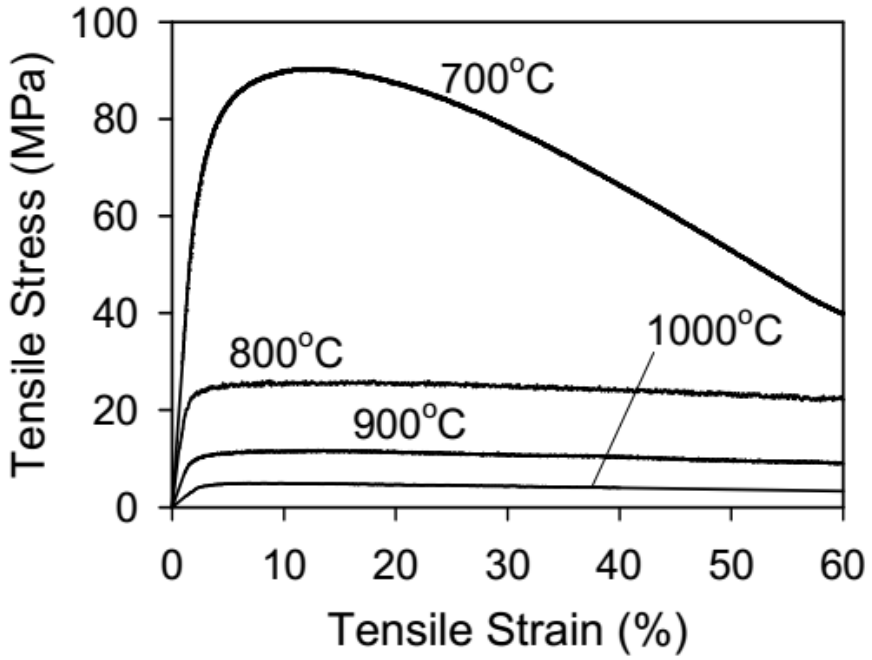

Fig. 2.21 Tensile stress-strain curves of AlCoCrCuFeNi HEA deformed at $10^{-3}s^{-1}$ strain rate [100].

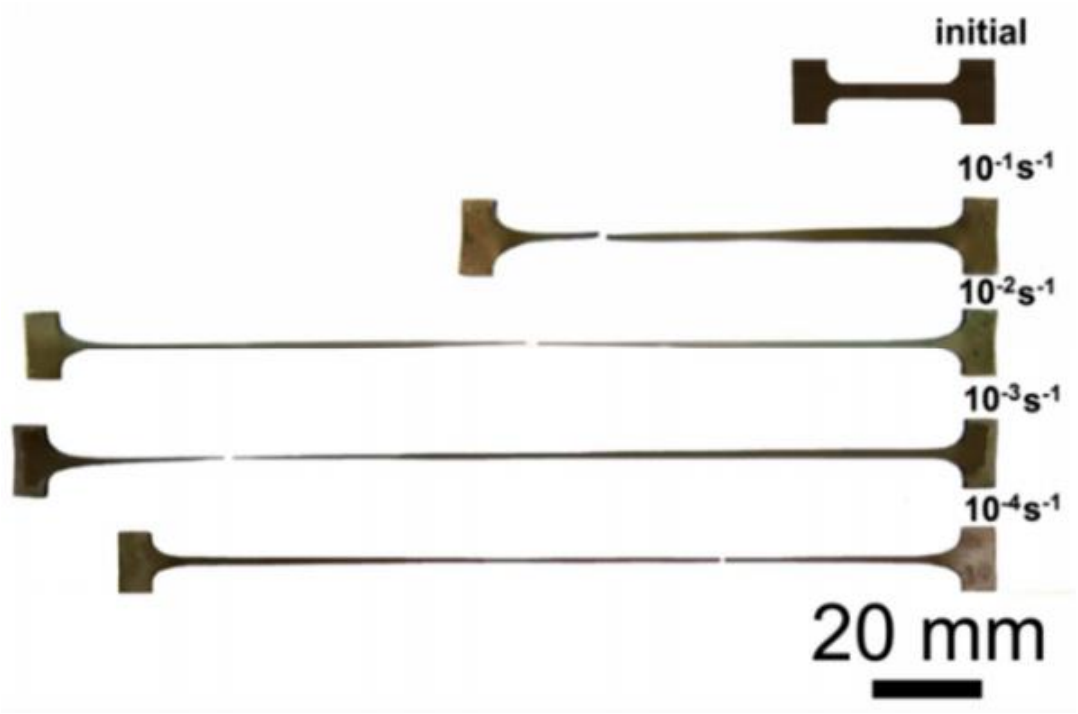

Fig. 2.22 AlCoCrCuFeNi HEA tensile samples, before and after testing at 1000 ºC [100].

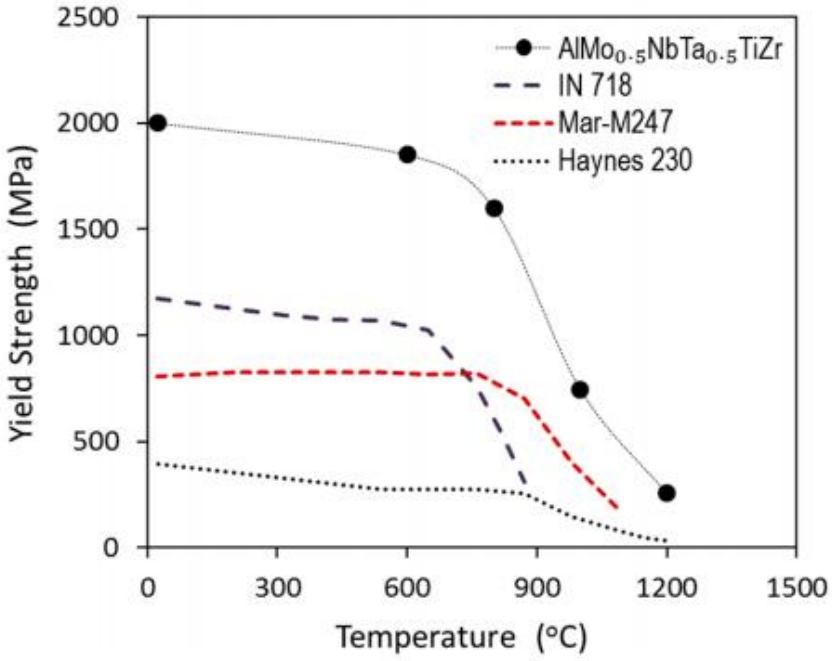

Fig. 2.23 Yield strength variation with temperature in different materials [69].

Fig. 2.22 shows the tensile test samples after deformation at 1000 ºC. The deformation at higher temperatures is attributed to the grain boundary sliding because at high temperatures grain boundaries are softer than grains.

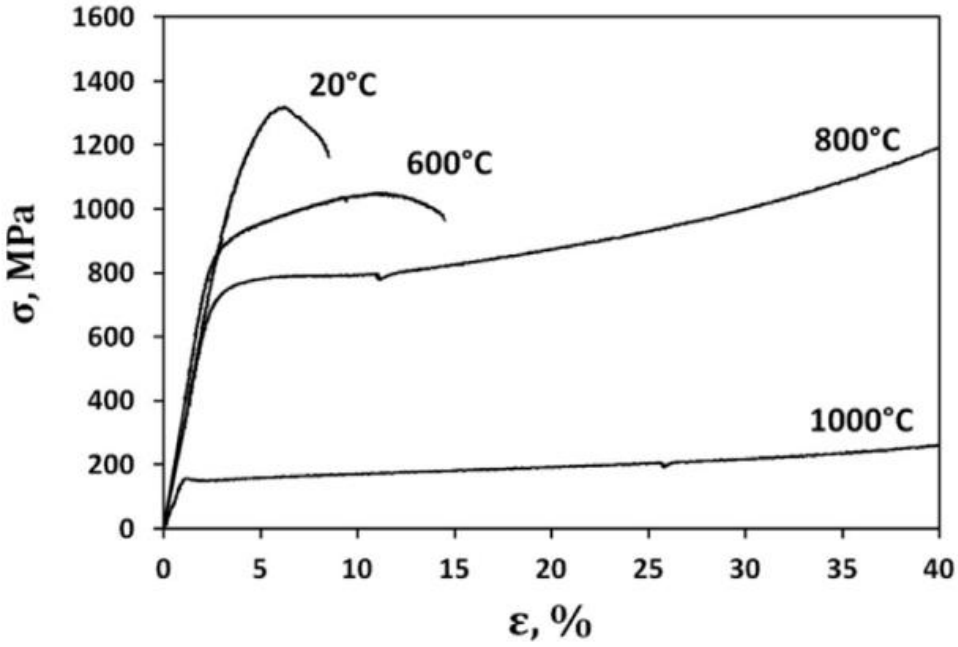

Fig. 2.24 Compressive stress-strain curves of AlNbTiV HEA at different temperatures [102].

The strain rate sensitivity (SRS) is as high as 0.6. Such high SRS obstructs necking and enhances superplasticity. Similar finding were reported by Shaysultanov et al [101]. On the other hand Senkov et al [69] worked on refractory high entropy superalloys. Superalloys are established materials for high temperature applications. Superalloys have high density and cannot withstand temperatures above 1300 ºC. However Senkov et al [69] showed that HEAs are candidate materials to replace superalloys. **Fig. 2.23** gives the comparison of $AlMo_{0.5}NbTa_{0.5}TiZr$ HEA with other Ni-base superalloys. This alloy having disordered bcc phase and nanoprecipitates of ordered B2 phase showed much higher yield strength up to 1200 ºC.

2.4.3 Compressive properties

Stepanov et al [102] fabricated light weight HEA, whose absolute density is 5.59 g/cc. AlNbTiV HEA has a bcc phase with coarse grains. The as-cast alloy is homogenized at 1200 ºC for 24 h to eliminate the dendritic structure. The compressive stress-strain curves of homogenized alloy tested at different temperatures are shown in

Fig. 2.24. The yield strength of the material is 1 GPa at room temperature, but failed early at 5 % strain with a brittle fracture. With increase in test temperature, the yield strength decreased and the alloy did not fail even after 50 % reduction. **Fig. 2.25** shows the comparison of AlNbTiV with other HEAs. They found that there is no significant difference in compressive yield strength. Fu et al [87] conducted compression tests on $Co_{25}Ni_{25}Fe_{25}Al_{7.5}Cu_{17.5}$ alloy in as-cast coarse grained form and bulk nanocrystalline form after mechanical alloying followed by SPS. The compressive stress-strain curves are given in **Fig. 2.26 (a)**. Sintered alloy has yield strength of 1.7 GPa and fractured at 10 % strain. However the as-cast alloy having yield strength of 192 MPa did not fracture up to 45 % strain. The yield strength values of $Co_{25}Ni_{25}Fe_{25}Al_{7.5}Cu_{17.5}$ HEA are compared

with other fcc HEAs in literature and are shown in **Fig. 2.26 (b)**. It was found that the nanocrystalline $Co_{25}Ni_{25}Fe_{25}Al_{7.5}Cu_{17.5}$ value is ultrahigh than other fcc HEAs.

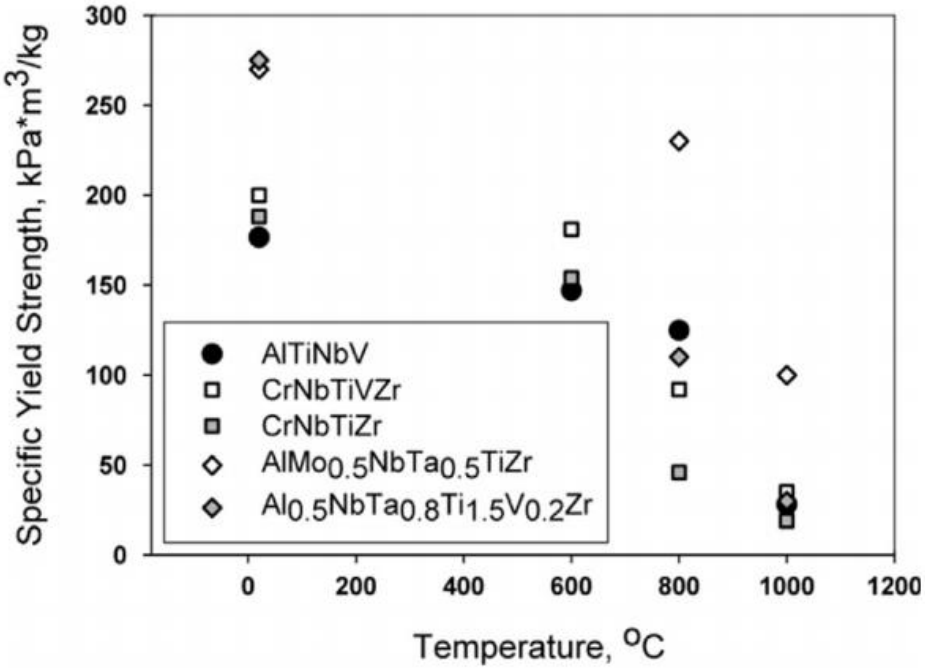

Fig. 2.25 Scatter plot of compressive yield strengths of different HEAs [102].

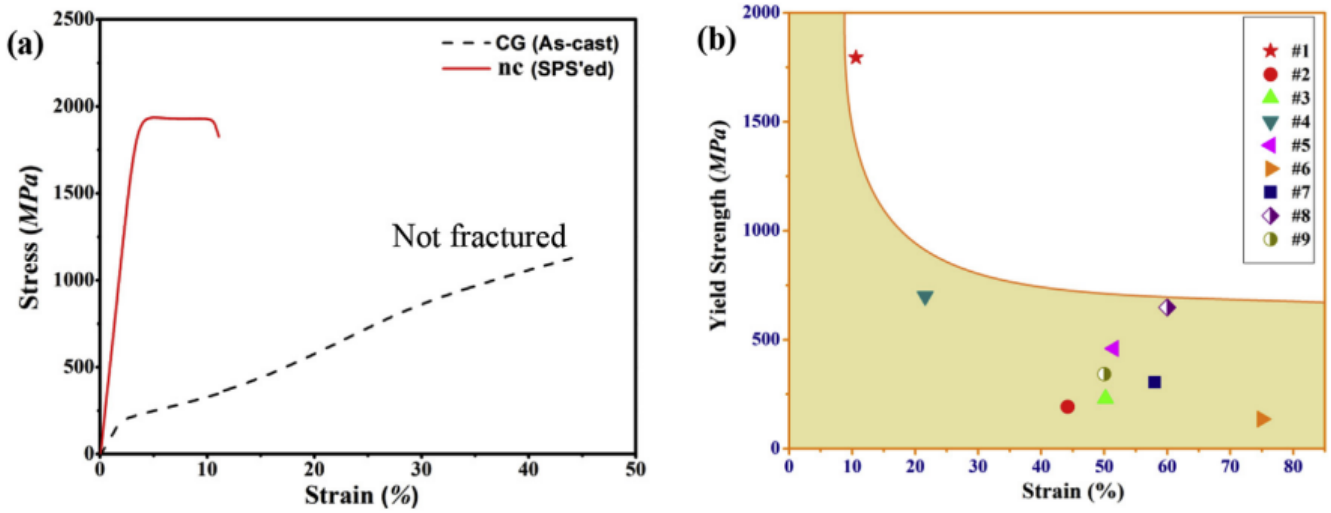

Fig. 2.26 (a) Compressive engineering stress-strain curve of Co25Ni25Fe25Al7.5Cu17.5 HEA, (b) a plot of yield strength and strain of different fcc HEAs. #1 and #2 are bulk nanocrystalline and as-cast coarse grained Co25Ni25Fe25Al7.5Cu17.5 alloy [87].

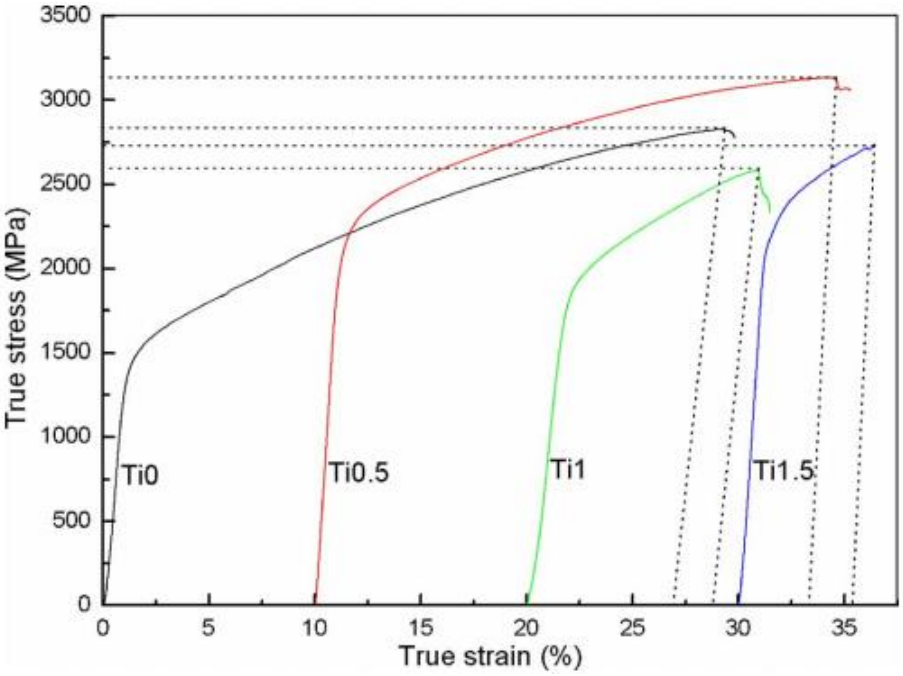

Fig. 2.27 Compressive stress-strain curve of AlCoCrFeNiTix HEA, where x = 0, 0.5, 1, 1.5 at. % [103, 104].

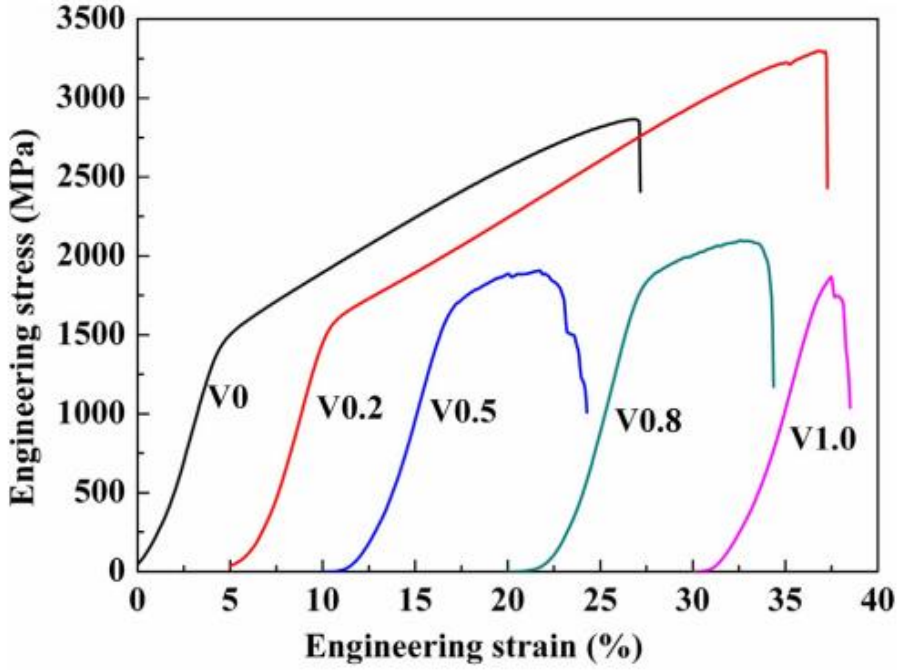

Fig. 2.28 Compressive stress-strain curve of AlCoCrFeNiVx HEA, where x = 0, 0.2, 0.5, 0.8 and 1 at. % [104, 105].

Zhou et al [103] carried compressive test on $AlCoCrFeNiTi_x$ HEA, where x = 0, 0.5, 1, 1.5 at. %. The as cast AlCoCrFeNi HEA contains bcc phase. With the increase in Ti concentration, Laves phase is formed along with bcc phase. Compression test is carried at room temperature and at a strain rate of 10^{-4} s^{-1}. The results of the compression test is given in **Fig. 2.27**. With the increase in Ti content from 0 to 0.5 at. %, the compressive yield strength increased from 1.5 to 2.26 GPa. This increase in strength is attributed to the larger size of Ti atoms in the bcc lattice creating lattice distortion, thereby increasing the yield strength. Similarly, effect of vanadium on AlCoCrFeNi HEA is studied by Dong et al [105]. This alloy has bcc phase and there was no new phase formation with V addition. With the increase in V content from 0 to 1 at. %, the compressive yield strength increased from 1.4 to 1.7GPa, however the strain to failure is decreased from 22 to 0.7 % respectively as shown in **Fig. 2.28**.

2.4.4 Fracture toughness

Seifi et al [106] investigated fracture toughness measurements in as-cast $Al_{0.2}CrFeNiTi_{0.2}$ and $AlCrFeNi_2Cu$ HEAs. The as-cast microstructure of both the alloys revealed bcc and fcc phases. The fracture toughness of $AlCrFeNi_2Cu$ is higher than $Al_{0.2}CrFeNiTi_{0.2}$ as shown in **Fig. 2.29**. Fracture toughness of $AlCrFeNi_2Cu$ is measured at 200 ºC and found it to be 45 MPa $m^{1/2}$. The load verses displacement curves are also shown as an insert in **Fig. 2.29**. A linear relationship is observed at room temperature measurements whereas at 200 ºC the curve is nonlinear. Mohanty et al [107] fabricated AlCoCrFeNi HEA using mechanical alloying and bulk material consolidation using SPS. Mechanical alloying resulted fcc and bcc phases while the SPS resulted the phase formation of bcc to α' and σ phases which are $L1_2$ ordered and unaltered fcc phase. Fracture toughness of the alloy sintered at 700 ºC is 3.9 MPa $m^{1/2}$ and at 1000 ºC is 1 MPa $m^{1/2}$. The fracture surface of the alloys sintered at different temperatures are shown in **Fig. 2.30**. It is clearly observed

that the failure is brittle in nature and is accredited to the formation of nanosized σ precipitates which are brittle.

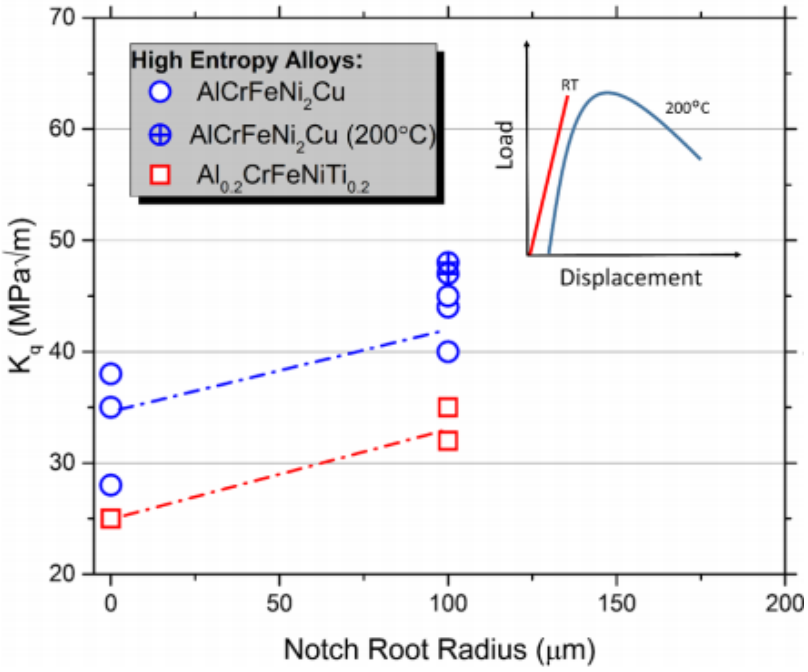

Fig. 2.29 The variation of fracture toughness with the notch root radius and load verses displacement curves in the insert [106].

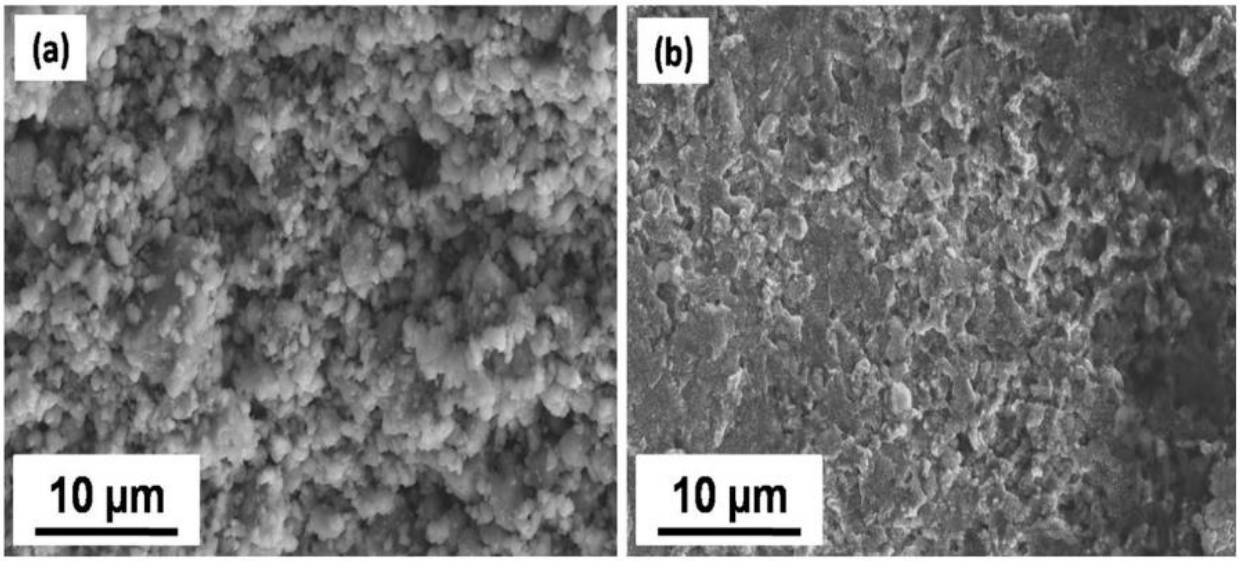

Fig. 2.30 Scanning electron micrograph of fracture surface of AlCoCrFeNi HEA sintered at (a) 800 ºC and (b) 1000 ºC [107].

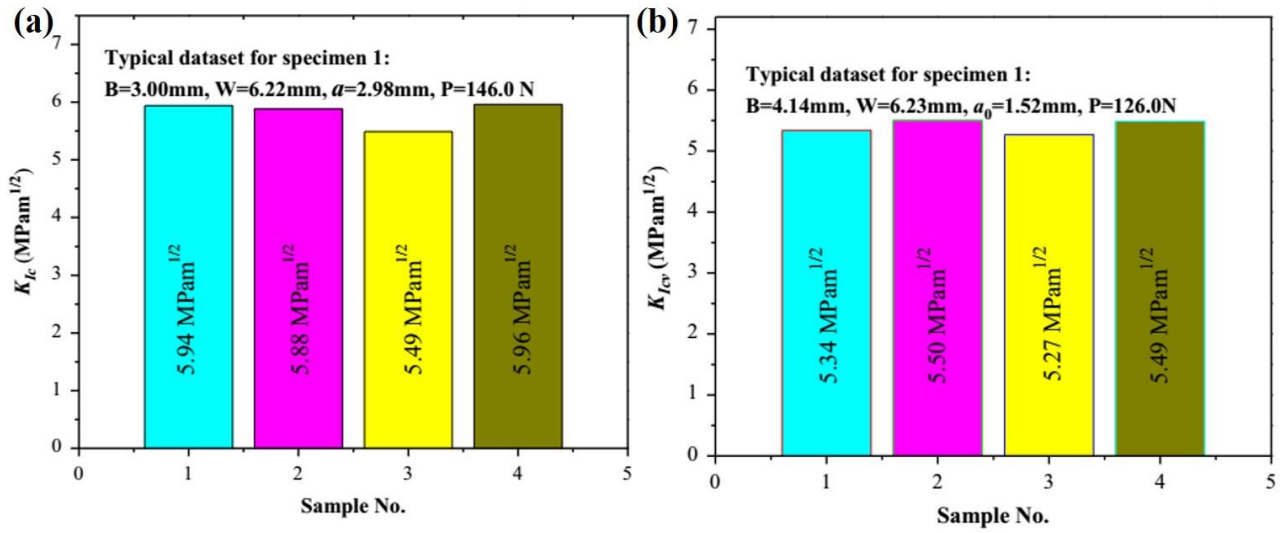

Fig. 2.31 Histograms of the fracture toughness values of (a) SENB and (b) CVNRB tests [108].

Roy et al [108] synthesized $Al_{23}Co_{15}Cr_{23}Cu_8Fe_{15}Ni_{15}$ HEA using melting and casting methods. As-cast alloy revealed a fcc and B2 phase with microhardness of 5.4 GPa. Fracture toughness was measured using two methods, single edge notched bend test (SENB) and chevron notched rectangular bar test (CVNRB). The average fracture toughness of SENB test is 5.8 MPa $m^{1/2}$ (see **Fig. 2.31(a)**). The average fracture toughness of CVNRB test is 5.4 MPa $m^{1/2}$ (see **Fig. 2.31(b)**). Gludovatz et al [109] worked with Cantor alloy (CoCrFeMnNi) which has a single fcc phase and found the fracture toughness value of 217 MPa $m^{1/2}$, 221 MPa $m^{1/2}$, and 219 MPa $m^{1/2}$ at 20 ºC, -73 ºC and liquid nitrogen temperature (-196 ºC) respectively as shown in **Fig. 2.32**. The fracture toughness values were compared with various materials and the Ashby map is shown in **Fig. 2.33**. Based on all these reports in the literature it is clear that plasticity and fraction of HEAs is fascinating. Therefore in the current investigation efforts have been made to understand these two phenomena in AlCoCrCuFeNi and AlCuTaVW HEAs.

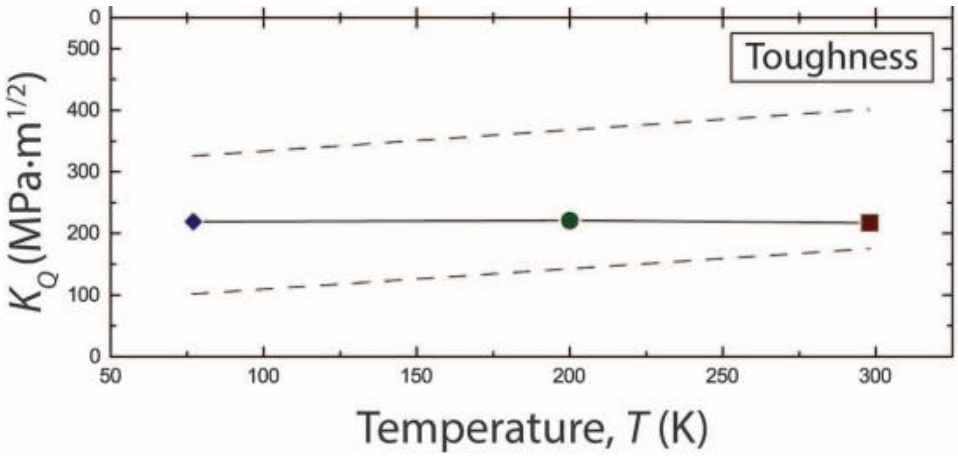

Fig. 2.32 Variation of fracture toughness values with the temperature. The dotted lines are the limits of the data from literature [109].

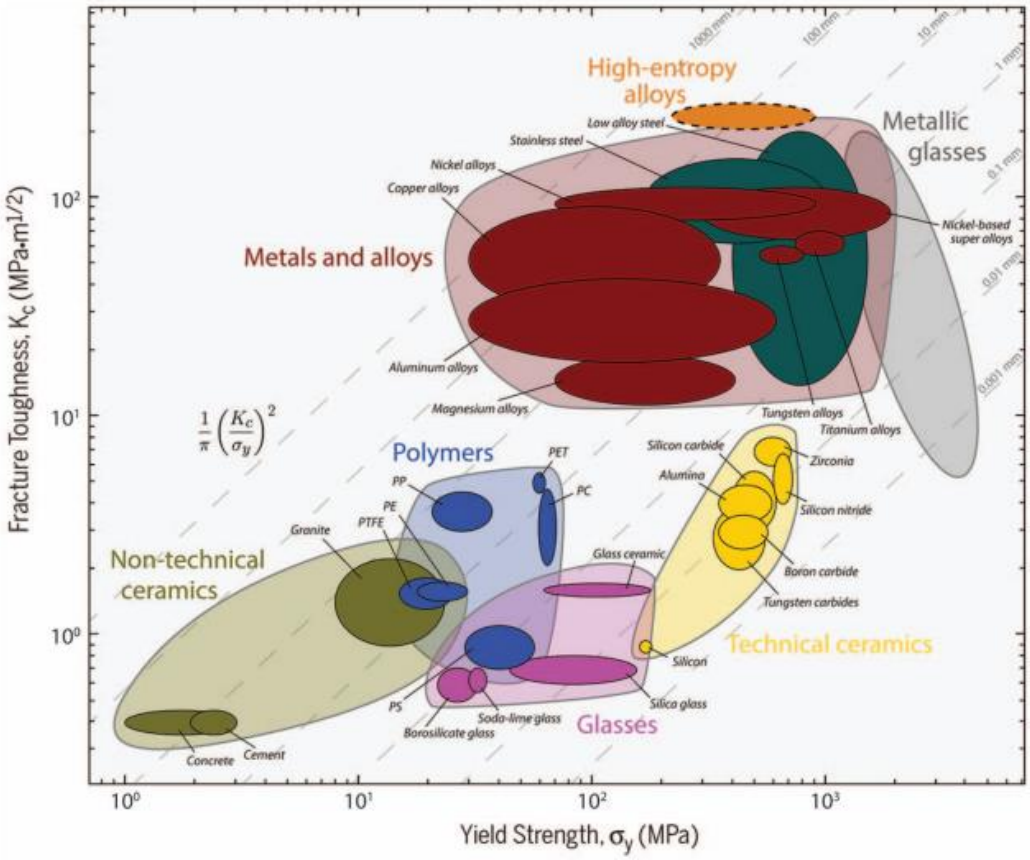

Fig. 2.33 The variation of fracture toughness values with yield strength of various materials where HEAs have high fracture toughness and yield strength among all materials [109].

References

1. Gaskell DR: **Introduction to the thermodynamics of materials**. DC, WA, USA: Taylor & Francis: Washington; 1995.
2. Kocks UF, Argon AS, Ashby MF: **Thermodynamics and kinetics of slip**. *Prog Mater Sci* 1975, **19**:1-281.
3. Liang S-M, Schmid-Fetzer R: **Thermodynamic assessment of the Al–Cu–Zn system, Part III: Al–Cu–Zn ternary system**. *Calphad* 2016, **52**:21-37.
4. Li A, Zhang X: **Thermodynamic analysis of the simple microstructure of AlCrFeNiCu high-entropy alloy with multi-principal elements**. *Acta Metallurgica Sinica (English Letters)* 2009, **22**(3):219-224.
5. Liu XL, Lindwall G, Gheno T, Liu Z-K: **Thermodynamic modeling of Al–Co–Cr, Al–Co–Ni, Co–Cr–Ni ternary systems towards a description for Al–Co–Cr–Ni**. *Calphad* 2016, **52**:125-142.
6. Melnick AB, Soolshenko VK: **Thermodynamic design of high-entropy refractory alloys**. *Journal of Alloys and Compounds* 2017, **694**:223-227.
7. Yeh J-W: **Alloy design strategies and future trends in high-entropy alloys**. *Jom* 2013, **65**(12):1759-1771.
8. Chang SY, Li CE, Huang YC, Hsu HF, Yeh JW, Lin SJ: **Structural and thermodynamic factors of suppressed interdiffusion kinetics in multi-component high-entropy materials**. *Sci Rep* 2014, **4**:4162.
9. Tsai MH, Yeh JW: **High-entropy alloys: a critical review**. *Material Research Letters* 2014, **2**:107-123.
10. Zhang Y, Qiao J-w, Liaw PK: **A Brief Review of High Entropy Alloys and Serration Behavior and Flow Units**. *Journal of Iron and Steel Research, International* 2016, **23**(1):2-6.
11. Miracle DB, Senkov ON: **A critical review of high entropy alloys and related concepts**. *Acta Materialia* 2017, **122**:488-511.
12. Miracle D, Miller J, Senkov O, Woodward C, Uchic M, Tiley J: **Exploration and development of high entropy alloys for structural applications**. *Entropy* 2014, **16**(1):494-525.

13. Ye YF, Wang Q, Lu J, Liu CT, Yang Y: **High-entropy alloy: challenges and prospects**. *Materials Today* 2015, **http://dx.doi.org/10.1016/j.mattod.2015.11.026**.
14. Zhang Y, Zhou YJ, Lin JP, Chen GL, Liaw PK: **Solid-solution phase formation rules for multi-component alloys**. *Advanced Engineering Materials* 2008, **10**(6):534-538.
15. Guo S, Hu Q, Ng C, Liu CT: **More than entropy in high-entropy alloys: Forming solid solutions or amorphous phase**. *Intermetallics* 2013, **41**:96-103.
16. Guo S, Liu CT: **Phase stability in high entropy alloys: formation of solid-solution phase or amorphous phase**. *Progress in Natural Science: Materials International* 2011, **21**:433-446.
17. Guo S: **Phase selection rules for cast high entropy alloys: an overview**. *Materials Science and Technology* 2015, **31**(10):1223-1230.
18. Zhang C, Zhang F, Chen S, Cao W: **Computational thermodynamics aided high-entropy alloy design**. *Jom* 2012, **64**(7):839-845.
19. He F, Wang Z, Li Y, Wu Q, Li J, Wang J, Liu CT: **Kinetic ways of tailoring phases in high entropy alloys**. *Sci Rep* 2016, **6**:34628.
20. Dwivedi A, Koch CC, Rajulapati KV: **On the single phase fcc solid solution in nanocrystalline Cr-Nb-Ti-V-Zn high-entropy alloy**. *Materials Letters* 2016, **183**:44-47.
21. Guo S, Ng C, Lu J, Liu CT: **Effect of valence electron concentration on stability of fcc or bcc phase in high entropy alloys**. *Journal of Applied Physics* 2011, **109**(10):103505 103501-103505.
22. Poletti MG, Battezzati L: **Electronic and thermodynamic criteria for the occurrence of high entropy alloys in metallic systems**. *Acta Materialia* 2014, **75**:297-306.
23. King DJM, Middleburgh SC, McGregor AG, Cortie MB: **Predicting the formation and stability of single phase high-entropy alloys**. *Acta Materialia* 2016, **104**:172-179.
24. Bhattacharjee PP, Sathiaraj GD, Zaid M, Gatti JR, Lee C, Tsai C-W, Yeh J-W: **Microstructure and texture evolution during annealing of equiatomic CoCrFeMnNi high-entropy alloy**. *Journal of Alloys and Compounds* 2014, **587**:544-552.
25. Wani IS, Bhattacharjee T, Sheikh S, Bhattacharjee PP, Guo S, Tsuji N: **Tailoring nanostructures and mechanical properties of AlCoCrFeNi2.1 eutectic high entropy alloy using thermo-mechanical processing**. *Materials Science and Engineering: A* 2016, **675**:99-109.

26. Wani IS, Bhattacharjee T, Sheikh S, Lu YP, Chatterjee S, Bhattacharjee PP, Guo S, Tsuji N: **Ultrafine-Grained AlCoCrFeNi2.1Eutectic High-Entropy Alloy**. *Materials Research Letters* 2016, **4**(3):174-179.
27. Senkov ON, Miller JD, Miracle DB, Woodward C: **Accelerated exploration of multi-principal element alloys with solid solution phases**. *Nature communications* 2015, **6**:6529.
28. Cheng C-Y, Yeh J-W: **High thermal stability of the amorphous structure of GexNbTaTiZr (x=0.5, 1) high-entropy alloys**. *Materials Letters* 2016, **181**:223-226.
29. Juan C-C, Tsai M-H, Tsai C-W, Hsu W-L, Lin C-M, Chen S-K, Lin S-J, Yeh J-W: **Simultaneously increasing the strength and ductility of a refractory high-entropy alloy via grain refining**. *Materials Letters* 2016, **184**:200-203.
30. Lee D-H, Choi I-C, Seok M-Y, He J, Lu Z, Suh J-Y, Kawasaki M, Langdon TG, Jang J-i: **Nanomechanical behavior and structural stability of a nanocrystalline CoCrFeNiMn high-entropy alloy processed by high-pressure torsion**. *Journal of Materials Research* 2015, **30**(18):2804-2815.
31. Lin M-I, Tsai M-H, Shen W-J, Yeh J-W: **Evolution of structure and properties of multi-component (AlCrTaTiZr)Ox films**. *Thin Solid Films* 2010, **518**(10):2732-2737.
32. Juan C-C, Tsai M-H, Tsai C-W, Lin C-M, Wang W-R, Yang C-C, Chen S-K, Lin S-J, Yeh J-W: **Enhanced mechanical properties of HfMoTaTiZr and HfMoNbTaTiZr refractory high-entropy alloys**. *Intermetallics* 2015, **62**:76-83.
33. Sharma A, Singh P, Johnson DD, Liaw PK, Balasubramanian G: **Atomistic clustering-ordering and high-strain deformation of an $Al_{0.1}$CrCoFeNi high-entropy alloy**. *Scientific Reports* 2016, **6**:31028.
34. Yeh JW, Chen SK, Gan JY, Lin SJ, Chin TS, Shun TT, Tsau CH, Chang SY: **Formation of simple crystal structures in Cu-Co-Ni-Cr-Al-Fe-Ti-V alloys with multiprincipal metallic elements**. *Metallurgical and Materials Transactions A* 2004, **35**:2533-2536.
35. Yeh J-W: **Physical metallurgy of high-entropy alloys**. *Jom* 2015, **67**(10):2254-2261.
36. wu W-H, Yang C-C, Yeh J-W: **Industrial development of high-entropy alloys**. *Annales de Chimie Science des Matériaux* 2006, **31**(6):737-747.
37. Tsai M-H: **Three Strategies for the Design of Advanced High-Entropy Alloys**. *Entropy* 2016, **18**(7):252.

38. Pickering EJ, Jones NG: **High-entropy alloys: a critical assessment of their founding principles and future prospects**. *International Materials Reviews* 2016, **61**(3):183-202.
39. Kumar NAPK, Li C, Leonard KJ, Bei H, Zinkle SJ: **Microstructural stability and mechanical behavior of FeNiMnCr high entropy alloy under ion irradiation**. *Acta Materialia* 2016, **113**:230-244.
40. Dolique V, Thomann AL, Brault P: **High-entropy alloys deposited by magnetron sputtering**. *IEEE Transactions on Plasma Science* 2011, **39**(11):2478-2479.
41. Braic M, Braic V, Balaceanu M, Zoita CN, Vladescu A, Grigore E: **Characteristics of (TiAlCrNbY)C films deposited by reactive magnetron sputtering**. *Surface and Coatings Technology* 2010, **204**(12-13):2010-2014.
42. Kottada RS, Chokshi AH: **Low temperature compressive creep in electrodeposited nanocrystalline nickel**. *Scripta Materialia* 2005, **53**(8):887-892.
43. Ang ASM, Berndt CC, Sesso ML, Anupam A, S P, Kottada RS, Murty BS: **Plasma-sprayed high entropy alloys: microstructure and properties of AlCoCrFeNi and MnCoCrFeNi**. *Metallurgical and Materials Transactions A* 2014, **46**(2):791-800.
44. Zhang S, Wu CL, Zhang CH: **Phase evolution characteristics of FeCoCrAlCuV$_x$Ni high entropy alloy coatings by laser high-entropy alloying**. *Materials Letters* 2015, **141**:7-9.
45. Yue T, Xie H, Lin X, Yang H, Meng G: **Microstructure of laser re-melted AlCoCrCuFeNi high entropy alloy coatings produced by plasma spraying**. *Entropy* 2013, **15**(7):2833-2845.
46. Feng XB, Zhang JY, Wang YQ, Hou ZQ, Wu K, Liu G, Sun J: **Size effects on the mechanical properties of nanocrystalline NbMoTaW refractory high entropy alloy thin films**. *International Journal of Plasticity* 2017, **http://dx.doi.org/10.1016/j.ijplas.2017.04.013**.
47. Chuang M-H, Tsai M-H, Wang W-R, Lin S-J, Yeh J-W: **Microstructure and wear behavior of Al$_x$Co$_{1.5}$CrFeNi$_{1.5}$Ti$_y$ high-entropy alloys**. *Acta Materialia* 2011, **59**(16):6308-6317.
48. Kou S: **A criterion for cracking during solidification**. *Acta Materialia* 2015, **88**:366-374.
49. Ma D, Yao M, Pradeep KG, Tasan CC, Springer H, Raabe D: **Phase stability of non-equiatomic CoCrFeMnNi high entropy alloys**. *Acta Materialia* 2015, **98**:288-296.

50. Singh S, Wanderka N, Murty BS, Glatzel U, Banhart J: **Decomposition in multi-component AlCoCrCuFeNi high-entropy alloy**. *Acta Materialia* 2011, **59**:182-190.
51. Zhang Q, Shi X, Yang H, Duan X: **Microstructure and properties of W-15Cu alloys prepared by mechanical alloying and spark plasma sintering process**. *Journal of Wuhan University of Technology-Materials Science Edition* 2008, **23**(3):399-402.
52. Praveen S, Anupam A, Sirasani T, Murty BS, Kottada RS: **Characterization of oxide dispersed AlCoCrFe high entropy alloy synthesized by mechanical alloying and spark plasma sintering**. *Transactions of the Indian Institute of Metals* 2013, **66**(4):369-373.
53. Ji W, Fu Z, Wang W, Wang H, Zhang J, Wang Y, Zhang F: **Mechanical alloying synthesis and spark plasma sintering consolidation of CoCrFeNiAl high-entropy alloy**. *Journal of Alloys and Compounds* 2014, **589**:61–66.
54. Kuk SW, Lim WJ, Kim SS, Hong SH, Ryu HJ: **Fabrication of W-Nb-Mo-Ta-V high entropy alloys by mechanical alloying and spark plasma sintering**. *Transactions of the Korean Nuclear Society Spring Meeting* 2015.
55. Varalakshmi S, Kamaraj M, Murty BS: **Synthesis and characterization of nanocrystalline AlFeTiCrZnCu high entropy solid solution by mechanical alloying**. *Journal of Alloys and Compounds* 2008, **460**(1-2):253-257.
56. Zhang KB, Fu ZY, Zhang JY, Shi J, Wang WM, Wang H, Wang YC, Zhang QJ: **Nanocrystalline CoCrFeNiCuAl high-entropy solid solution synthesized by mechanical alloying**. *Journal of Alloys and Compounds* 2009, **485**:L31–L34.
57. Gómez-Esparza CD, Campos-Venegas K, Solis-Canto O, Alvarado-Orozco JM, Muñoz-Saldaña J, Herrera-Ramírez JM, Martínez-Sánchez R: **Nanohardness and microstructure of NiCoAlFeCu and NiCoAlFeCuCr alloys produced by mechanical alloying**. *Microscopy and Microanalysis* 2014, **20**:2106-2107.
58. Maulik O, Kumar V: **Synthesis of AlFeCuCrMg$_x$ (x=0, 0.5, 1, 1.7) alloy powders by mechanical alloying**. *Materials Characterization* 2015, **110**:116-125.
59. Senkov ON, Senkova SV, Miracle DB, Woodward C: **Mechanical properties of low-density, refractory multi-principal element alloys of the Cr–Nb–Ti–V–Zr system**. *Materials Science and Engineering: A* 2013, **565**:51-62.

60. Senkov ON, Wilks GB, Scott JM, Miracle DB: **Mechanical properties of $Nb_{25}Mo_{25}Ta_{25}W_{25}$ and $V_{20}Nb_{20}Mo_{20}Ta_{20}W_{20}$ refractory high entropy alloys**. *Intermetallics* 2011, **19**(5):698-706.
61. Liu WH, Wu Y, He JY, Nieh TG, Lu ZP: **Grain growth and the Hall–Petch relationship in a high-entropy FeCrNiCoMn alloy**. *Scripta Materialia* 2013, **68**(7):526-529.
62. Fazakas É, Wang JQ, Zadorozhnyy V, Louzguine-Luzgin DV, Varga LK: **Microstructural evolution and corrosion behavior of Al25Ti25Ga25Be25equi-molar composition alloy**. *Materials and Corrosion* 2014, **65**(7):691-695.
63. Chen YY, Duval T, Hung UD, Yeh JW, Shih HC: **Microstructure and electrochemical properties of high entropy alloys—a comparison with type-304 stainless steel**. *Corrosion Science* 2005, **47**(9):2257-2279.
64. Gong P, Jin J, Deng L, Wang S, Gu J, Yao K, Wang X: **Room temperature nanoindentation creep behavior of TiZrHfBeCu(Ni) high entropy bulk metallic glasses**. *Materials Science and Engineering: A* 2017, **688**:174-179.
65. Sheikh S, Shafeie S, Hu Q, Ahlström J, Persson C, Veselý J, Zýka J, Klement U, Guo S: **Alloy design for intrinsically ductile refractory high-entropy alloys**. *Journal of Applied Physics* 2016, **120**(16):164902 164901-164905.
66. M.C. Gao CSC, O.N. Dogan, P.D. Jablonksi, J.A. Hawk, D.E. Alman: **Design of Refractory High-Entropy Alloys**. *Jom* 2015, **67**(11):2653-2669.
67. Senkov ON, Senkova SV, Woodward C: **Effect of aluminum on the microstructure and properties of two refractory high-entropy alloys**. *Acta Materialia* 2014, **68**:214-228.
68. Fazakas É, Zadorozhnyy V, Varga LK, Inoue A, Louzguine-Luzgin DV, Tian F, Vitos L: **Experimental and theoretical study of $Ti_{20}Zr_{20}Hf_{20}Nb_{20}X_{20}$ (X=V or Cr) refractory high-entropy alloys**. *International Journal of Refractory Metals and Hard Materials* 2014, **47**:131-138.
69. Senkov O, Isheim D, Seidman D, Pilchak A: **Development of a refractory high entropy superalloy**. *Entropy* 2016, **18**(3):102.
70. Senkov ON, Senkova SV, Woodward C, Miracle DB: **Low-density, refractory multi-principal element alloys of the Cr–Nb–Ti–V–Zr system: Microstructure and phase analysis**. *Acta Materialia* 2013, **61**(5):1545-1557.

71. Youssef KM, Zaddach AJ, Niu C, Irving DL, Koch CC: **A novel low-density, high-hardness, high-entropy alloy with close-packed single-phase nanocrystalline structures**. *Materials Research Letters* 2014, **3**(2):95-99.
72. Samaei AT, Mirsayar MM, Aliha MRM: **The microstructure and mechanical behavior of modern high temperature alloys**. *Engineering Solid Mechanics* 2015, **3**(1):1-20.
73. Yeh JW, Chen SK, Lin SJ, Gan JY, Chin TS, Shun TT, Tsua CH, Chang SY: **Nanostructured high entropy alloys with multiple principal elements: novel alloy design concepts and outcomes**. *Advanced Engineering Materials* 2004, **6**:299-302.
74. Cantor B, Chang ITH, Knight P, Vincent AJB: **Microstructural development in equiatomic multicomponent alloys**. *Materials Science and Engineering A* 2004, **375-377**:213-218.
75. Tung CC, Yeh JW, Shun TT, Chen SK, Huang YS, Chen HC: **On the elemental effect of AlCoCrCuFeNi high-entropy alloy system**. *Materials Letters* 2007, **61**:1-5.
76. Santodonato LJ, Zhang Y, Feygenson M, Parish CM, Gao MC, Weber RJ, Neuefeind JC, Tang Z, Liaw PK: **Deviation from high-entropy configurations in the atomic distributions of a multi-principal-element alloy**. *Nature communications* 2015, **6**:1-13.
77. Zhang B, Gao MC, Zhang Y, Guo SM: **Supporting data for senary refractory high-entropy alloy Cr_xMoNbTaVW**. *Data in brief* 2015, **5**:730-735.
78. Jin K, Sales BC, Stocks GM, Samolyuk GD, Daene M, Weber WJ, Zhang Y, Bei H: **Tailoring the physical properties of Ni-based single-phase equiatomic alloys by modifying the chemical complexity**. *Scientific Reports* 2016, **6**:20159.
79. Sriharitha R, Murty BS, Kottada RS: **Phase formation in mechanically alloyed Al_xCoCrCuFeNi (x = 0.45, 1, 2.5, 5 mol) high entropy alloys**. *Intermetallics* 2013, **32**:119-126.
80. Sriharitha R, Murty BS, Kottada RS: **Alloying, thermal stability and strengthening in spark plasma sintered Al_xCoCrCuFeNi high entropy alloys**. *Journal of Alloys and Compounds* 2014, **583**:419-426.
81. Murty BS, Yeh JW, Ranganathan S: **High-entropy alloys**. Boston: Butterworth-Heinemann; 2014.
82. Gao MC, Alman DE: **Searching for next single-phase high-entropy alloy compositions**. *Entropy* 2013, **15**:4504-4519.

83. Li BS, Wang YP, Ren MX, Yang C, Fu HZ: **Effects of Mn, Ti and V on the microstructure and properties of AlCrFeCoNiCu high entropy alloy**. *Materials Science and Engineering: A* 2008, **498**(1-2):482-486.
84. Li Z, Pradeep KG, Deng Y, Raabe D, Tasan CC: **Metastable high-entropy dual-phase alloys overcome the strength-ductility trade-off**. *Nature* 2016, **534**(7606):227-230.
85. Wang Z, Baker I, Guo W, Poplawsky JD: **The effect of carbon on the microstructures, mechanical properties, and deformation mechanisms of thermo-mechanically treated $Fe_{40.4}Ni_{11.3}Mn_{34.8}Al_{7.5}Cr_6$ high entropy alloys**. *Acta Materialia* 2017, **126**:346-360.
86. Schuh B, Mendez-Martin F, Völker B, George EP, Clemens H, Pippan R, Hohenwarter A: **Mechanical properties, microstructure and thermal stability of a nanocrystalline CoCrFeMnNi high-entropy alloy after severe plastic deformation**. *Acta Materialia* 2015, **96**:258-268.
87. Fu Z, Chen W, Wen H, Zhang D, Chen Z, Zheng B, Zhou Y, Lavernia EJ: **Microstructure and strengthening mechanisms in an fcc structured single-phase nanocrystalline $Co_{25}Ni_{25}Fe_{25}Al_{7.5}Cu_{17.5}$ high-entropy alloy**. *Acta Materialia* 2016, **107**:59-71.
88. Pradeep KG, Wanderka N, Choi P, Banhart J, Murty BS, Raabe D: **Atomic-scale compositional characterization of a nanocrystalline AlCrCuFeNiZn high-entropy alloy using atom probe tomography**. *Acta Materialia* 2013, **61**(12):4696-4706.
89. Ji W, Wang W, Wang H, Zhang J, Wang Y, Zhang F, Fu Z: **Alloying behavior and novel properties of CoCrFeNiMn high-entropy alloy fabricated by mechanical alloying and spark plasma sintering**. *Intermetallics* 2015, **56**:24-27.
90. Liu B, Wang J, Liu Y, Fang Q, Wu Y, Chen S, Liu CT: **Microstructure and mechanical properties of equimolar FeCoCrNi high entropy alloy prepared via powder extrusion**. *Intermetallics* 2016, **75**:25-30.
91. Yang T, Xia S, Liu S, Wang C, Liu S, Fang Y, Zhang Y, Xue J, Yan S, Wang Y: **Precipitation behavior of $Al_xCoCrFeNi$ high entropy alloys under ion irradiation**. *Scientific Reports* 2016, **6**(1).
92. Pickering EJ, Muñoz-Moreno R, Stone HJ, Jones NG: **Precipitation in the equiatomic high-entropy alloy CrMnFeCoNi**. *Scripta Materialia* 2016, **113**:106-109.

93. He JY, Wang H, Wu Y, Liu XJ, Mao HH, Nieh TG, Lu ZP: **Precipitation behavior and its effects on tensile properties of FeCoNiCr high-entropy alloys**. *Intermetallics* 2016, **79**:41-52.

94. Liu WH, Lu ZP, He JY, Luan JH, Wang ZJ, Liu B, Liu Y, Chen MW, Liu CT: **Ductile $CoCrFeNiMo_x$ high entropy alloys strengthened by hard intermetallic phases**. *Acta Materialia* 2016, **116**:332-342.

95. Maiti S, Steurer W: **Structural-disorder and its effect on mechanical properties in single-phase TaNbHfZr high-entropy alloy**. *Acta Materialia* 2016, **106**:87-97.

96. Zou Y, Maiti S, Steurer W, Spolenak R: **Size-dependent plasticity in an $Nb_{25}Mo_{25}Ta_{25}W_{25}$ refractory high-entropy alloy**. *Acta Materialia* 2014, **65**:85-97.

97. Ye X, Ma M, Liu W, Li L, Zhong M, Liu Y, Wu Q: **Synthesis and characterization of high-entropy alloy $Al_XFeCoNiCuCr$ by laser cladding**. *Advances in Materials Science and Engineering* 2011, **2011**.

98. Manzoni A, Singh S, Daoud H, Popp R, Völkl R, Glatzel U, Wanderka N: **On the path to optimizing the Al-Co-Cr-Cu-Fe-Ni-Ti high entropy alloy family for high temperature applications**. *Entropy* 2016, **18**(4):104.

99. He JY, Wang H, Huang HL, Xu XD, Chen MW, Wu Y, Liu XJ, Nieh TG, An K, Lu ZP: **A precipitation-hardened high-entropy alloy with outstanding tensile properties**. *Acta Materialia* 2016, **102**:187-196.

100. Kuznetsov AV, Shaisultanov DG, Stepanov ND, Salishchev GA, Senkov ON: **Superplasticity of AlCoCrCuFeNi high entropy alloy**. *Materials Science Forum* 2012, **735**:146-151.

101. Shaysultanov DG, Stepanov ND, Kuznetsov AV, Salishchev GA, Senkov ON: **Phase composition and superplastic behavior of a wrought AlCoCrCuFeNi high-entropy alloy**. *Jom* 2013, **65**(12):1815-1828.

102. Stepanov ND, Shaysultanov DG, Salishchev GA, Tikhonovsky MA: **Structure and mechanical properties of a light-weight AlNbTiV high entropy alloy**. *Materials Letters* 2015, **142**:153-155.

103. Zhou YJ, Zhang Y, Wang YL, Chen GL: **Solid solution alloys of $AlCoCrFeNiTi_x$ with excellent room-temperature mechanical properties**. *Applied Physics Letters* 2007, **90**(18):181904.

104. Alaneme KK, Bodunrin MO, Oke SR: **Processing, alloy composition and phase transition effect on the mechanical and corrosion properties of high entropy alloys: a review**. *Journal of Materials Research and Technology* 2016, **5**(4):384-393.

105. Dong Y, Zhou K, Lu Y, Gao X, Wang T, Li T: **Effect of vanadium addition on the microstructure and properties of AlCoCrFeNi high entropy alloy**. *Materials & Design* 2014, **57**:67-72.

106. Seifi M, Li D, Yong Z, Liaw PK, Lewandowski JJ: **Fracture toughness and fatigue crack growth behavior of as-cast high-entropy alloys**. *Jom* 2015, **67**(10):2288-2295.

107. Mohanty S, Maity TN, Mukhopadhyay S, Sarkar S, Gurao NP, Bhowmick S, Biswas K: **Powder metallurgical processing of equiatomic AlCoCrFeNi high entropy alloy: Microstructure and mechanical properties**. *Materials Science and Engineering: A* 2017, **679**:299-313.

108. Roy U, Roy H, Daoud H, Glatzel U, Ray KK: **Fracture toughness and fracture micromechanism in a cast AlCoCrCuFeNi high entropy alloy system**. *Materials Letters* 2014, **132**:186-189.

109. Gludovatz B, Hohenwarter A, Catoor D, Chang EH, George EP, Ritchie RO: **A fracture-resistant high-entropy alloy for cryogenic applications**. *Science* 2014, **345**(6201):1153-1158.

Chapter 3 Experimental details

To synthesize the high entropy alloys (HEAs), mechanical alloying (MA) followed by spark plasma sintering (SPS) techniques has been used in the current investigation. Two different HEA compositions have been synthesized in equal atomic ratios, AlCoCrCuFeNi and AlCuTaVW HEAs. AlCoCrCuFeNi HEA is milled for 60 hours and AlCuTaVW HEA is milled for 25 hours. Different SPS parameters are adopted to study the effect of sintering parameters on the nanocrystalline bulk material. Structural characterization was done using X-ray diffractometry (XRD), scanning electron microscopy (SEM) and transmission electron microscopy (TEM). Vickers microindentation and depth sensing nanoindentation techniques were employed to measure the mechanical properties of both the multi principal alloys.

3.1 Materials used

Table 3. 1 Physical properties of the elements in the HEA.

Element	Atomic number (Z)	Atomic radius (Å)	Atomic mass (amu†)	Density, (g/cc)	Melting point (°C)	Lattice parameter (Å)	Crystal structure
Al	13	1.18	26.981	2.7	660	4.05	FCC
Cr	24	1.66	51.996	7.15	1907	2.88	BCC
Cu	29	1.45	63.546	8.96	1083	3.61	FCC
Co	27	1.52	58.933	8.86	1495	2.51	HCP
Fe	26	1.56	55.845	7.87	1538	2.87	BCC
Ni	28	1.49	58.693	8.91	1455	3.52	FCC
Ta	73	2.00	180.94	16.65	2996	3.31	BCC
V	23	1.71	50.941	5.8	1887	3.02	BCC
W	74	1.93	183.84	19.3	3407	3.16	BCC

† Atomic mass unit.

The elemental powders of Al, Cu, Cr, Co, Fe, Ni, Ta, V and W of purity greater than 99.5 % and the initial particle size was about 44 μm i.e., -325 mesh were used as the initial raw materials. The handling of the metal powders was done in a high purity argon atmosphere inside the glove box to avoid contamination of the powders. The physical properties of HEA are given in **Table 3.** *1*.

3.2 Processing nanocrystalline HEAs

There are two different approaches to synthesis nanocrystalline materials. They are broadly classified into two categories, 'bottom-up approach' and 'top-down approach'. Bottom-up approach builds atom by atom → molecules → clusters → nanoparticles. Electrodeposition, magnetron sputtering are the examples bottom-up methods. Top-down approach begins by breaking down microstructural features from coarse scale to nano scales. Attrition and milling are typical top-down synthesizing methods to produce nanocrystallite. Wherein MA introduces lattice defects internal stress, surface defects etc.

3.2.1 Mechanical alloying

Table 3.2 Parameters used for MA of equiatomic HEAs.

Type of Mill	High energy ball mill
Make	SPEX 8000D shaker mill
Milling media material	Hardened Steel
Milling condition	Dry
Milling temperature	Room temperature
Milling atmosphere	Argon
Ball to powder weight ratio	5:1
Process controlling agent	1 weight% Stearic acid

MA is a top-down approach where the mechanism of MA is a repetitive process of fracturing and cold welding of different particles [1, 2]. The micron sized particles are weighed and loaded into the vials in desired proportions along with weighed grinding medium. The sealed vials are milled for a particular period of time until the alloy has homogenous composition and the particle/crytallite size is reduced to below 100nm. The MA process parameters used to produce nanocrystalline HEAs are given in **Table 3.2**. The vials in SPEX mill move as the symbol infinity '∞', the ends of the vials are moved in lateral motion so that the balls hit the powders to mix and mill. The length of the vial is 5 cm and the speed of the clamp motion is about 1200 rpm, then each ball will have a very high velocity of 5 m/s [3]. The total force together with which they impact on the powders is very high hence it is considered as high energy ball milling. A 20 mins break is given to the milling after each hour in order to cool the motor and the vials. Samples were collected at an interval of 5h to have a record of structural/microstructural variations. When the powders were stuck to the vials and balls because of cold welding, 1 wt. % stearic acid was added to the powders as a process controlling agent. The recent investigations found that the dry milling or milling with toluene or ethanol resulted in contaminations. Moravcik et al [4] reported that the carbon from the process controlling agent (methanol) reacted with Ti in the alloy and formed TiC nano particles. However milling with stearic acid led a very less contamination [5].

3.2.2 Spark plasma sintering

Spark plasma sintering (SPS) is a rapid sintering technique, where DC pulsed current and a simultaneous compaction pressure is employed. A localized plasma is generated between the particles with temperatures of few thousands which melt the surfaces and create a neck between them. The compaction force helps the neck to grow and plastically deform the surface of the particle to result a high dense product. As the process of localized heating and compaction is fast,

the grain growth is appreciably low hence retains the nanocrystalline structures [6-8]. The SPS process parameters used to produce bulk nanocrystalline HEAs are given in **Table 3.3**. A preload is applied to make sure that all particles contact each other.

Table 3.3 Parameters used for SPS of equiatomic HEAs.

Type of Press	Spark plasma sintering
Make	DR SINTER 1050 apparatus (SPS Syntex Inc., Tokyo, Japan)
Pressure applied	80 MPa
Pulse on-off ratio	10:2
Sintering temperature	750 ºC for AlCoCrCuFeNi HEA Ranges 415 ºC – 1250 ºC for AlCuTaVW
Sintering atmosphere	Vacuum (6 Pa)
Heating rate	600 ºC/s
Holding time	Ranges 5 – 15 mins for AlCoCrCuFeNi 5 mins for AlCuTaVW
Die material	Graphite (die, punches and foil of 0.2 mm thick)
Pellet size	15 mm diameter and 2 mm height

3.3 Characterization methods

Milled powders were consolidated into discs of 15 mm in diameter using SPS at 750 ºC and at a uni-axial pressure of 80 MPa. The holding time during sintering has been varied as 5, 10 and 15 min. The densities of the sintered discs were measured using the Archimedes principle method [9]. The sintered pellet is polished gently to remove the graphite foil attached to it during SPS process.

Later it is sonicated for 15 mins and allowed to dry. The dry weight (Dry) of the specimen is measured and soaked in distilled water for 24 hours. Using Archimedes weighing balance, weight of the sample is measured while it is suspended (Suspended) in the distilled water. The excess water on the sample is wiped off carefully and saturated weight (Saturated) has been measure. The Achimedes density is then calculated using Equation 3.1.

$$Density, \rho\ \% = \frac{Dry}{Saturated - Suspended}\ x\ \frac{1}{Theroritical\ density}\ x\ 100 \ldots\ldots (3.1)$$

The MA and SPS processed materials have been characterized for phase identification, microstructural evolution and mechanical properties. The methods and the parameters used to characterize both the powder and bulk samples are briefly discussed below.

3.3.1 X-ray Diffraction

BRUKER D8 ADVANCE X-ray diffractometer equipment was used to evaluate the phases present, crystal structures, crystallite size, atomic spacing and the lattice constants. A monochromatic or single wavelength x-rays are generated from cathode ray tube with Cu target. Nickel filters are used to filter K_β line of copper and allow K_α radiations (wavelength = 1.5418 Å) to interact with the sample. The constructive interference is produced only when Bragg's law is satisfied and is given as,

$$n\lambda = 2d \sin\theta \ldots\ldots\ldots\ldots\ldots\ldots\ldots\ldots\ldots\ldots\ldots\ldots\ldots\ldots (3.2)$$

where λ is wavelength of x-rays, d is interplanar spacing, θ is the diffraction angle. The crystallites in the polycrystalline materials are oriented in different directions. The reflections of X-rays obtain only when the Equation 3.2 is fulfilled as shown in **Fig. 3.1**. The scan is performed between a 2θ of 20-110° with a step size of 0.05° and scan rate of 3 sec/step. Scintillating detector is used to record the angles and the intensities.

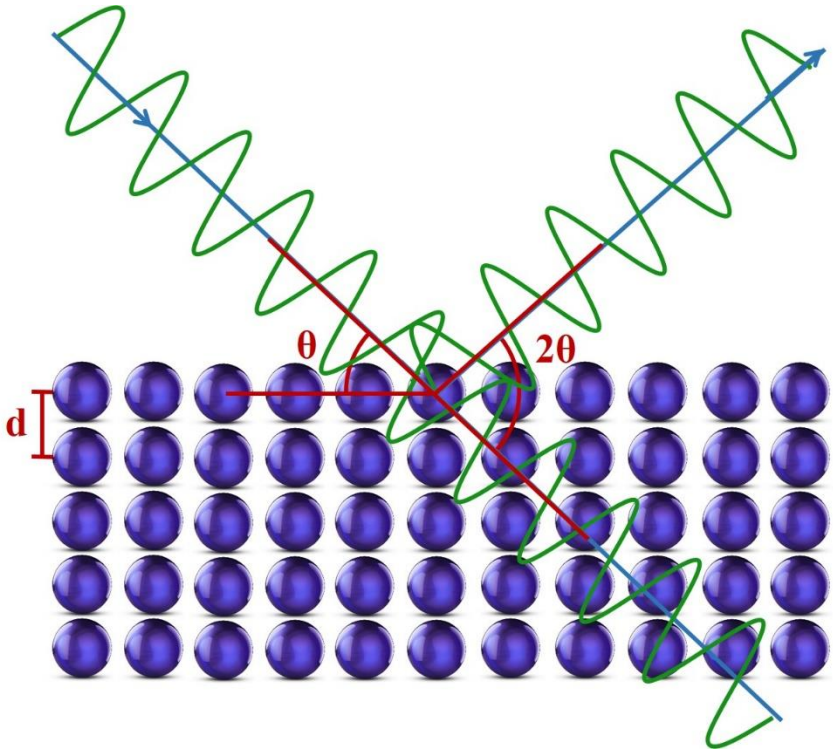

Fig. 3.1 Incident X-ray beam on a crystal lattice, coherent reflection with a constructive interference.

From the obtained XRD pattern, the peak positions are identified and interplanar spacing (d) is calculated using Equation 3.2. Each reflection has to be indexed with h,k,l. and this indexing is done with the help of extension rules. To calculate the lattice parameter (a) below Equation 3.3 is used for cubic systems. The precise lattice parameter is calculated using Nelson-Riley extrapolation function given in 3.4. An error is involved in the measurements not with a or d, but with θ. Hence even the Bragg equation contains sinθ, not just θ. The error increases while calculating sinθ with the increase in θ. Lattice parameters plotted against Nelson-Riley function will result a straight line. Extrapolating the straight line and the y-intercept will give the true lattice parameter.

$$\frac{1}{d^2} = \frac{h^2 + k^2 + l^2}{a^2} \quad \ldots\ldots\ldots\ldots\ldots\ldots\ldots\ldots\ldots\ldots\ldots\ldots\ldots\ldots\ldots\ldots (3.3)$$

$$\frac{\cos^2\theta}{\sin\theta} + \frac{\cos^2\theta}{\theta} \ldots\ldots\ldots\ldots\ldots\ldots\ldots\ldots\ldots\ldots\ldots\ldots\ldots\ldots\ldots\ldots (3.4)$$

Smaller crystallite size and the presence of lattice strain broadens the peak. So the width of the broadened peak in radians is used to evaluate the crystallite size. Instrumental broadening effect is first excluded from the experimental data and then full width half maxima (β) is calculated. Crystallite size, *L* is calculated from Scherrer formula given in Equation 3.5.

$$L = \frac{k\lambda}{\beta\cos\theta} = \frac{k\lambda}{\left(\beta_o{}^2 - \beta_i{}^2\right)^{1/2}\cos\theta} \ldots\ldots\ldots\ldots\ldots\ldots\ldots\ldots\ldots\ldots\ldots (3.5)$$

where λ is the wavelength of the X-rays used, θ is the Bragg angle, K is constant (for Gaussian line profiles and for cubic structures, k = 0.94), $\beta_o$is observed peak width, β_i is instrumental broadening peak width (0.045 deg in the current investigation). The relationship to find the lattice strain (ε) in the alloy using full width half maxima (β) is given by Stokes-Wilson formula and is shown in Equation 3.6.

$$\varepsilon = \frac{\beta}{4\tan\theta} \ldots\ldots\ldots\ldots\ldots\ldots\ldots\ldots\ldots\ldots\ldots\ldots\ldots\ldots\ldots\ldots (3.6)$$

3.3.2 Scanning Electron Microscopy

HITACHI S3400N SEM coupled with energy dispersive spectroscopy (EDS) were used for structural characterization in the present investigation. SEM is an analytical tool for surface morphology imaging, and the chemical composition is determined using EDS. The interaction of high energy electron beam with the atoms on the surface of the specimen produces elastic and inelastic scattered electrons. The elastic scattering of electrons do not provide any morphological information but the inelastic scattering of electrons gives the microstructural information in SEM. Few other signals are photons, Auger electrons, characteristic X-rays, backscattered electrons,

secondary electrons, etc. as shown in **Fig. 3.2**. Backscattered electrons are electrons ejected from the sample surface effected so much by the elastic scattering and reflects right back with relatively high energy. This beam of electrons mainly depends on the atomic number (Z) of the elements in the sample. Images produced using BSE detectors are in different shades of grey color representing the atomic number difference. This mode is mainly applicable for multiphase materials. Secondary electrons are produced because of inelastic scattering i.e. the energy of the electron beam is completely transferred to the atoms on the surface, and the loosely bonded electrons in the outer shell will be ejected. These electrons have low energy that they move freely on surface of the sample and hence are very useful to detect the morphology of the alloy with high resolution. The voltage and the emission current used while examination in SEM is 10-15 V and 167-173 μA respectively. The working distance of 4.2 mm is used in the current research work.

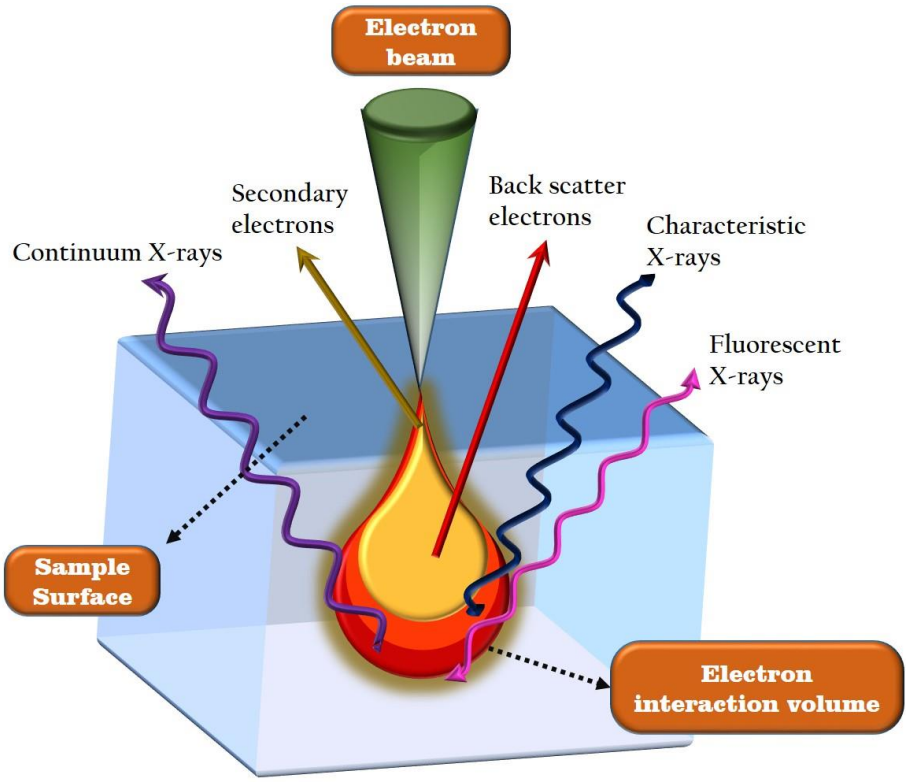

Fig. 3.2 Schematic of electron beam interaction with the bulk sample in scanning electron microscopy.

3.3.2.1 SEM sample preparation

The bulk samples to be examined in SEM should have a mirror finished surface. The basic metallographic techniques of polishing are used for this preparation. The process of SPS uses 0.2 μm graphite foil around the powders, acts like a lubricant in order to facilitate easy ejection of samples from that of the graphite die and punches. After SPS, this graphite foil is intact with the sample. A rough emery paper is needed to remove the graphite layer on all sides of the samples. Polishing the sample against emery papers of grades 400, 620, 800, 1000 and 1200 is done. Final polishing with diamond paste on velvet cloth is carefully done until the sample is free from scratches. Later the polished sample is washed and sonicated using ultrasonication in order to remove the contaminations or excess diamond paste present.

3.3.2.2 SEM imaging

The image information is collected scanning the specimen surface with the focused electron probe in steps. The electrons go through the surface of the sample and line scans are made on the sample to collect the microstructure. After one line scan in x-axis, the probe comes back to the zero position and continues another line scan with a specified increment in the y-direction. Line by line, once the complete image is obtained the electron probe will go back to the zero position of (x,y) coordinates and can collect the information of another image frame. Thus time taken to scan an image frame depends on the multiplication of number of line in frame and dwell time in each pixel positions.

3.3.3 Transmission electron microscopy

Transmission electron microscope (TEM) is a tool to identify the microstructure of the material at nano scale and provides crystallographic information which require a thin electron transparent sample. The magnification of the images obtained using TEM is an order of magnitude higher than

that offered by SEM. The TEM has a resolution of about 0.3 μm to 0.1 nm, which ranges from the wavelength of a visible light to lattice planes of a crystal structure. The wavelength of the electron beam is very much less than the lattice parameters of the individual unit cell of a crystal. The electron gun used in TEM has the voltage typically of 100-400 kV. FEI-TecnaiG2 S-Twin TEM is used in the current work to examine the material for microstructural and crystallographic information. The elemental analysis is also possible in TEM when it is coupled with either EDS or electron energy loss spectroscopy (EELS).

3.3.3.1 Sample preparation for TEM

Sample preparation is a crucial step and needs a careful handling of the samples not to bend or break. To examine nano powders produced by mechanical alloying using TEM needs a carbon coated copper grid of 200 or 300 mesh. The mechanically alloyed powders were dispersed in methanol solution and sonicated for 15mins in high energy ultrasonicator to break the powder agglomerates into appreciably small pieces. A schematic of the sample preparation process is shown in **Fig. 3.3 (a)**. For better results, the sonication process is repeated several times. Each time half of the methanol with nano powders is discarded and methanol is again added to dilute the solution. A drop of the sonicated liquid having nano powder is poured on the copper grid kept on a filter paper as shown in **Fig. 3.3 (a)**. The sample is allowed to dry for at least an hour and made sure that the examination of prepared sample is done within 24h.

The process of sample preparation of bulk sample is slightly different from that of the powders on copper grid. The schematic of the sample preparation from the bulk material is shown in **Fig. 3.3 (b)**. It begins with the slicing of the sample to as thin as possible using EDM (electro discharge machine) wire cutting. Then the sample is thinned down to 100 – 50 μm thick using metallographic

methods of polishing on different grade emery papers. Polishing is done on rough emery paper of about 300, 420, 600 depending on the hardness of the sample to reduce the initial thickness of the sample and care has to be taken to get a even thickness surface. A final polishing is done on velvet cloth with diamond paste, not to get a mirror like finish but was aimed to have a smooth surface. 3 mm discs are punched on the 15 μm out of thick samples. There are two commonly used methods to further thin down the sample. One is using twin jet polishing and other is Ion beam milling. The former is an electropolishing process where the sample is held in the electrolyte and a suitable temperature and potential are supplied. A pump provided in the machine will jet the electrolyte on either sides of the sample to thin down the center region of the disc.

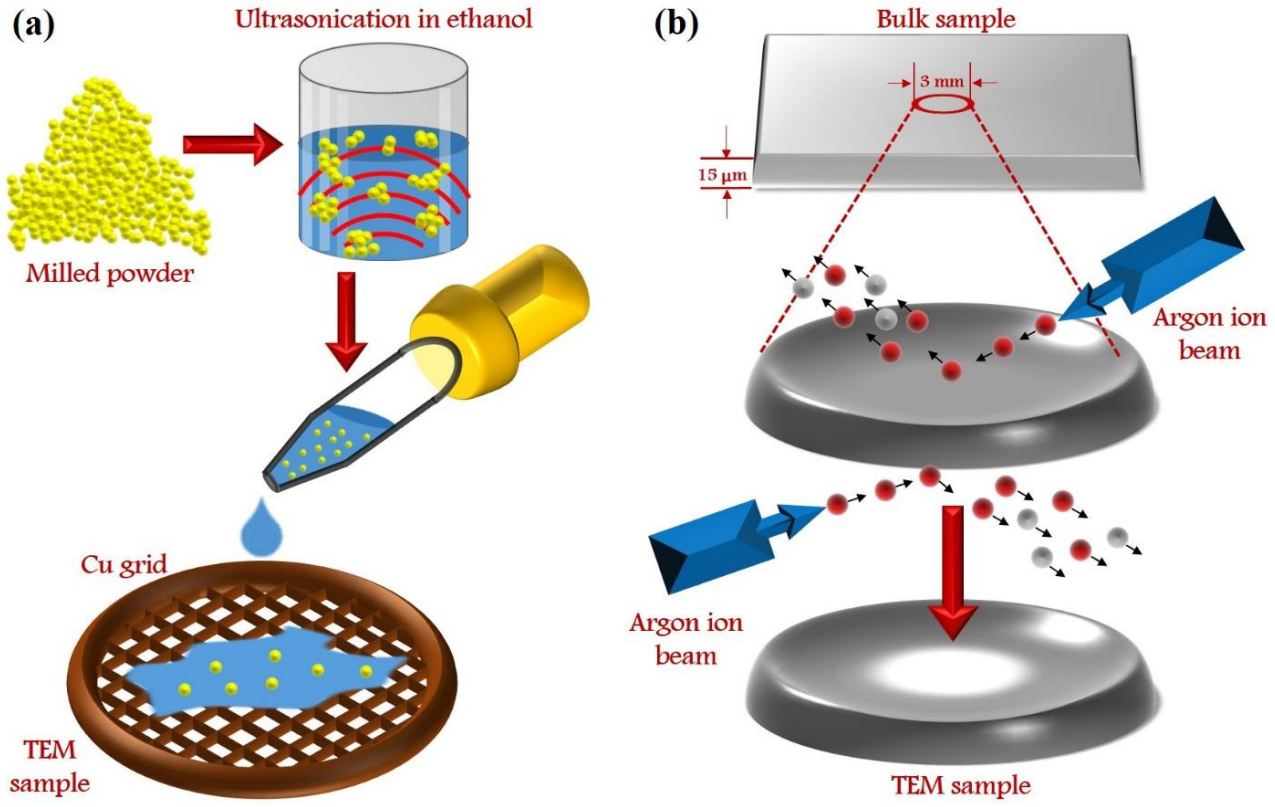

Fig. 3.3 Schematic representation of TEM sample preparation (a) from mechanical alloyed powders, (b) from SPSed bulk sample.

The polishing stops automatically when a perforated region is created for electron transparency by the light-fiber optic sensors placed on both sides of the sample. The later process is a sputtering process where neutral atoms or ions strike the disc at a particular angle so that the material on the 3 mm disc is knocked off creating a perforated region as shown in **Fig. 3.3 (b)**. In the current investigation a precision ion polishing system (PIPS, Gatan) is used to ion beam mill the HEAs.

3.3.2.2 TEM examination

The high velocity beam of electrons from the electron gun are focused to fall on sample by the electromagnetic condenser lens in high vacuum (10^{-6} Torr) by adjusting the lens currents rather than lens position as in case of optical microscope. The electrons pass through the 0.1μm thick sample and they interact with the atoms in the material and produce elastic and inelastic scattered electrons. The elastic scattering of electrons result when the electrons reflect with the same energy and inelastic scattering of electrons result when the electrons transmit through the sample and loses its energy. These scattered electrons are processed into final image on fluorescent screen. There are two modes of examination in TEM, one is selected area diffraction mode and convergent beam diffraction mode. These results in bright field images and dark field images respectively. Bright field and dark field images are generated because of diffraction contrast. Like in XRD, Bragg's law of diffraction (Equation 3.2) is also applicable here. The diffraction contrast arises with the change in the amplitude of scattering electrons from diffracting planes to that of the incident electron beam.

High resolution TEM (HRTEM) images are obtained because of the phase contrast. HRTEM images are sensitive to focusing objective lens and the sample thickness [10]. At this higher magnification, the atomic planes are recorded by varying intensity. A row of atoms with high atomic number are seen as bright regions but different factors effect such lattice images like the

lattice potentials which are different for different phases. Thus may results to misinterpretation of the boundary displacements. However, HRTEM images play a vital role in morphological details at atomic scales for phases, grain boundaries, dislocations, stacking faults, twins, etc. The inverse fast fourier transform (IFFT) image of the HRTEM image is used to identify the features for proper analysis using Gatan Digital micrograph software.

3.2.4 Vickers Hardness

Hardness of a material is defined as "resistance to plastic deformation" by the material [11]. It is an important tool to know the bulk behavior of the material. Vickers hardness test is one of the hardness measuring techniques well adopted by engineers which is indentation hardness measuring type.

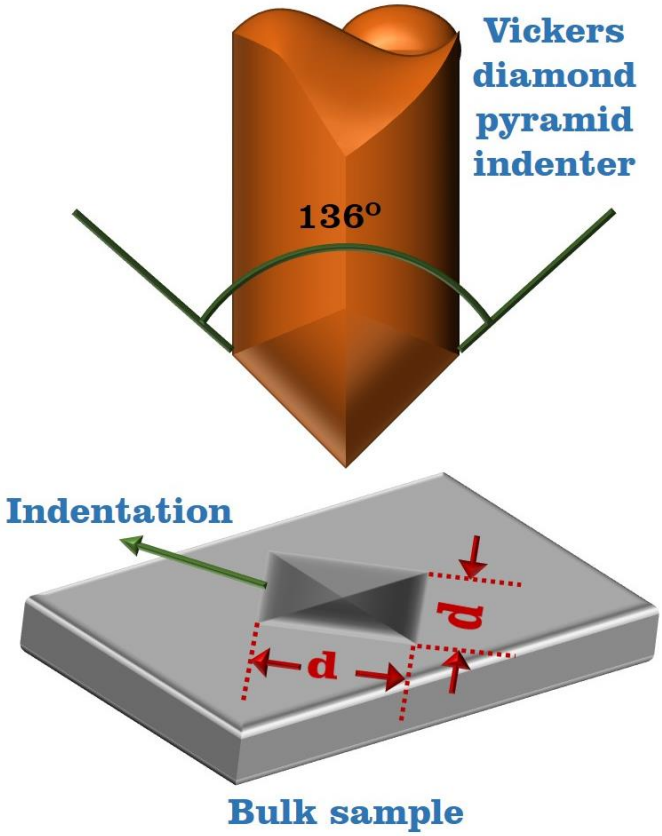

Fig. 3. 4 Geometry of the Vickers pyramid indenter and the indentation on the bulk sample.

Vickers hardness test is operated using a square-base diamond pyramid indenter whose included angle of the opposite faces in the pyramid is 136º as shown in

Fig. 3. *4.*The geometry of the indenter is designed such that the Vickers measurements are load independent. The Vickers hardness number (HV) is defined as the ratio of the load to the surface area of the indentation and is expressed as,

$$HV = \frac{1.854\,P}{L^2} \ldots\ldots\ldots\ldots\ldots\ldots\ldots\ldots\ldots\ldots\ldots\ldots\ldots\ldots\ldots\ldots (3.7)$$

where P is the applied load and L is the average length of the diagonals of the indentation measured using microscopic facility attached to the instrument. Hence the careful sample polishing has to be carried out for a clear surface and also care has to be taken to avoid surface work hardening. The type of indentation tests are classified based on applied loads. Macroindentation test uses loads ranges from 1 to 120 kg whereas microindentation hardness test uses load below 1000 g load. Microindentation test are useful for the hardness determination of individual phases in the alloy. For the lower loads there is a possibility for elastic recovery of the material. This elastic recovery is more pronounced at lower loads below 300 g [12-14]. Walters UHL Vickers microindentation (Model: VMH- I04) is used in the current research work. Hardness was determined at various loads in the range 100-500 g and at a dwell time of 15 sec. Each Vickers hardness value is an average of 10 indents taken on a mirror-like surface.

3.2.5. Nanoindentation

Nanoindentation is a unique technique to measure the phase hardness and elastic modulus using 0.01 g load. Nanoindenter measures the area of contact between the indenter and the specimen. The indenting tip used in nanoindentation is a Berkovich tips whose geometry is designed such that at any indentation depth, the projected area or mean contact pressure is equal to the surface

indentation area to indentation depth made using a Vickers diamond pyramid indenter. The face angle of the Berkovich tip is 65.03º. By measuring the indentation depth of penetration coupled with known geometry of the indenter gives the in direct measurement of hardness. Hence it is also named as depth sensing indentation testing. When the indenter tip is brought in contact with the specimen with a steady increasing load, the load and penetration depth is recorded. As shown in the

Fig *3. 5*, after reaching the maximum load (P), after the set holding segment the load is removed and the depth of penetration is recorded. If the material tested had an initial elastic contact, later a plastic deformation, the unloading curve follows a different path until zero. The hardness and elastic modulus data is retrieved from the maximum depth of penetration (h_{max}) and the slope (dP/dh) of unloading curve of the indentations. The hardness, H equation for a Berkovich indenter is expressed in Equation. 3.8 and the reduced modulus, E^* is given in Equation. 3.9.

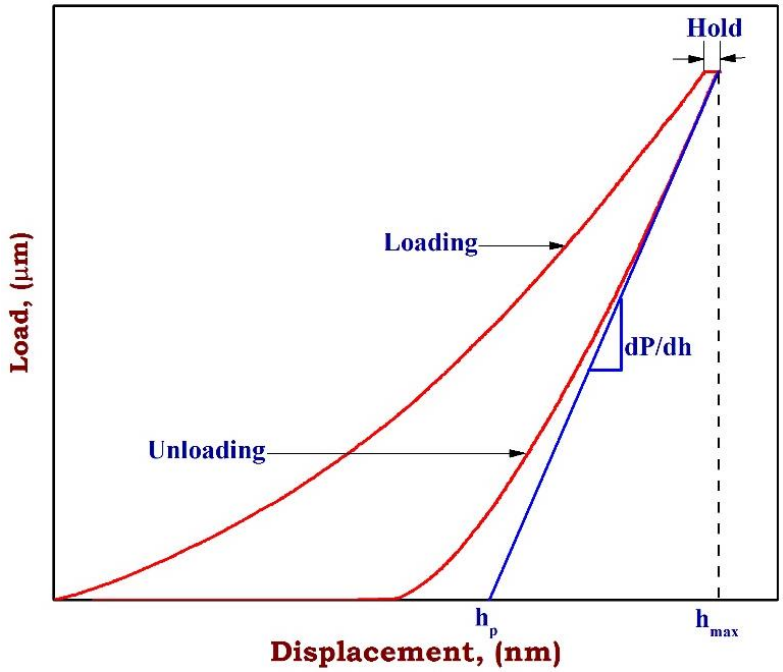

Fig 3. 5 A load-displacement curve for an elastic-plastic solid.

$$H = \frac{P}{24.5\ {h_p}^2} \ldots\ldots\ldots\ldots\ldots\ldots\ldots\ldots\ldots\ldots\ldots\ldots\ldots\ldots\ldots\ldots (3.8)$$

$$\frac{1}{E^*} = \frac{(1-\nu^2)}{E} + \frac{\left(1-\nu'^2\right)}{E'} \ldots\ldots\ldots\ldots\ldots\ldots\ldots\ldots\ldots\ldots\ldots\ldots (3.9)$$

where E' and ν' are indenters Young's modulus (1140 GPa) and Poisson's ratio (0.07) respectively [15], E and ν are sample Young's modulus and Poisson's ratio (0.33) respectively

Power law equation at constant strain and temperature, the strain rate ($\dot{\varepsilon}$) and flow stress (σ) are related as follows,

$$\sigma = C\ (\dot{\varepsilon})^m \ \ldots\ldots\ldots\ldots\ldots\ldots\ldots\ldots\ldots\ldots\ldots\ldots\ldots\ldots\ldots\ldots (3.10)$$

where C is a constant and m is strain rate sensitivity (SRS) [16]. In the current investigation, SRS is the slope obtained from the plot of log σ and log $\dot{\varepsilon}$.

$$m = \left(\frac{\partial\ ln\ \sigma}{\partial\ ln\ \dot{\varepsilon}}\right)_{\varepsilon,T} \ldots\ldots\ldots\ldots\ldots\ldots\ldots\ldots\ldots\ldots\ldots\ldots\ldots\ldots\ldots\ldots (3.11)$$

Activation volume (υ*) gives valuable information about the deformation because of the definite values and is dependent on the flow stress [11]. Activation volume is expressed as follows,

$$\upsilon^* = \sqrt{3}kT\left(\frac{\partial \ln\dot{\varepsilon}}{\partial\sigma}\right) \ldots\ldots\ldots\ldots\ldots\ldots\ldots\ldots\ldots\ldots\ldots\ldots\ldots\ldots\ldots\ldots (3.12)$$

where σ is flow stress ($\approx hardness/3$), $\dot{\varepsilon}$ is strain rate, ε is strain, T is temperature, k is the Boltzmann constant. In the current investigation, activation volume is the slope obtained from the plot of kTln($\dot{\varepsilon}$) and σ. Plot σ, flow stress values in GPa. The resulted slope of the linear fit line is in m^3 units. The obtained activation volume in m^3 is normalized to the burgers vector of an element and is expressed in the units of b^3.

References

1. Murty BS, Ranganathan S: **Novel materials synthesis by mechanical alloying/milling**. *International Materials Reviews* 1998, **43**(3):101-141.
2. Gilman PS, Benjamin JS: **Mechanical alloying**. *Annual Reviews of Material Science* 1983, **13**:279-300.
3. Suryanarayana C: **Mechanical alloying and milling**. *Progress in Materials Science* 2001, **46**:1-184.
4. Moravcik I, Cizek J, Gavendova P, Sheikh S, Guo S, Dlouhy I: **Effect of heat treatment on microstructure and mechanical properties of spark plasma sintered AlCoCrFeNiTi$_{0.5}$ high entropy alloy**. *Materials Letters* 2016, **174**:53-56.
5. Varam S, Rajulapati KV, Bhanu Sankara Rao K: **Strain rate sensitivity studies on bulk nanocrystalline aluminium by nanoindentation**. *Journal of Alloys and Compounds* 2014, **585**:795-799.
6. Mamedov V: **Spark plasma sintering as advanced PM sintering method**. *Powder Metallurgy* 2013, **45**(4):322-328.
7. Han Y-H, Nishimura T: **Spark plasma sintering**. *Advances in Applied Ceramics* 2014, **113**(2):65-66.
8. Grasso S, Sakka Y, Maizza G: **Electric current activated/assisted sintering (ECAS): a review of patents 1906-2008**. *Science and technology of advanced materials* 2009, **10**(5):053001.
9. **ASTM C 373 - 88**. In.; 1999.
10. Brandon D, Kaplan WD: **Microstructural characterization of materials**. England: John Wiley & Sons, Ltd; 2008.
11. Dieter GE: **Mechanical metallurgy**. New York: McGraw-Hill; 1988.
12. Li H, Bradt RC: **The microhardness indentation load/size effect in rutile and cassiterite single crystals**. *Journal of Materials Sciene* 1993, **28**:917-926.
13. Jiang D: **Recent progresses in the phenomenological description for the indentation size effect in microhardness testing of brittle ceramics**. *Journal of Advanced Ceramics* 2012, **1**(1):38-49.

14. Oliver WC, Pharr GM: **Measurement of hardness and elastic modulus by instrumented indentation: adavances in understanding and refinements to methodology**. *J Mater Res* 2004, **19**:3-20.

15. Bailey E, Ray NMT, Hector AL, Crozier P, Petuskey WT, McMillan PF: **Mechanical Properties of Titanium Nitride Nanocomposites Produced by Chemical Precursor Synthesis Followed by High-P,T Treatment**. *Materials* 2011, **4**(12):1747-1762.

16. Rajulapati KV, Koch CC: **Nanocrystalline materials: mechanical properties**. *Reference Module in Materials Science and Materials Engineering* 2016, **doi: 10.1016/b978-0-12-803581-8.02570-4**.

Chapter 4 Results and Discussion

4.1 Microstructural evolution in equiatomic ultrafine grained AlCoCrCuFeNi high-entropy alloy

4.1.1 Introduction

Several HEA systems have been developed using melting and casting route [1-15], however one of the major drawbacks of this method is formation of dendritic structure and selective segregation of the alloying elements during solidification. Often an additional step of heat treatment is required to homogenize the cast structure [7, 16-19]. Out of many HEA systems that were developed so far [20-23], AlCoCrCuFeNi received major attention by the researchers probably because the atomic radii of the participating elements is close and there is a major tendency to form a solid solution in this case [6, 20, 24]. It is regarded as the basic system and most of the other reported systems are derivatives of it [20]. The cast alloy has a mixture of fcc and bcc crystal structure. The annealing treatments below 800 ºC enhances BCC formation and above 800 ºC enhances FCC formation [8]. Grain refinement and solid solution strengthening are two classic ways of strengthening engineering materials [25, 26]. These two effects can be realized by synthesizing HEAs using ball milling [27-35]. In addition to structural refinement, homogeneous mixing of participating elements can also be ensured using mechanical milling. In this study, mechanical alloying has been used to synthesize single phase solid solution in equiatomic AlCoCrCuFeNi system and the structural evolution has been studied in detail using X-ray diffraction and electron microscopy. Subsequently spark plasma sintering was used to fabricate bulk components out of the milled powders.

4.1.2 Results

Fig. 4.1.1 shows X-ray diffractograms of the alloy at different durations of mechanical milling. Initially milling was done for 1 hour to ensure that all the elemental powders are mixed homogeneously and this sample is regarded as "0 h" sample which shows the presence of all the alloying elements in their elemental form. As the milling time is increased, several elemental peaks have disappeared and remaining peaks are broadened (**Fig. 4.1.2 (a)**), finally leading to the formation of a single phase fcc structure with Cu seemingly as the host lattice. The difference in atomic radii and the difference in lattice constants among these elements, calculated assuming that Cu is the host lattice, is shown in **Fig. 4.1.2 (b)**. The morphology of the milled (60 h) sample is observed using SEM and the corresponding micrographs are shown in **Fig. 4.1.3 (a&b)**.

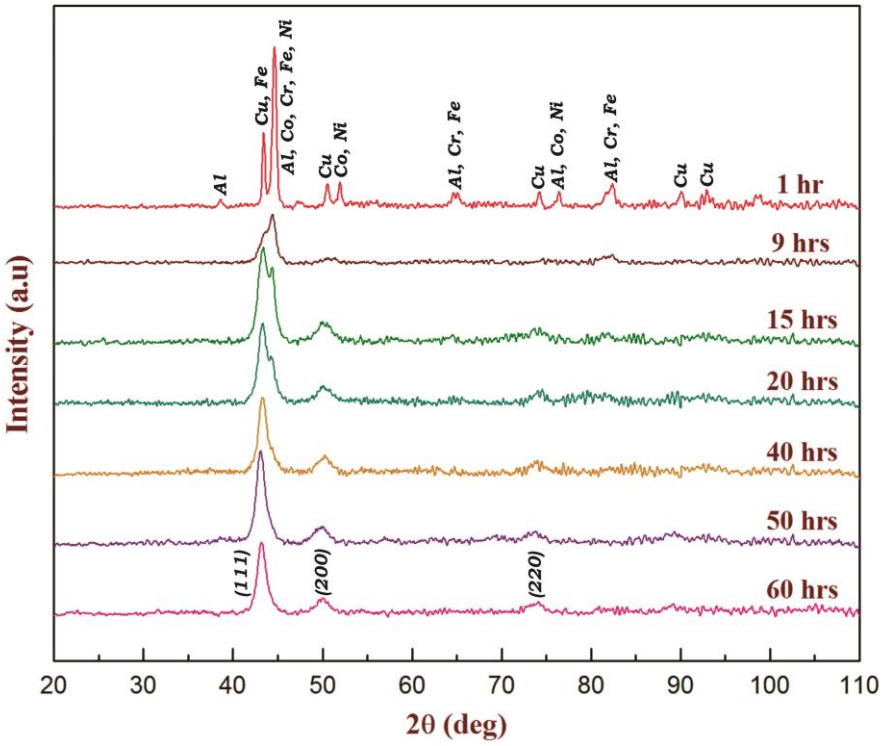

Fig. 4.1.1 X-ray diffraction patterns of AlCoCrCuFeNi HEA powders at 0 to 60 h of milling period.

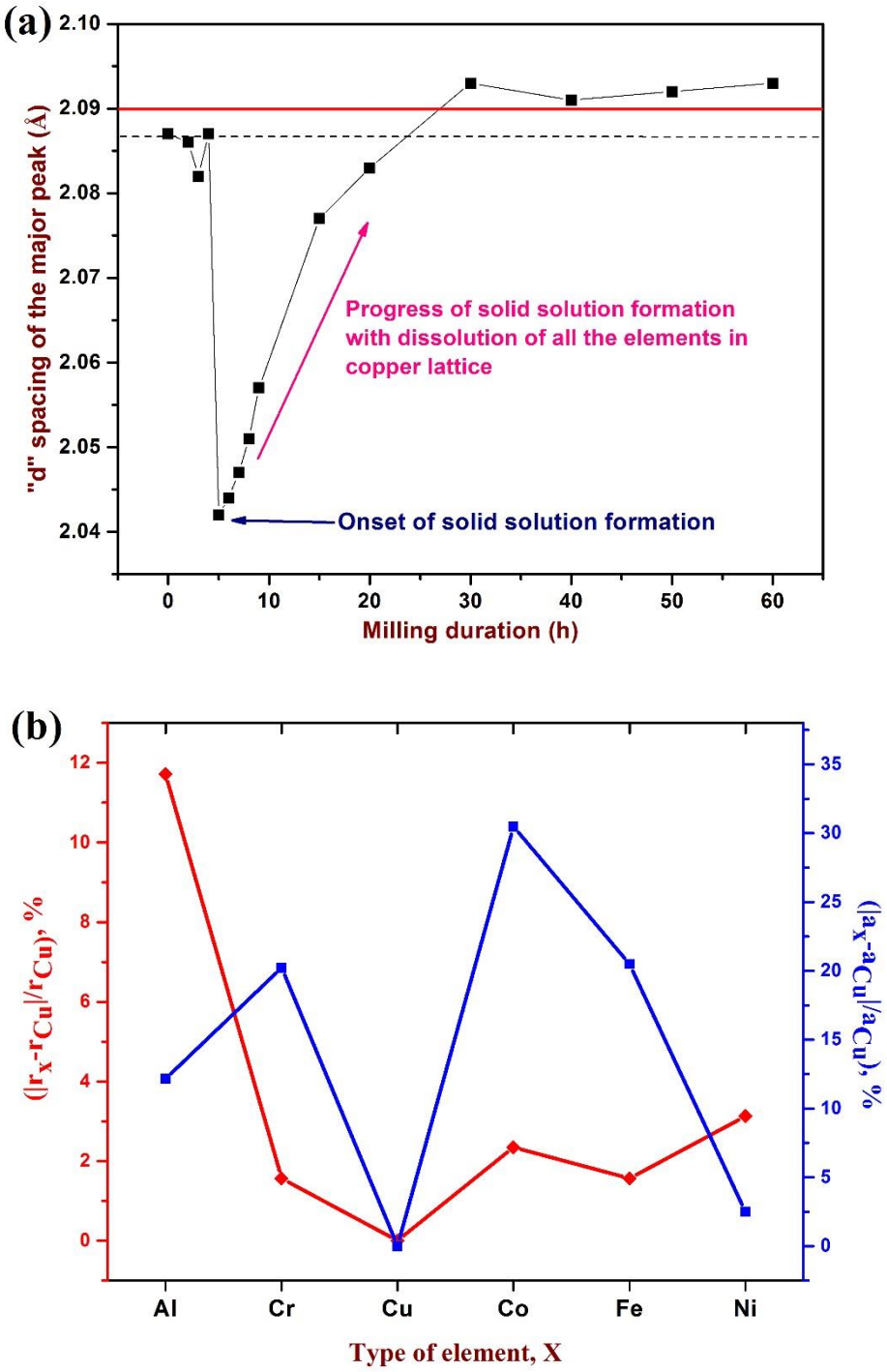

Fig. 4.1.2 (a) Variation in "d" spacing values with milling time (b) The difference in atomic radii and the difference in lattice parameters among the participating elements. These calculations are done considering that Cu is the host lattice. Where r_x is the atomic radius and a_x is the lattice constant of the element, x in AlCoCrCuFeNi HEA.

It is evident from these micrographs that "plate-like" particles have formed with micron sized dimensions. This "plate-like" morphology is probably an indication towards the ductile nature of this alloy in nanocrytalline state. However, the same fcc structure with the observed morphology is beneficial for structural applications only when these structural/microstructural features are retained when these powders are compacted into bulk forms which normally demands the adaption of elevated temperatures.The representative bright field, dark field, corresponding selected area diffraction pattern and grain size distribution are shown in **Fig. 4.1.4 (a-d)**. Careful indexing of the diffraction pattern shown in *Fig. 4.1.1***Fig. 4.1.4 (c)** indicates that it is a polycrystaline fcc structured solid solution, confirming the results of XRD analysis of **Fig. 4.1.1**. The average grain size computed using 295 grains from several dark field images captured from different regions of the sample is about 10 ± 6 nm with a very narrow grain size distribution (**Fig. 4.1.4 (d)**). Further analysis was performed using HRTEM and the corresponding micrograph is shown in **Fig. 4.1.5**. A random arrangement of grains with dimensions less than 10 nm and different lattice orientations are observed (marked in dotted shapes).

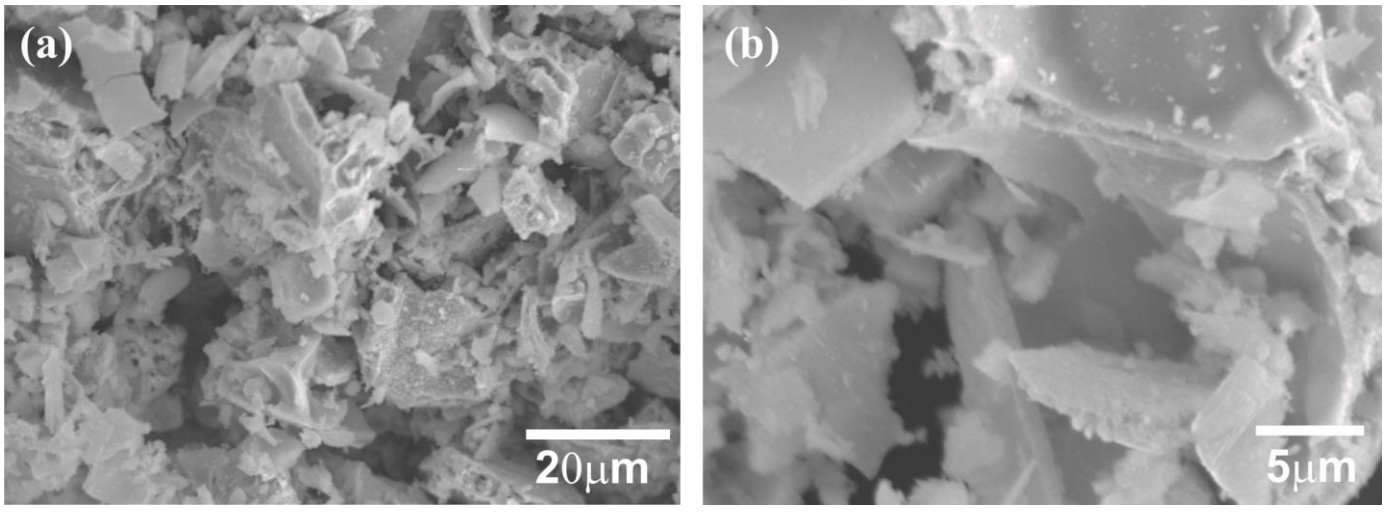

Fig. 4.1.3 SEM micrographs of 60 h mechanical alloyed AlCoCrCuFeNi powders. Plate-like morphology can be seen.

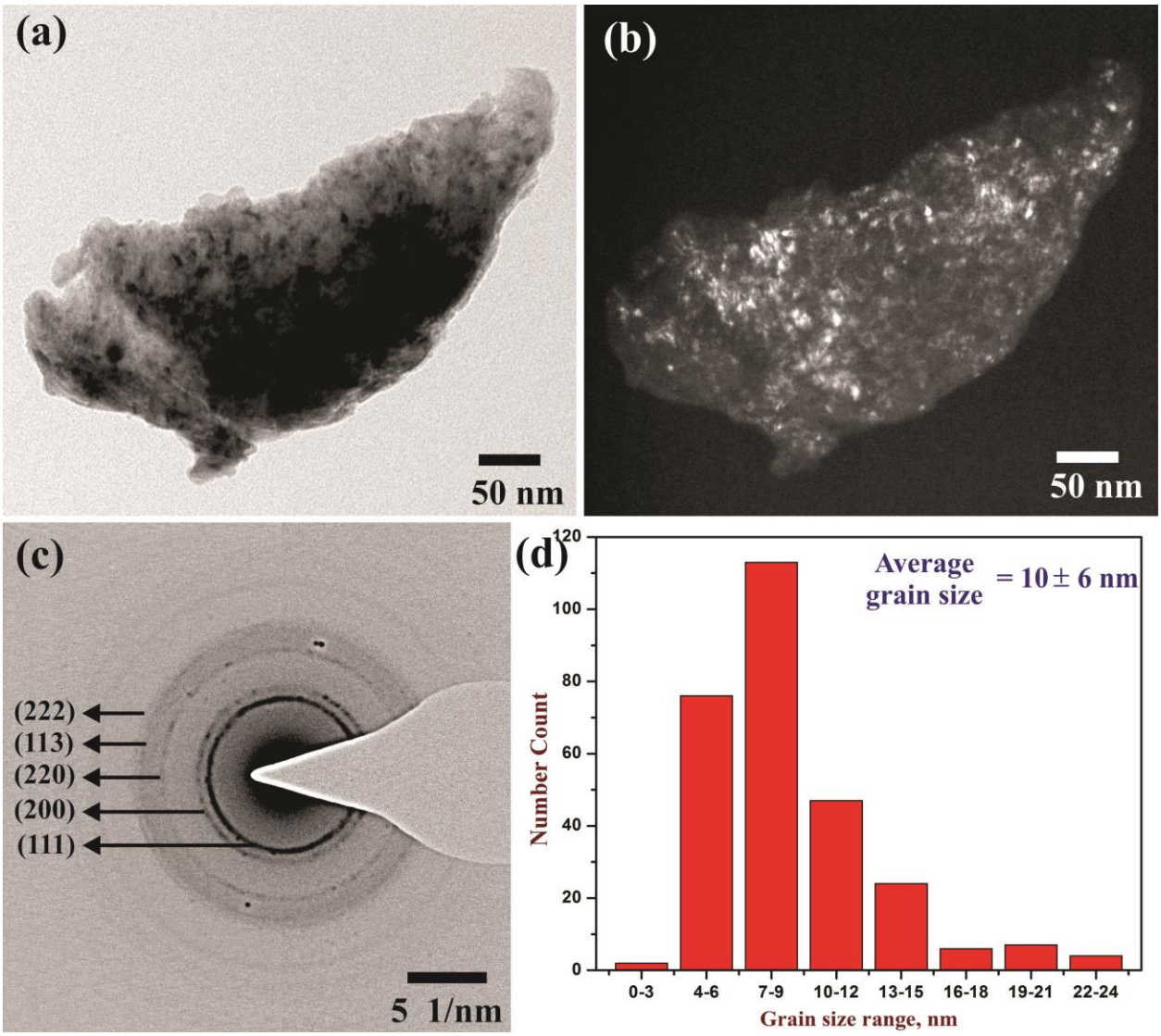

Fig. 4.1.4 TEM images of AlCoCrCuFeNi HEA alloy (a) bright field image, (b) dark field image, (c) diffraction pattern and (d) grain size distribution plot.

The inverse fast Fourier transform (IFFT) image from the red coloured region is shown in the inset and the interplanar spacing from these fine crystallites turns out to be 2.05 Å against 2.09 Å computed form XRD analysis (**Fig. 4.1.2 (a)**). It is also evident that the crystal lattice planes are distorted indicating the presence of different types of atoms in the solid solution.

X-ray diffractograms of the sintered products are shown in **Fig. 4.1.6** and the corresponding X-ray reflections are indexed to be of two different phases (fcc + B2). It appears that during SPS, a new

B2 phase has precipitated out of the fcc based matrix which was the product of milling. The precise lattice parameters of these two phases were calculated to be 3.5 ± 0.001 Å for fcc and 2.9 ± 0.001 Å for the B2 phases respectively. It is plausible that some elements might have migrated out of the initial Cu-based lattice and formed a new second phase with B2 structure. The absolute density of the sintered compacts, using the Archimedes principle method, was measured to be 7.12 g/cc against a theoretical estimated rule of mixtures value of 7.068 g/cc for this equiatomic alloy. The compacts were appeared to be sound and no visible porosity was observed during SEM investigations. It is to be noted that sintered compact was of two phase structure (fcc + B2) whose inherent densities are unknown. Therefore the observed discrepancy between the measured and calculated densities may be attributed to this. The morphological variations with time during sintering are presented in **Fig. 4.1.7 (a-c)**. All the three specimens demonstrate similar two phase, porous-free features in the SEM images. It is important to note from the EDS data (**Fig. 4.1.7 (d)**) that both the phases contain all the participating elements. TEM data of the sintered alloy (15 min) is presented in **Fig. 4.1.8 (a-e)** and **Fig. 4.1.9 (a-d)**. This data suggests that the sample possesses a two phase structure (fcc + B2) with bimodal grain size distribution. The average grain sizes computed from a total of 313 grains are 112±46 nm and 1550±500 nm for the two regimes identified. The number fraction of larger grains (>250 nm) is not significant. However twins are observed to be present in both the larger (**Fig. 4.1.9 (c)**) and smaller grains (**Fig. 4.1.9 (d)**).

4.1.3 Discussion

As the participating elements in majority of HEAs are in equal atomic proportions, the probability/possibility for any individual element to occupy a given substitutional lattice site could be the same under favourable thermodynamic conditions. It has to be noted that in AlCoCrCuFeNi alloy, although both fcc and bcc stabilizers are in equal atomic ratios, 60 h of milling resulted in

fcc phase formation with Cu as seemingly the host lattice. This suggests that all the elements dissolved into Cu lattice forming a complete fcc solid solution. The HEA without Cu element, $Al_xCoCrFeNi$ is reported to be of bcc crystal structure [36]. The X-ray peaks of Cu have not shifted significantly, with the gradual dissolution of all the participating elements, probably due to the fact that the atomic radii of all the participating elements are very close. In an effort to track the progress of this solid solution formation in the current study, the interplanar (d) spacing of the X-ray peak corresponding to 100% intensity is plotted with milling time and is shown in Fig 4.2 (a). The initial "d" spacing of Cu (100% intensity) is 2.087 Å(dotted line in **Fig. 4.1.2 (a)**) and it decreased to 2.04 Å after 5 h of mechanical milling, indicating dissolution of some of the participating elements. With the increase in milling duration, the interplanar spacing gradually increased and reached a saturated value around 2.09 Å (red line in **Fig. 4.1.2 (a)**). The precise lattice parameter of this fcc based solid solution, calculated using Nelson-Riley extrapolation analysis [37], is 3.64 Å and is well comparable with the lattice parameter of Cu (3. 61 Å). In accordance with the traditional Hume-Rothery rule, it is clear that all the elements of this system should readily form a solid solution with Cu as the difference in atomic radii is not exceeding 15% [38]. In fact, sparing Al, this difference is as low as 2% suggesting that the probability of formation of solid solution is very high. The difference in lattice constants is also shown for comparison (**Fig. 4.1.2 (b)**).

It is evident that a single phase (fcc) solid solution with an average grain size of 10 nm and very narrow grain size distribution is formed (**Fig. 4.1.4 (a-d)**). Zhang et al [39] have reported a two phase structure with bcc as a major and an fcc as minor phases in AlCoCrCuFeNi HEA using planetary ball milling at a BPR of 15:1. In a separate study on the same alloy system [40, 41] during high energy ball milling (at a BPR of 5:1), a combination of fcc and bcc phases have been observed with dominant presence of fcc phase with increased milling duration.

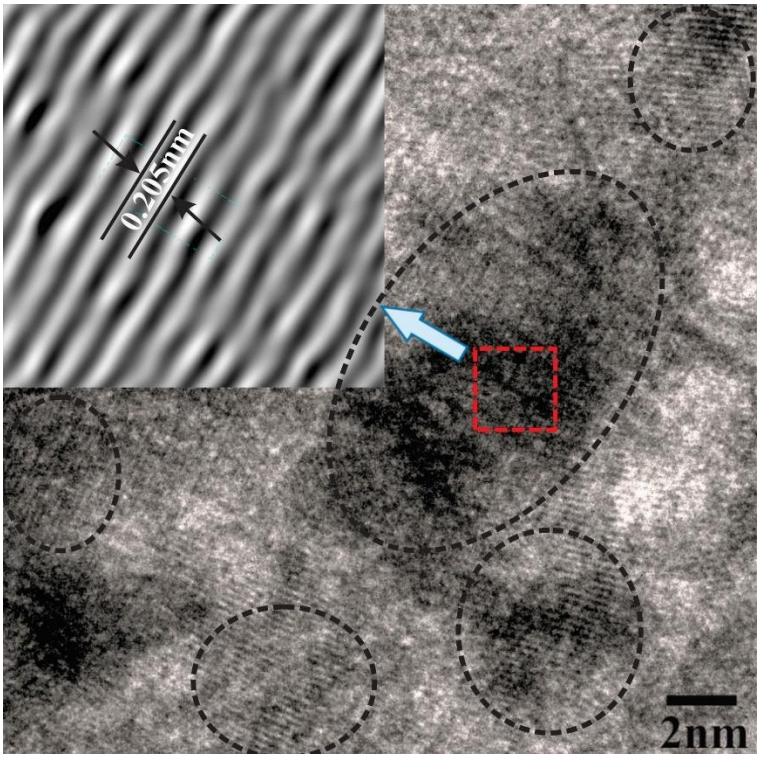

Fig. 4.1.5 High resolution TEM image of AlCoCrCuFeNi high entropy alloy. IFFT figure in the inset reveals the distorted lattice places which is one of key proposed signatures of HEAs.

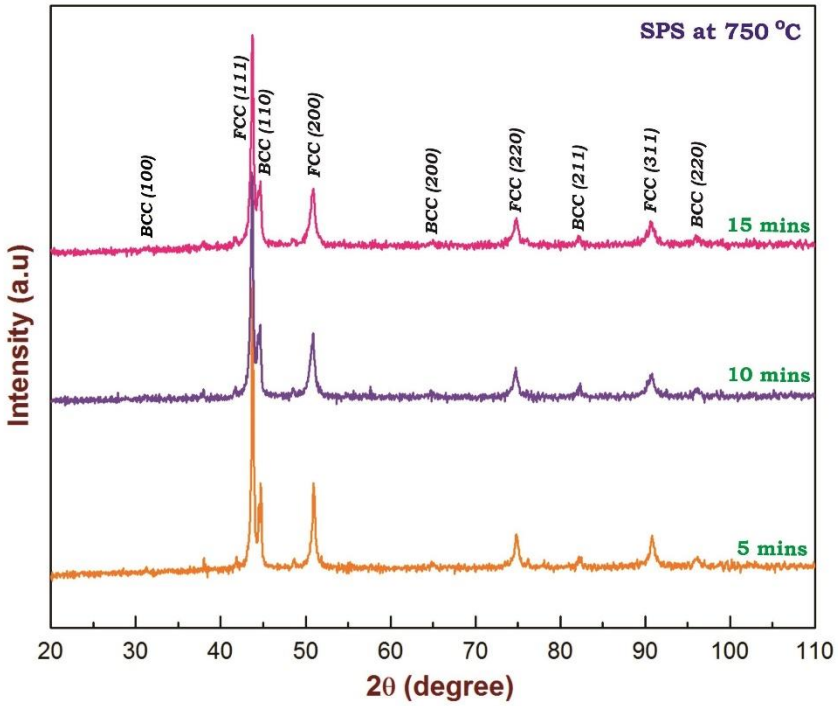

Fig. 4.1.6 X-ray diffractograms of AlCoCrCuFeNi alloy subjected to SPS at 750 ºC for various holding times. Evolution of B2 phase can clearly be evidenced.

Three phase mixture consisting of two fcc phases and a bcc phase were realized in the same system with varied Al content during planetary milling at a BPR of 10:1 [42]. The present study reports that ball milling of AlCoCrCuFeNi HEA taken in equiatomic proportions has led to the realization of a single fcc phase. The local micro strain arising out of the complex solid solution might be causing a distortion in the lattice as seen in **Fig. 4.1.5**. This observation is in line with the one of the proposed core effects "lattice distrtion effect" of HEAs [20]. This suggests that processing method and associated process parameters will influence the structural as well as microstructural evolution in HEAs.

As it is seen in **Fig. 4.1.7**, the microstructure is of two different contrasts (white and black). The white phase could be the final milled product (after 60 h) and it is anticipated that this phase was continuous before the sample was heated during SPS. At high temperature, a new black (dark) phase might have precipitated out. It is visible that as the holding time is increased, the fraction of white phase has decreased and that of black phase has increased (**Fig. 4.1.7 (a-c)**). The EDS studies performed on 15 min sintered sample (**Fig. 4.1.7 (d)**) suggest that these two phases are not compositionally different, although they are of two different crystal structures (fcc and B2). In cast AlCoCrCuFeNi HEA, Cu is segregated in to the interdendritic regions because its mixing enthalpy is different from that of the other elements [3]. Whereas in this study both the phases (white and dark) are comprised of all the elements of the alloy (**Fig. 4.1.7 (d)**). There could be a background influence on this analysis because the precipitate sizes are less than 100 nm, which are very small to focus in SEM. It is plausible that processes such as recovery, recrystallization and grain growth might have occurred during SPS. Therefore the post-sintering microstructure contains bi-modal grain size distribution with averages of 112 nm and 1550 nm respectively (**Fig. 4.1.8**).

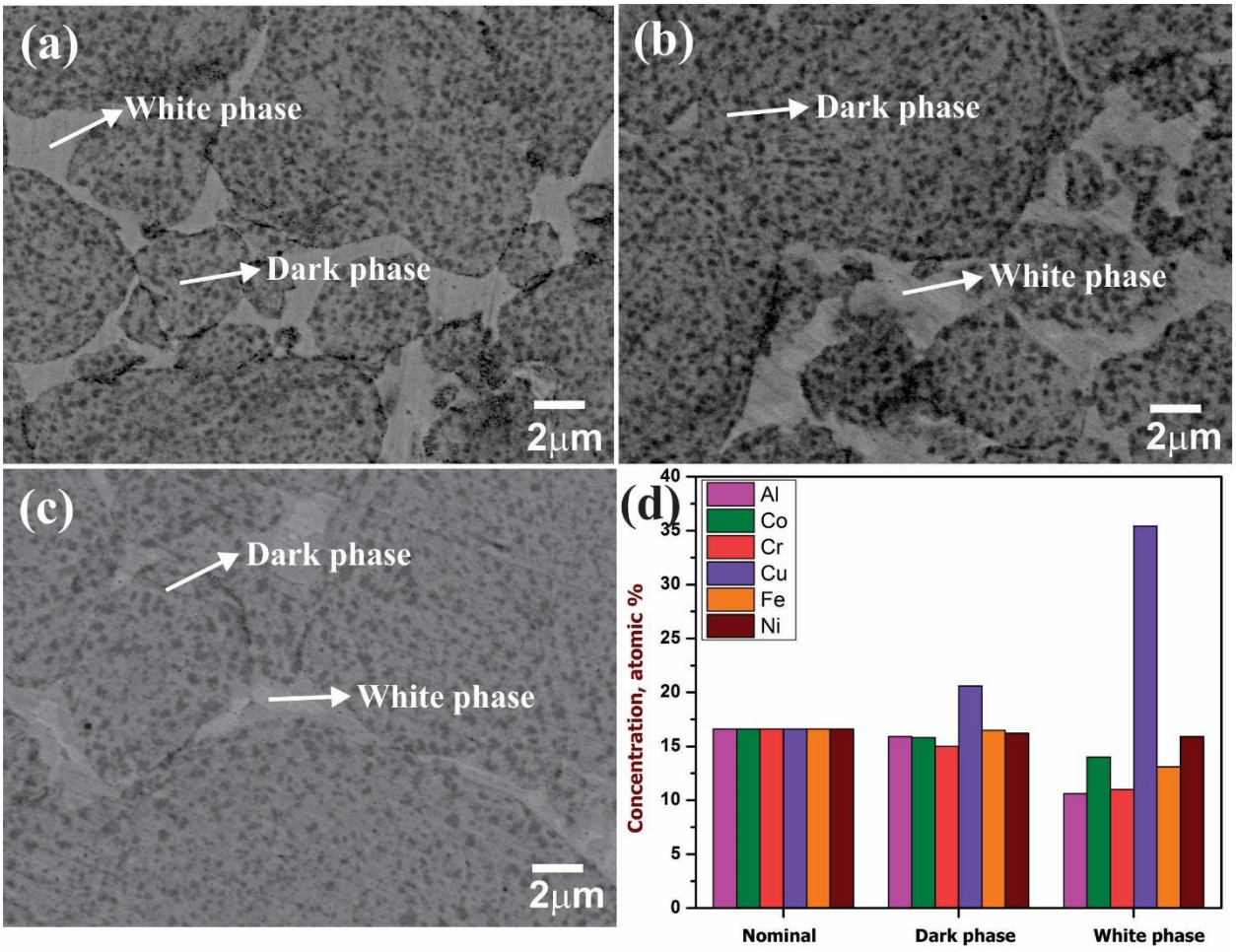

Fig. 4.1.7 Scanning electron micrographs (BSE mode) of AlCoCrCuFeNi alloy sintered at 750 °C for (a) 5 min (b) 10 min and (c) 15 min and (d) EDS data obtained from (c). It suggests that white phase is richer in copper whereas dark phase is nearly homogeneous. It is to be noted that both dark and white phases are comprised of all the alloying elements of this alloy.

The microstructure of the alloy sintered at 900 ºC [43] contained white, grey and black spot phases where the black spots are porosity and no new phase was found after sintering. The XRD investigations performed on the sintered sample in ref. [29] indicate the presence of fcc and bcc phases. In addition to Cu rich solid solution, a new Cr rich solid solution phase was also observed. Tung et al [3] fabricated AlCoCrCuFeNi HEA using melting and casting route. By reducing each element by 0.5 mole fraction, the effect of each element on the crystal structure was explained.

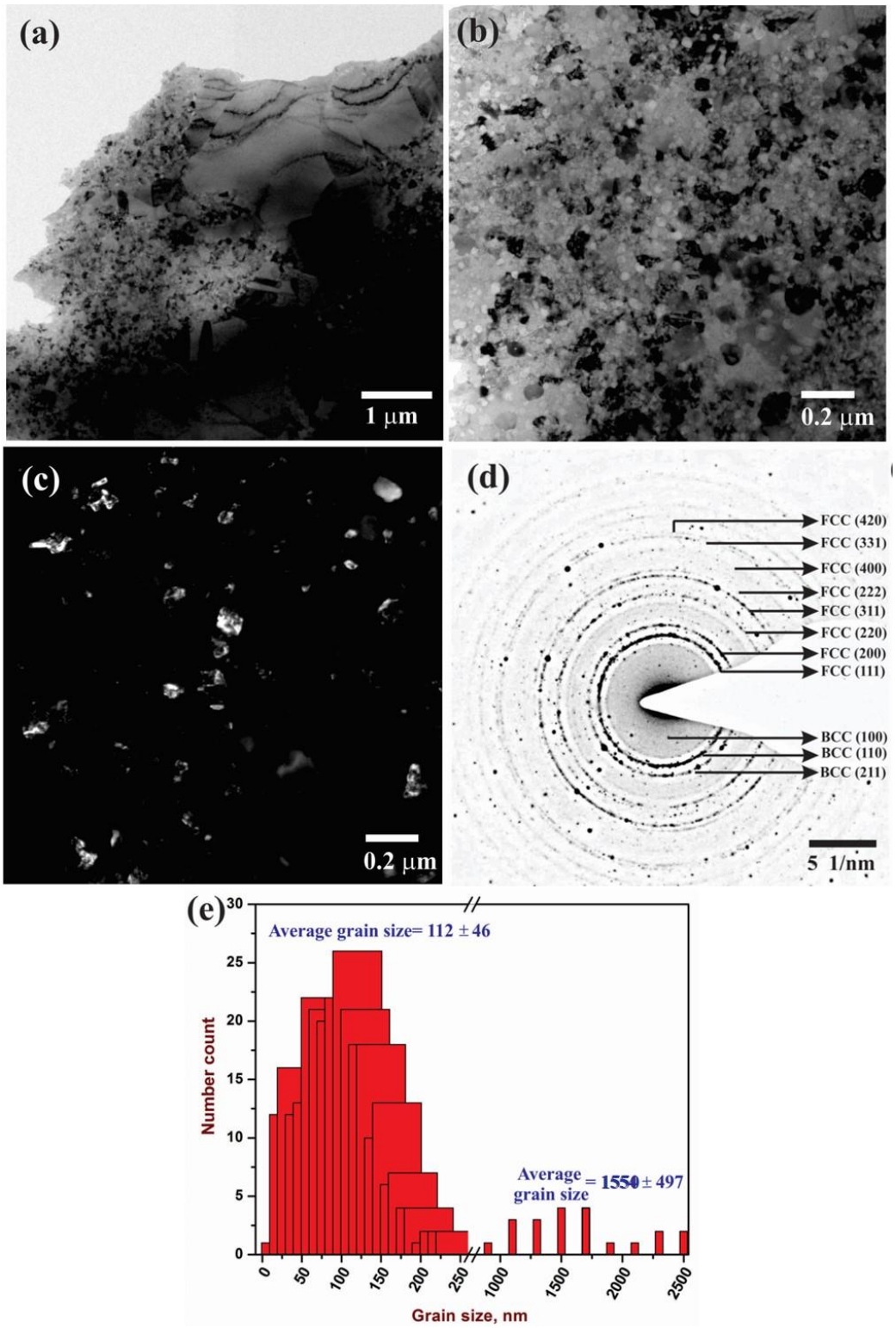

Fig. 4.1.8 TEM images of AlCoCrCuFeNi HEA alloy after sintering at 750 ºC/15 min (a,b) bright field image, (c) dark field image, (d) TEM diffraction pattern and (e) histogram showing the bi-modal grain size distribution with averages of 112 nm and 1550 nm.

It was further showed that Cu, Co and Ni enable fcc phase formation whereas Cr and Al are reasons for bcc phase formation. Copper segregation at the inter-dendritic regions is probably because of larger enthalpy of mixing. Dolique et al [44, 45] made similar conclusions from their work on AlCoCrCuFeNi HEA produced by magnetron sputtering. The XRD analysis has revealed an unmixed bcc, fcc and a disordered phase. Singh et al [46] synthesized AlCoCrCuFeNi HEA using splat quenching technique and casting route. Interestingly splat quenched material resulted in a bcc phase and as-cast material showed bcc and two fcc phases. Tong et al [1, 47] varied Al concentration and synthesized Al_xCoCrCuFeNi HEAs using casting route and investigated their microstructure and mechanical behaviour. Dendritic and inter-dendritic structures were found with little Cu segregations at inter-dendrites in their study. When x=1, the alloy has exhibited fcc, bcc and B2 phases. However the present study reports only two phase structure (fcc + B2) in the sintered product. Therefore it suggests that processing route as well as process parameters would govern the type of phases observed in AlCoCrCuFeNi system. Unlike in other studies on AlCoCrCuFeNi HEA system, detailed TEM investigations indicate that twins with wide distribution in their spacing have also formed during SPS (**Fig. 4.1.9 c&d**).

Sheng et al [7] casted $Al_{0.5}$CoCrCuFeNi HEA and studied the properties after annealing and quenching. The XRD of the as-cast alloy revealed two fcc phases and a bcc phase after annealing treatments. Liu et al [48] stated that fcc HEA shows greater ductility at -196 ºC but have less strength. Their study on σ and μ intermetallic formation as shown in **Fig. 4.1.10** in $CoCrFeNiMo_{0.3}$ HEA increased the strength instead of embrittlement. The interesting feature they explained is the lattice distortion which was carefully measured using line broadening in XRD. This distortion is reported to solid solution strengthening.

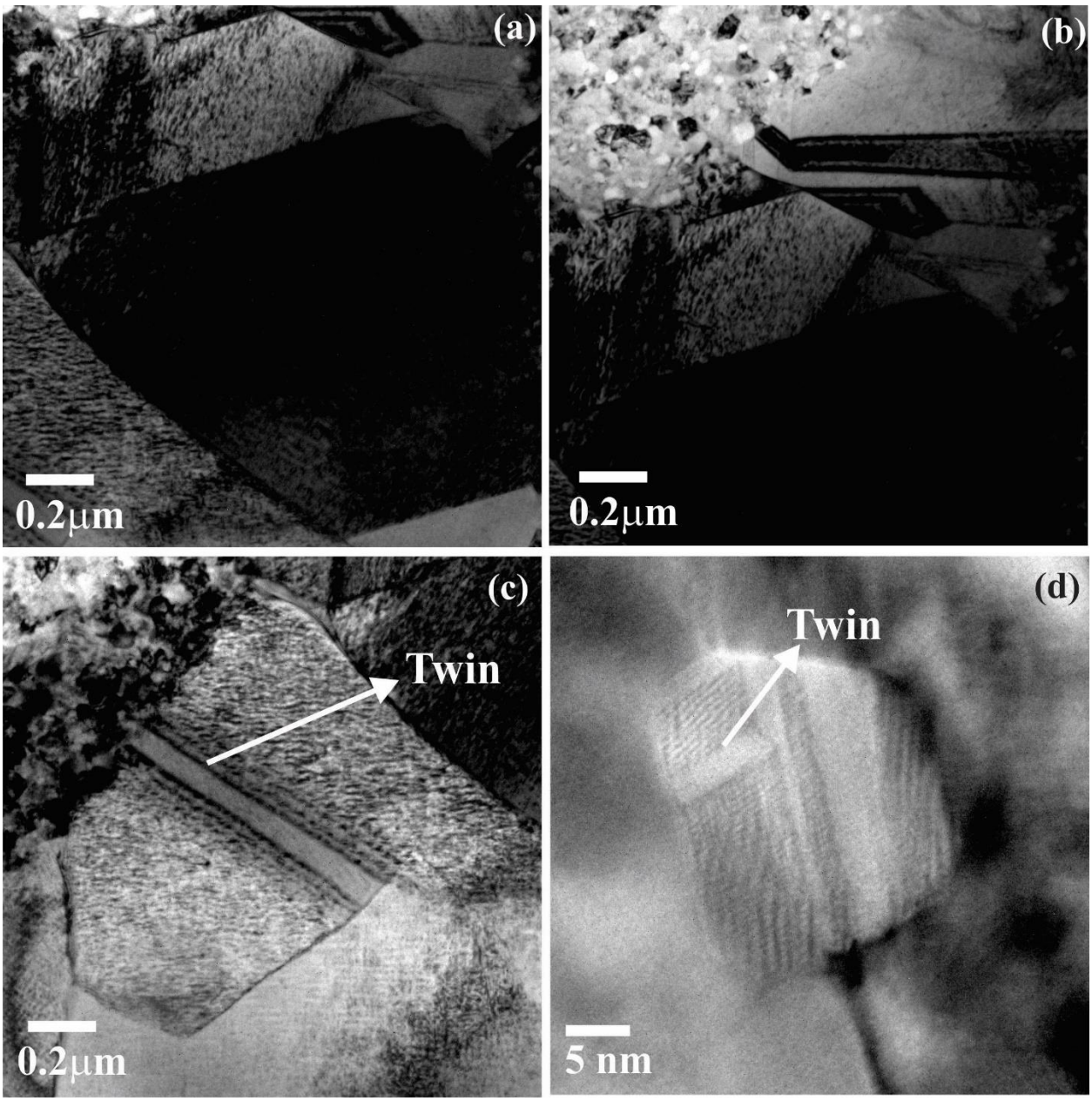

Fig. 4.1.9 TEM images showing twins formed in AlCoCrCuFeNi HEA after SPS at 750 °C (a) shows larger grain, (b) shows both larger and smaller grains, (c) & (d) shows twins formed during SPS.

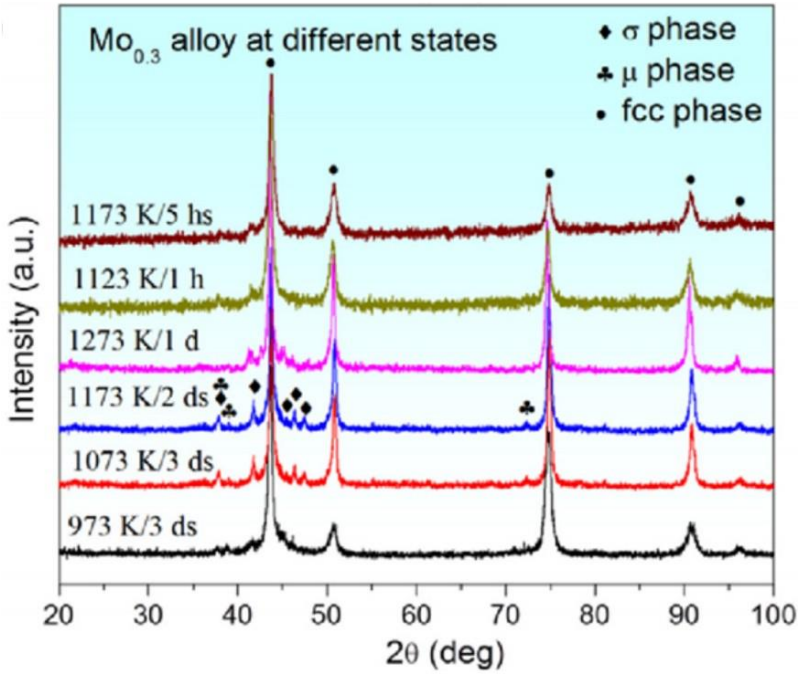

Fig. 4.1.10 X-ray diffractograms of CoCrFeNiMo0.3 HEA after rolling up to 60% reduction and at various annealing conditions [48].

Recent investigations show the precipitation in AlCoCrCuFeNi HEA system, which aided to the improvement of mechanical properties. Tsai et al [49] reported about the morphology of the precipitates in $Al_{0.3}CoCrCu_{0.5}FeNi$ HEA. This group confirmed the presence of $L1_2$ precipitates with large needle like morphology and small spherical morphology from the superlattice spots as shown in **Fig. 4.1.11**. Their detailed EDS analysis showed that the needle like precipitates are $(Ni,Cu)_3Al$ type precipitates with $L1_2$ structure just as γ' precipitates in Ni-base superalloy and spherical precipitates are rich in Ni,Cu and Al elements. Jones et al [50] studied the phase equilibria of $Al_{0.5}CoCrCuFeNi$ HEA by heat treating the cast alloy for 1000 h at different temperatures as shown in **Fig. 4.1.12**. They saw that the material had two fcc phases which stable till its melting temperatures. At 700 and 850 ºC, this alloy has decomposed and formed B2 and σ phases. They also observed $L1_2$ type precipitates at 700 ºC in the interdendritic regions which are similar kind of γ' intermetallic precipitates found in superalloys.

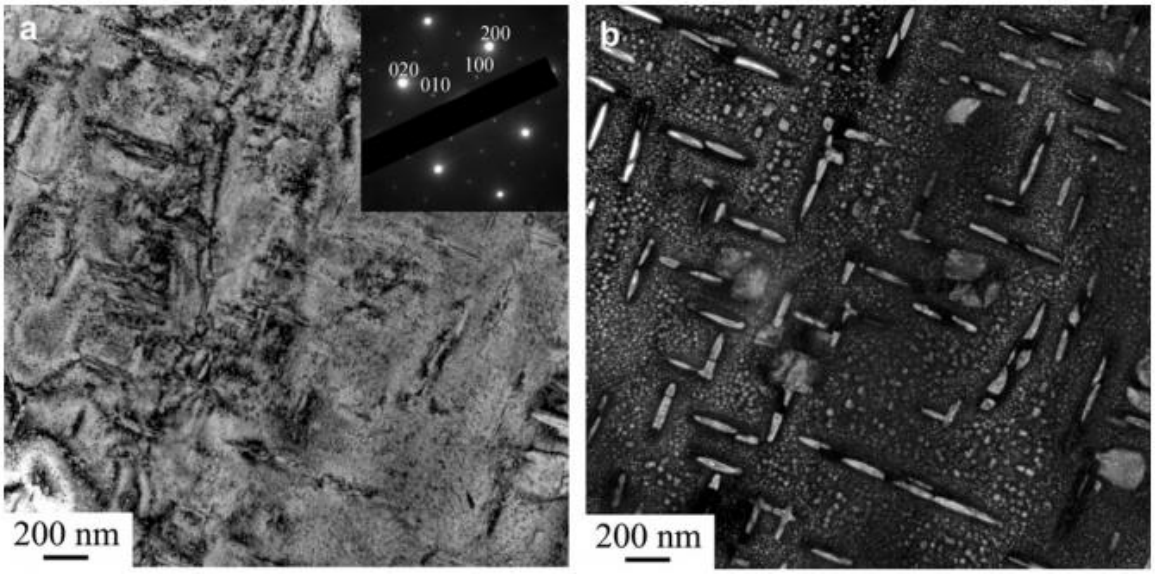

Fig. 4.1.11 (a) TEM bright-field image (b) corresponding dark-field image from weak superlattice spots of the Al0.3CoCrCu0.5FeNi alloy observed from <100> different zone axis [49].

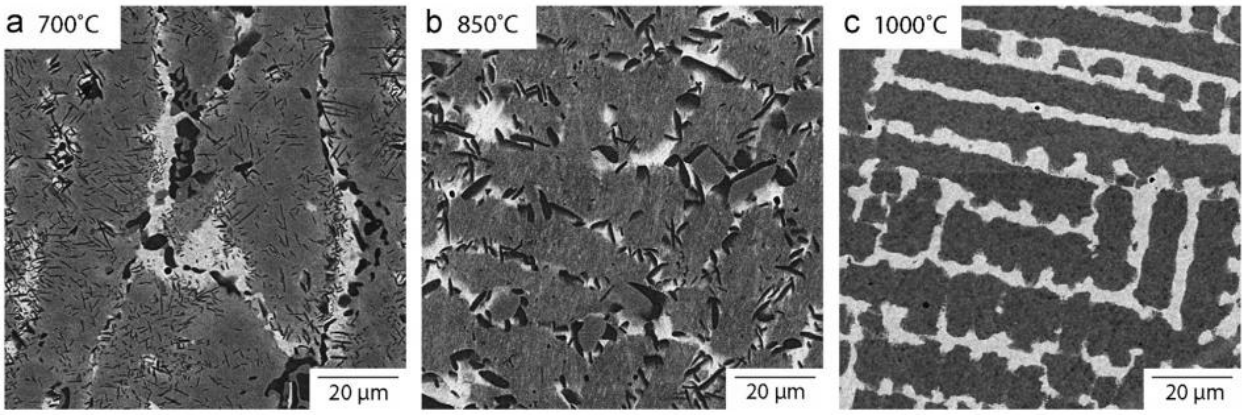

Fig. 4.1.12 Back scattering micrographs of Al0.5CoCrCuFeNi HEA after heat treatment for 1000 h at different temperatures [50].

Santodonato et al [51] investigated the cast $Al_{1.3}$CoCrCuFeNi HEA. This alloy resulted a large grains in the microstructure instead of an obvious dendritic structure. They found bcc/B2 phase, rod shaped fcc phase and a Cu rich precipitates in the alloy as shown in **Fig. 4.1.13**. The EDS results show Cr, Co and Fe rich bcc phase and Cu rich fcc phase.

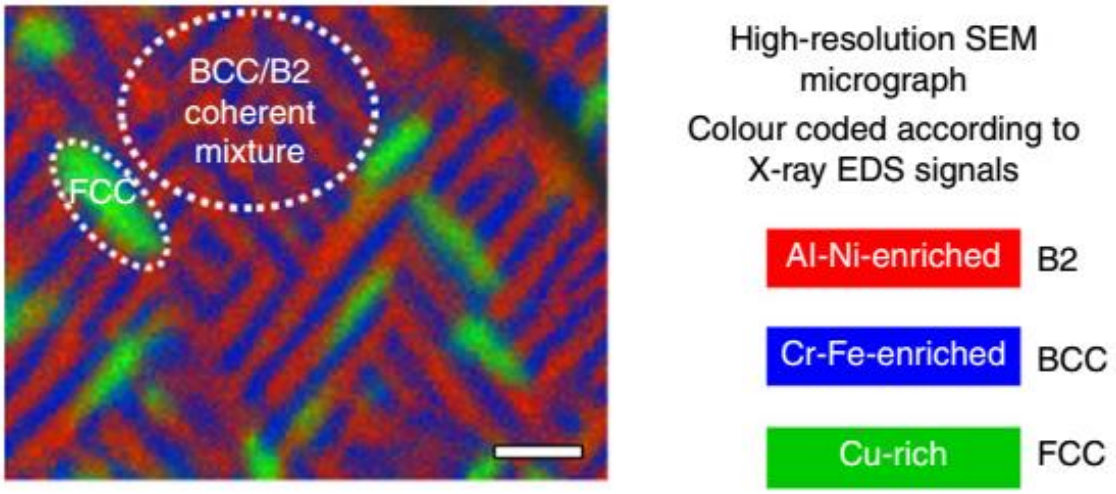

Fig. 4.1.13 EDS elemental map of a high-resolution SEM showing segregation of different phases (B2, BCC and FCC). Scale bar in the micrograph is 0.5 µm [51].

Tong et al [1] fabricated $Al_xCoCrCuFeNi$ HEA with varied Al concentration from 0 to 3 atomic%. There was a phase transformation from fcc to bcc when x = 0.8 and spinodal decomposition when x = 1. An ordered bcc is found when x > 2.8. Other than these simple structures, TEM analysis revealed 5-10 nm Cu rich precipitates in the disordered matrix with face centered orthorhombic crystal structure, Widmanstätten precipitates (**Fig. 4.1.14**) and spherical precipitates. Such morphological structures influenced mechanical properties improvement [47]. A similar finding were reported by Tsai et al [52], who casted the $Al_{0.5}CoCrCuFeNi$ HEA and hot forged. They reported that the cast alloy resulted an fcc phase. The same alloy on forging resulted a bcc and an additional Cu-rich fcc phase in the interdendritic regions. The forged alloy on homogenization treatment at 1100 ºC for 24 h, followed by furnace cooling resulted Cu rich needle like precipitates (**Fig. 4.1.15 (a)**). These were increasing in number with increase in plastic deformation. A 5% cold rolled introduced nanotwins amongst the needle like precipitates as shown in **Fig. 4.1.15 (b)**. They explained that the high strength is not only by solid solution strengthening but also because of the precipitates and nanotwins which further block the dislocations to slip and resist the plastic deformation.

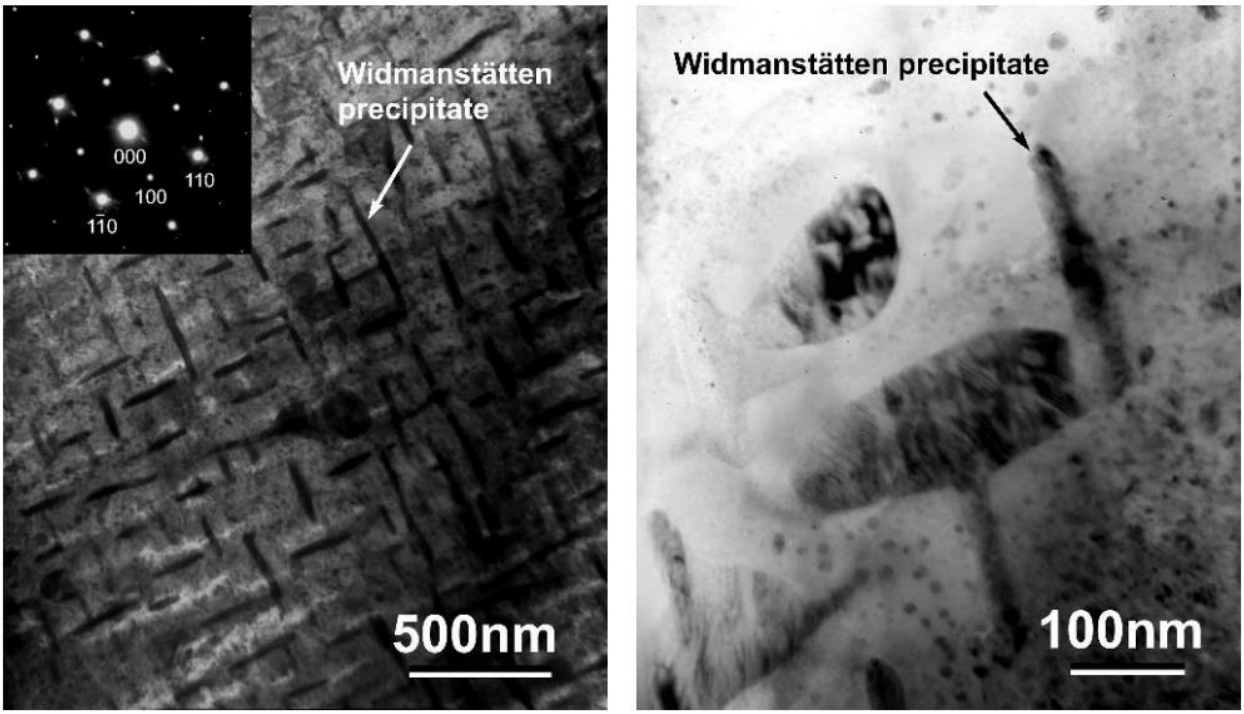

Fig. 4.1.14 Transmission electron micrographs of Al1.5CoCrCuFeNi HEA showing the Widmanstätten precipitates in dendrites [1].

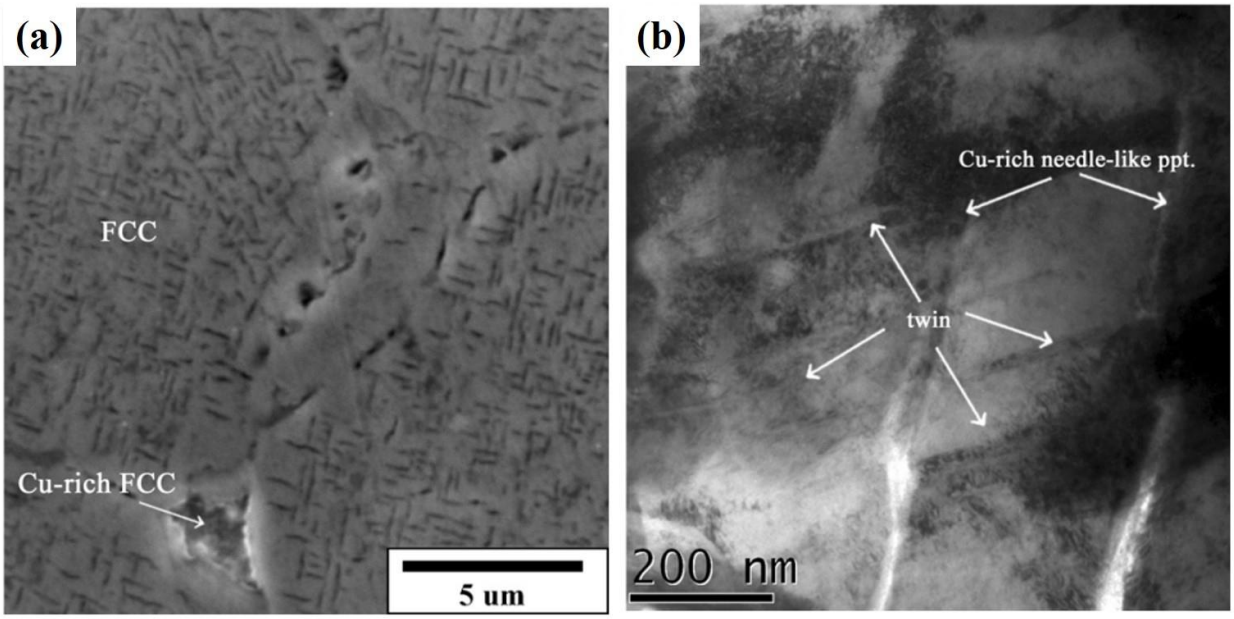

Fig. 4.1.15 (a) Cu needle like precipitates and (b) nanotwins in Al0.5CoCrCuFeNi HEA [52].

Singh et al [2] synthesized AlCoCrCuFeNi HEA using both casting and splat quenching methods. The former method resulted in fcc and bcc phases and the later resulted in ordered bcc phase. They found different shaped Cu rich precipitates in the dendritic regions of as-cast AlCoCrCuFeNi alloy as shown in **Fig. 4.1.16**. They area coherent plate like structures with ordered B2 crystal structure, 5-15 nm spherical precipitated and $L1_2$ structured rhombohedron shaped precipitates. Wang et al [53] fabricated Cu free AlCoCrFeNi HEA using vacuum arc melting. They found the spherical shaped nano sized precipitates in the dendritic regions with major concentration of Cr and Fe. They saw an increase in compressive strength because of the formation of nano sized precipitates in the dendrites and the basket weave morphology in interdendritic regions as shown in **Fig. 4.1.17**.

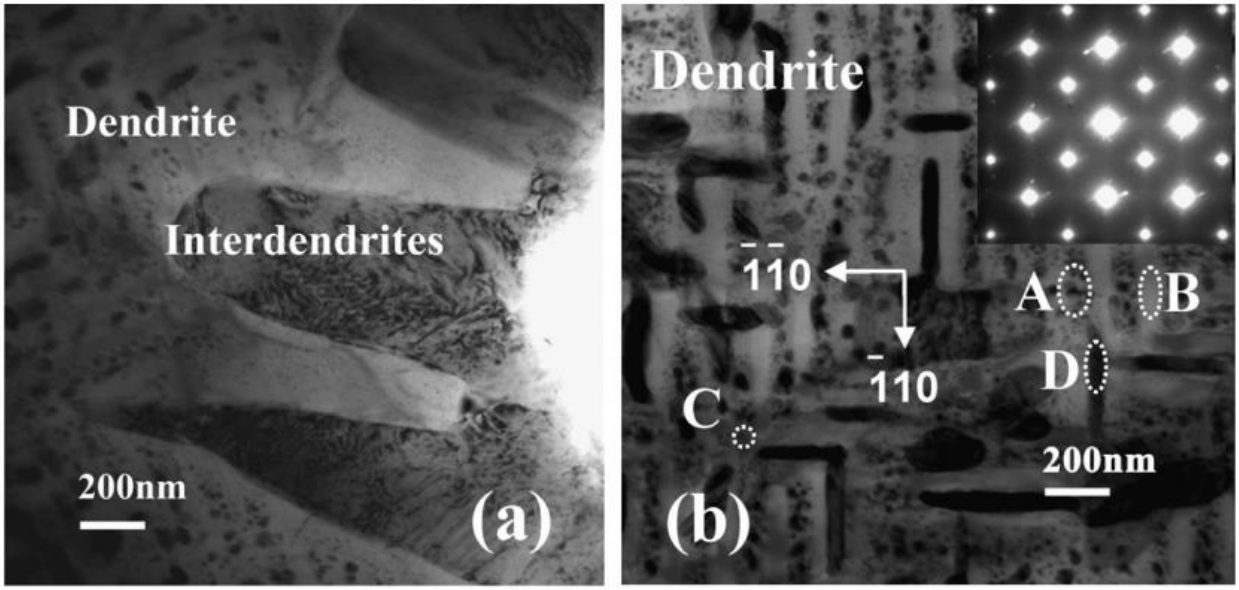

Fig. 4.1.16 Bright field images of as-cast AlCoCrCuFeNi HEA [2].

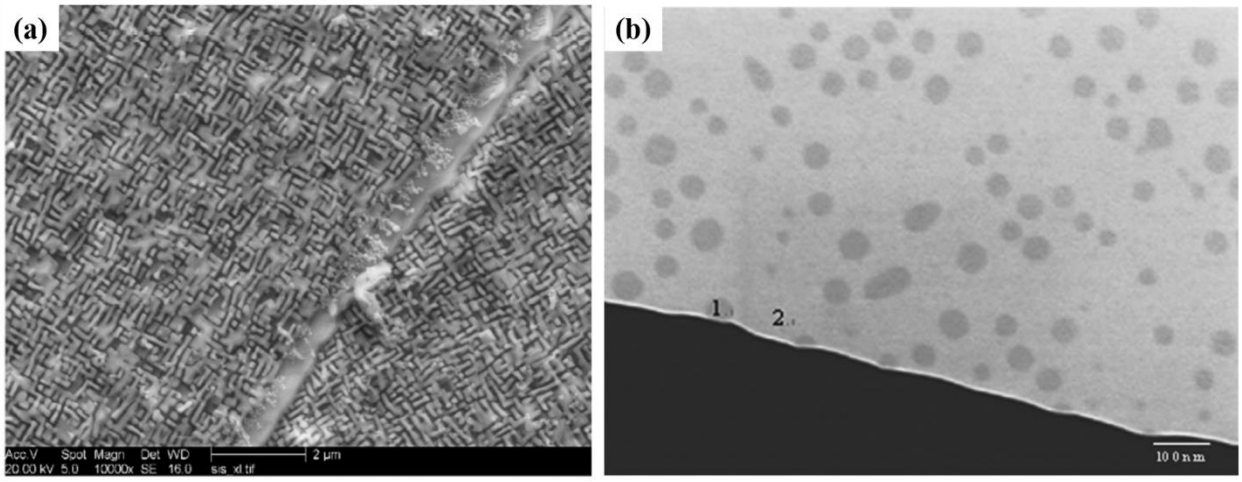

Fig. 4.1.17 (a) Basket weave morphology in the interdendrities and (b) spherical nanoprecipitate in dendrite region of AlCoCrFeNi HEA [53].

4.1.4 Summary

A combination of high energy ball milling and SPS has been utilized to fabricate an ultrafine grained equiatomic AlCoCrCuFeNi HEA possessing an fcc and an ordered bcc (B2) phases. The sintered product (with no porosity observed during SEM investigations) has an absolute density of 7.12 g/cc, measured using the Archimedes principle method, against rule of mixtures value of 7.068 g/cc. Structural and microstructural investigations revealed the presence of solid solutions, dislocations, bimodal grain structures and nano twins.

Except in few cases, majority of the alloy systems studied have resulted in multiphase as well as complex microstructures. In addition several complex phases, often ordered structures have also been formed with wide variation in their crystal structures. Therefore structural as well as microstructural evolution of HEAs is a very important aspect and has to be thoroughly understood as these features and their length scales greatly influence their mechanical behaviour.

References

1. Tong CJ, Chen YL, Chen SK, Yeh JW, Shun TT, Tsau CH, Lin SJ, Chang SY: **Microstructure characterization of Al_xCoCrCuFeNi high entropy alloy system with multi principal elements**. *Metallurgical and Materials Transactions A* 2005, **36**:1-13.
2. Singh S, Wanderka N, Murty BS, Glatzel U, Banhart J: **Decomposition in multi-component AlCoCrCuFeNi high-entropy alloy**. *Acta Materialia* 2011, **59**:182-190.
3. Tung CC, Yeh JW, Shun TT, Chen SK, Huang YS, Chen HC: **On the elemental effect of AlCoCrCuFeNi high-entropy alloy system**. *Materials Letters* 2007, **61**:1-5.
4. Kuznetsov AV, Shaisultanov DG, Stepanov ND, Salishchev GA, Senkov ON: **Superplasticity of AlCoCrCuFeNi high entropy alloy**. *Materials Science Forum* 2012, **735**:146-151.
5. Zhiyuan Liu SG, Xiongjun Liu, Jianchao Ye, Yong Yang, Xun-Li Wang, Ling Yang, Ke An and C.T. Liu: **Micromechanical characterization of casting-induced inhomogeneity in an $Al_{0.8}$CoCrCuFeNi high-entropy alloy**. *Scripta Materialia* 2011, **64**:868–871.
6. Kuznetsov AV, Shaysultanov DG, Stepanov ND, Salishchev GA, Senkov ON: **Tensile properties of an AlCrCuNiFeCo high-entropy alloy in as-cast and wrought conditions**. *Materials Science and Engineering: A* 2012, **533**:107-118.
7. Sheng HF, Gong M, Peng LM: **Microstructural characterization and mechanical properties of an $Al_{0.5}$CoCrFeCuNi high-entropy alloy in as-cast and heat-treated/quenched conditions**. *Materials Science and Engineering: A* 2013, **567**:14-20.
8. Manzoni A, Daoud H, Volkl R, Glatzel U, Wanderka N: **Phase separation in equiatomic AlCoCrFeNi high-entropy alloy**. *Ultramicroscopy* 2013, **132**:212-215.
9. Roy U, Roy H, Daoud H, Glatzel U, Ray KK: **Fracture toughness and fracture micromechanism in a cast AlCoCrCuFeNi high entropy alloy system**. *Materials Letters* 2014, **132**:186-189.
10. Chellali R, Hamou A, Zheng L, Adjdir M: **Investigation on relationship between intermediate temperature embrittlement and intergranular precipitation in AlCoCrCuFeNi alloy**. *Internationaljournal of Cast Metals Research* 2014, **27**:199-201.
11. Guo S: **Phase selection rules for cast high entropy alloys: an overview**. *Materials Science and Technology* 2015, **31**(10):1223-1230.

12. Toda-Caraballo I, Rivera-Díaz-del-Castillo PEJ: **Modelling solid solution hardening in high entropy alloys**. *Acta Materialia* 2015, **85**:14-23.
13. Seifi M, Li D, Yong Z, Liaw PK, Lewandowski JJ: **Fracture toughness and fatigue crack growth behavior of as-cast high-entropy alloys**. *Jom* 2015, **67**(10):2288-2295.
14. Toda-Caraballo I, Rivera-Díaz-del-Castillo PEJ: **A criterion for the formation of high entropy alloys based on lattice distortion**. *Intermetallics* 2016, **71**:76-87.
15. Lu Y, Gao X, Jiang L, Chen Z, Wang T, Jie J, Kang H, Zhang Y, Guo S, Ruan H *et al*: **Directly cast bulk eutectic and near-eutectic high entropy alloys with balanced strength and ductility in a wide temperature range**. *Acta Mater* 2017, **124**:143-150.
16. Wang Z, Baker I, Guo W, Poplawsky JD: **The effect of carbon on the microstructures, mechanical properties, and deformation mechanisms of thermo-mechanically treated $Fe_{40.4}Ni_{11.3}Mn_{34.8}Al_{7.5}Cr_6$ high entropy alloys**. *Acta Materialia* 2017, **126**:346-360.
17. Lu Xie PB, Anne-Lise Thomann, Jean-Marc Bauchire: **AlCoCrCuFeNi high entropy alloy cluster growth and annealing on silicon: A classical molecular dynamics simulation study.** *Applied Surface Science* 2013, **285P**:810-816.
18. Jablonski PD, Licavoli JJ, Gao MC, Hawk JA: **Manufacturing of high entropy alloys**. *Jom* 2015, **67**(10):2278-2287.
19. Kumar N, Komarasamy M, Nelaturu P, Tang Z, Liaw PK, Mishra RS: **Friction stir processing of a high entropy alloy $Al_{0.1}CoCrFeNi$**. *Jom* 2015, **67**(5):1007-1013.
20. Tsai MH, Yeh JW: **High-entropy alloys: a critical review**. *Material Research Letters* 2014, **2**:107-123.
21. Guo S, Liu CT: **Phase stability in high entropy alloys: formation of solid-solution phase or amorphous phase**. *Progress in Natural Science: Materials International* 2011, **21**:433-446.
22. Miracle DB: **The physical and mechanical properties of NiA1**. *Acta Metall* 1993, **41**(3):649-684.
23. Miracle DB, Senkov ON: **A critical review of high entropy alloys and related concepts**. *Acta Materialia* 2017, **122**:488-511.
24. Li BS, Wang YP, Ren MX, Yang C, Fu HZ: **Effects of Mn, Ti and V on the microstructure and properties of AlCrFeCoNiCu high entropy alloy**. *Materials Science and Engineering: A* 2008, **498**(1-2):482-486.

25. Maulik O, Kumar D, Kumar S, Fabijanic DM, Kumar V: **Structural evolution of spark plasma sintered AlFeCuCrMg$_x$ (x = 0, 0.5, 1, 1.7) high entropy alloys**. *Intermetallics* 2016, **77**:46-56.
26. Okamoto NL, Fujimoto S, Kambara Y, Kawamura M, Chen ZM, Matsunoshita H, Tanaka K, Inui H, George EP: **Size effect, critical resolved shear stress, stacking fault energy, and solid solution strengthening in the CrMnFeCoNi high-entropy alloy**. *Sci Rep* 2016, **6**:35863.
27. Ji W, Fu Z, Wang W, Wang H, Zhang J, Wang Y, Zhang F: **Mechanical alloying synthesis and spark plasma sintering consolidation of CoCrFeNiAl high-entropy alloy**. *Journal of Alloys and Compounds* 2014, **589**:61–66.
28. babu CS, Sivaprasad K, Muthupandi V, Szpunar JA: **Characterization of Nanocrystalline AlCoCrCuNiFeZn High Entropy Alloy Produced by Mechanical Alloying**. *Procedia Materials Science* 2014, **5**:1020-1026.
29. Gómez-Esparza CD, Campos-Venegas K, Solis-Canto O, Alvarado-Orozco JM, Muñoz-Saldaña J, Herrera-Ramírez JM, Martínez-Sánchez R: **Nanohardness and microstructure of NiCoAlFeCu and NiCoAlFeCuCr alloys produced by mechanical alloying**. *Microscopy and Microanalysis* 2014, **20**:2106-2107.
30. Ji W, Wang W, Wang H, Zhang J, Wang Y, Zhang F, Fu Z: **Alloying behavior and novel properties of CoCrFeNiMn high-entropy alloy fabricated by mechanical alloying and spark plasma sintering**. *Intermetallics* 2015, **56**:24-27.
31. Maulik O, Kumar V: **Synthesis of AlFeCuCrMg$_x$ (x=0, 0.5, 1, 1.7) alloy powders by mechanical alloying**. *Materials Characterization* 2015, **110**:116-125.
32. Baldenebro-Lopez FJ, Herrera-Ramírez JM, Arredondo-Rea SP, Gómez-Esparza CD, Martínez-Sánchez R: **Simultaneous effect of mechanical alloying and arc-melting processes in the microstructure and hardness of an AlCoFeMoNiTi high-entropy alloy**. *Journal of Alloys and Compounds* 2015, **643**:S250-S255.
33. Li X, Tian F, Schonecker S, Zhao J, Vitos L: **Ab initio-predicted micro-mechanical performance of refractory high-entropy alloys**. *Sci Rep* 2015, **5**:12334.
34. Kuk SW, Lim WJ, Kim SS, Hong SH, Ryu HJ: **Fabrication of W-Nb-Mo-Ta-V high entropy alloys by mechanical alloying and spark plasma sintering**. *Transactions of the Korean Nuclear Society Spring Meeting* 2015.

35. Lv ZY, Liu XJ, Jia B, Wang H, Wu Y, Lu ZP: **Development of a novel high-entropy alloy with eminent efficiency of degrading azo dye solutions**. *Sci Rep* 2016, **6**:34213.

36. Wang WR, Wang WL, Wang SC, Tsai YC, Lai CH, Yeh JW: **Effects of Al addition on the microstructure and mechanical property of $Al_xCoCrFeNi$ high-entropy alloys**. *Intermetallics* 2012, **26**:44-51.

37. Suryanarayana C, Grant Norton M: **X-Ray diffraction; a practical approach**. New York: Plenum Press; 1998.

38. Cahn RW, Haasen P: **Physical metallurgy**, vol. 1. North Holland: Elsevier Science B.V; 1996.

39. Zhang KB, Fu ZY, Zhang JY, Shi J, Wang WM, Wang H, Wang YC, Zhang QJ: **Nanocrystalline CoCrFeNiCuAl high-entropy solid solution synthesized by mechanical alloying**. *Journal of Alloys and Compounds* 2009, **485**:L31–L34.

40. Gómez-Esparza CD, Estrada-Guel I, Antúnez-Flores W, Herrera-Ramírez JM, Martínez-Sánchez R: **Microstructural characterization of NiCoAlFeCuCr high-entropy alloys**. *Microscopy and Microanalysis* 2010, **16**:1252-1253.

41. Gómez-Esparza CD, Ochoa-Gamboa RA, Estrada-Guel I, Cabañas-Moreno JG, Barajas-Villarruel JI, Arizmendi-Morquecho A, Herrera-Ramírez JM, Martínez-Sánchez R: **Microstructure of NiCoAlFeCuCr multi-component systems synthesized by mechanical alloying**. *Journal of Alloys and Compounds* 2011, **509**:S279-S283.

42. Sriharitha R, Murty BS, Kottada RS: **Phase formation in mechanically alloyed $Al_xCoCrCuFeNi$ (x = 0.45, 1, 2.5, 5 mol) high entropy alloys**. *Intermetallics* 2013, **32**:119-126.

43. Sriharitha R, Murty BS, Kottada RS: **Alloying, thermal stability and strengthening in spark plasma sintered $Al_xCoCrCuFeNi$ high entropy alloys**. *Journal of Alloys and Compounds* 2014, **583**:419-426.

44. Dolique V, Thomann AL, Brault P, Tessier Y, Gillon P: **Complex structure/composition relationship in thin films of AlCoCrCuFeNi high entropy alloy**. *Materials Chemistry and Physics* 2009, **117**:142-147.

45. Dolique V, Thomann AL, Brault P, Tessier Y, Gillon P: **Thermal stability of AlCoCrCuFeNi high entropy alloy thin films studied by in-situ XRD analysis**. *Surface and Coatings Technology* 2010, **204**:1989-1992.

46. Singh S, Wanderka N, Kiefer K, Siemensmeyer K, Banhart J: **Effect of decomposition of the Cr–Fe–Co rich phase of AlCoCrCuFeNi high entropy alloy on magnetic properties**. *Ultramicroscopy* 2011, **111**:619–622.

47. Tong CJ, Chen MR, Chen SK, Yeh JW, Shun TT, Lin SJ, Chang SY: **Mechanical performance of the $Al_xCoCrCuFeNi$ high-entropy alloy system with multiprincipal elements**. *Metallurgical and Materials Transactions A* 2005, **36**:1263-1271.

48. Liu WH, Lu ZP, He JY, Luan JH, Wang ZJ, Liu B, Liu Y, Chen MW, Liu CT: **Ductile $CoCrFeNiMo_x$ high entropy alloys strengthened by hard intermetallic phases**. *Acta Materialia* 2016, **116**:332-342.

49. Tsai M-H, Yuan H, Cheng G, Xu W, Tsai K-Y, Tsai C-W, Jian WW, Juan C-C, Shen W-J, Chuang M-H *et al*: **Morphology, structure and composition of precipitates in $Al_{0.3}CoCrCu_{0.5}FeNi$ high-entropy alloy**. *Intermetallics* 2013, **32**:329-336.

50. Jones NG, Frezza A, Stone HJ: **Phase equilibria of an $Al_{0.5}CrFeCoNiCu$ high entropy alloy**. *Materials Science and Engineering: A* 2014, **615**:214-221.

51. Santodonato LJ, Zhang Y, Feygenson M, Parish CM, Gao MC, Weber RJ, Neuefeind JC, Tang Z, Liaw PK: **Deviation from high-entropy configurations in the atomic distributions of a multi-principal-element alloy**. *Nature communications* 2015, **6**:1-13.

52. Tsai C-W, Chen Y-L, Tsai M-H, Yeh J-W, Shun T-T, Chen S-K: **Deformation and annealing behaviors of high-entropy alloy $Al_{0.5}CoCrCuFeNi$**. *Journal of Alloys and Compounds* 2009, **486**(1-2):427-435.

53. Wang YP, Li BS, Ren MX, Yang C, Fu HZ: **Microstructure and compressive properties of AlCrFeCoNi high entropy alloy**. *Materials Science and Engineering: A* 2008, **491**(1-2):154-158.

4.2 Strengthening mechanisms in equiatomic ultrafine grained AlCoCrCuFeNi high-entropy alloy studied by micro and nanoindentation methods

4.2.1 Introduction

A plastic deformation of a metal is process of movement of huge number of dislocations to slip on application of external force. If the movement of these mobile dislocations is blocked or restricted, the strength of the material is increased [1]. It is clear that the strength of the material is inversely proportional to dislocation mobility. Single crystals are the ideal material to analyze the dislocation motion. However the plastic deformation information drawn from them cannot be applicable to the commercial materials, as most of them are polycrystalline. The basic factors which effect towards the strength and high temperature strength of single or polycrystalline materials are,

- Purity of raw materials and the method of preparation.
- Crystal structure of the material which have different number and type of the slip systems.
- Lattice frictional stress which is related to the Burgers vector of a particular slip system.
- Closed packed structures with different stacking fault energies.

Apart from these basic factors, engineers uses different strengthening mechanisms to design a material. These mechanisms involve creation of the obstacles to resist the dislocation motion [2]. Applied force has to be increased to an order of magnitude to cut or bypass the obstacles by the dislocations. Slip is sequential process of bonds breaking and bonds reforming while sliding a plane of atoms over another plane of atoms. Dislocations are of two types, edge dislocation and screw dislocation. With the increase in dislocation density (number of dislocations in a unit volume), the strength increases. Generally while increasing in strength, the ductility of the material

is suffered or reduced [3]. There are many strengthening mechanisms like work hardening, solid solution strengthening, precipitation hardening, grain boundary strengthening, twin boundary strengthening, strengthening from second phase, strain ageing, martensitic strengthening, fiber strengthening, fine particle strengthening, transformation hardening [1, 4]. Few of them are explained in detail below.

1. Strain/work hardening

The interaction of a dislocations with another dislocation is called strain/work hardening. Cold working is most commonly used method to introduce a huge amount of dislocations into the lattice where they multiply on deformation. The high strain hardening occur when dislocations interact with the stress field of other dislocation and interpenetration of a slip system into another slip system forming dislocation jogs. The basic relationship between strain hardening and the structure is,

$$\sigma_0 = \sigma_i + \alpha G b \rho^{1/2} \quad \ldots\ldots\ldots\ldots\ldots\ldots\ldots\ldots\ldots\ldots (Eq\ 4.2.1)$$

Cold working is the process of severe deformation by reducing one or two dimensions of the materials and increase in other direction as shown in the **Fig. 4.2.1**. During this process, grains are orientation in the cold working directions and induces a high internal energy. Annealing treatment is given to the cold worked materials as the most common procedures. Recovery, recrystallization and grain growth processes are the intrinsic mechanisms involved [5]. Recovery is the process of restoration of the yield strength of the materials, recrystallization is the process of formation of new grains at the expense of badly damaged grains and grain growth is the process of increasing the fine recrystallized grains.

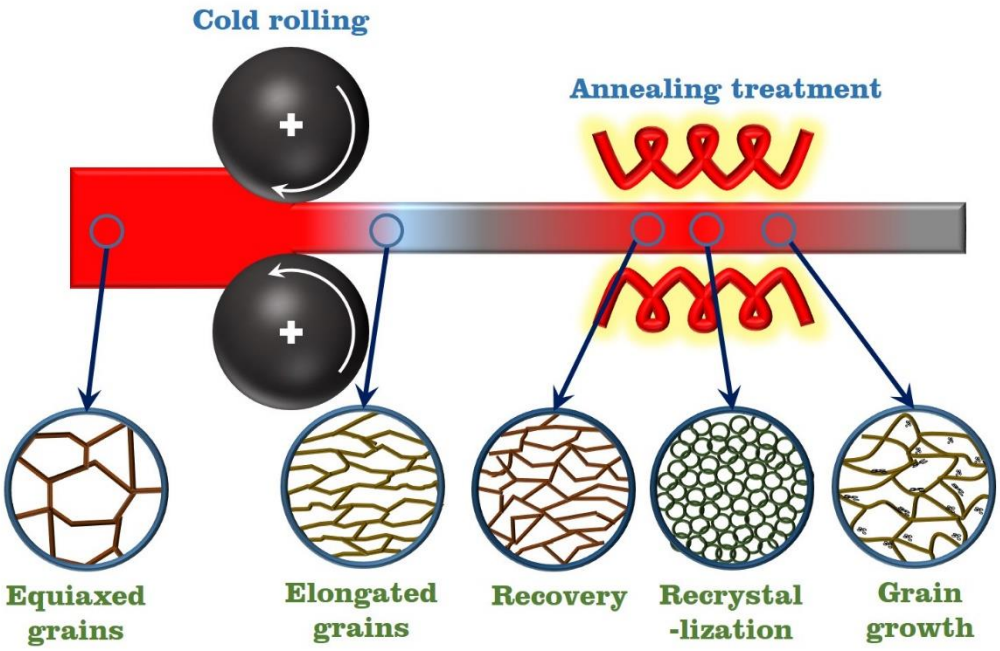

Fig. 4.2.1 Schematic of cold rolling, representing various microstructure at different stages of work hardening process.

2. Grain boundary strengthening

The interaction of a dislocations with grain boundaries is called grain boundary strengthening. The coincidence sites of two grains with different crystal orientation are called the grain boundaries as shown in **Fig. 4.2.2**. All grains have different crystallographic orientation and they are separated by a grain boundary. Grain boundary have inherent strength in the material because the mutual slip is blocked at the grain boundary. It is difficult for a dislocation to change the orientation and move into another slip plane, because of the random arrangement of atoms at the grain boundaries. Grain boundaries act as the barriers for the dislocation motion and the dislocations pile up at the grain boundaries resulting high strength. It was found that the yield strength of the material increase linearly with the misorientation across grain boundary. Hall-Petch equation [6] gives the relationship for the yield stress (σ_0) and grain diameter (D) as follows,

$$\sigma_0 = \sigma_i + kD^{-1/2} \ldots\ldots\ldots\ldots\ldots\ldots\ldots\ldots\ldots\ldots\ldots\ldots (Eq\ 4.2.2)$$

where σ_i is the frictional stress and k is the constant associated with the hardening contribution of grain boundaries. k is the slope of the linear line obtained from the plot of yield stress (σ_0) and grain diameter (D). Nanomaterials are ideal grain boundary strengthening materials because of more grain boundary area than the grain area.

3. Solid solution strengthening

The interaction of a dislocations with solute atoms is called solid solution strengthening. The solute atoms are added in the solid solution containing solvent atoms. These solute atoms either occupy the interstitial site or a substitutional site in the solvent lattice, creating high strain field. If the solute atomic size is relatively equal to the solvent atomic size, the solute atom occupy the solvent lattice point forming a substitutional solid solution as shown in **Fig. 4.2.3**.

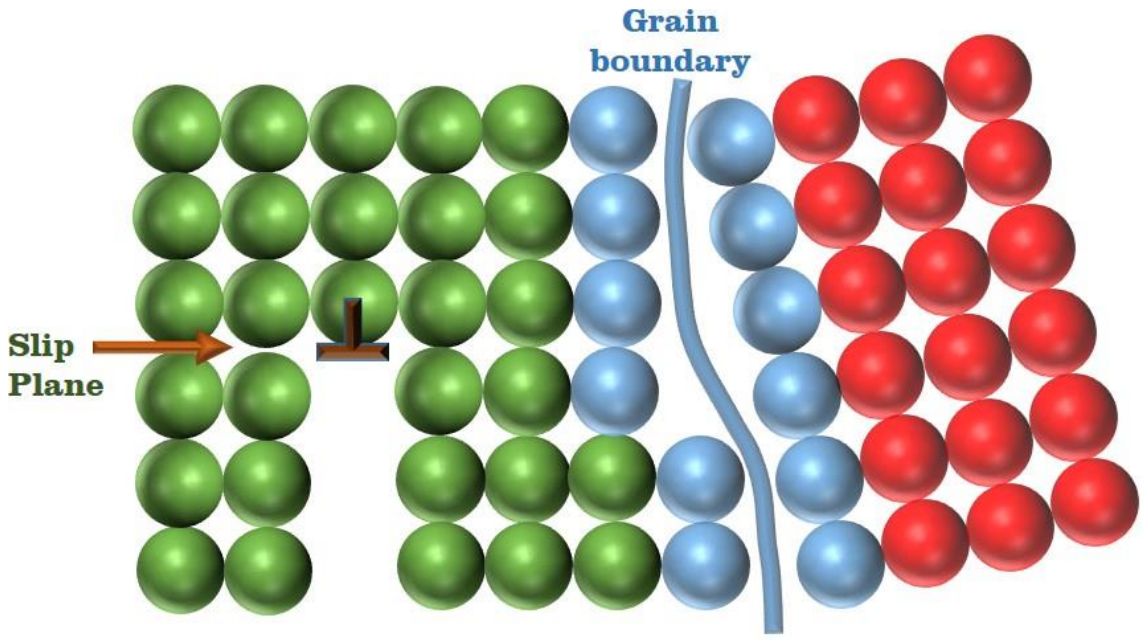

Fig. 4.2.2 Schematic of grain boundary strengthening where grain boundaries act as barrier to the moving dislocation in the slip plane.

If the atomic size of the solvent atom is much smaller than the solute atomic size, the solute atom occupies the interstitial sites of solute forming interstitial solid solution. Also if the solvent atomic size is much higher than the solvent atomic size, the solute atom occupy the interstitial site. This could be tensile lattice strain or compressive lattice strain depends on the atomic size of the solute atoms. However, HEAs do not have solute atoms but have different atomic sized solvent atoms create high lattice strain. The interaction of such strain field of dislocation with the strain field around different sized atoms increase the strength of the material [7, 8].

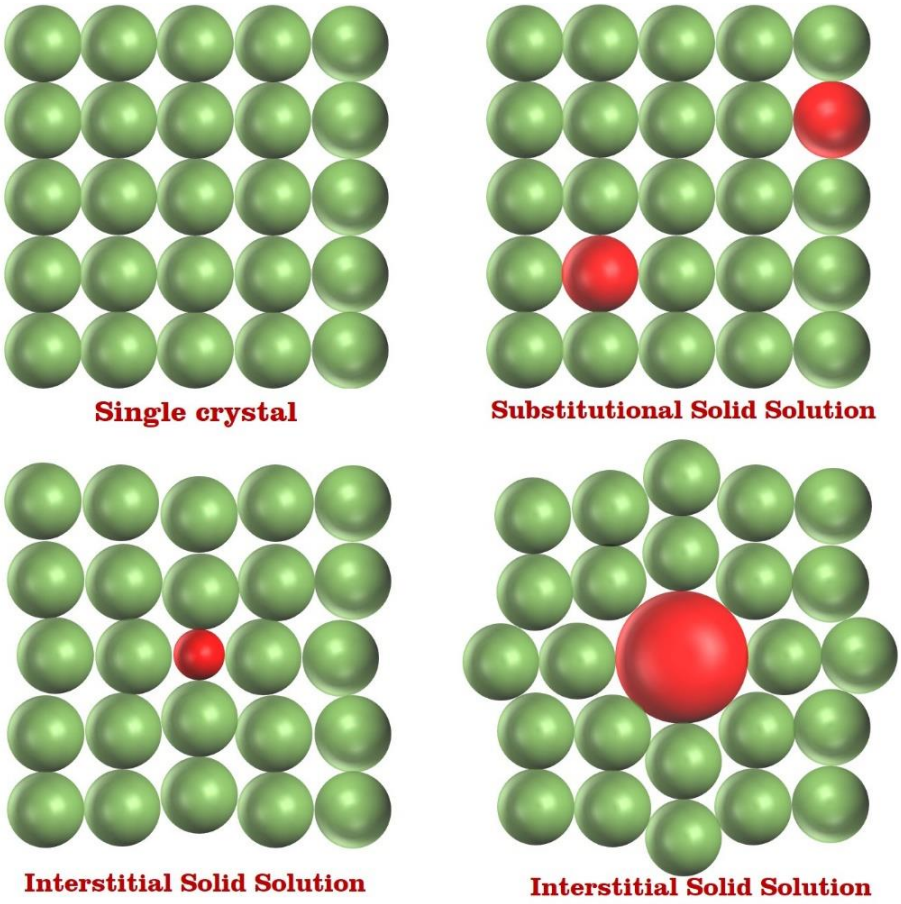

Fig. 4.2.3 Schematic of different solid solution strengthening mechanisms.

4. Precipitation strengthening

Second phase particles or precipitates, that are homogenously distributed in the matrix interact with the dislocations and result in high strength. If the precipitates are coherent with the matrix, it is called precipitation strengthening. If the second phase particles are incoherent with the matrix, it is called dispersion strengthening. Precipitates are formed by solution treating and followed by quenching. They are soluble in the matrix forming a solid solution at elevated temperatures but are insoluble and precipitate out while cooling to room temperature. Whereas dispersoids are hard particles mixed in the matrix and produced by powder metallurgy methods. These dispersoids are very little soluble at elevated temperatures. As shown in **Fig. 4.2.4**, dislocations either have to cut through the precipitate or form a loop around the precipitate to move, which is called Orowan shearing or Orowan looping respectively. The precipitate size, shape, volume fraction and distribution are mainly altered for high strength [1, 9].

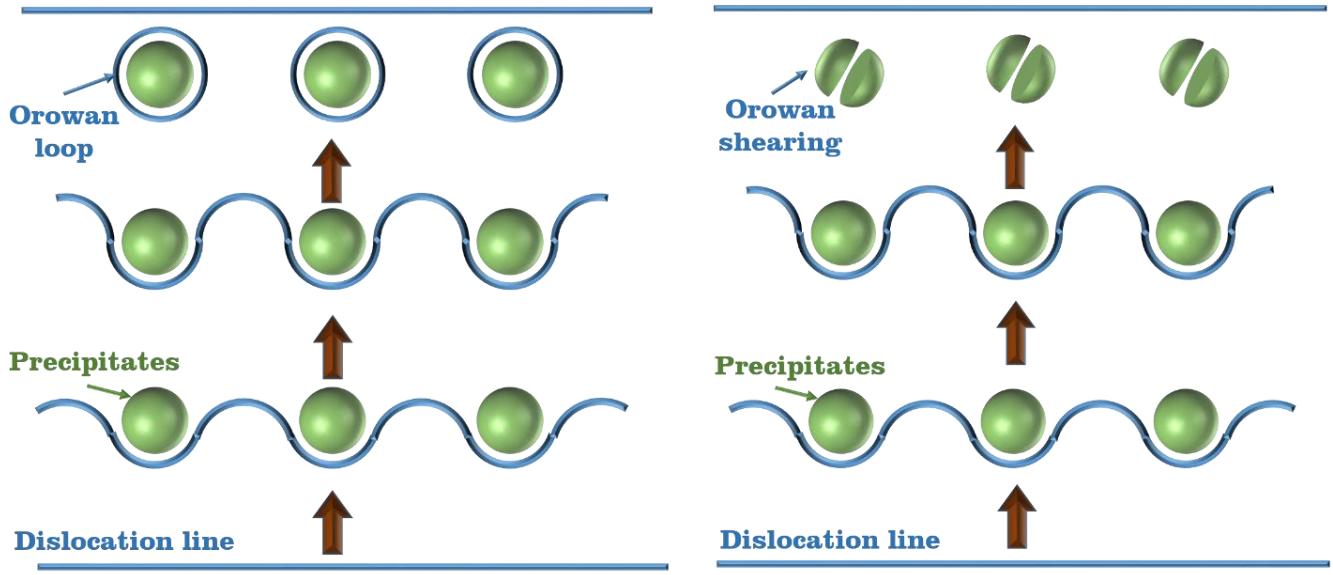

Fig. 4.2.4 Schematic of precipitation hardening where the dislocations either forming a loop around the precipitate or shearing the precipitate.

There are many other strengthening mechanism like twin boundary strengthening, strengthening from second phase, strain ageing, martensitic strengthening, fiber strengthening, fine particle strengthening, transformation hardening [4]. These are the strengthening mechanism in conventional materials. Our interest is to see how they are operated in HEAs.

Ultrafine AlCoCrCuFeNi HEA is achieved by mechanical alloying and subsequently spark plasma sintering techniques. 60 h mechanical alloying resulted a single phase solid solution with fcc crystal structure. Bulk components after spark plasma sintering precipitated an ordered B2 phase. The detailed mechanical properties of this system with nanocrystalline/ultrafine grained (ufg) features have not been reported to date. Mechanical properties have been evaluated using Vickers microindentation and depth sensing nanoindentation. A comprehensive understanding on the various strengthening mechanisms operating in this novel alloy has been presented in this paper. Strain rate sensitivity (SRS) and activation volume are reported and the governing mechanisms are also identified. While performing nanoindentation (Hysitron Triboindenter) at room temperature, a constant loading rate profile was used to reach a peak load of 8000 μN, followed by a hold segment at the peak load for 10 sec and unloading at the same loading rate. Various loading rates in the range 1000-8000 μN/s were adapted. Each nanohardness value is an average of 49 indents (7x7 matrix) performed under identical set of parameters. For a given condition, the quotient of loading rate and peak load is considered as effective strain rate.

4.2.2 Results

Vickers microindentation behavior observed on various samples sintered at 750 ºC for different hold times (5, 10 and 15 mins) is represented in **Fig. 4.2.5**. As the applied load is increased from 100-500g, there was a slight decrease in the hardness and recorded a value of 6.5 GPa for the sample held for 15 min at 750 ºC during SPS. Fig 5.2 (a) depicts the response of this alloy to

nanoindentation at an applied peak force of 8000 μN and at various loading rates in the range 1000-8000 μN/s. It yielded a hardness value of 8.13 GPa and an elastic modulus of 172 GPa calculated using Oliver-Pharr analysis [10, 11]. The slope of the plot between logarithmic flow stress on Y-axis and logarithmic strain rate on X-axis is shown in Fig 5.2 (b) and it represents SRS which is 0.0084 in this case.

4.2.3 Discussion

4.2.3.1 Strengthening mechanisms

Vickers microindentation was performed on the sintered samples and the data is presented in **Fig. 4.2.5**. As the applied load was varied between 100 and 500 g, the hardness has a values between 6.3 and 6. 8 GPa for samples sintered for various hold times of SPS. The average diagonals of Vickers indents are 16, 29 and 37 μm at the loads of 100, 300 and 500 g respectively. Therefore the Vickers indents at all applied loads are very large in comparison to the microstructural features (**Figs. 4.1.7, 4.1.8 (a-c)** and **4.1.9 (a-d)**) and they would deform both the larger and smaller grains. It is also to be noted that this hardness data is derived from several grains belonging to both the dark and white phases, hence this microindentation data indeed represents the bulk mechanical behaviour of the alloy studied. It is reported that the cast AlCoCrCuFeNi alloy possessed a hardness of 4.5 GPa [12]. Zhang et al [13] replaced Cu with Ti and synthesized the same alloy in the similar route and its Vickers hardness was measured to be 432 HV. Stefanoiu et al [14] excluded Cu element from this alloy and achieved an hardness of 407 HV. Therefore it is clearly evident that the present study reports superior mechanical properties for this equiatomic alloy in comparison to that reported in the literature. It is to be noted that hardness derived from higher loads i.e., more indentation depths is more representative of the bulk behaviour of the material as significantly larger volume is involved in the deformation.

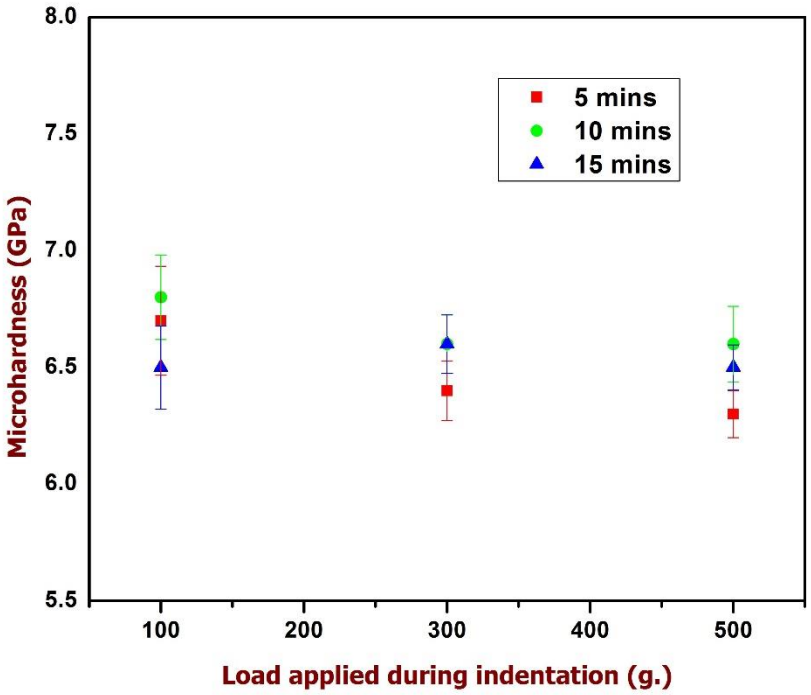

Fig. 4.2.5 Variation of microhardness with load in samples sintered with different holding times. At all the indent covered both larger and smaller grains as the diagonals of the Vickers indent were ~38 µm. Therefore it represents the bulk behavior.

Therefore the microhardness measurement made at a load of 500 g., for the sample sintered for 15 min, has been used in the analysis to identify the strengthening mechanisms in this alloy. From **Fig. 4.2.5**, this value is 6.5 GPa. Using Tabor's equation [15], $H = 3\,\sigma_{flow}$; where H is the hardness and σ_{flow} is the yield/flow stress of the material, σ_{flow} is 2.16 GPa. It is clear that microstructure (**Figs. 4.1.8** and **4.1.9**) of the sintered sample contains larger ufg, smaller nanocrystalline grains, twins with varied twin spacing. In addition, it is a two phase structure comprising of two solid solutions (fcc and B2). Hence the flow stress is expected to have the contributions from frictional stress offered by the complex lattice to the mobile dislocations, strengthening due to intersecting dislocations (Taylor hardening), grain boundary strengthening (Hall-Petch strengthening), solid solution strengthening and twin boundary strengthening. Therefore it is proposed that the following superposition equation can be utilized to identify different mechanisms contributing to overall flow stress of the alloy:

$$\boldsymbol{\sigma_{flow} = \sigma_i + \Delta\sigma_{SH} + \Delta\sigma_{HP} + \Delta\sigma_{SS} + \Delta\sigma_{TB}} \ldots\ldots\ldots\ldots\ldots\ldots\ldots\ldots\ldots (Eq\ 4.2.3)$$

σ_i is the frictional stress offered by the lattice for mobile dislocations. This stress exists in the lattice that is made of all the participating elements. As these HEAs are recently emerged novel class of alloys, to the authors' knowledge, their frictional stress data is not available in the literature. Hence, in line with the approximations made in ref. [11], rule of mixtures analysis has been used to estimate the frictional stress of this lattice and is calculated as 105 MPa.

$\Delta\sigma_{SH}$ (dislocations hardening /Taylor hardening/strain hardening) is the strengthening arising out of intersection of dislocations during deformation in relatively larger grains.

$$\boldsymbol{\Delta\sigma_{SH} = M\,\alpha\,G\,b\,\rho^{\frac{1}{2}}} \ldots\ldots\ldots\ldots\ldots\ldots\ldots\ldots\ldots\ldots\ldots\ldots (Eq\ 4.2.4)$$

M is the Taylor factor (3.06 for both fcc and bcc materials) [16], α is a correction factor specific to the material. As it is a novel HEA in the present study, α is assumed to be unity. G is the shear modulus, b is the Burgers vector, ρ is dislocation density. Elastic modulus (E) of this alloy, measured using nanoindentation, is 172 GPa. Based on the assumption that the cubic alloy in the current study is an isotropic and homogeneous material, shear modulus (G) can be calculated as $\boldsymbol{G = E/2(1+\upsilon)}$, where υ is the Poisson's ratio (≈ 0.33). For this alloy, G is calculated to be 65 GPa. Burgers vector of an fcc based lattice can be represented as, $\boldsymbol{b = (a/2)\langle 110\rangle}$ and its magnitude is calculated as, $\boldsymbol{|b| = (a/2)\sqrt{2}}$; In the current study, as it is a two phase alloy with lattice parameters of 0.359 nm (fcc) and 0.292 nm (bcc), an average of these two values is taken as the effective lattice parameter and is calculated to be 0.325 nm. Accordingly, |b| is computed to be 0.23 nm. Dislocation density (ρ) is calculated from the following equation [17]:

$$\boldsymbol{\rho = \frac{2\sqrt{3}\,\varepsilon}{d\,b}} \ldots\ldots\ldots\ldots\ldots\ldots\ldots\ldots\ldots\ldots\ldots\ldots\ldots (Eq\ 4.2.5)$$

In this Equation 4.2.5, ε is lattice strain, d is grain size, b is the Burgers vector (0.23 nm). Lattice strain for both the phases, using Stokes-Wilson formula [18], was estimated to be 0.003. The sintered sample (15 min. hold time) revealed a bi-modal grain size distribution with an average grain sizes of 112±46 nm and 1550±500 nm. Therefore it is suggested that the dislocation densities be separately calculated for these two grain size regimes as the grain dimensions could influence the total dislocation densities that they may contain. For a grain size of 112 nm, the dislocation density is calculated to be 4.03×10^{14} m^{-2} and for 1550 nm size regime it is calculated as 2.9×10^{13} m^{-2} using Equation 4.2.5. The total dislocation density, estimated by the addition these two values, is 42.9×10^{13} m^{-2}.

With all the above parameters, Δσ for strain hardening (Taylor hardening) arising from large dislocation densities present in this material is estimated to be 949 MPa using Equation 4.2.4.

$\Delta\sigma_{HP}$ is the Hall-Petch strengthening or grain size dependent strengthening.

$$\Delta\boldsymbol{\sigma_{HP}} = \boldsymbol{K_{HP}}\, \boldsymbol{d^{-0.5}} \quad \ldots\ldots\ldots\ldots\ldots\ldots\ldots\ldots\ldots\ldots\ldots\ldots\ldots\ldots (Eq\ 4.2.5)$$

K_{HP} is the Hall-Petch constant and 'd' is the average grain size. For 112 nm regime, by considering the K_{HP} values discussed in ref. [11], K_{HP} is assumed to be 0.27 MPa $m^{1/2}$ for this alloy and K_{HP} for 1550 nm regime is taken as 0.33 MPa $m^{1/2}$. Now the contribution from Hall-Petch (grain size) strengthening is estimated to be 806 MPa from smaller grain size regime (112 nm) and 264 MPa from larger grain size regime (1550 nm) using Equation 4.2.6. Therefore the total Hall-Petch strengthening is 1070 MPa. $\Delta\sigma_{SS}$ is contribution from solid solution strengthening. This component is also significant as both the phases (fcc and B2) are essentially solid solutions comprising of all the participating elements. In conventional binary solid solutions, elastic interactions between dislocations and stress fields created by solute atoms govern the associated strengthening mechanisms and all the established models for solid solution strengthening

mechanism are valid for binary solid solutions [19-22]. As HEAs are complex concentrated alloys, Senkov et al [23] have suggested the following equation to estimate solid solution strengthening for concentrated systems:

$$\Delta\boldsymbol{\sigma_{SS}} = \boldsymbol{A\ G\ \varepsilon^{\frac{4}{3}} C^{\frac{2}{3}}} \quad \ldots\ldots\ldots\ldots\ldots\ldots\ldots\ldots\ldots\ldots\ldots\ldots\ldots\ldots (Eq\ 4.2.7)$$

In this Equation 4.2.7, A is a dimensionless parameter of the order of 0.1. C is concentration of the solute atoms (0.16), G is the shear modulus of the alloy (65 GPa) and ε is lattice strain due to the solute. One caveat here is that the concept of solute and solvent which are valid for traditional dilute solid solutions may not be valid for HEAs as these are highly concentrated and nominally equiatomic. In AlCoCrCuFeNi system, when the atomic radii mismatch is calculated among different binaries (**Fig 4.1.2 (b)**), it suggests that Al might cause more strain to the copper based lattice of this complex concentrated solid solution with a strain of 12% (from atomic radii mismatch). Therefore for practical reasons, it is approximated that the concentration of Al (0.16) may be taken as the concentration of the solute and the strain caused by Al atom as the effective strain. With these parameters, the solid solution strengthening component assumes to be 112 MPa from Equation 4.2.7.

Twins (with spacing in nm) observed in relatively large ultrafine grains also will contribute via Hall-Petch type strengthening [24-26]. $\Delta\sigma_{TB}$ is given as,

$$\Delta\boldsymbol{\sigma_{TB}} = \ \boldsymbol{V_f K_{TB}\ l^{-0.5}} \quad \ldots\ldots\ldots\ldots\ldots\ldots\ldots\ldots\ldots\ldots\ldots\ldots\ldots\ldots (Eq\ 4.2.8)$$

K_{TB} is a constant and can be approximated to that of a Hall-Petch constant of the nanocrystalline regime of a corresponding alloy (0.27 MPa $m^{1/2}$ [27]) as the twin spacing (l) is in nm. V_f is the total volume fraction of twins. These twins are not present in all the grains. They are observed to be present relatively in fewer grains and their total volume fraction seems to be not that significant. From the micrographs, twin width (l) was measured to be as low as 2.3 nm (**Fig 4.1.9 (d)**) to as

high as 83 nm (**Fig 4.1.9 (c)**), however statistical estimation of twin spacing distribution is not possible as there are not many twins. Therefore, average "l" is found to be 43 nm. The average area fraction of these twins is estimated to be 11% and it is considered as volume fraction of the twins for all practical reasons and calculations. With these parameters and as per the Hall-Petch type dependence, the contribution of twins to strengthening is calculated to be 143 MPa using Equation 4.2.8. It is widely agreed that coherent twin boundaries present in ufg grains increase the strength [28] as well as result in enhanced strain hardening [26]. Based on the above calculations and from Equation 4.2.3, the overall contribution from various plausible mechanisms to the flow stress (σ_{flow}) is 2.38 GPa. The Vickers hardness (H) for this sample was measured as 6.55 GPa (**Fig. 4.2.5**). Therefore the ratio, (H/σ_{flow}) is 2.7. According to Tabor's analysis [15], this ratio for conventional materials was varied between 2.8 and 3.2. Therefore with the calculated ratio of 2.7, which is in close agreement with that of conventional polycrystalline materials, for this HEA it is not unreasonable to state that above mentioned strengthening mechanisms are responsible for the overall flow stress realized. As the two solid solutions observed (fcc and B2) in the sintered alloy contain all the elements (**Fig 4.1.7(d)**), the present authors have cautiously given them the same treatment while estimating various strengthening contributions to the overall flow stress. From **Table 4.2.1** and **Fig. 4.2.6**, it is clear that Taylor hardening and grain boundary strengthening are the dominant strengthening mechanisms in this alloy accounting for nearly 85% of the flow stress. The other mechanisms such as solid solution strengthening and twin boundary strengthening have minor contributions to the overall flow stress.

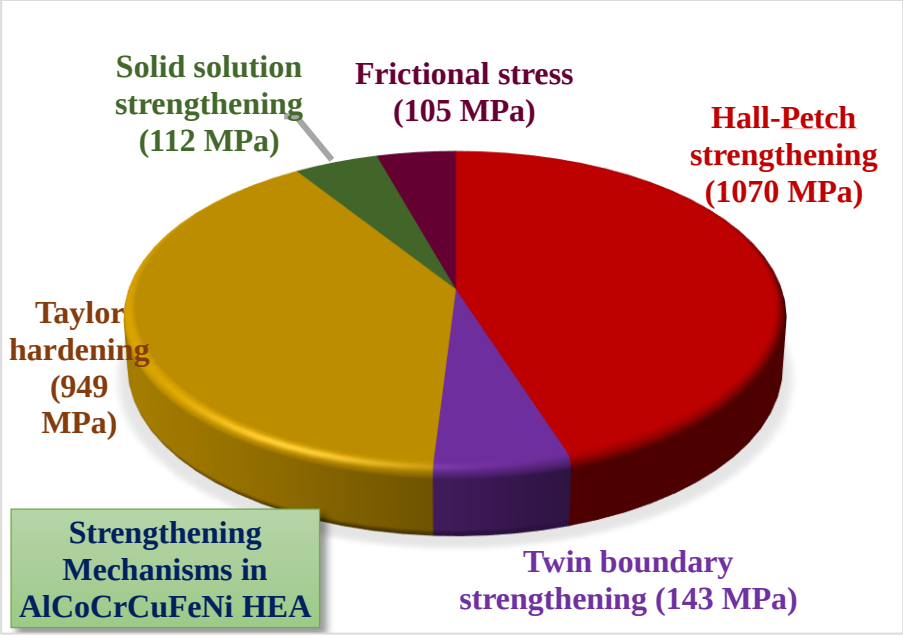

Fig. 4.2.6 Pie chart of strengthening mechanism representing contributions of different mechanisms operated in AlCoCrCuFeNi HEA.

Table 4.2.1 Various strengthening mechanisms identified in nanocrystalline equiatomic AlCoCrCuFeNi system.

Mechanisms	**Strength contribution (MPa)**
Frictional stress	105
Taylor hardening	949
Hall-Petch strengthening	1070
Solid solution strengthening	112
Twin boundary strengthening	143
Total strengthening	**2379**

To date, there are very few detailed efforts in identifying the strengthening mechanisms operating in HEAs despite their fascinating mechanical properties [29]. A good combination of strength, strain hardening rate, ductility and fracture toughness have been reported in CrMnFeCoNi system

even at -196 ºC by Otto et al [30]. The alloy was melted and casted into ingots and cold rolled upto 87% reduction and annealed at 1200 ºC for 45 h. This alloy resulted equiaxed grains with three different grain sizes. The alloy displayed high yield strength of 300 MPa at -196 ºC temperature. They observed that nano-twins were operating at high strain of 20% and at lower strain i.e at yielding 2% strain there were no evidence for nano-twin formation. This they attributed to high ductility at lower temperature and high strength at high temperature was because of additional deformation mode by nano-twins. Detailed mechanical testing at -196 ºC and 20 ºC as shown in **Fig. 4.2.7** and comprehensive TEM investigations suggest that formation of twins in the early stages of deformation in this system provides additional strain hardening rate leading to improved strength and ductility even at -196 ºC [31]. Fu et al [32] have observed the similar microstructural features and strengthening mechanisms in fcc based $Co_{25}Ni_{25}Fe_{25}Al_{7.5}Cu_{17.5}$ HEA prepared by ball milling followed by SPS. They investigated $Co_{25}Ni_{25}Fe_{25}Al_{7.5}Cu_{17.5}$ HEA in nanocrystalline and coarse grained forms using mechanical alloying followed by spark plasma sintering and vacuum arc melting routes respectively. The mechanical alloying of 49 h resulted a single fcc phase and the sintering at 1000 ºC did not result any phase transformation. The milled powder morphology is similar to the one we reported like lamellar or flake. The strengthening mechanisms were discussed with assumptions available in the literature. Concluded that the high strength of the alloy is from grain boundary and dislocation strengthening.

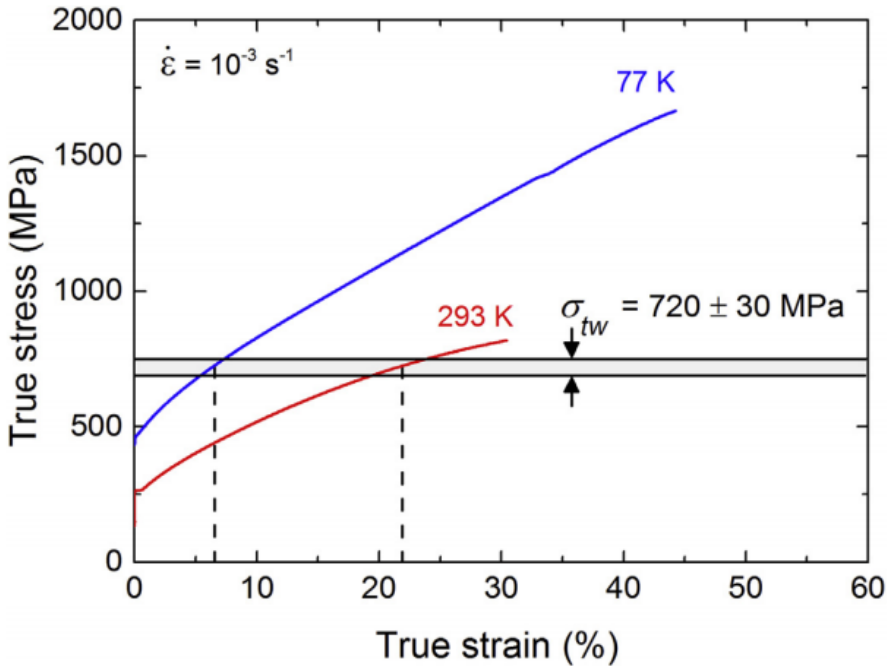

Fig. 4.2.7 True stress-strain curves measured at -196 ºC (77K) and 20 ºC (293K) where critical stress for twin formation is presented [31].

Liu et al [33] have presented that ductility of $CoCrFeNiMo_{0.3}$ HEAs could be enhanced by hard σ and μ type intermetallic compounds to a level of 19% with simultaneous possession of good strength. It was attributed that the fcc structure of the HEA matrix favors a high work hardening rate which may be suppressing the propagation of microcracks originated at the particle/matrix interfaces. It should be mentioned that the current study is a comprehensive report on strengthening mechanisms operating in ultrafine grained AlCoCrCuFeNi system. Senkov et al [23] fabricated $Ta_{20}Nb_{20}Hf_{20}Zr_{20}Ti_{20}$ refractory HEA using vacuum arc melting and hot isostatic pressing at 1200 ºC for 3 h. All the elements in the alloy have bcc structure and the alloy after melting resulted a bcc structure. The hot isostatic pressing did not change the crystal structure. **Fig. 4.2.8** gives the compressive stress-strain curve, where the yield strength of $Ta_{20}Nb_{20}Hf_{20}Zr_{20}Ti_{20}$ HEA is 929 MPa. The high compressional yield strength is supported by solid solution strengthening. The same assumptions and the formula is used for the solid solution strengthening contributions in the

current investigations. It is also reported by Tsai et al that the nanotwins occur during deformation and he reason it as the result of low stacking fault energy and high solid solution hardening.

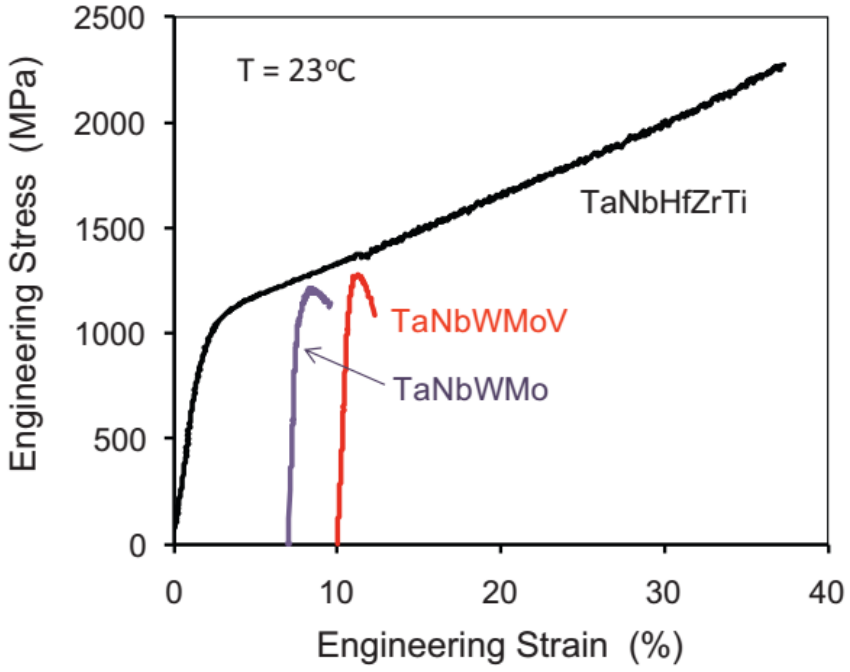

Fig. 4.2.8 Compressive stress-strain curves of different HEAs [23].

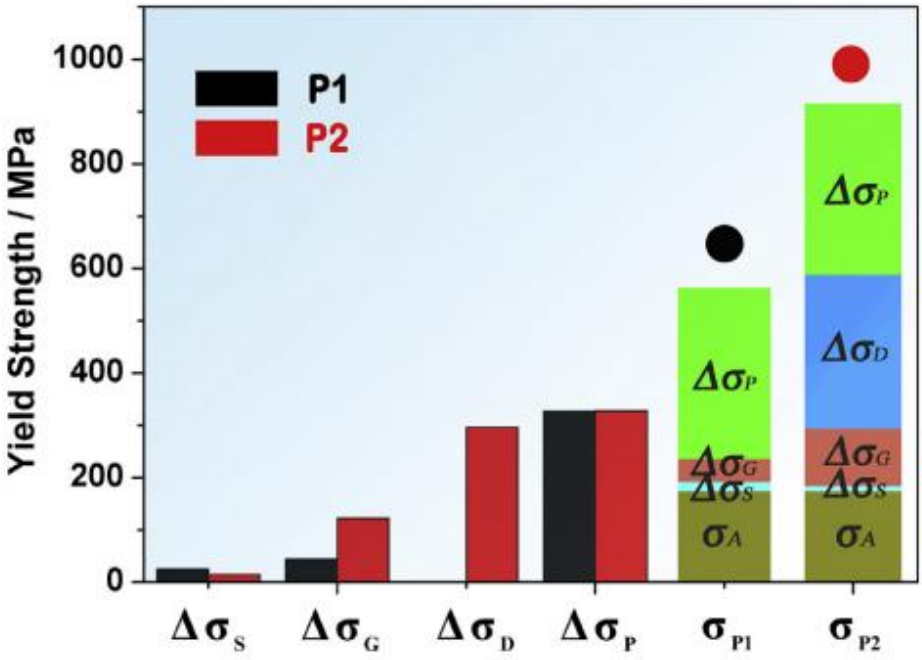

Fig. 4.2.9 Different contributions to the strength of HEAs (details of P1 and P2 given in ref [34]).

He et al [34] prepared FeCoNiCr and $(FeCoNiCr)_{94}Ti_2Al_4$ HEAs by melting and casting methods. The later alloy has been given two different thermomechanical treatments named P1 and P2 (details given in ref [34]). FeCoNiCr and $(FeCoNiCr)_{94}Ti_2Al_4$ HEAs have fcc phase, P1 alloy has additional $L1_2$ type precipitates and P2 alloy reveal secondary phases as well. Strengthening mechanisms operated in all the four alloys have been studied in detail and are shown in **Fig. 4.2.9**. Different contributions towards the overall strengthening of the alloy they considered are frictional strength, solid solution strengthening, grain-boundary strengthening, dislocation strengthening and precipitation strengthening. As the yield strength of the alloy is the intrinsic property of the alloy, it is considered as the frictional strength from the lattice. There were no evidence of twins in the microstructure so contributions from the twin is not considered. The grain boundary strength in P2 is 3 times more than P1. Dislocation strength in P1 is zero, where in P2 is 274 MPa. Precipitation strengthening contributions of both P1 and P2 are same. From **Fig. 4.2.9**, it is clear that the strength of the all the alloys is majorly from precipitation strengthening and least contributions from solid solution strengthening. However in the current investigation in AlCoCrCuFeNi HEA, the major contribution is from Hall-Petch strengthening and Taylor hardening mechanisms to the overall strength of the alloy.

4.2.3.2 Rate sensitivity of flow stress

Understanding the loading rate dependence of mechanical properties and the associated deformation characteristics is also vital for structural engineering alloys [35]. Nanoindentation was performed on 750 ºC/15 min sintered sample at various loading rates in the range 1000-8000 µN/s and at a peak load of 8000 µN. It is to be noted that this was performed on the composite region of white and darker phases. The corresponding variations are shown in **Fig. 4.2.10 (a)** and the average hardness value obtained was 8.13 ± 0.15 GPa. Elastic modulus was measured to be 172±10

GPa and this is in agreement with the estimated value of 163 GPa for this alloy using rule of mixtures. Strain rate sensitivity (sensitivity of flow stress/hardness to the loading/strain rate) and activation volume (υ*) are two key parameters to understand the influence of loading/strain rate on the flow stress [35]. Activation volume is the volume over which work is performed in a deformation event and the magnitude of this volume suggests the type of lattice defects involved during deformation. Therefore SRS (m) and υ* of this alloy were calculated, using the nanoindentation data, at room temperature and the results are shown in **Fig. 4.2.10 (b)**.

$$\boldsymbol{m} = \left(\frac{\boldsymbol{\partial\, ln\, \sigma}}{\boldsymbol{\partial\, ln\, \dot{\varepsilon}}}\right)_{\varepsilon,\boldsymbol{T}} \quad \ldots\ldots\ldots\ldots\ldots\ldots\ldots\ldots\ldots\ldots\ldots\ldots\ldots\ldots (Eq\ 4.2.9)$$

$$\boldsymbol{v}^{*} = \sqrt{\boldsymbol{3}}\boldsymbol{kT}\left(\frac{\boldsymbol{\partial \ln \dot{\varepsilon}}}{\boldsymbol{\partial \sigma}}\right) \quad \ldots\ldots\ldots\ldots\ldots\ldots\ldots\ldots\ldots\ldots\ldots\ldots\ldots\ldots (Eq\ 4.2.10)$$

σ is flow stress ($\approx hardness/3$), $\dot{\varepsilon}$ is strain rate, ε is strain, T is temperature, k is the Boltzmann constant. As the loading rate is increased, hardness also has increased (**Fig. 4.2.10 (a)**). An SRS value of 0.0084 and an activation volume of 0.168 nm^3 which is equivalent to 13 b^3 (b= 0.23 nm) were obtained. It is to emphasize that the major two phases (fcc and B2) of this alloy are solid solutions containing all the participating elements.

The detailed loading rate sensitive characteristics of various HEAs are yet to be reported in the scientific literature. Kuznetsov et al [36] have reported an SRS value of 0.6 for AlCoCrCuFeNi HEA which was superplastic when the cast alloy was subjected to multi-directional isothermal hot forging. Wei et al [37] have summarized that fcc elemental metals will show increased SRS whereas bcc elemental metals will show decreased SRS as the grain size is decreased to ultrafine grained/nanocrystalline regime from microns. From the **Fig. 4.2.11**, the SRS value of cold rolled Cu is 0.015. Cu which is equal channel angular pressed (ECAP) and cold rolled shown SRS value of 0.019.

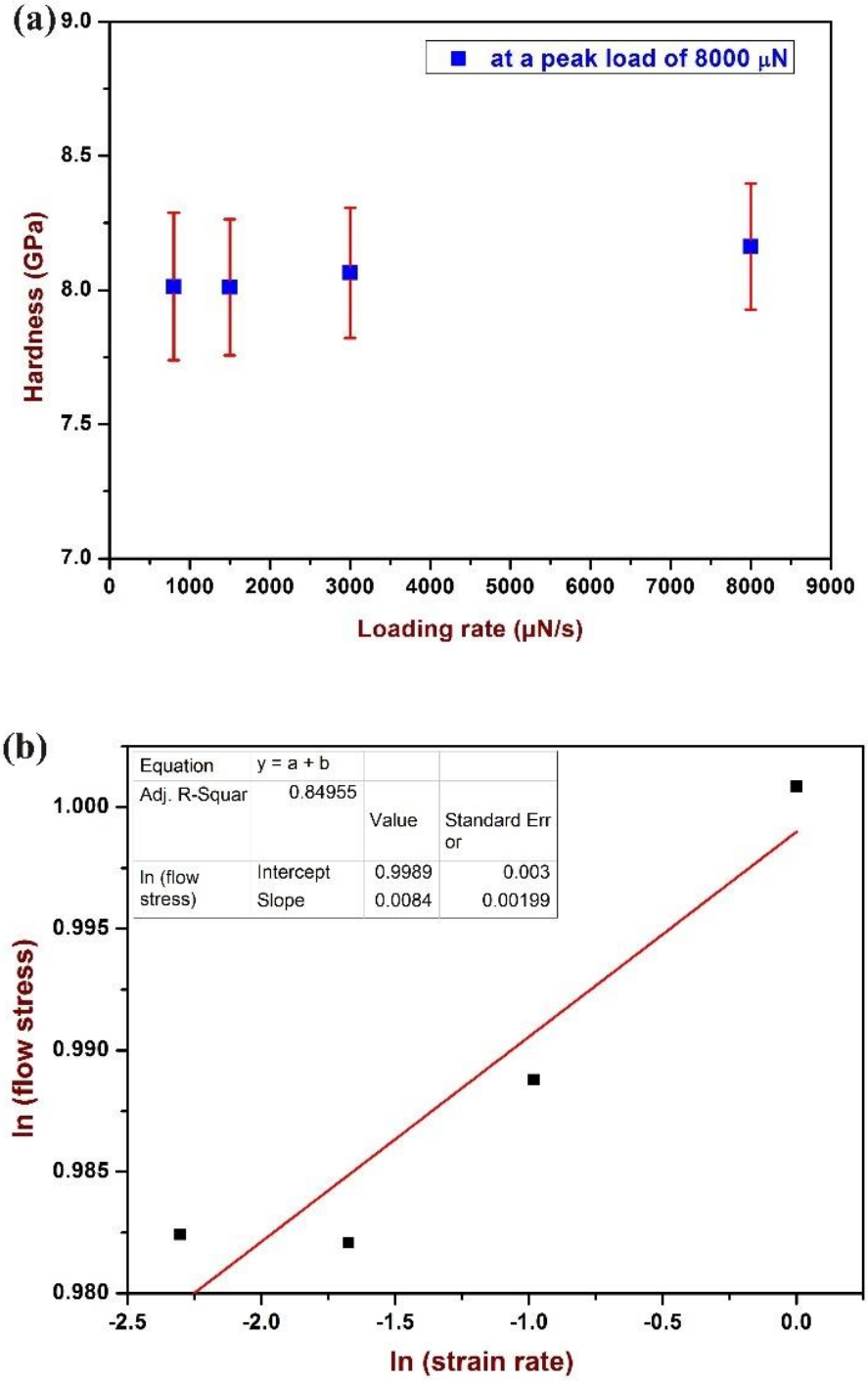

Fig. 4.2.10 (a) Variation of hardness of 750 °C/15 min sintered sample at different loads during nanoindentation, (b) plot showing the strain rate sensitivity.

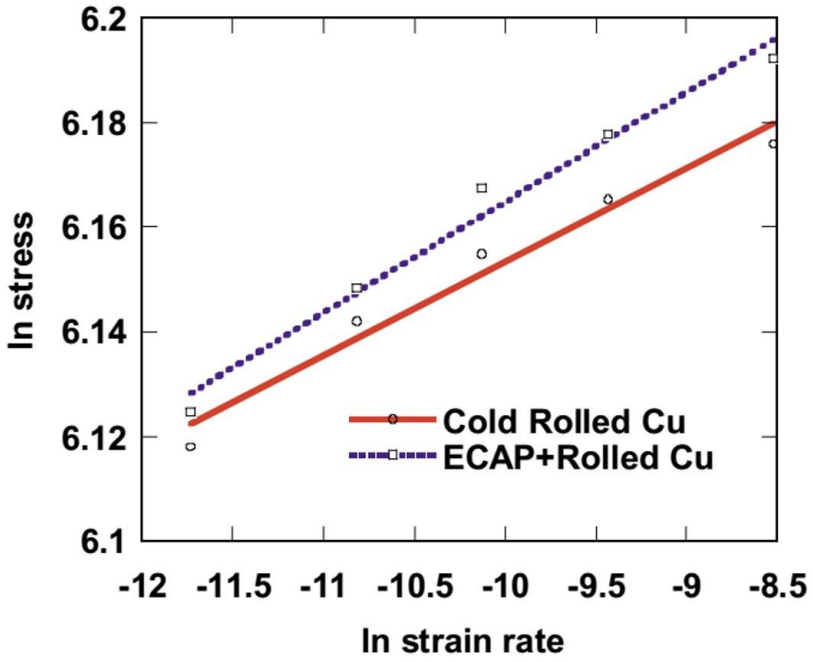

Fig. 4.2.11 The slope of the linear fit lines gives the SRS value. The SRS value of cold rolled Cu is 0.015 and the SRS value of ECAP and cold rolled Cu is 0.019 [37].

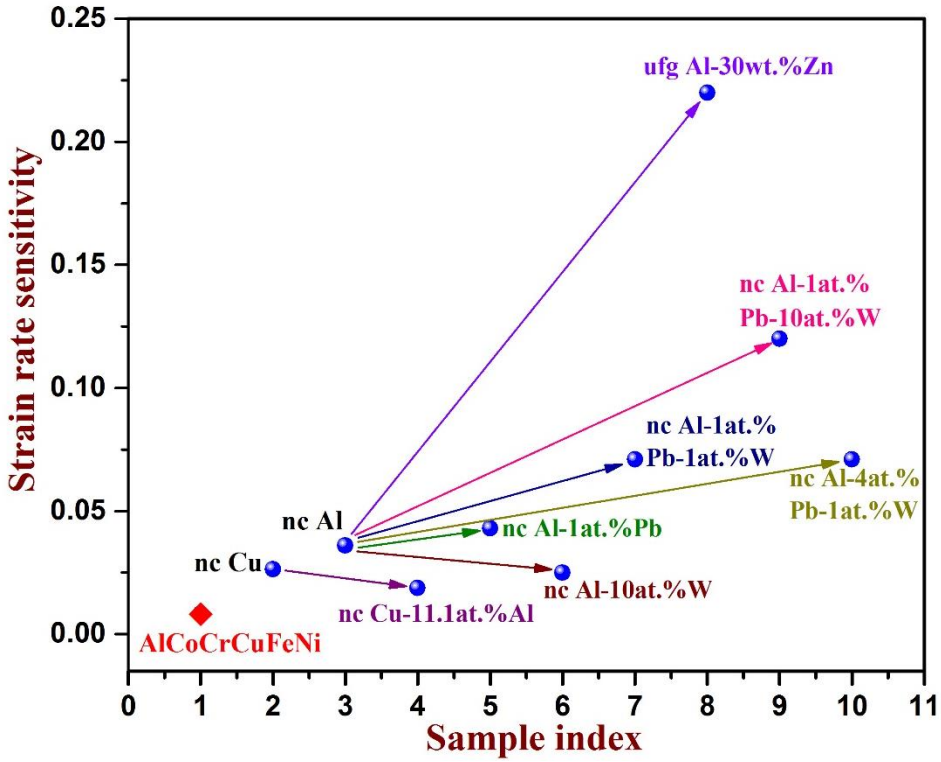

Fig. 4.2.12 The variation of SRS in different nanocrystalline (nc) Al and Cu alloys [40].

Nanocrystalline multi-phase structures have exhibited varied SRS behaviour, influenced by the type of second phase (s) [38, 39]. Varam et al [40-43] explained how the SRS, activation volume and the plastic deformation mechanisms are key factors to dictate the alloy's hardness, ductility and toughness in multiphase alloys. Usually high SRS materials are ductile. The variation of SRS in nanocrystalline Al alloys and in nanocrystalline Cu are shown in **Fig. 4.2.12** plotted by Varam et al [40]. Addition of Pb (fcc) increased SRS of nanocrystalline Al (fcc) [43] whereas addition of W (bcc) has decreased SRS of nanocrystalline Al (fcc) [41]. Addition of both Pb and W elements together in the Al alloy increased SRS. Zn addition to nanocrystalline Al increased the SRS up to 0.22. Al addition in nanocrystalline Cu decreased the SRS. It is essential to note that the alloying additions or the solvent has effect on the SRS and the activation volume which in turn effect the mechanical properties of the alloy. However it would be too early to apply the same analogy to HEAs in general, to the present alloy system of AlCoCrCuFeNi in particular. The major obstacle for this is both the phases (fcc, B2) of current HEA are solid solutions out of which one is ordered (B2). Traditional binary solid solutions have always exhibited a weak strain rate dependence of flow stress [44] and sometimes a negative SRS as well [45]. A low SRS, often a negative one, was also observed in the conventional alloys reinforced with particles of ordered phases [46].

Therefore in agreement with the observations made on conventional solid solutions, ordered alloys, a low SRS of 0.0084 has been measured in this alloy composed of an fcc solid solution and an ordered B2 phase as indicated in **Fig. 4.2.12**. In microcrystalline materials, forest dislocations and their intersections during a deformation process usually result in an activation volume of about 1000 b^3 [47]. However a low activation volume of 13 b^3 seen in this alloy indicate towards the participation of interfaces such as grain boundaries, twin boundaries and inter-phase boundaries (fcc/B2) in the deformation event. Conventionally, SRS and activation volume calculations are

done under the premise that the testing is carried out under constant strain and constant microstructure conditions [47]. However, in the current investigation, nanoindentation was performed at various locations on the sintered sample using a Berkovich indenter, in an effort to capture a reasonably acceptable bulk deformation characteristics. Therefore these (SRS, activation volume) are regarded as apparent values.

Feng et al [48] in their recent work fabricated NbMoTaW HEA thin films varying in thickness using magnetron sputtering. The thickness of the films are varied from 100 to 2000 nm with a single bcc crystal structure. They studied the film thickness effect on hardness, strain rate sensitivity and activation volume as shown in **Fig. 4.2.13**. With the increase in film thickness, the SRS of the material was decreasing from 0.009 to 0.029. Whereas the activation volume increased from 2.1 b^3 to 9 b^3, with the increase of film thickness.

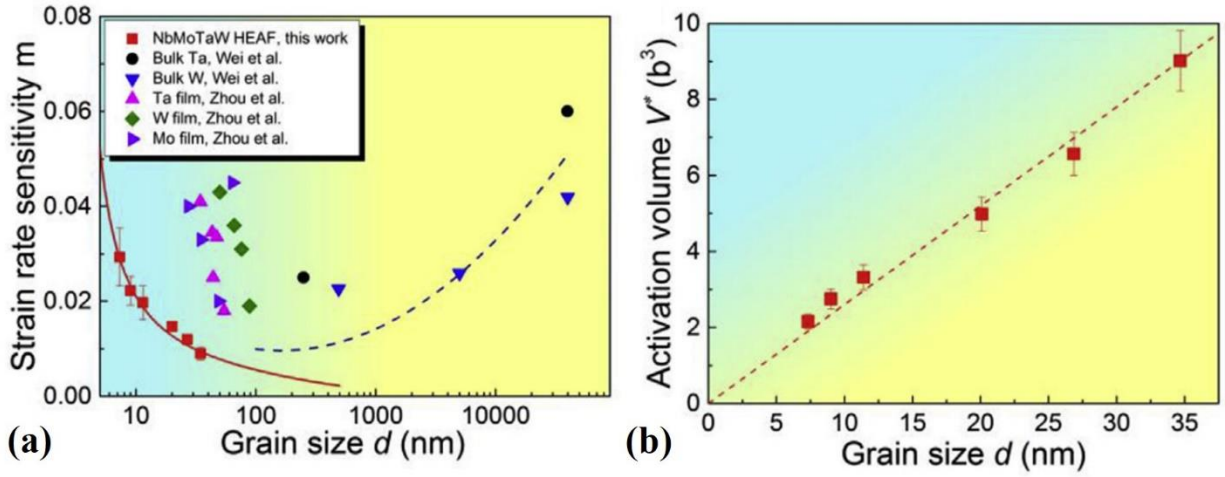

Fig. 4.2.13 Variation of (a) SRS and (b) activation volume with the grain size in NbMoTaW HEA thin films. SRS values of individual elemental thin films from the literature is also presented in (a) [48].

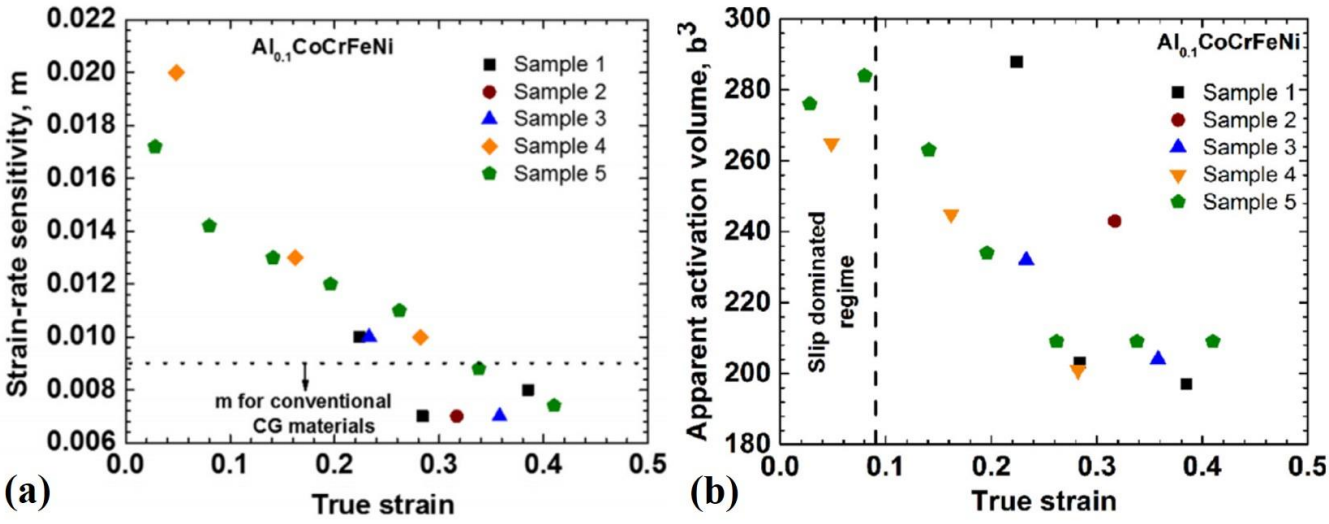

Fig. 4.2.14 Variation of (a) Strain rate sensitivity and (b) activation volume measured from different samples with the true strain [49].

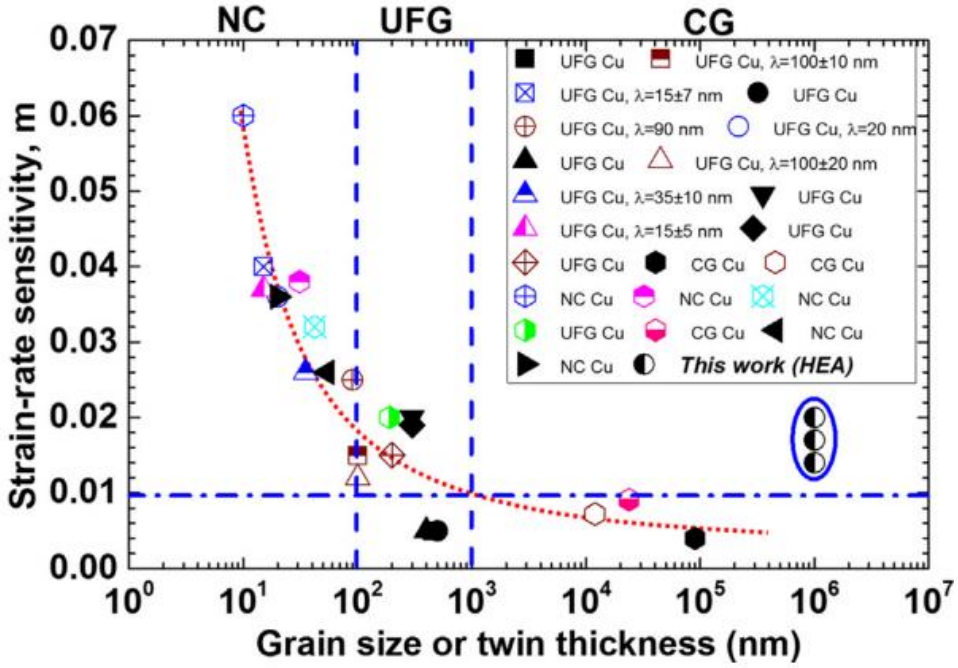

Fig. 4.2.15 The scatter plot of SRS values in nanocrystalline (nc), ultrafine (ufg) and coarse grained (cg) conventional materials [49].

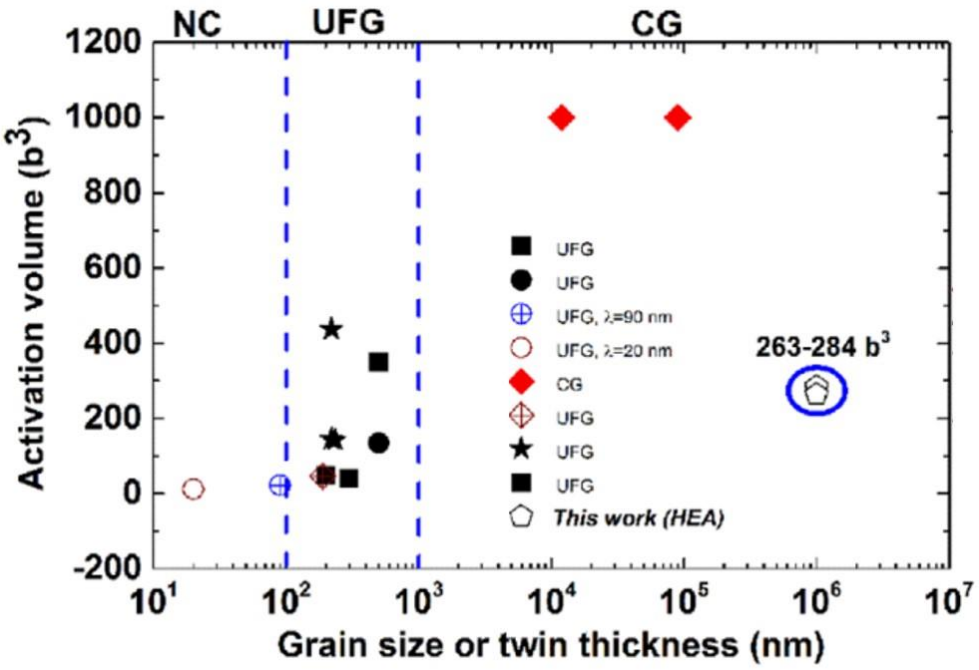

Fig. 4.2.16 The scatter plot of activation volume in nanocrystalline (NC), ultrafine (UFG) and coarse grained (CG) conventional materials [49].

Komarasamy et al [49-51] studied the tensile properties of $Al_{0.1}$CoCrFeNi HEA by performing different strain rate jump tests from 10^{-5} sec^{-1} to 10^{-3} sec^{-1} strain rate. The alloy has a single fcc solid solution with coarse grains. This alloy displayed yield strength of 160 MPa and 44 % elongation. At lower strain rates, SRS value observed is 0.02 – 0.017 and at higher strain rate, SRS value is 0.007 as shown in **Fig. 4.2.14 (a)**. The activation volume reported by them is 288 b^3 for lower strain rates and 197 b^3 for high strain rates as shown in **Fig. 4.2.14 (b)**. The SRS values are compared with conventional alloys with different grains and are plotted in **Fig. 4.2.15**. The SRS value of coarse grains of HEAs are much higher than the SRS values of conventional coarse grain material. However HEAs with nanotwins have equal SRS values as that of coarse grained HEAs. The activation volumes of $Al_{0.1}$CoCrFeNi HEA are compared with conventional alloys with different grains and are plotted in **Fig. 4.2.16**. The activation volume of coarse grains of HEAs are much lower than the activation volume of conventional coarse grain material because of the

presence of forest dislocations. However activation volume of HEAs is equal to ultrafine grained conventional alloys. The distinct nature of SRS and activation volume in HEAs is attributed to the severe lattice distortion in Komarasamy et al [49] work because there are no huge grain boundaries, nano twins to obstruct the dislocation movement. To study the SRS in CoCrFeMnNi HEA, strain rate jump tests were performed by Moon et al [39]. The SRS and activation volume measured at room temperature are higher than at liquid nitrogen temperature as shown in **Fig. 4.2.17**. This is attributed to the twin formation at lower temperatures, where the nanotwin boundaries are acting as obstacles to the dislocation movement. The increased volume fraction of nanotwins with the increase in strain is the reason for the insensitivity of activation volume at lower temperature.

Therefore based on our investigation and the data presented in the literature on strain rate sensitive characteristics of HEAs, it is clear that structural and microstructural features have a great influence on the observed SRS. Some of the systems had a weak dependence of flow stress on strain rate and few other systems have reported to have a strong dependence of flow stress on strain rate. However the activation volume appears to be similar in majority of the systems studied.

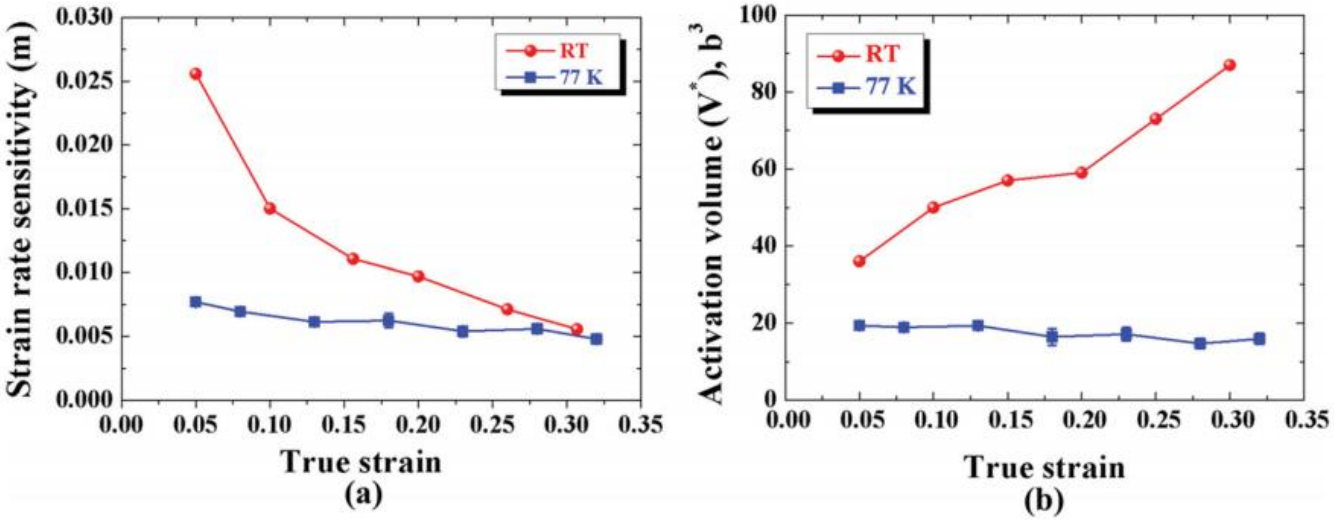

Fig. 4.2.17 Variation of (a) SRS and (b) activation volume at different temperatures [39].

4.2.4 Summary

Vickers microindentation performed on the sample sintered at 750 ºC resulted in a high hardness value of 6.5 GPa reported for this alloy so far. Comprehensive analysis on probable strengthening mechanisms suggest that strain hardening (Taylor hardening) and grain boundary (Hall-Petch) strengthening are the predominant mechanisms in this alloy with contributions from frictional (Peirls-Nabarro) stress, solid solution strengthening and twin boundary strengthening mechanisms. Nanomechanical testing performed at a peak force of 8000 μN resulted in a hardness of 8.13 GPa and an elastic modulus of 172 GPa. A very low strain rate sensitivity of 0.0084 and an activation volume of 13 b^3 were measured using nanoindentation at room temperature. It appears that interfaces such as grain boundaries, twin boundaries, fcc/B2 interphase boundaries could be playing a key role in dictating the deformation kinetics of this HEA.

References

1. Dieter GE: **Mechanical metallurgy**. New York: McGraw-Hill; 1988.
2. Callister WD: **Fundamental of materials science and engineering an interactive e. text.** New York: John Willey & Sons, Inc; 2001.
3. Reed-Hill RE: **Physical metallurgy principles**. New York: D. Van Nostrand company; 2009.
4. Courtney TH: **Mechanical behavior of materials, second ed.** New York: McGraw Hill Education; 2012.
5. Hull D, Bacon DJ: **Introduction to dislocations**. Amsterdam: Butterworth-Heinemann; 2011.
6. Hansen N: **Hall–Petch relation and boundary strengthening**. *Scripta Materialia* 2004, **51**(8):801-806.
7. Varvenne C, Luque A, Curtin WA: **Theory of strengthening in fcc high entropy alloys**. *Acta Materialia* 2016, **118**:164-176.

8. Rupert TJ, Trenkle JC, Schuh CA: **Enhanced solid solution effects on the strength of nanocrystalline alloys**. *Acta Materialia* 2011, **59**(4):1619-1631.
9. Hertzberg RW: **Deforamtion and fracture mechanics of engineering materials**: John wiley & sons, Inc.
10. Oliver WC, Pharr GM: **An improved technique for dertermining hardness and elastic modulus using load and displacement sensing indentation experiments**. *Journal of Materials Research* 1992, **7**:1564-1583.
11. Sriharitha R, Murty BS, Kottada RS: **Alloying, thermal stability and strengthening in spark plasma sintered $Al_xCoCrCuFeNi$ high entropy alloys**. *Journal of Alloys and Compounds* 2014, **583**:419-426.
12. Tung CC, Yeh JW, Shun TT, Chen SK, Huang YS, Chen HC: **On the elemental effect of AlCoCrCuFeNi high-entropy alloy system**. *Materials Letters* 2007, **61**:1-5.
13. Zhang KB, Fu ZY, Zhang JY, Wang WM, Lee SW, Niihara K: **Characterization of nanocrystalline CoCrFeNiTiAl high-entropy solid solution processed by mechanical alloying**. *Journal of Alloys and Compounds* 2010, **495**:33–38.
14. Stefanoiu R, Geanta V, Voiculescu I, Csaki I, Ghiban N: **Researches regarding the influence of chemical composition on the properties of $Al_xCrFeCoNi$ alloys**. *Chemistry magazine* 2014, **7**:819-821.
15. Sheikh S, Shafeie S, Hu Q, Ahlström J, Persson C, Veselý J, Zýka J, Klement U, Guo S: **Alloy design for intrinsically ductile refractory high-entropy alloys**. *Journal of Applied Physics* 2016, **120**(16):164902 164901-164905.
16. Maulik O, Kumar D, Kumar S, Fabijanic DM, Kumar V: **Structural evolution of spark plasma sintered $AlFeCuCrMg_x$ (x = 0, 0.5, 1, 1.7) high entropy alloys**. *Intermetallics* 2016, **77**:46-56.
17. Chen S, Xie X, Chen B, Qiao J, Zhang Y, Ren Y, Dahmen KA, Liaw PK: **Effects of temperature on serrated flows of $Al_{0.5}CoCrCuFeNi$ high-entropy alloy**. *Jom* 2015, **67**(10):2314-2320.
18. He JY, Wang H, Wu Y, Liu XJ, Mao HH, Nieh TG, Lu ZP: **Precipitation behavior and its effects on tensile properties of FeCoNiCr high-entropy alloys**. *Intermetallics* 2016, **79**:41-52.

19. Labusch R: **A statistical theory of solid solution hardening**. *Physica Status Solidi* 1970, **41**:659-669.
20. Labusch R: **Statistical theories of solid solution hardening**. *Acta Metallurgica* 1972, **20**:917-927.
21. Fleischer RL: **Solution hardening**. *Acta Metallurgica* 1961, **9**:996-1000.
22. Fleischer RL: **Substitutional solution hardening**. *Acta Metallurgica* 1963, **11**:203-209.
23. Senkov ON, Scott JM, Senkova SV, Miracle DB, Woodward CF: **Microstructure and room temperature properties of a high-entropy TaNbHfZrTi alloy**. *Journal of Alloys and Compounds* 2011, **509**:6043-6048.
24. Lu L, Schwaiger R, Shan ZW, Dao M, Lu K, Suresh S: **Nano-sized twins induce high rate sensitivity of flow stress in pure copper**. *Acta Materialia* 2005, **53**:2169-2179.
25. Liu B, Wang J, Liu Y, Fang Q, Wu Y, Chen S, Liu CT: **Microstructure and mechanical properties of equimolar FeCoCrNi high entropy alloy prepared via powder extrusion**. *Intermetallics* 2016, **75**:25-30.
26. Rao ZY, Wang X, Zhu J, Chen XH, Wang L, Si JJ, Wu YD, Hui XD: **Affordable FeCrNiMnCu high entropy alloys with excellent comprehensive tensile properties**. *Intermetallics* 2016, **77**:23-33.
27. Senkov ON, Miracle DB: **Effect of the atomic size distribution on glass forming ability of amorphous metallic alloys**. *Materials Research Bulletin* 2001, **36**:2183-2198.
28. Shen YF, Lu L, Lu QH, Jin ZH, Lu K: **Tensile properties of copper with nano-scale twins**. *Scripta Materialia* 2005, **52**(10):989-994.
29. Gludovatz B, Hohenwarter A, Catoor D, Chang EH, George EP, Ritchie RO: **A fracture-resistant high-entropy alloy for cryogenic applications**. *Science* 2014, **345**(6201):1153-1158.
30. Otto F, Dlouhý A, Somsen C, Bei H, Eggeler G, George EP: **The influences of temperature and microstructure on the tensile properties of a CoCrFeMnNi high-entropy alloy**. *Acta Materialia* 2013, **61**(15):5743-5755.
31. Laplanche G, Kostka A, Horst OM, Eggeler G, George EP: **Microstructure evolution and critical stress for twinning in the CrMnFeCoNi high-entropy alloy**. *Acta Materialia* 2016, **118**:152-163.

32. Fu Z, Chen W, Wen H, Zhang D, Chen Z, Zheng B, Zhou Y, Lavernia EJ: **Microstructure and strengthening mechanisms in an fcc structured single-phase nanocrystalline $Co_{25}Ni_{25}Fe_{25}Al_{7.5}Cu_{17.5}$ high-entropy alloy**. *Acta Materialia* 2016, **107**:59-71.
33. Liu WH, Lu ZP, He JY, Luan JH, Wang ZJ, Liu B, Liu Y, Chen MW, Liu CT: **Ductile $CoCrFeNiMo_x$ high entropy alloys strengthened by hard intermetallic phases**. *Acta Materialia* 2016, **116**:332-342.
34. He JY, Wang H, Huang HL, Xu XD, Chen MW, Wu Y, Liu XJ, Nieh TG, An K, Lu ZP: **A precipitation-hardened high-entropy alloy with outstanding tensile properties**. *Acta Materialia* 2016, **102**:187-196.
35. Rajulapati KV, Koch CC: **Nanocrystalline materials: mechanical properties**. *Reference Module in Materials Science and Materials Engineering* 2016, **doi: 10.1016/b978-0-12-803581-8.02570-4**.
36. Kuznetsov AV, Shaisultanov DG, Stepanov ND, Salishchev GA, Senkov ON: **Superplasticity of AlCoCrCuFeNi high entropy alloy**. *Materials Science Forum* 2012, **735**:146-151.
37. Wei Q, Cheng S, Ramesh KT, Ma E: **Effect of nanocrystalline and ultrafine grain sizes on the strain rate sensitivity and activation volume: fcc versus bcc metals**. *Mater Sci Eng A* 2004, **381**:71-79.
38. Ye YF, Liu XD, Wang S, Liu CT, Yang Y: **The general effect of atomic size misfit on glass formation in conventional and high-entropy alloys**. *Intermetallics* 2016, **78**:30-41.
39. Moon J, Hong SI, Bae JW, Jang MJ, Yim D, Kim HS: **On the strain rate-dependent deformation mechanism of CoCrFeMnNi high-entropy alloy at liquid nitrogen temperature**. *Material Research Letters* 2017, **http://dx.doi.org/10.1080/21663831.2017.1323807**.
40. Varam S, Bhanu Sankara Rao K, Rajulapati KV: **On the Strain Rate Sensitive Characteristics of Nanocrystalline Aluminum Alloys**. In *Mechanical and Creep Behavior of Advanced Materials.* The Minerals, Metals & Materials Society; 2017: 133-148 http://dx.doi.org/110.1007/1978-1003-1319-51097-51092_51011.
41. Varam S, Narayana PVSL, Prasad MD, Chakravarty D, Rajulapati KV, Bhanu Sankara Rao K: **Strain rate sensitivity of bulk multi-phase nanocrystalline Al–W-based alloy**. *Philosophical Magazine Letters* 2014, **94**:582-591.

42. Varam S, Prasad MD, Bhanu Sankara Rao K, Rajulapati KV: **Mechanical properties of in situ consolidated nanocrystalline multi-phase Al–Pb–W alloy studied by nanoindentation**. *Philosophical Magazine* 2016, **96**(35):3671-3685.
43. Varam S, Rajulapati KV, Bhanu Sankara Rao K, Scattergood RO, Murty KL, Koch CC: **Loading rate-dependent mechanical properties of bulk two-phase nanocrystalline Al-Pb alloys studied by nanoindentation**. *Metallurgical and Materials Transactions A* 2014, **45**:5249-5258.
44. Zhu ZG, Ma KH, Wang Q, Shek CH: **Compositional dependence of phase formation and mechanical properties in three CoCrFeNi-(Mn/Al/Cu) high entropy alloys**. *Intermetallics* 2016, **79**:1-11.
45. Picu RC: **A mechanism for the negative strain-rate sensitivity of dilute solid solutions**. *Acta Materialia* 2004, **52**:3447-3458.
46. Manzoni A, Singh S, Daoud H, Popp R, Völkl R, Glatzel U, Wanderka N: **On the path to optimizing the Al-Co-Cr-Cu-Fe-Ni-Ti high entropy alloy family for high temperature applications**. *Entropy* 2016, **18**(4):104.
47. Yeh JW, Chen S-K, Gan JY, Lin SJ, Chin T-S, Shun T-T, Tsau C-H, Chang SY: **Formation of Simple Crystal Structures in Cu-Co-Ni-Cr-Al-Fe-Ti-V Alloys with Multiprincipal Metallic Elements**. *Metallurgical and Materials Transactions A* 2004, **35 A**:2533-2536.
48. Feng XB, Zhang JY, Wang YQ, Hou ZQ, Wu K, Liu G, Sun J: **Size effects on the mechanical properties of nanocrystalline NbMoTaW refractory high entropy alloy thin films**. *International Journal of Plasticity* 2017, **http://dx.doi.org/10.1016/j.ijplas.2017.04.013**.
49. Komarasamy M, Kumar N, Mishra RS, Liaw PK: **Anomalies in the deformation mechanism and kinetics of coarse-grained high entropy alloy**. *Materials Science and Engineering: A* 2016, **654**:256-263.
50. Komarasamy M, Kumar N, Tang Z, Mishra RS, Liaw PK: **Effect of Microstructure on the Deformation Mechanism of Friction Stir-Processed Al0.1CoCrFeNi High Entropy Alloy**. *Materials Research Letters* 2014, **3**(1):30-34.
51. Kumar N, Komarasamy M, Nelaturu P, Tang Z, Liaw PK, Mishra RS: **Friction stir processing of a high entropy alloy $Al_{0.1}$CoCrFeNi**. *Jom* 2015, **67**(5):1007-1013.

4.3 A novel AlCuTaVW high entropy alloy synthesized using mechanical alloying and spark plasma sintering: microstructural evolution and mechanical properties

4.3.1 Introduction

High entropy alloys (HEAs) form simple solid structures instead of intermetallic phases because of high configurational entropy, ΔS. By definition a HEA is attributed as a combination of 5 or more elements in equiatomic ratio. The choice of 118 elements in periodic table makes it possible for fabricating/designing innumerable combinations of HEAs in this pattern. Thus far there have been numerous HEA's designed and successfully used for multiple applications adopting this principle. HEA AlCuTaVW is developed espousing this principle and adhering to that fundamental pattern. The objective of choosing this combination is that the high strength elements Ta V and W and the ductile elements Cu, Al would contribute to the formation of the new alloy with greater strength at high temperatures and good ductility. This alloy is synthesized using mechanical alloying and the milled powders are consolidated using spark plasma sintering. Mechanical alloying is a way easy technique to synthesize an alloy. It uses high energy to mill different elements with different densities, sizes and structures to form a homogenous alloy.

The mechanical properties of HEAs are high compared to conventional alloy due to the complex composition and the simple crystal structures of the HEAs. These HEAs have high strength at high temperatures. Han et al [1] fabricated NbNiTiCoZr and NbNiTiCoZrHf refractory HEA by casting methods. The former alloy has two bcc phases and the later alloy has one bcc, one fcc and NbNi intermetallic phases. The hardness of NbNiTiCoZr is 5.2 GPa and yield strength is 2.3 GPa. The hardness of NbNiTiCoZrHf is 5 GPa and yield strength is 1.5 GPa. The former alloy having high

hardness and strength values is attributed to bcc phase formation and in the latter's case the fcc phase softened the material. He et al [2] varied the composition of Al from 0 to 20 atomic percentage in FeCoNiCrMn HEA and studied its effect on structure and mechanical properties. They noticed that with increase in Al content, there is a phase transformation from fcc to bcc. They showed that the hardness and the yield strength increased with increased Al content. The effect of Cu on any HEA was not studied in specific but Tung et al [3] studied the elemental effect on AlCoCrCuFeNi HEA by reducing each element to 0.5 % concentration. They found that Cu tends to segregate to the interdendritic regions and is the fcc stabilizer. Wang et al [4] stated that the Cu forms intermetallic phases. Such segregation decreases the mechanical properties of the alloy. Jiang et al [5] varied the Ta composition in $CoFeNi_2W_{0.5}Ta_x$ HEA and studied its effect on microstructure and mechanical properties. These alloys were casted in water cooled copper crucible resulting a single fcc phase without Ta. On increasing the concentration of Ta, there is an increase in precipitation of the Co_2Ta type laves phases. Because of the larger atomic size, the lattice parameter increased. They reported that this increase in lattice parameter is the indication for higher lattice distortion. With increase in Ta concentration from 0 to 0.6 atomic %, the Vickers hardness value increased from 1.7 to 6.3 GPa and the compressive yield strength increased from 0.3 to 1.1 GPa compromising on the ductility. This increase in mechanical properties is attributed to the presence of laves phase and high solid solution strengthening. Xia et al [6] studied $Al_xCrFeNiV$ HEA. They found that in $Al_{0.5}CrFeNiV$ HEA, an unknown nano phase rich in Cr and V is precipitated. This effect increased the yield strength to 2 GPa and decreased micro hardness when compared to the hardness of $Al_{0.3}CrFeNiV$. They claimed that decrement in hardness is due to the brittle nature of Cr and V rich nano precipitates. Senkov et al [7] investigated the changes made by addition of V in WNbMoTa HEA. They saw that the there is no new phase formation

but it has a tendency to form a new component with any element. They also suggest that the V being the smallest atomic radius element may have induced lattice strain and enhance the solid solution strengthening, thereby increasing the Vickers hardness. Li et al [8] also investigated effect of V on AlCoCrCuFeNi HEA. They found that V has changed the morphology of dendrite from plate like structure to ellipsoidal particles, thereby increased the overall strength of the alloy. The effect of W element on the microstructure of AlCoCrCuFeNi HEA has been studied by Tariq et al [9] by mechanical alloying for 60 h. The addition of W element to AlCoCrCuFeNi HEA transformed the amorphous phase to a recrystallized bcc phase, which is W based. It also shifted the melting point to the higher level because of increased lattice strain and the grain boundary area. The present chapter involves the synthesis of the AlCuTaVW HEA in equal atomic ratio by mechanical alloying (MA) for 25h and followed by consolidation using spark plasma sintering (SPS) at different temperatures. Al, Cu, Ta, V and W elemental powders are weighed in equiatomic ratios and are loaded in hardened steel vials with 5:1 ball to powder ratio. 0.5 weight% stearic acid is added to avoid cold welding with the vials. The sample at regular interval of 5 h. The 25 h milled sample was sintering at 875, 1050 and 1250 ºC temperatures for 15 minutes under uniaxial load of 80 MPa. The phase evolution of this novel AlCuTaVW HEA is investigated using XRD, SEM and TEM.

4.3.2 Results and Discussion

4.3.2.1 XRD analysis of milled AlCuTaVW powder

The phase evolution of AlCuTaVW alloy after 25 h of milling was observed using XRD. The X-ray diffractograms obtained from mechanical alloyed AlCuTaVW HEA nanocrystalline powder are shown in **Fig. 4.3.1**. The XRD pattern of 0 h milling of the alloy blend shows all the elemental peaks. After 5 h of milling, the disappearance of few elemental peaks depicts beginning of the

alloying process. 100% intensity peaks of Al and Cu were evident in 0 h pattern but disappeared after 5 h milling indicating the beginning of alloying in this HEA system. This primary dissolution is because of the low melting points of Al and Cu compared to other elements in the alloy. The 100% peak of W element remained stable until 25 h of milling. However a steep increase of the W peak intensity at 40.4º is observed at 5 h milling and there is a steady decrease in the intensity thereafter. Ta and V peaks were visible up to 10 h of milling. 25 h of milling resulted a bcc phase with a lattice parameter of 3.17 Å. The lattice parameter of the newly formed phase matches with that of W (3.16 Å), where W seemingly as host lattice. With the milling time, the increase in peak broadening is attributed to the nanocrystalline powder formation.

The crystallite size measured using Scherrer formula is 7 ± 1 nm after 25h milling. The plot for crystallite size variation with the milling duration is given in **Fig. 4.3.2 (a)**. It is evident that there is gradual decrement in crystallite size with milling time. The lattice strain is calculated using Stokes-Wilson formula and the variation with the milling time is shown in **Fig. 4.3.2 (b)**. The lattice strain increased until 10 h of milling and decreased thereafter. This increase in earlier stage is attributed to the defect incorporation into the lattice. The ball milling introduces defects like vacancies, dislocations, stacking faults into the lattice. On further increase in milling duration, these defects annihilate to reduce overall free energy of the alloy thereby the lattice strain decreases to a saturation level.

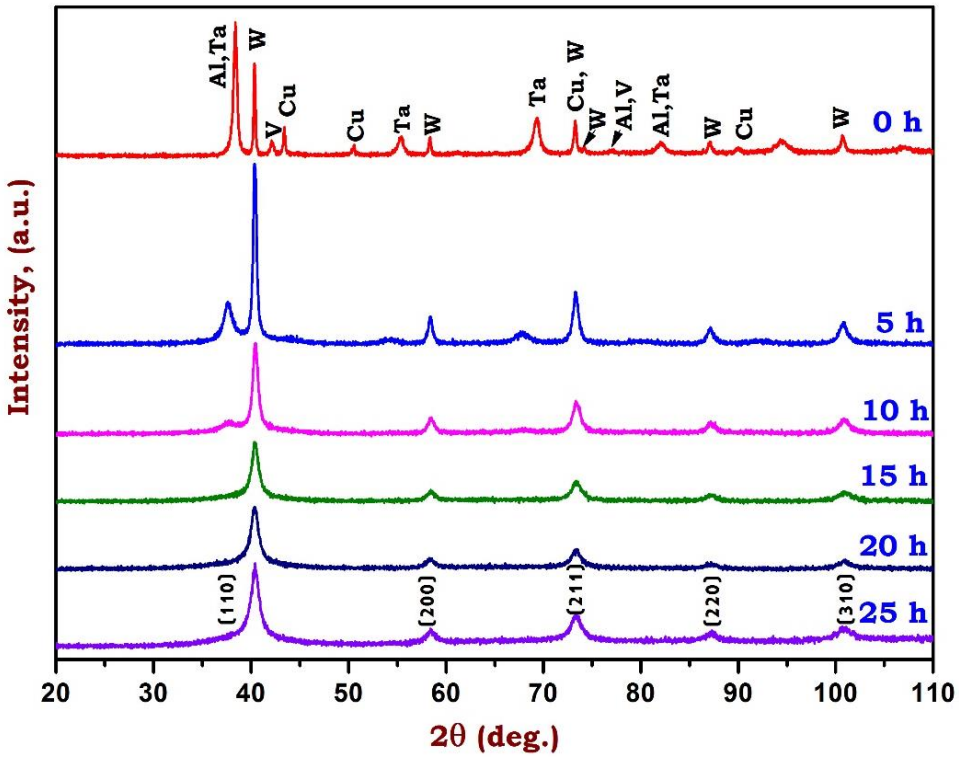

Fig. 4.3.1 XRD patterns of AlCuTaVW HEA at different milling time.

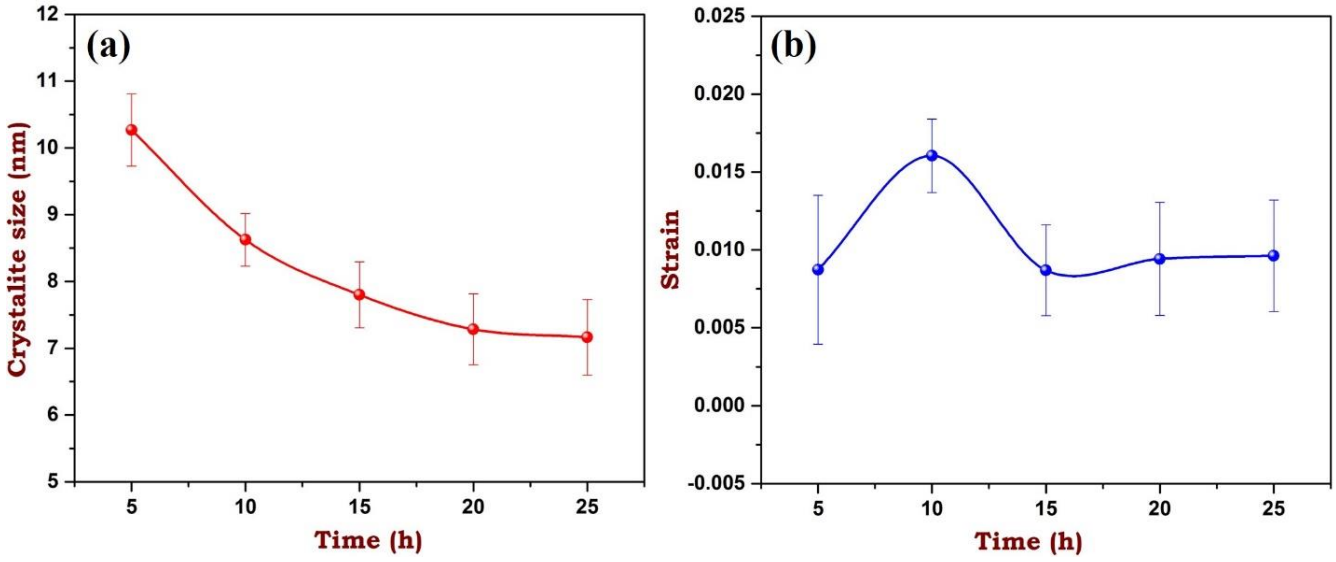

Fig. 4.3.2 Variation of (a) crystallite size and (b) lattice strain with milling duration of AlCuTaVW HEA.

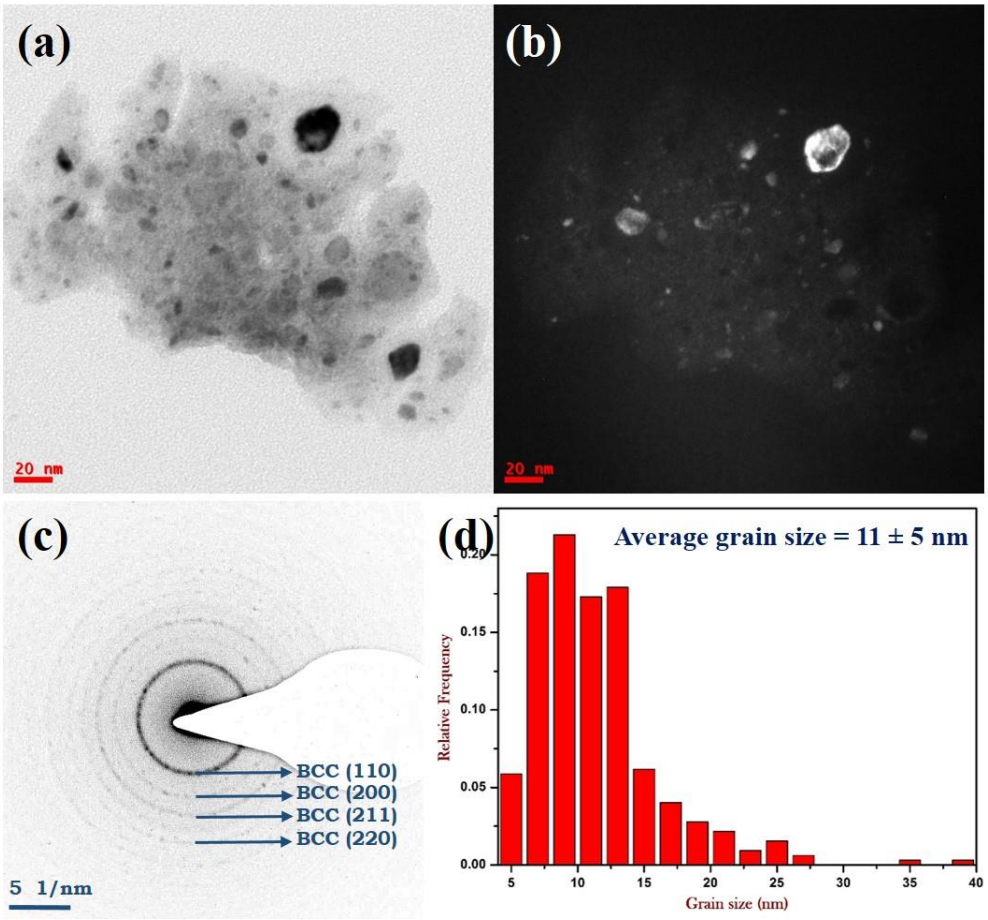

Fig. 4.3.3 TEM image of AlCuTaVW 25 h milled HEA (a) bright field image, (b) corresponding dark field image, (c) diffraction pattern indexed and (d) grain size distribution plot.

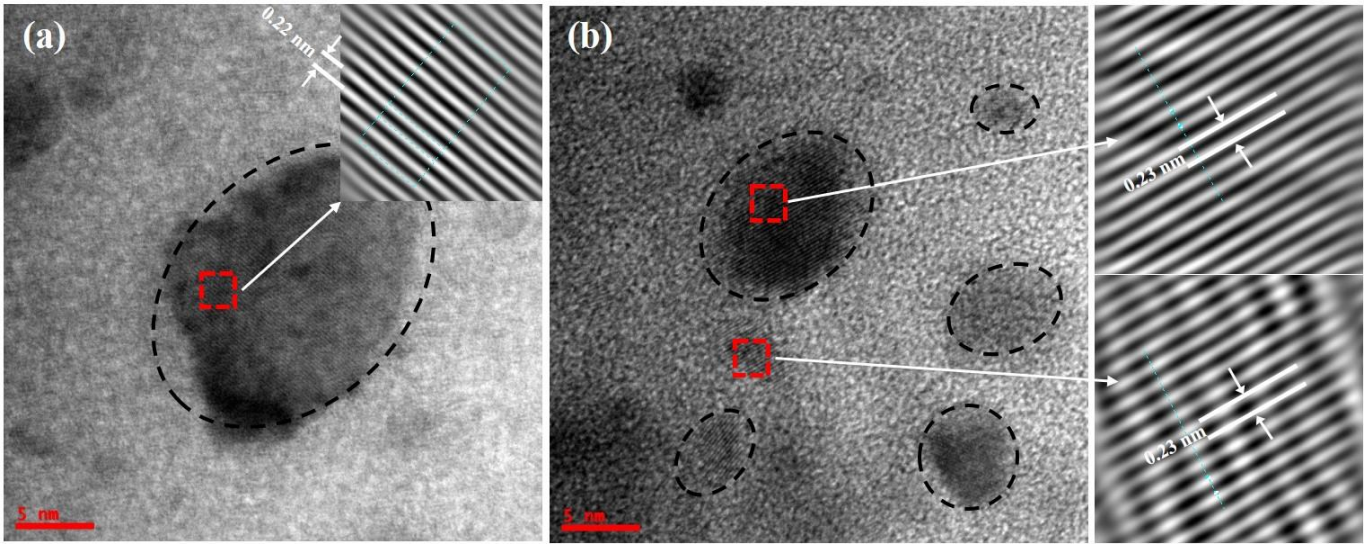

Fig. 4.3.4 HRTEM images of AlCuTaVW HEA 25 milled powders. Insets are IFFT images showing the atomic plains and the d spacings.

4.3.2.2 Microstructural analysis of milled AlCuTaVW powder

The bright field image and corresponding dark field image of TEM is shown in **Fig. 4.3.3 (a,b)**. The indexed diffraction pattern (**Fig. 4.3.3 (c)**) shows that the alloy has a bcc phase, which is consistent with XRD result. The average grain size measured from 324 grains is 11 ± 5 nm and the histogram of grain size distribution is shown in **Fig. 4.3.3 (d)**. The HRTEM image of the alloy is shown in **Fig. 4.3.4**. There are different grain oriented in different directions. The d spacing measured from the inverse fast Fourier transform (IFFT) image (inset image in **Fig. 4.3.4 (a)**) is 0.22 nm. This value corresponds to the W element d-spacing value. Another HRTEM image (**Fig. 4.3.4 (b)**) shows d-spacing value of 0.23 nm. The value of 0.23 nm corresponds to both Al and Ta elements d-spacing. It is quite possible that these planes (Al/Ta) overlap.

4.3.2.3 XRD analysis of sintered AlCuTaVW HEA

Spark plasma sintering (SPS) process is the advanced sintering technique, where sintering takes place in a very short time with minimum grain growth because of the high electric field and rapid rate of heating. The 25 h milled powder has been sintered at 875, 1050 and 1250 ºC temperatures for 15 mins holding time under uniaxial pressure of 80 MPa using SPS technique. Archimedes method is used to measure the density of the sintered samples. The theoretical density, ρ_{mix} is calculated using rule of mixtures formula (Equation. 4.3.1),

$$Density, \rho_{mix} = \frac{\sum_{i=1}^{n} C_i W_i}{\sum_{i=1}^{n} \frac{C_i W_i}{\rho_i}} \ldots\ldots\ldots\ldots\ldots\ldots\ldots\ldots\ldots\ldots\ldots\ldots\ldots\ldots (Eq\ 4.3.1)$$

where n is total number of elements, C is the molar composition, W is the atomic weight and ρ_i is the density of the i^{th} element. The theoretical density of AlCuTaVW HEA calculated from Equation 4.3.1 is 11.04 g/cc. The absolute density values measured for samples sintered at 875, 1050 and 1250 ºC are 8.7, 11.02 and 11.5 g/cc respectively. It is evident that 875 ºC or 0.5 T_m

sintering temperature is insufficient to consolidate the samples completely because absolute density attained is very low compared to theoretical density. Whereas sample sintered at 1050 ºC or 0.58 T_m attained 11.02 g/cc density and at 1250 ºC or 0.66 T_m sintering temperature has 11.5 g/cc absolute density. These two densities are closer to the theoretical density. At 1250 ºC temperature, a small fragment of the alloy melted and dribbled down from the graphite die as tiny droplets while sintering. However Sriharitha et al [10] and Maulik et al [11] suggested that 0.7 T_m is best suited temperature for sintering.

The X-ray diffractograms for all the samples sintered at different temperatures are given in **Fig. 4.3.5**. For comparison the 25 h milled data is incorporated in the **Fig. 4.3.5**. In the sample sintered at 875 ºC, the parent bcc phase formed in the milling state is predominant and another new bcc phase is formed. There are many peaks in this pattern which could not be indexed. Attempts have been made to check whether they are a new fcc/bcc phases or intermetallic phases. But the d-spacing of the peaks were not matching with any particular phase available in the literature. These peak reflections could be from the intermediate phases which were transforming to another new phase. Sintering at 1050 ºC temperature resulted in evolution of new equilibrium phases. Two fcc phases and an ordered B2 phase along with the parent bcc phase is evident from the **Fig. 4.3.5** and **Fig. 4.3.6**. Similarly the 1250 ºC sintered alloy resulted two fcc phases and an ordered B2 phase. These phases display higher peak intensity than the phases in 1050 ºC sample. However the parent bcc phase which was formed during mechanical alloying slightly faded away. The peak intensity of bcc phase (110) plane visible at 40.43º gradually decreased with the increase in sintering temperature and the peak intensity of B2 phase (100) plane seen at 26.61º is increasing with the sintering temperature. This is attributed to the phase transformation from bcc phase to a stable ordered B2 phase. Clear deconvolution profiles for both 1050 ºC sintered alloy and 1250 ºC

sintered alloy depicting the presence of different structural phase transitions are shown in **Fig. 4.3.6** and **Fig. 4.3.7** respectively. The peak reflections were overlapping as the d spacings of different phases are very close to each other. Hence the peaks deconvoluted into different phase components.

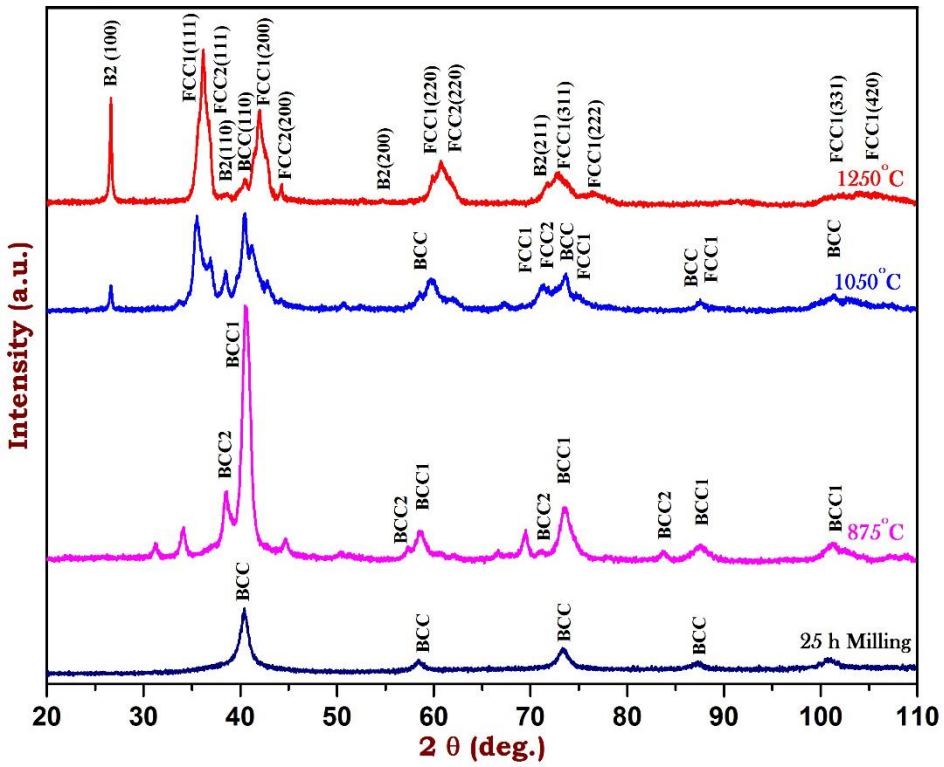

Fig. 4.3.5 X-ray diffractograms of AlCuTaVW sintered at different sintering temperatures.

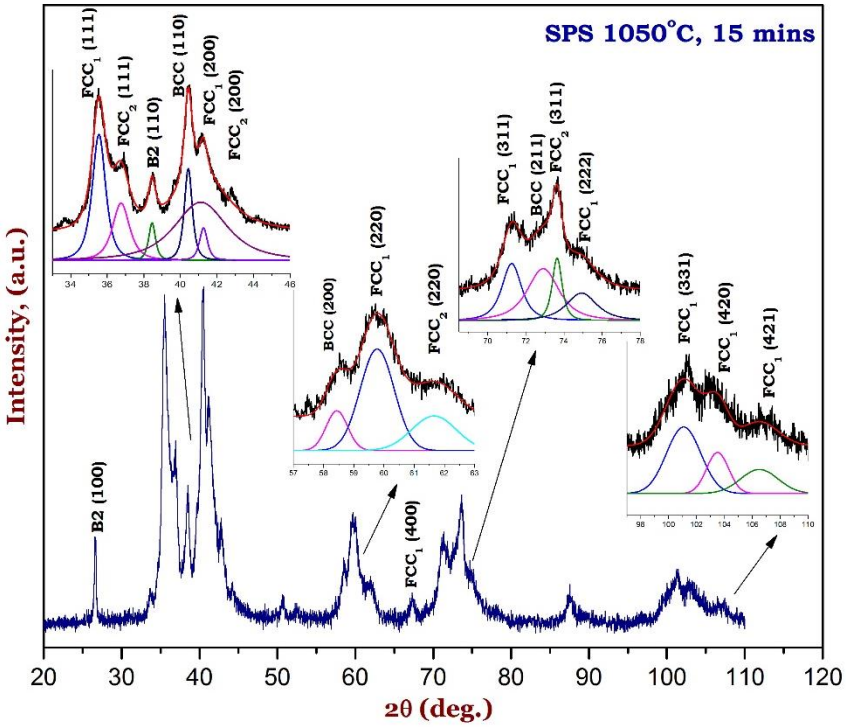

Fig. 4.3.6 X-ray diffractograms of AlCuTaVW HEA sintered at 1050 ºC showing a clear de-convolution of with diffracted peaks.

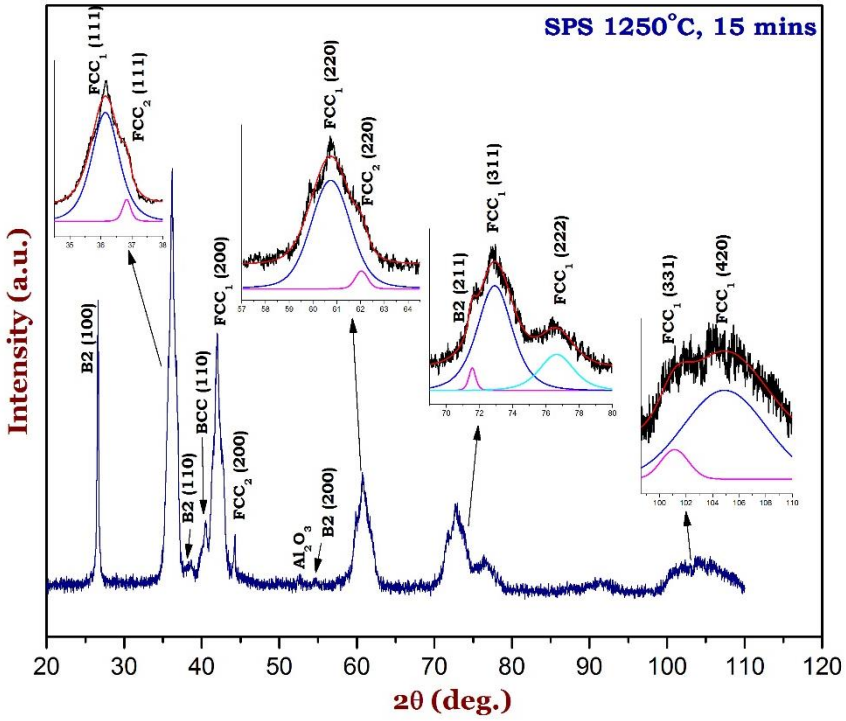

Fig. 4.3.7 X-ray diffractograms of AlCuTaVW HEA sintered at 1250 ºC showing a clear de-convolution of with diffracted peaks.

4.3.2.4 Microstructural analysis of sintered AlCuTaVW HEA

Microstructural evolution of the samples sintered at different temperatures has been investigated using scanning electron microscopy (SEM) and the findings are shown in **Fig. 4.3.8**. Qualitative elemental distribution maps of the samples are obtained using electron dispersive spectroscopy (EDS) which is coupled with SEM and the maps are shown in **Fig. 4.3.9** and **Fig. 4.3.10**.

SEM micrograph of samples sintered at 875 ºC (**Fig. 4.3.8 (a,b)**) reveal pores and voids along the particle boundaries resulting a poor compact. This could be the reason for lower absolute density of 8.7 g/cc measured at 875 ºC temperature. Micrograph depicts that it is the intermediate stage where the milled powders begin to fuse as particles. However a sound compaction could not be achieved possibly due to the insufficient sintering temperature or sintering holding duration. It is observed in **Fig. 4.3.8 (c,d)** that the samples sintered at 1050 ºC have a continuous white phase and a discontinuous dark phase homogenously distributed in the white phase. Samples sintered at 1250 ºC contains similar microstructural white and dark phases distribution as shown in **Fig. 4.3.8 (e,f)** with a slight grain growth. The EDS analysis in **Table 4.3.1** shows that in both the samples sintered at afore mentioned temperatures the dark phase is rich in Al and the continuous white phase contains all elements in almost equiatomic ratio except Al deficiency. The elemental mapping of dark phase at both the temperatures shown in **Fig. 4.3.9** and **Fig. 4.3.10** reveal that the dark phase is rich in Al. The grey color phase visible in **Fig. 4.3.8 (f)** has similar morphology as dark phase. The back scatter electron (BSE) micrograph of 1250 ºC sintered sample in **Fig. 4.3.11 (b)** shows different phases and it is noted that both grey phase and dark phase have similar morphology. The variation could be because of mass-thickness contrast.

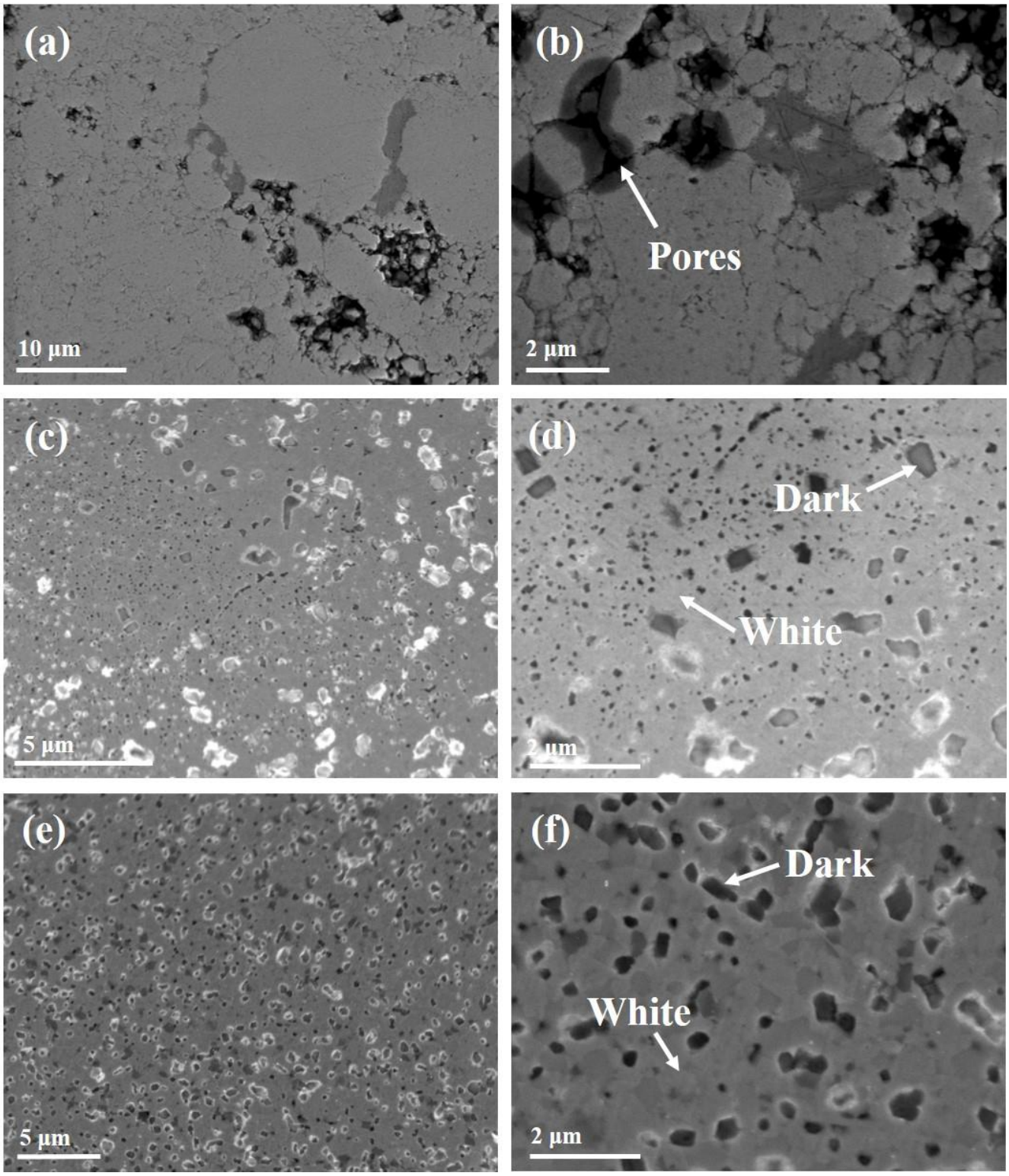

Fig. 4.3.8 SEM images of AlCuTaVW HEA sintered at (a,b) 875 ºC, (c.d) 1050 ºC, (e,f) 1250 ºC depicting different phases formed during sintering.

Table 4.3.1 Elemental distribution of dark and white phases in atomic %.

Sintering temperature	**Elements / Phases**	**Al**	**V**	**Cu**	**Ta**	**W**
Nominal composition		20	20	20	20	20
1050 ºC	Dark phase	50.45	14.41	8.64	14.78	11.73
	White phase	10.21	21.69	20.52	25.54	22.05
1250 ºC	Dark phase	53.31	11.76	3.92	16.93	14.08
	White phase	8.88	19.30	7.50	37.84	26.48
	Grey phase	8.13	24.73	5.55	36.17	25.42

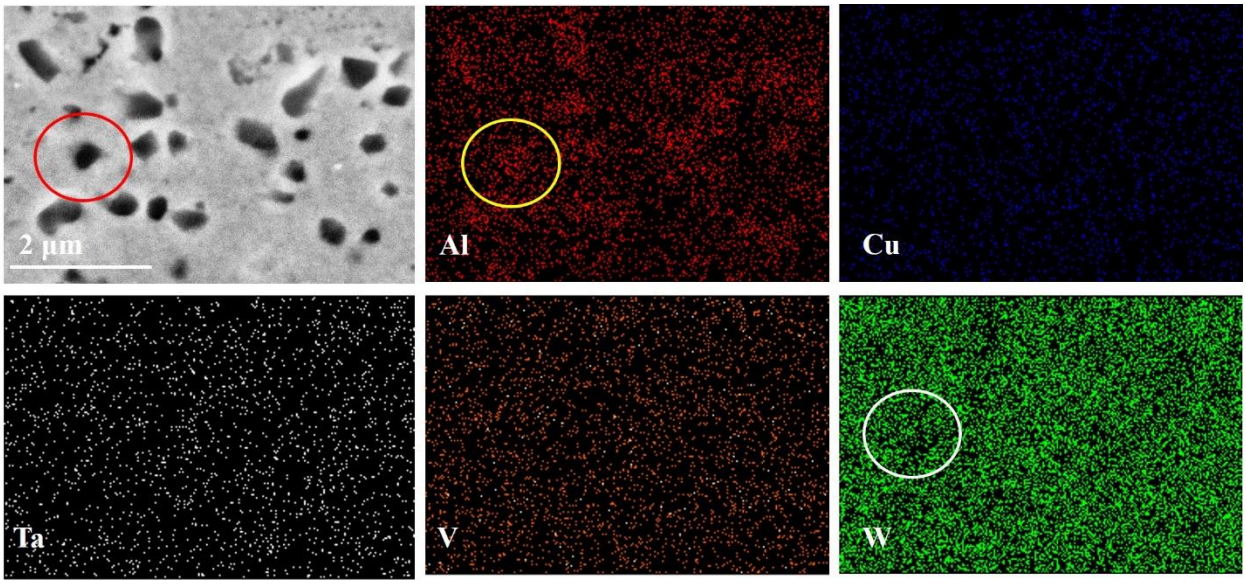

Fig. 4.3.9 EDS mapping of AlCuTaVW HEA sintered at 1050 ºC showing the dark phase rich in Al and the white phase is deficient of Al.

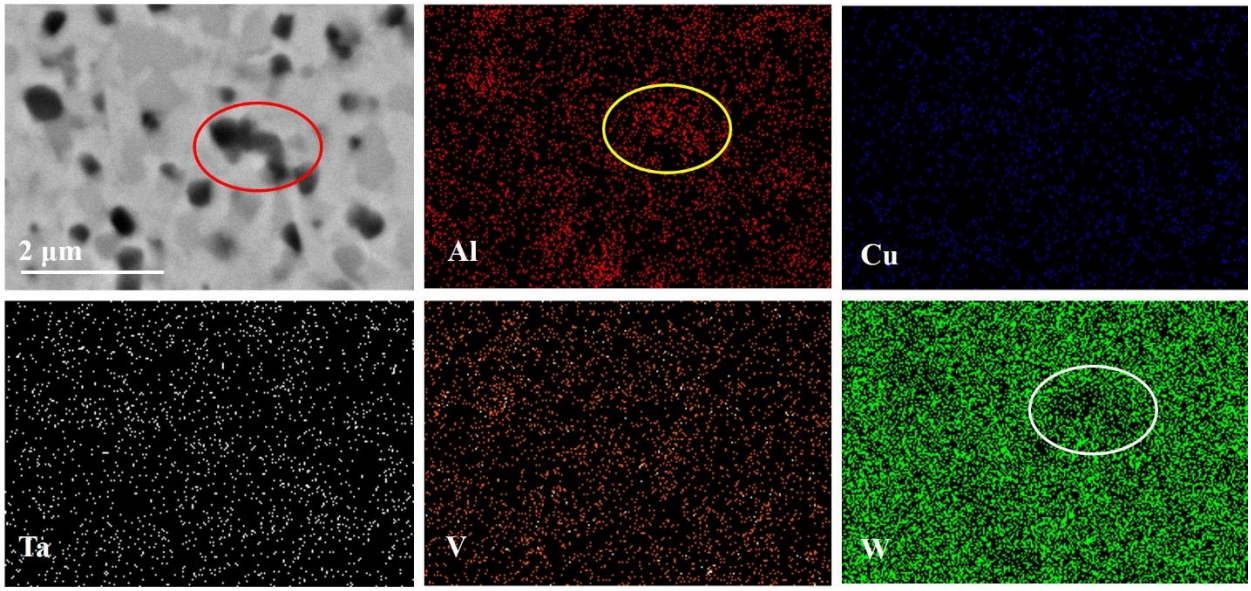

Fig. 4.3.10 EDS mapping of AlCuTaVW HEA sintered at 1250 ºC showing the dark phase rich in Al and the white phase is deficient of Al.

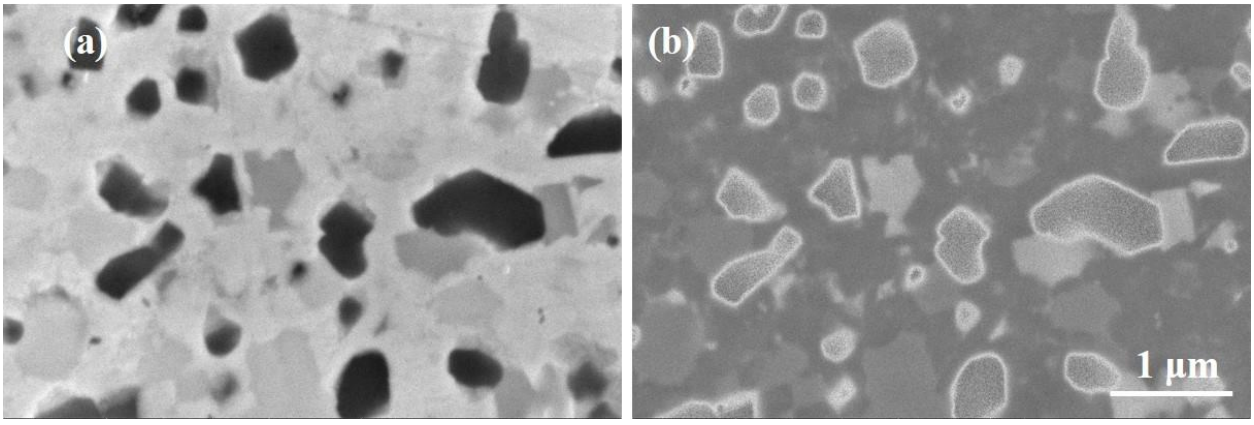

Fig. 4.3.11 (a) SEM image and (b) corresponding back scattering electron image of AlCuTaVW HEA sintered at 1250 ºC.

Senkov et al [7] fabricated MoNbTaW and MoNbTaVW using melting and casting process where both the alloys resulted in single bcc phase with lattice parameters of 3.21 and 3.18 Å respectively. This group explained that since all elements in these alloys have same crystal structure, valence number, high entropy of mixing and near atomic radii, single bcc phase formation is rightly anticipated. Microstructure of the alloys have respective values of 200 µm and 80 µm sized grains with dendritic and interdendritic regions within the grain. The quantitative analysis shows that the

W is preferably segregated to dendritic regions and Mo, V and Nb moved to interdendritic regions in both the alloys. The micro Vickers hardness values of NbMoTaW and NbMoTaVW HEA are 4.5 GPa and 5.2 GPa respectively. They reasoned that the high hardness in NbMoTaVW is because of small grain size and also Vanadium in the alloy as it enhances the solid solution hardening.

The same compositions were subjected to annealing treatment till 1400 ºC [12] and identified that the bcc phase is stable and is disordered. At room temperature the compressive yield strength of NbMoTaW is 1.05 GPa, and the ultimate strength is 1.2 GPa. The strength of the material increased up to 600 ºC and then decreased on further increase in temperature. The fracture analysis showed that the fracture is along the grain boundary and at the void interface.

Feng et al [13] in their recent work fabricated NbMoTaW HEA thin films with varied thickness using magnetron sputtering. The thickness of the films was varied from 100 to 2000 nm with a single bcc crystal structure. They studied the film thickness effect on hardness, strain rate sensitivity and activation volume. With increase in film thickness, the morphology changed from spherical to needle like structures and the grain size increased from 7 nm to 35 nm. The less thick (250 nm) films displayed high hardness of about 16 GPa because of less penetration depth. However the 2000 nm thick film showed 10.6 GPa hardness. In another work of Senkov et al [14] on $CrMo_{0.5}NbTa_{0.5}TiZr$ refractory HEA produced by melting and casting route, followed by hot isostatic pressing resulted two bcc phases and one fcc phase. They observed a selective segregation of elements in all the phases. Bcc 1 phase is rich in Nb, Mo and Ta, bcc 2 is rich in Zr and Ti, and fcc is Cr rich laves phase because of wide atomic radii difference. The Vickers hardness measured is 5.2 GPa and the compressive yield strength at room temperature is 1.5 GPa.

Table 4.3.2 Different HEA compositions and their mechanical properties from the literature.

Alloy	**Processing route**	**Phases**	**Hardness, GPa**	**Compressive yield strength, GPa†**	**Ref**
$Al_{23}Co_{15}Cr_{23}Cu_8Fe_{15}Ni_{15}$	Casting	bcc, B2	5.34	1.26	[15]
MoNbTaW	Casting	bcc	4.5	1.05	[7, 12]
MoNbTaVW	Casting	bcc	5.2	1.2	[7, 12]
$CrMo_{0.5}NbTa_{0.5}TiZr$	Casting	bcc 1,bcc 2, fcc	5.2	1.5	[14]
HfNbTaTiZr	Casting	Bcc	3.8	1	[16]
$Ti_{35}Zr_{27.5}Hf_{27.5}Ta_5Nb_5$	Casting	Orthorhombic	2.4	-	[17]
$AlMo_{0.5}NbTa_{0.5}TiZr$	Casting	bcc, B2	5.8	2	[18]
NbTiVZr	Casting	Bcc	3.29	1.1	[19, 20]
$NbTiV_2Zr$	Casting	bcc1, bcc2, bcc3	2.99	0.91	[19, 20]

CrNbTiZr	Casting	bcc, ordered fcc (Laves C15)	4.10	1.3	[19, 20]
CrNbTiVZr	Casting	bcc, ordered fcc (Laves C15)	4.72	1.3	[19, 20]
WNbMoTaV	MA-SPS	bcc 1, bcc 2	10.8	-	[21]
$AlCoCrFeNiTi_{0.5}$	MA-SPS	fcc, bcc, σ phase, TiC nanoparticles	0.7	-	[22]
AlFeCuCr	MA-SPS	bcc1, bcc 2	6.4	-	[11, 23]
$AlFeCuCrMg_{0.5}$	MA-SPS	bcc, ordered AlFe,Cu_2Mg, σ	8.4	-	[11, 23]
AlFeCuCrMg	MA-SPS	bcc, ordered AlFe	7.3	-	[11, 23]

$AlFeCuCrMg_{1.7}$	MA-SPS	bcc, ordered AlFe,Cu_2Mg, Mg_2Cu, σ, Mg	5.2	-	[11, 23]
CoCrFeMnNi	Gas atomization - SPS	fcc	-	0.7	[24]
CoCrFeMnNi	MA-SPS	fcc	6.3	1.9	[25]
AlCoCrFeNiTi	MA-SPS	bcc, fcc	4.2	-	[26]
AlCoCrFeNi	Casting	bcc	-	1.2	[27]
CrCuFeMnMo0.5Ti	MA-Sintering	bcc	4.7	-	[28]
CoCrFeMnNi	Gas atomization - MA - SPS	fcc	5.1	-	[29]

† All compressive yield strength values reported are measured at room temperature.

Senkov et al [18] fabricated $AlMo_{0.5}NbTa_{0.5}TiZr$ using casting methods which formed a bcc phase. The alloy on hot isostatic pressing and annealing treatments transformed bcc phase into a disordered bcc and an ordered B2 phase. They named this alloy as "refractory HEA superalloy" because of the disordered bcc which has a cuboid structure rich in Mo, Nb ,Ta and also precipitation of the ordered B2 solid solution phase rich in Al, Ti and Zr . They assumed that the ordering is because of the interaction of Al atoms with those of the Ti and Zr atoms. The AlMoNbTaTiZr demonstrated a very high Vickers micro hardness of 5.8 GPa, compression yield strength of 2 GPa, fracture strength of 2.3 GPa and a compression ductility of 10%.

Senkov et al [19] synthesized NbTiVZr, $NbTiV_2Zr$, CrNbTiZr and CrNbTiVZr, refractory HEAs addressing the demand for low density refractory metals for aerospace industry. The alloys had densities as low as 6.52 ± 0.01, 6.34 ± 0.01, 6.67 ± 0.01 and 6.57 ± 0.01 g/cc respectively. The hardness and compressive yield strength [20] of the alloys are given in **Table 4.3.2**. NbTiVZr and $NbTiV_2Zr$ show good ductility at all tested temperatures. The CrNbTiZr and CrNbTiVZr showed brittle failure up to 600 ºC due to laves phase particles containing Cr element. In this study they made an attempt to compare the properties with the Ni-base superalloys and found that the HEA has high temperature strength and considerably lower density. Senkov et al [16] casted HfNbTaTiZr HEA that has bcc structure. This alloy has a hardness of 3.8 GPa and displays high compressive strength of 1 GPa at room temperature. The strengthening of the alloy is attributed to solid solution strengthening and its mechanism is discussed in detail. The compressive properties at high temperatures were also studied [30]. The compressive yield strength of the alloy increased linearly up to 600ºC and then decreased with increase in temperature. The fracture of the compressed samples is due to the cavity formation and the grain boundary sliding. The strength increased with increasing strain rate. Couzinie et al [31] casted the same alloy (HfNbTaTiZr HEA)

which also resulted a bcc structure. The dendritic regions are rich in Nb, Ta and the interdendritic regions have Ti, Zr and Hf. Lilensten et al [17] fabricated a near equiatomic HfNbTaTiZr HEA that resulted in microhardness of 2.4 GPa. This group analyzed the XRD data using Rietveld analysis and for the first time reported an orthorhombic crystal structure in HEAs. Zou et al [32] made interesting investigations on NbMoTaW HEA in equiatomic ratios after casting and homogenizing. This group also addressed the current problem of HEA having less ductility and toughness at room temperatures. Using focused ion beam milling (FIB) single crystal pillars were made and compressed. This alloy exhibits a hardness of 4.5 GPa and significant ductility. Pillar with high size (200 nm) resulted in high hardness. Dislocations created can move out easily in smaller sized pillars resulting in lower hardness values.

4.3.2.5 Mechanical properties of AlCuTaVW HEA

Vickers microindentation was performed to understand the bulk mechanical behavior of AlCuTaVW HEA. Different loads from 100 to 1000 g were employed. The Vickers hardness value, HV is calculated using the formula,

$$HV = \frac{1.854\,P}{L^2} \dots\dots\dots\dots\dots\dots\dots\dots\dots\dots\dots\dots\dots\dots\dots\dots\dots (Eq\ 4.3.2)$$

where P is the applied load and L is the average length of the diagonals of the indentation. The variation of bulk hardness with the load applied is shown in **Fig. 4.3.12**. The hardness of the specimen sintered at 1050 ºC is 14 ± 1 GPa and for the sample sintered at 1250 ºC is 13 ± 1 GPa at 100g load, which is considerably huge in comparison with other refractory HEAs. With increase in applied load to 1000 g, the hardness values were decreasing to 10 ± 1 and 11 ± 0.3 GPa in samples sintered at 1050 and 1250 ºC respectively. There is no much variation in the hardness values with the sintering temperature at all loads. The hardness measurements in the current investigation follow the indentation size effect (ISE). When indentation load increases, the

indentation sizes and depth of the indent increase, thereby the hardness of the material decreases. This is called ISE [33, 34]. Some of the factors contributing to the ISE are formation of dislocation loops on the surface of the indent, different phase interactions with dislocation, difficulty to measure small indent, elastic recovery of the material after indentation, friction between the surface of the material and the indenter, resistance of the material, strain gradient plasticity [35-38]. A reduced ISE is observed at low loads and in ultrafine grains or nanomaterials, where the indentation lengths are very lows [39]. The diagonal lengths of the sample sintered at 1050 and 1250 ºC at 1000 g load are 43.4 ± 2 and 41.6 ± 1 µm respectively.

Tabor [40, 41] gave the empirical relationship between hardness and the yield strength or flow stress of the material as $\sigma_{flow} = H/3$. According to Tabor's equation, the yield strength of AlCuTaVW HEA sintered at 1050 ºC could be around 4.56 GPa and 1250 ºC is 4.36 GPa. The values are higher than conventional alloys and also the refractory HEAs shown in **Table 4.3.2**.

The nanoindentation hardness values of AlCuTaVW HEA measured at 8000 µN peak force and at a loading rate of 1000 µN/s is represented in **Fig. 4.3.13**. The plot clearly demonstrates that the hardness is decreasing with increase in sintering temperature, similar to the trend of Vickers microhardness plot. The microstructure of AlCuTaVW HEA sintered at 875 ºC has a porous structure and contains large sized grains. Indentations are made on grains of size higher than 2.7 µm and resulted an unusual hardness of 18 ± 0.7 GPa. The nanohardness of the specimen sintered at 1050 ºC is 14 ± 0.4 GPa, whereas at 1250 ºC is 13 ± 0.8 GPa. The elastic modulus of the alloy sintered at 1050 ºC is 206 ± 2 GPa, whereas at 1250 ºC is 194 ± 5 GPa.

Babu et al [42] made nanoindentation studies on AlCrFeNiZn synthesized by mechanical alloying and hot pressing at 800 ºC. The nanoindentation tests were performed at 40 mN load for 10 s. 30 h of milling resulted a bcc solid solution and sintering resulted fcc1, fcc2 and bcc phases. The

nanohardness value reported is 7.4 GPa and the elastic modulus is 153 GPa. They reasoned that the presence of Zn with hcp crystal structure created a high lattice distortion which blocked the dislocation mobility.

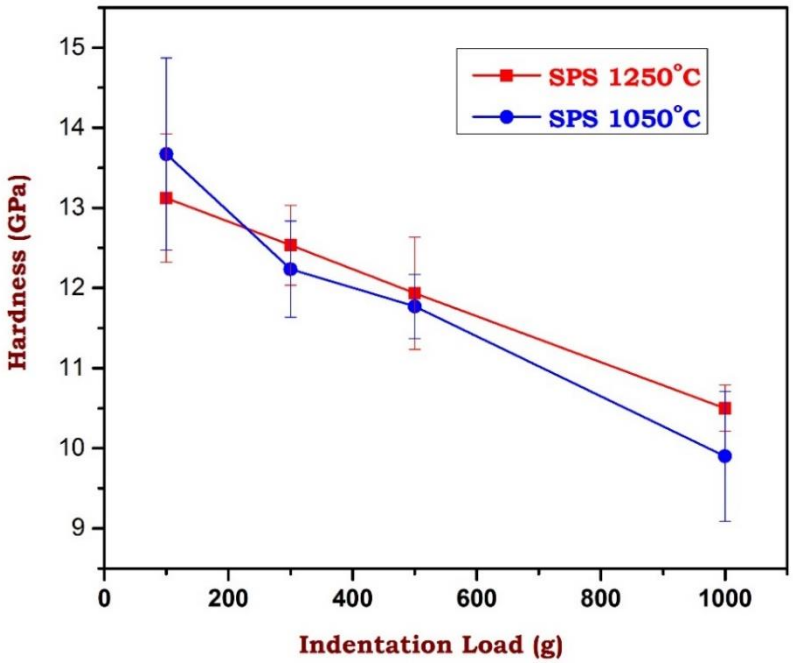

Fig. 4.3.12 Variation of hardness with the load applied of AlCuTaVW HEA sintered alloy.

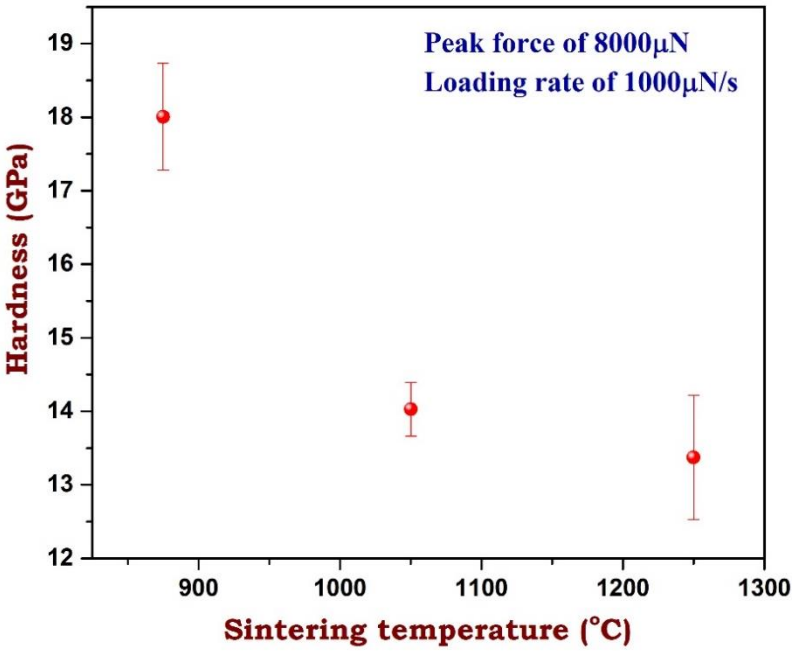

Fig. 4.3.13 The change of hardness with the sintering temperature measured using nanoindentation technique at peak force of 8000 μN load.

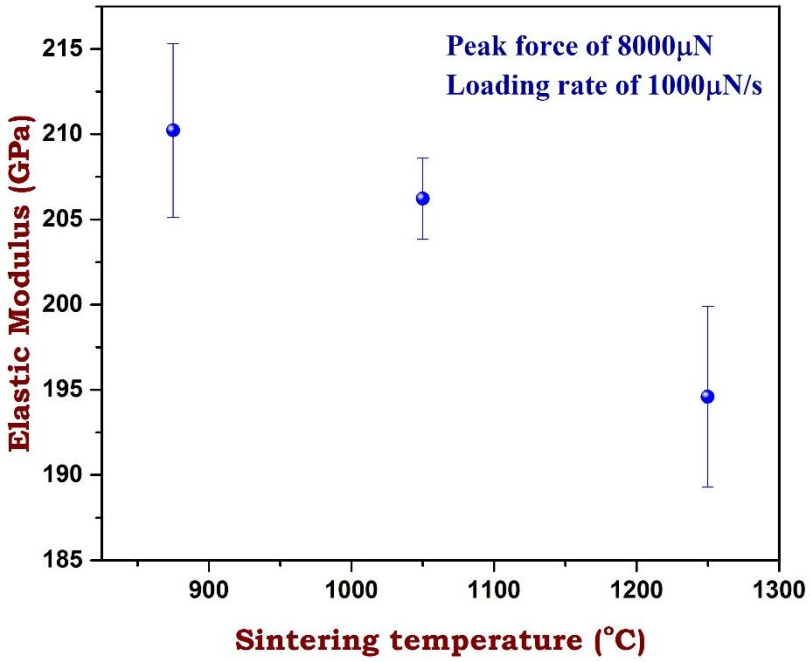

Fig. 4.3.14 The change of elastic modulus with the sintering temperature measured using nanoindentation technique at peak force of 8000 μN load.

Fracture toughness is defined as the amount of energy absorbed by the material to fracture. This is a material property used while designing a material. Fracture toughness is measured by various methods namely single edge notched beam (SENB), chevron notch or single edge pre-cracked beam (SEPB), single edge V notched beam (SEVNB) and indentation fracture (IF) method. IF method uses the crack lengths generated at the tips of the indentation made by the Vickers indenter. The crack length is inversely proportionally to the fracture toughness [43]. The advantage of IF method over other methods is that there are no prior procedural preparations for the test sample. However this method is not accurate when the cracks have sub cracks and it is difficult to measure the exact crack length. Moradkhani et al [44] proposed a new method to estimate the fracture toughness when the cracks are not radial and constitute sub cracks. In such cases the measured linear crack length is inaccurate. Hence they have considered and measured the area of the crack from SEM images using Image analyzer software and used that parameter for calculating fracture

toughness. Strecker et al [43] did a comparative study on SEVNB method and IF method. They found that the fracture toughness values obtained by the IF method are lower than the estimated actual material toughness values. Whereas the SEVNB method resulted more accurate values because of the proper care taken to prepare the V notch. Hence the accuracy in measuring the fracture toughness is primarily dependent on the measurement of crack length rather than formula used. In general, there are two types of cracks formations in IF method. One is Palmqvist crack and other is median/ radial/ half penny crack. The schematic of the crack types is shown in **Fig. 4.3.15**. There are many formulae to estimate the fracture toughness for both the types of cracks [45]. The choice of the formula is based on the type of cracks. Amongst all Shetty formula [46] is widely used to calculate fracture toughness for most of the materials having Palmqvist cracks [45, 47].

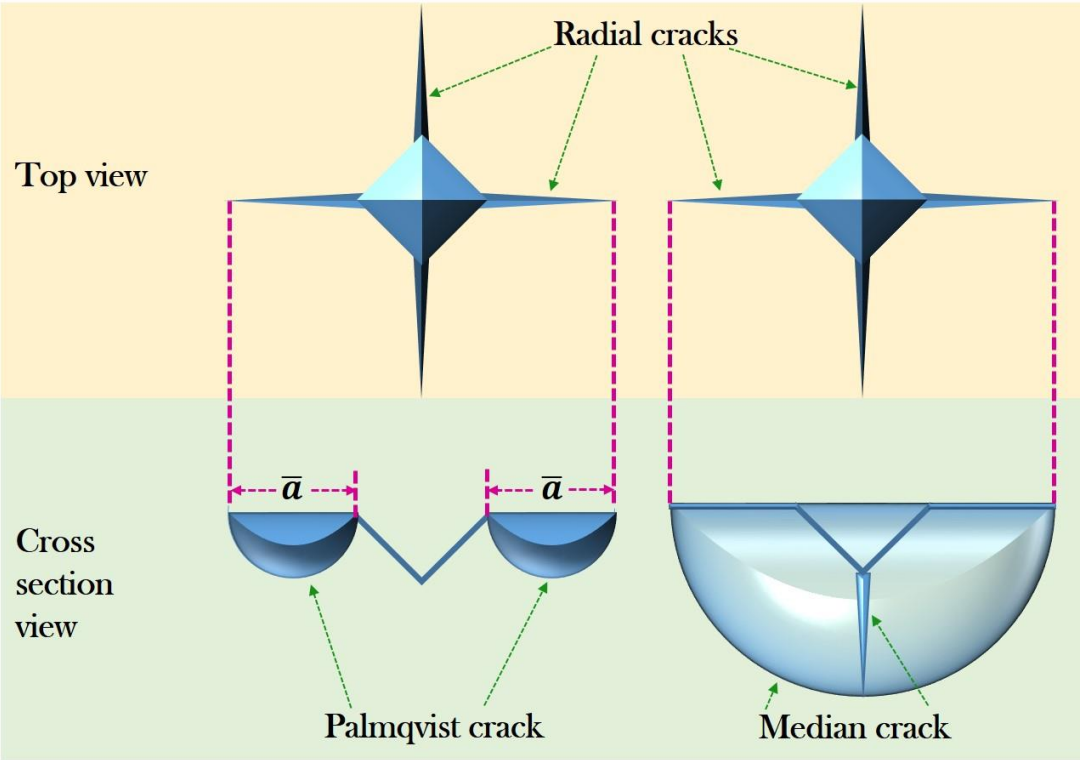

Fig. 4.3.15 Schematic showing different types of crack formation in indentation fracture method (adopted and redrawn from ref. [43]).

Fracture toughness is measured at 3 kg load using indentation micro fracture method (IF) on the sintered specimen. Cracks are visible at the indentation tip/edges as shown in the **Fig. 4.3.16**. All the four crack lengths of the indentation and their diagonal lengths measured from the SEM images are used to calculate the fracture toughness. In the current investigation, from the SEM micrographs of the indentation shown in **Fig. 4.3.16**, it can be observed that the cracks are of Palmqvist type. **Fig. 4.3.16 (a)** is the SEM image of the sample sintered at 875 ºC. As discussed earlier and shown in **Fig. 4.3.8 (a,b)**, the microstructure of the sample sintered at 875 ºC has pores. Therefore the indentation at 3 kg might have landed into the pores and no visible radial cracks were observed. **Fig. 4.3.16 (b)** and **(c)** are the micrographs of the samples sintered at 1050 and 1250 ºC respectively.

The fracture toughness, K_{Ic} is calculated using Shetty formula [46],

$$K_{Ic} = \frac{1}{3(1-\nu^2)\left(2^{\frac{1}{2}}\pi\tan\psi\right)^{\frac{1}{3}}} \frac{(HP)^{\frac{1}{2}}}{(4\,\bar{a})^{\frac{1}{2}}} \ldots\ldots\ldots\ldots\ldots\ldots\ldots\ldots\ldots (Eq\ 4.3.3)$$

where H is the hardness of the material in N/m^2, P is the indentation load in N, ν is the Poisson's ratio. For bcc materials Poisson's ratio is 0.33, ψ is the apex or half of face angle of standard Vickers pyramid indenter ($2\psi = 136°$), $\bar{a}$ is the average radial crack length expressed in m. This formula has been developed to measure the fracture toughness from the Vickers indent crack lengths for brittle materials like WC-Co Cermets. Shetty and his co-workers [46] compared different equations using test data of different materials and surprisingly found that Palmqvist cracks model is more suitable than half penny crack model for WC-Co Cermets. However, modelling Palmqvist cracks or radial/median cracks is difficult than the half penny/median/ radial cracks. To understand the fracture mechanics, they explained the linear load dependence of crack lengths and the relation of fracture toughness with hardness of the material.

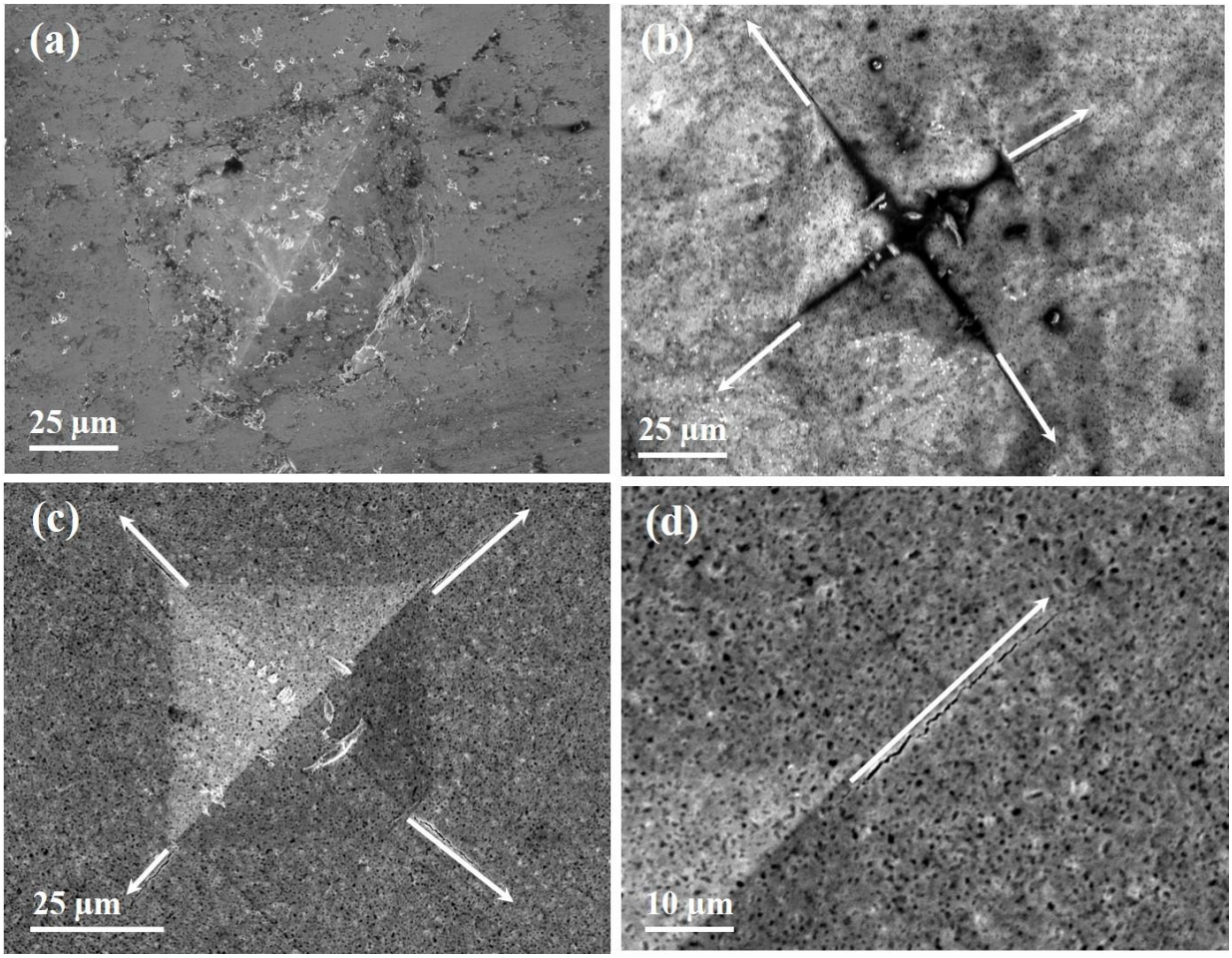

Fig. 4.3.16 SEM images of the radial cracks at the edge of Vickers hardness indentations at 3 Kg load on specimens sintered at (a) 875 ºC, (b) 1050 ºC and (c,d) 1250 ºC.

They assumed that with increasing load the Palmqvist cracks prolong on the surface of the material instead forming a three dimensional surface crack. They included the material property ν (Poisson's ratio) and the apex angle $2\psi = 136°$ of Vickers pyramid indenter in the fracture toughness equation (Equation. 4.3.3). The fracture toughness values of AlCuTaVW HEA milled for 25 h and sintered at 1050 and 1250 ºC are 10.9 and 11 MPa $m^{1/2}$ respectively. To the best knowledge of the authors, the fracture toughness values reported are the highest values using Vickers indentation cracks lengths in HEAs. A very limited literature is available for fracture toughness measured from Vickers indentation cracks in HEAs. The current investigation by

employing the Vickers indentation is first of this kind in measuring the fracture toughness values in HEAs.

Roy et al [15] casted $Al_{23}Co_{15}Cr_{23}Cu_8Fe_{15}Ni_{15}$ HEA resulting in a mixture of bcc and an ordered bcc phase. The fracture toughness was determined by single edge notched bend test and chevron notched rectangular bar test. The fracture toughness values measured are 5.8 MPa $m^{1/2}$ and 5.4 MPa $m^{1/2}$ by respective methods. These values reported are close to NiAl intermetallic materials. Seifi et al [48] studied the fracture toughness and fatigue behavior in cast $Al_{0.2}CrFeNiTi_{0.2}$ and $AlCrFeNi_2Cu$ HEAs. The fracture toughness measured using single edge notch test samples are 33 MPa $m^{1/2}$ and 42 MPa $m^{1/2}$ respectively. Zhang et al [49] fabricated $FeCoNiCrCuTiMoAlSiB_{0.5}$ a 10 element HEA using laser solidification process. This alloy after annealing has a bcc phase and B2 phase. This alloy displayed high fracture toughness of 50.9 MPa $m^{1/2}$. Gludovatz et al [50] studied Cantor alloy (CrMnFeNiCo) in cast form. The microstructure revealed an equiaxed grains after deformation and subsequent annealing treatment. The yield strength measured at room temperature is 350 MPa and at -196 ºC is 600 MPa. The fracture toughness of 6μm grain sized sample using a notch is 200 MPa $m^{1/2}$. It is interesting that the values deduced in the current investigation from IF method are reasonably comparable with values reported in the literature.

The fracture toughness of AlCuTaVW HEA is also compared with high hard ceramics and cermets and are given in Error! Reference source not found.. The fracture toughness of AlCuTaVW HEA s relatively higher than ceramic and cermets. Krüger et al [51] worked on four different Mo-Si-B alloys using mechanical alloying. They have 3 different phases. The fracture toughness was high (12.7 and 13.6 MPa $m^{1/2}$) for a continuous Mo matrix and less (6-6.7 MPa $m^{1/2}$) for intermetallic matrix.

Table 4. 3. 3 Fracture toughness values of various materials of ceramics and cermets.

Materials	Formula		Fracture toughness, MPa $m^{1/2}$	Ref
WC-6.5%Co	Shetty	$K_c = 0.0319\ (P/al^{1/2})$	10	[45]
WC-Co	Shetty	$K_{Ic} = 0.0889\ (HW)^{1/2}$	17.5	[47]
Lanthanum Alumino Silicate glasses	Anstis	$K_c = 0.016\ \frac{F(E/H_v)^{0.5}}{C^{1.5}}$	0.75	[52]
Si_3N_4 Ceramic	Evan	$K_c = 0.079\frac{P}{a^{3/2}}\log\left(4.5\frac{a}{c}\right)$	4.54	[53]
ZTA Ceramic	Evan	$K_c = 0.079\frac{P}{a^{3/2}}\log\left(4.5\frac{a}{c}\right)$	5.19	[53]
ZrO_2 Ceramic	Evan	$K_c = 0.079\frac{P}{a^{3/2}}\log\left(4.5\frac{a}{c}\right)$	5.28	[53]
Al_2O_3 Ceramic	Evan	$K_c = 0.079\frac{P}{a^{3/2}}\log\left(4.5\frac{a}{c}\right)$	4.44	[53]

SiC Ceramic	Antis	$K_c = \chi \left(\frac{E}{H}\right)^{1/2} \frac{P}{a^{3/2}}$	2.3	[54]
WC9Co-1 Cemented carbide	Shetty	$K_{Ic} = 0.0889\ (HW)^{1/2}$	9.29	[55]
WC9Co-2 Cemented carbide	Shetty	$K_{Ic} = 0.0889\ (HW)^{1/2}$	9.07	[55]
WC6Co-1 Cemented carbide	Shetty	$K_{Ic} = 0.0889\ (HW)^{1/2}$	8.90	[55]
WC6Co-1 Cemented carbide	Shetty	$K_{Ic} = 0.0889\ (HW)^{1/2}$	9.03	[55]
WC4Co Cemented carbide	Shetty	$K_{Ic} = 0.0889\ (HW)^{1/2}$	8.62	[55]

4.3.3 Summary

A novel equiatomic AlCuTaVW HEA was successfully fabricated using the mechanical alloying followed by spark plasma sintering. Microstructural features and mechanical properties of the nanocrystalline alloy have been studied in detail. 25 h of milling resulted a single solid solution comprising a bcc crystal structure with a crystallite size of 7 nm and the grain size measured from TEM images is 11 nm. It was seen that sintering at both 1050 and 1250 ºC resulted dense products with better mechanical properties. Two fcc phases and an ordered B2 phase evolved in the alloy after sintering. However the microstructure has two phases, a continuous white phase and a discontinuous dark phase. The Vickers hardness measured at 100 g load for the specimen sintered at 1050 ºC is 14 GPa and for the sample sintered at 1250 ºC is 13 GPa. The yield strength calculated using Tabor equation is 4.6 and 4.3 GPa at 1050 and 1250 ºC sintering temperatures respectively. These values are extraordinarily high when compared to other HEAs, ceramics and cermets. Such a high strength is attributed to the solid solution strengthening, interaction between different phases and the ordering of B2 phase in a disordered lattice. Fracture toughness of nanocrystalline AlCuTaVW alloys is 11 MPa $m^{1/2}$ at both the sintering temperatures of 1050 and 1250 ºC.

References

1. Han Z, Liu X, Zhao S, Shao Y, Li J, Yao K: **Microstructure, phase stability and mechanical properties of Nb–Ni–Ti–Co–Zr and Nb–Ni–Ti–Co–Zr–Hf high entropy alloys**. *Progress in Natural Science: Materials International* 2015, **25**(5):365-369.
2. He JY, Liu WH, Wang H, Wu Y, Liu XJ, Nieh TG, Lu ZP: **Effects of Al addition on structural evolution and tensile properties of the FeCoNiCrMn high-entropy alloy system**. *Acta Materialia* 2014, **62**:105-113.
3. Tung CC, Yeh JW, Shun TT, Chen SK, Huang YS, Chen HC: **On the elemental effect of AlCoCrCuFeNi high-entropy alloy system**. *Materials Letters* 2007, **61**:1-5.

4. Wang XF, Zhang Y, Qiao Y, Chen GL: **Novel microstructure and properties of multicomponent CoCrCuFeNiTix alloys**. *Intermetallics* 2007, **15**(3):357-362.
5. Jiang L, Dong Y, Jiang H, Lu YP, Cao ZQ, Li TJ: **Effect of Ta Addition on Structural Evolution and Mechanical Properties of the $CoFeNi_2W_{0.5}$ High Entropy Alloy**. *Materials Science Forum* 2016, **849**:34-39.
6. Xia S, Yang X, Chen M, Yang T, Zhang Y: **The Al effects of Co-free and V-containing high-entropy alloys**. *Metals* 2017, **7**(1):18.
7. Senkov ON, Wilks GB, Miracle DB, Chuang CP, Liaw PK: **Refractory high-entropy alloys**. *Intermetallics* 2010, **18**(9):1758-1765.
8. Li BS, Wang YP, Ren MX, Yang C, Fu HZ: **Effects of Mn, Ti and V on the microstructure and properties of AlCrFeCoNiCu high entropy alloy**. *Materials Science and Engineering: A* 2008, **498**(1-2):482-486.
9. Tariq NH, Naeem M, Hasan BA, Akhter JI, Siddique M: **Effect of W and Zr on structural, thermal and magnetic properties of AlCoCrCuFeNi high entropy alloy**. *Journal of Alloys and Compounds* 2013, **556**:79-85.
10. Sriharitha R, Murty BS, Kottada RS: **Alloying, thermal stability and strengthening in spark plasma sintered $Al_xCoCrCuFeNi$ high entropy alloys**. *Journal of Alloys and Compounds* 2014, **583**:419-426.
11. Maulik O, Kumar D, Kumar S, Fabijanic DM, Kumar V: **Structural evolution of spark plasma sintered $AlFeCuCrMg_x$ (x = 0, 0.5, 1, 1.7) high entropy alloys**. *Intermetallics* 2016, **77**:46-56.
12. Senkov ON, Wilks GB, Scott JM, Miracle DB: **Mechanical properties of $Nb_{25}Mo_{25}Ta_{25}W_{25}$ and $V_{20}Nb_{20}Mo_{20}Ta_{20}W_{20}$ refractory high entropy alloys**. *Intermetallics* 2011, **19**(5):698-706.
13. Feng XB, Zhang JY, Wang YQ, Hou ZQ, Wu K, Liu G, Sun J: **Size effects on the mechanical properties of nanocrystalline NbMoTaW refractory high entropy alloy thin films**. *International Journal of Plasticity* 2017, **http://dx.doi.org/10.1016/j.ijplas.2017.04.013**.
14. Senkov ON, Woodward CF: **Microstructure and properties of a refractory $NbCrMo_{0.5}Ta_{0.5}TiZr$ alloy**. *Materials Science and Engineering: A* 2011, **529**:311-320.

15. Roy U, Roy H, Daoud H, Glatzel U, Ray KK: **Fracture toughness and fracture micromechanism in a cast AlCoCrCuFeNi high entropy alloy system**. *Materials Letters* 2014, **132**:186-189.
16. Senkov ON, Scott JM, Senkova SV, Miracle DB, Woodward CF: **Microstructure and room temperature properties of a high-entropy TaNbHfZrTi alloy**. *Journal of Alloys and Compounds* 2011, **509**:6043-6048.
17. Lilensten L, Couzinié JP, Perrière L, Bourgon J, Emery N, Guillot I: **New structure in refractory high-entropy alloys**. *Materials Letters* 2014, **132**:123-125.
18. Senkov O, Isheim D, Seidman D, Pilchak A: **Development of a refractory high entropy superalloy**. *Entropy* 2016, **18**(3):102.
19. Senkov ON, Senkova SV, Woodward C, Miracle DB: **Low-density, refractory multi-principal element alloys of the Cr–Nb–Ti–V–Zr system: Microstructure and phase analysis**. *Acta Materialia* 2013, **61**(5):1545-1557.
20. Senkov ON, Senkova SV, Miracle DB, Woodward C: **Mechanical properties of low-density, refractory multi-principal element alloys of the Cr–Nb–Ti–V–Zr system**. *Materials Science and Engineering: A* 2013, **565**:51-62.
21. Kuk SW, Lim WJ, Kim SS, Hong SH, Ryu HJ: **Fabrication of W-Nb-Mo-Ta-V high entropy alloys by mechanical alloying and spark plasma sintering**. *Transactions of the Korean Nuclear Society Spring Meeting* 2015.
22. Moravcik I, Cizek J, Gavendova P, Sheikh S, Guo S, Dlouhy I: **Effect of heat treatment on microstructure and mechanical properties of spark plasma sintered $AlCoCrFeNiTi_{0.5}$ high entropy alloy**. *Materials Letters* 2016, **174**:53-56.
23. Maulik O, Kumar V: **Synthesis of $AlFeCuCrMg_x$ (x=0, 0.5, 1, 1.7) alloy powders by mechanical alloying**. *Materials Characterization* 2015, **110**:116-125.
24. Wang B, Fu A, Huang X, Liu B, Liu Y, Li Z, Zan X: **Mechanical properties and microstructure of the CoCrFeMnNi high entropy alloy under high strain rate compression**. *Journal of Materials Engineering and Performance* 2016, **25**(7):2985-2992.
25. Ji W, Wang W, Wang H, Zhang J, Wang Y, Zhang F, Fu Z: **Alloying behavior and novel properties of CoCrFeNiMn high-entropy alloy fabricated by mechanical alloying and spark plasma sintering**. *Intermetallics* 2015, **56**:24-27.

26. Zhang KB, Fu ZY, Zhang JY, Wang WM, Lee SW, Niihara K: **Characterization of nanocrystalline CoCrFeNiTiAl high-entropy solid solution processed by mechanical alloying**. *Journal of Alloys and Compounds* 2010, **495**:33–38.
27. Wang YP, Li BS, Ren MX, Yang C, Fu HZ: **Microstructure and compressive properties of AlCrFeCoNi high entropy alloy**. *Materials Science and Engineering: A* 2008, **491**(1-2):154-158.
28. Zhang K, Wen G, Dai H, Teng Y, Li Y: **Synthesis and characterization of CrCuFeMnMo$_{0.5}$Ti multicomponent alloy bulks by powder metallurgy**. *Jom* 2014, **66**(10):2043-2049.
29. Liu Y, Wang J, Fang Q, Liu B, Wu Y, Chen S: **Preparation of superfine-grained high entropy alloy by spark plasma sintering gas atomized powder**. *Intermetallics* 2016, **68**:16-22.
30. Senkov ON, Scott JM, Senkova SV, Meisenkothen F, Miracle DB, Woodward CF: **Microstructure and elevated temperature properties of a refractory TaNbHfZrTi alloy**. *Journal of Materials Science* 2012, **47**(9):4062-4074.
31. Couzinié JP, Dirras G, Perrière L, Chauveau T, Leroy E, Champion Y, Guillot I: **Microstructure of a near-equimolar refractory high-entropy alloy**. *Materials Letters* 2014, **126**:285-287.
32. Zou Y, Maiti S, Steurer W, Spolenak R: **Size-dependent plasticity in an Nb$_{25}$Mo$_{25}$Ta$_{25}$W$_{25}$ refractory high-entropy alloy**. *Acta Materialia* 2014, **65**:85-97.
33. Nix WD, Gao H: **Indentation size effects in crystalline materials: A law for strain gradient plasticity**. *Journal of the Mechanics and Physics of Solids* 1998, **46**(3):411-425.
34. Gerberich WW, Tymiak NI, Grunlan JC, Horstemeyer MF, Baskes MI: **Interpretations of Indentation Size Effects**. *Journal of Applied Mechanics* 2002, **69**(4):433.
35. Mukhopadhyay NK, Paufler P: **Micro- and nanoindentation techniques for mechanical characterisation of materials**. *International Materials Reviews* 2006, **51**(4):209-245.
36. Swadener JG, Misra A, Hoagland RG, Nastasi M: **A mechanistic description of combined hardening and size effects**. *Scripta Materialia* 2002, **47**:343–348.
37. Elmustafa AA, Stone DS: **Indentation size effect in polycrystalline F.C.C. metals**. *Acta Materialia* 2002, **50**:3641-3650.

38. Elmustafa AA, Stone DS: **Nanoindentation and the indentation size effect: Kinetics of deformation and strain gradient plasticity**. *Journal of the Mechanics and Physics of Solids* 2003, **51**:357–381.
39. Marr T, Freudenberger J, Maier V, Höppel H, Göken M, Schultz L: **The strengthening effect of phase boundaries in a severely plastically deformed Ti-Al composite wire**. *Metals* 2014, **4**(1):37-54.
40. Tabor D: **The hardness and strength of metals**. *Journal of the Institute of Metals* 1951, **79**:1-18.
41. Hutchings IM: **The contributions of David Tabor to the science of indentation hardness**. *Journal of Materials Research* 2011, **24**(03):581-589.
42. Babu CS, Koundinya NTBN, Sivaprasad K, Szpunar JA: **Thermal analysis and nanoindentaion studies on nanocrystalline AlCrNiFeZn high entropy alloy**. *Procedia Materials Science* 2014, **6**:641-647.
43. Strecker K, Ribeiroa S, Hoffmannb M-J: **Fracture toughness measurements of LPS-SiC: A comparison of the indentation technique and the SEVNB method**. *Materials Research* 2005, **8**(2):121-124.
44. Moradkhani A, Baharvandi H, Tajdari M, Latifi H, Martikainen J: **Determination of fracture toughness using the area of micro-crack tracks left in brittle materials by Vickers indentation test**. *Journal of Advanced Ceramics* 2013, **2**(1):87-102.
45. Bouteghmes D, Hamidouche M, Bouaouadja N: **Study of indentation fracture toughness of WC-6.5% Co cermet**. *International Review of Mechanical Engineering* 2012, **6**(4):803-809.
46. Shetty D K, Wright I G, Mincer P N, H CA: **Indentation fracture of WC-Co cermets**. *Journal of Materials Science* 1985, **20**:1873-1882.
47. Spiegler R, Schmauder S, Sigl LS: **Fracture toughness evaluation of WC-Co alloys by indentation testing**. *Journal of hard materials* 1990, **1**(3):147-158.
48. Seifi M, Li D, Yong Z, Liaw PK, Lewandowski JJ: **Fracture toughness and fatigue crack growth behavior of as-cast high-entropy alloys**. *Jom* 2015, **67**(10):2288-2295.
49. Zhang H, He Y, Pan Y: **Enhanced hardness and fracture toughness of the laser-solidified FeCoNiCrCuTiMoAlSiB$_{0.5}$ high-entropy alloy by martensite strengthening**. *Scripta Materialia* 2013, **69**(4):342-345.

50. Gludovatz B, George EP, Ritchie RO: **Processing, microstructure and mechanical properties of the CrMnFeCoNi high-entropy alloy**. *Jom* 2015, **67**(10):2262-2270.

51. Krüger M, Jain P, Kumar KS, Heilmaier M: **Correlation between microstructure and properties of fine grained Mo-Mo_3Si-Mo_5SiB_2 alloys**. *Intermetallics* 2014, **48**:10-18.

52. Tiegel M, Hosseinabadi R, Kuhn S, Herrmann A, Rüssel C: **Young′s modulus, Vickers hardness and indentation fracture toughness of alumino silicate glasses**. *Ceramics International* 2015, **41**(6):7267-7275.

53. Ma D, Wang J, Sun L: **Methodology for measuring fracture toughness of ceramic materials by instrumented indentation test with vickers indenter**. *Journal of the American Ceramic Society* 2017.

54. Kruzic JJ, Ritchie RO: **Determining the Toughness of Ceramics from Vickers Indentations Using the Crack-Opening Displacements: An Experimental Study**. *Journal of American Ceramic Society* 2003, **86**(8):1433-1436.

55. Aleksandrov Fabijanić T, Ćorić D, Šnajdar Musa M, Sakoman M: **Vickers indentation fracture toughness of near-nano and nanostructured WC-Co cemented carbides**. *Metals* 2017, **7**(4):143.

Chapter 5 Summary and Conclusions

High entropy alloys (HEAs) are the materials having 5 or more elements in equal atomic ratios. Such materials are forming simple solid solutions instead of complex intermetallic phases. The reason for such formation is high enthalpy of mixing. These HEAs display better microstructural and mechanical properties. And the reasons for good properties is explained using four core effects, high mixing entropy effect, sluggish diffusion effect, the lattice distortion effect and the cocktail effect. The present work is on the AlCoCrCuFeNi and AlCuTaVW HEA. The materials have been synthesized using mechanical alloying for 60 h and 25 h respectively. The powders were consolidated into bulk materials using spark plasma sintering at different temperatures and holding durations. Both the powdered samples and the bulk samples are characterized to know the structural evolution and the mechanical properties. Structure property correlations is done in detail.

AlCoCrCuFeNi HEA contains a simple solid solution with fcc crystal structure after 60 h of mechanical alloying and its precise lattice parameter is computed to be 3.641 Å. The 60 h milled powders have "plate-like" morphology. The average grain size measured from the TEM dark field images is about 10 ± 6 nm and the d-spacing measured from HRTEM image planes is 2.05 Å with a well distorted lattice. The lattice parameter and the d-spacing are well close to Cu element. It was observed that the processing method and associated process parameters influence the structural as well as microstructural evolution in HEAs. Consolidation using SPS resulted an additional ordered B2 phase along with fcc phase. The precise lattice parameter of fcc phase is 3.598±0.001 Å and B2 phase is 2.920±0.001 Å. The average grain size of the sintered alloy displayed a bimodal distribution of 112 nm and 1550 nm. The microstructure revealed the presence of twins in both the grains with different sizes.

Strengthening mechanisms have been studied for the ultrafine AlCoCrCuFeNi HEA fabricated by mechanical alloying and subsequent spark plasma sintering at 750 ºC temperature. The bulk behavior of the sintered sample has been evaluated using Vickers microindentation and depth sensing nanoindentation where indentations are made using higher loads such that maximum volume of the material can be deformed and studied. The microhardness of AlCoCrCuFeNi HEA is 6.5 GPa, the nanohardness is 8.13 GPa and the elastic modulus is 172 GPa. Using Tabor's equation, the yield strength of the material is calculated as 2.16 GPa. The results reported are superior to the AlCoCrCuFeNi alloys synthesized using other techniques and also to other HEAs with different compositions. As the microstructure of AlCoCrCuFeNi HEA has two phases (fcc and B2), different grain sizes and nano twins, the strengthening contributions could be from 5 different factors. The individual contributions have been evaluated and reported in the current investigation. The frictional stress due to the interaction between the lattice and the mobile dislocation is 105MPa. Taylor hardening rising due to the dislocation interaction with the larger grains is calculated to be 949 MPa. Hall-Petch strengthening is based on the bimodal distribution of grains and the contribution is computed to be 1070 MPa. The solid solution strengthening is owing to fcc and B2 phases. The contribution of solid solution strengthening is assumed to be 112 MPa. The contribution of twin boundary strengthening to overall strengthening of the material is 143MPa arising from the twin formed in the grains. The addition of strength values from all factors is 2.3 GPa. This result is in close agreement with the yield strength. Among all Taylor hardening and Hall-Petch strengthening are major contributors to the strength of the material. Strain rate sensitivity (SRS) calculated from nanoindentation data is 0.0084 and the activation volume is 13 b^3. SRS and the activation volume values reported are apparent values because of high loads used

while indentations to deform more volume of the material. Hence it is concluded that the reason for the low SRS and the activation volume is the interactions by the interfaces of grain boundaries, twin boundaries and fcc/B2 interphase boundaries.

The novel AlCuTaVW HEA is synthesized using 25 h of mechanical alloying and consolidation is done using SPS at different temperatures. The combination of elements with different strengths are intended to have reasonable ductility and strength in the alloy. The 25 h of mechanical alloying resulted a nanocrystalline material with a bcc phase having 7 nm crystallite size. The theoretical density of AlCuTaVW HEA calculated using rules of mixtures is 11 g/cc. Sintering of the milled powder is carried at 875, 1050 and 1250 ºC sintering temperatures. The samples sintered at 875, 1050 and 1250 ºC sintering temperatures have absolute density of 8.7, 11.02 and 11.5 g/cc respectively. Samples sintered at 875 ºC have two bcc phases, among them the major phase is the same phase formed while mechanical alloying. Its microstructure has pores and voids. Sample with sintering temperature as 1050 ºC resulted fcc1, fcc2, bcc and an ordered B2 phase. Consolidation at 1250 ºC evolved two fcc phases and an ordered B2 phase. The latter two alloys have a continuous white phase and a discontinuous Al rich dark phase homogenously distributed in the white phase in the microstructure. The microhardness and the nanohardness measured is 14 GPa and 13 GPa for the samples sintered at 1050 and 1250 ºC respectively. Fracture toughness is measured from the crack lengths generated at the tips of the indentation made by the Vickers indenter at 3 Kg load. Shetty formula is used to calculate fracture toughness using the lengths of the cracks at the tip of the indents. Fracture toughness of AlCuTaVW HEA is calculated as 10.9 and 11 MPa $m^{1/2}$ for samples sintered at 1050 and 1250 ºC respectively. The reported values are high when compared to WC materials, ceramics and cermets.

Chapter 6 Future scope of work

- In AlCoCrCuFeNi HEA, nano twins are formed during SPS in both the grain sizes. The detailed study on twin coherency could be conducted.
- The TEM analysis of sintered AlCuTaVW HEA may be carried to understand the reasons for high hardness and high fracture toughness.
- AlCuTaVW HEA displayed a brittle nature. To balance the strength and ductility of the alloy, the composition could be modified and studied. Preferably decreasing the W concentration and increasing the Al and Cu concentration.
- An intermittent milling process may be employed to preferentially incorporate second phase. Thereby increasing the mechanical properties of the alloy.
- AlCuW and CuTaV HEAs could be synthesized and studied to know the individual effect of the elements on the system.